AFRL-RX-TY-TR-2010-0092

FIRST-PRINCIPLE SIMULATION OF BLAST BARRIER EFFECTIVENESS FOR THE DEVELOPMENT OF SIMPLIFIED DESIGN TOOLS

Bryan T. Bewick
Air Force Research Laboratory
139 Barnes Drive, Suite 2
Tyndall Air Force Base, FL 32403-5323

Ian Flood
University of Florida
Rinker School, Department of Design, Construction, and Planning
331 Arch, P.O. Box 115701
Gainesville, FL 32611

DECEMBER 2010

**AIR FORCE RESEARCH LABORATORY
MATERIALS AND MANUFACTURING DIRECTORATE**

■ **Air Force Materiel Command** ■ **United States Air Force** ■ **Tyndall Air Force Base, FL 32403-5323**

DISCLAIMER

Reference herein to any specific commercial product, process, or service by trade name, trademark, manufacturer, or otherwise does not constitute or imply its endorsement, recommendation, or approval by the United States Air Force. The views and opinions of authors expressed herein do not necessarily state or reflect those of the United States Air Force.

This report was prepared as an account of work sponsored by the United States Air Force. Neither the United States Air Force, nor any of its employees, makes any warranty, expressed or implied, or assumes any legal liability or responsibility for the accuracy, completeness, or usefulness of any information, apparatus, product, or process disclosed, or represents that its use would not infringe privately owned rights.

NOTICE AND SIGNATURE PAGE

BRYAN T. BEWICK, PhD
Work Unit Manager
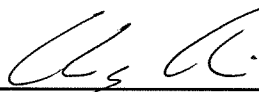
CHRISTOPHER L. GENELIN, Captain, USAF
Chief, Engineering Mechanics Section

ALBERT N. RHODES, PhD
Chief, Airbase Technologies Division

REPORT DOCUMENTATION PAGE

Form Approved
OMB No. 0704-0188

1. REPORT DATE *(DD-MM-YYYY)*	2. REPORT TYPE	3. DATES COVERED *(From - To)*
29-DEC-2010	Interim Technical Report	01-OCT-2008 -- 21-MAY-2010

4. TITLE AND SUBTITLE	5a. CONTRACT NUMBER
First-Principle Simulation of Blast Barrier Effectiveness for the Development of Simplified Design Tools	FA8903-08-D-8768-0002

5b. GRANT NUMBER

5c. PROGRAM ELEMENT NUMBER
0909999F

6. AUTHOR(S)	5d. PROJECT NUMBER
*Bewick, Bryan t.; **Flood, Ian	GOVT

5e. TASK NUMBER
F0

5f. WORK UNIT NUMBER
QF101000

7. PERFORMING ORGANIZATION NAME(S) AND ADDRESS(ES)	8. PERFORMING ORGANIZATION REPORT NUMBER
**University of Florida, Rinker School, Department of Design, Construction, and Planning, 331 Arch, P.O. Box 11570, Gainesville, FL 32611	

9. SPONSORING/MONITORING AGENCY NAME(S) AND ADDRESS(ES)	10. SPONSOR/MONITOR'S ACRONYM(S)

*Air Force Research Laboratory
  Materials and Manufacturing Directorate
  Airbase Technologies Division
  139 Barnes Drive, Suite 2
  Tyndall Air Force Base, FL 32403-5323
	AFRL/RXQEM

	11. SPONSOR/MONITOR'S REPORT NUMBER(S) AFRL-RX-TY-TR-2010-0092

12. DISTRIBUTION/AVAILABILITY STATEMENT

Distribution Statement A: Approved for public release; distribution unlimited.

13. SUPPLEMENTARY NOTES

Ref AFRL/RXQ Public Affairs Case # 10-198. Document contains color images.

14. ABSTRACT
Blast barrier walls have been shown to reduce the blast load on structures in most scenarios. Analysis of existing data for blast barrier response reveals that a need exists to determine the bounds of the problem and produce a fast-running accurate model for the effects of barrier walls on blast wave propagation. Since blast experiments are very time intensive and extremely cost prohibitive, it is vital that computational capabilities be developed to generate the required data set that can be utilized to produce simplified design tools. The combination of high fidelity first principles model-based simulation with artificial neural network techniques for providing solutions to blast barrier problems results in a very effective means to tackle the challenging problem. A review of current methods of modeling blast wave propagation identifies a need for a modeling approach that is both fast and versatile in its scope for application. Artificial neural network approaches to modeling the propagation of blast waves in a built-up environment are developed. A comprehensive study of numerical simulation approaches for modeling blast propagation is presented and applied to populating data for blast barrier site configurations. The proposed approach is demonstrated to estimate the peak pressure, impulse, time of arrival, and time of duration of blast loads on buildings protected by simple barriers, using data generated from validated computational hydrocode simulations. Once verified and validated, the proposed neural-network model-based simulation procedure provides an efficient engineering tool for predicting blast loads on structures which are protected by blast barrier walls.

15. SUBJECT TERMS

blast barrier, artificial neural network, blast modeling, simplified design tool

16. SECURITY CLASSIFICATION OF:			17. LIMITATION OF ABSTRACT	18. NUMBER OF PAGES	19a. NAME OF RESPONSIBLE PERSON
a. REPORT	b. ABSTRACT	c. THIS PAGE			Bryan Bewick
U	U	U	UU	212	19b. TELEPHONE NUMBER *(Include area code)*

Reset

Standard Form 298 (Rev. 8/98)
Prescribed by ANSI Std. Z39.18

TABLE OF CONTENTS

LIST OF FIGURES

LIST OF TABLES

1. SUMMARY

Blast barrier walls have been shown to reduce the blast load on structures in most scenarios. Analysis of existing data for blast barrier response reveals that a need exists to determine the bounds of the problem and produce a fast-running, accurate model for the effects of barrier walls on blast wave propagation. Since blast experiments are very time intensive and extremely cost prohibitive, it is vital that computational capabilities be developed to generate the required set of results that can be utilized to produce simplified design tools. The combination of high-fidelity first-principles-model-based simulation with artificial neural network techniques for providing solutions to blast barrier problems results in a very effective means to tackle this challenging problem. A review of current methods of modeling blast wave propagation identifies a need for a modeling approach that is both fast and versatile in its scope for application. Artificial neural network approaches to modeling the propagation of blast waves in a built-up environment are developed. A comprehensive study of numerical simulation approaches for modeling blast propagation is presented and applied to populating data for blast barrier site configurations. The proposed approach is demonstrated to estimate the peak pressure, impulse, time of arrival, and time of duration of blast loads on buildings protected by simple barriers, using data generated from validated computational hydrocode simulations. Once verified and validated, the proposed neural-network-model-based simulation procedure provides an efficient engineering tool for predicting blast loads on structures protected by blast barrier walls.

2. INTRODUCTION

There is an important class of problems involving the effectiveness of blast barrier protective walls that are used to protect structures and facilities from blast threats. Blast barrier protective walls are often used to protect structures and facilities by creating a perimeter security setup that doubles as protection against varying levels of blast threats. Blast barrier walls can be designed to be architectural and blend into urban environments, or may be in the form of metal revetments or bastions for expeditionary environments. The most common forms of blast barrier walls include concrete or masonry walls in urban environments. For expeditionary environments, the most common implementations of blast barrier walls include metal revetments, T-walls, Texas barriers, earth-filled bastions, or earthen berms. Anti-climb steel fences are also utilized by security engineers to enforce standoff distances, although this class of protective perimeter wall does not provide the same blast protection as typical blast barrier walls. These blast walls, when used efficiently, increase the level of protection for military and government facilities in multiple aspects.

Department of Defense (DoD) and Government agencies are constantly facing threats from insurgents and terrorist organizations. Most of these threats come in the form of explosive charges placed in satchels, backpacks, cars, small trucks, large trucks, and even dump trucks. There are countless examples of such threats. Arguably the most recognizable event of this type in recent United States history is the bombing of the Oklahoma City Alfred P. Murrah Federal Building (Oklahoma City National Memorial & Museum History). Timothy McVeigh drove a small moving van close the structure and detonated a large amount of explosives, killing 168 people in the process. In 1998, suicide bombers parked trucks laden with explosives outside US embassies in Dar es Salaam, Tanzania and Nairobi, Kenya (1998 United States Embassy Bombings). It was estimated that there were 212 killed and 4,000 injured in Nairobi, and 11 killed and 85 wounded in Dar es Salaam. More recently, a Danish embassy in Islamabad, Pakistan, was attacked in 2008 (2008 Danish Embassy Bombing in Islamabad). The attacker drove a sedan up to the gate of the embassy and detonated a charge killing between 6 and 8 and injuring about 27. Also in 2008, an attack was carried out on a civilian building at the Islamabad Marriott Hotel (Islamabad Marriott Hotel Bombing). In this attack, a dump truck was laden with explosives. The Marriott hotel had a perimeter wall and the vehicle was stopped at the gate. It subsequently detonated and was a large enough explosive device that there was a great amount of damage. There are several other examples of such attacks. With the constant threat of vehicle bombs in both expeditionary and urban environments, the use of every security measure available is of the utmost importance. Blast barrier walls are the first line of defense against such threats and are deployed for this reason around government and military facilities for increased levels of protection.

The implementation of blast barrier walls provides a means of protection by increasing the two factors that impact the magnitude of the blast pressure loading imposed upon structural components during a blast event. The first factor, which is inherently affected by the placement of barrier walls, is the standoff of any possible event. This factor is site dependent, but is very important because the magnitude of the peak reflected pressure and reflected impulse decays exponentially as the standoff is increased. The second factor that bears heavily upon the resulting structural loads is the time of arrival. The height of the barrier can be configured to force the blast wave to propagate a longer distance. A longer time of arrival greatly reduces the blast pressures.

Given the importance of the increased protection afforded with the use of blast barrier walls, there is a need to have simplified design tools to help blast engineers develop site layouts and designs that provide increased perimeter protection for government and military facilities. A survey of available approaches for predicting blast loads on structures that are protected by blast walls identifies a need for better approaches for both accuracy and efficiency. The goal of the work contained herein is to develop a simplified tool for blast engineers to design perimeter blast walls efficiently and accurately. With the use of a few parameters, a blast engineer should be able to quickly examine the factors of how a particular configuration will affect the blast loads to the structure of interest. In this way, the engineer can iterate on several site layouts and perimeter blast wall designs to find the most advantageous configuration.

Section 3 reviews a background of the work done to date on producing blast barrier design tools. The utility of blast walls is considered. A review of blast barrier design tools produced to date shows there is still a need for accurate and efficient design tools for predicting peak pressure, peak impulse, time of arrival and duration.

Section 4 summarizes the approach to developing the simplified blast barrier design tool. It is proposed that computational modeling is used to develop a matrix of blast data, which can be used to train an artificial neural network (ANN) model for predicting blast loads on a structure protected by a blast barrier wall. The scope of experiments required for training the ANN models is developed and the matrix of computational experiments to be simulated is presented.

The approach of using an ANN to predict blast loads on structures protected by blast barrier walls is explored in Section 5. Initial studies are performed to confirm the validity of the ANN approach. The results show that the ANN technology is capable of learning the data sufficiently to be able to produce a predictive methodology for predicting blast loads on structures that are protected by blast barriers.

The computational modeling implemented to produce the data required to train the ANN models must be proven to be accurate. Section 6 explores the possibilities of computational modeling tools that are available for completing such a task. Grid convergence studies are performed and the chosen codes are then validated against live blast experiments.

In Section 7 the modeling approach for producing the computational experimental results is presented, the effectiveness of blast barrier walls in the range of data explored is discussed, and the ANN models are developed. A study of the most-accurate method for training the ANN models is presented. The ANN models are then tested against randomly generated test data that have not been included in the training of the ANN models. The performance of the ANN models is discussed.

The results of this research are ANN models for structure loads as well as roof loads. The ANN models are trained for predicting peak pressure, peak impulse, time of arrival of the peak pressure, and the positive phase duration each for the structure face and the roof surface. Each of these models predicts loads along the height as well as the width of the structure and roof surface. Accuracy and the benefits of the methodology are discussed.

3. BACKGROUND

3.1. Blast Wall Concepts

A blast barrier wall is a perimeter wall that is placed around the property edge of a building, facility, or compound. The intention of having such a wall is twofold. The wall mitigates the level of blast loading that propagates to the asset that is to be protected. It also provides an effective means of forcing a standoff for any blast threat. It ensures that any vehicles containing explosive threats cannot get any closer to the asset than the perimeter blast wall. It is important to have the blast wall rated to be an anti-ram wall so that there is not a threat of vehicles' ramming through the walls and setting off an explosive device.

Blast walls affect the way that a structure is loaded under a blast event. A blast load in general is very different from a traditional dynamic load. In an explosion event, high energy from the explosive is transferred into the air in the form of a high-density shock wave. This shock wave propagates through the atmosphere shocking up the air it impacts along the way. When the shock wave impacts a rigid surface, the band of high-density air that defines the shock wave is compressed against the rigid surface as it is forced to reflect off of the surface. This produces a higher pressure than if the shock wave were propagating through the air unimpeded. The reflection creates the peak pressure loading to the structure and is often referred to as the peak reflected pressure. Blast loads have a peak pressure that decays exponentially over a very short duration (Baker, 1973) compared to common dynamic loading events such as wind loads. The blast pressure is a very high load, but is applied to a structure over a matter of only milliseconds. As the blast wave reflects away from the structure, it generates a vacuum that causes the air pressure to drop below the ambient air pressure, or 100 kPa (14.7 psi) at sea level. This is called the negative phase. The area under the pressure–time history curve is called the *impulse* and is a measure of the energy imparted to the structural components. These terms are illustrated in Figure 1.
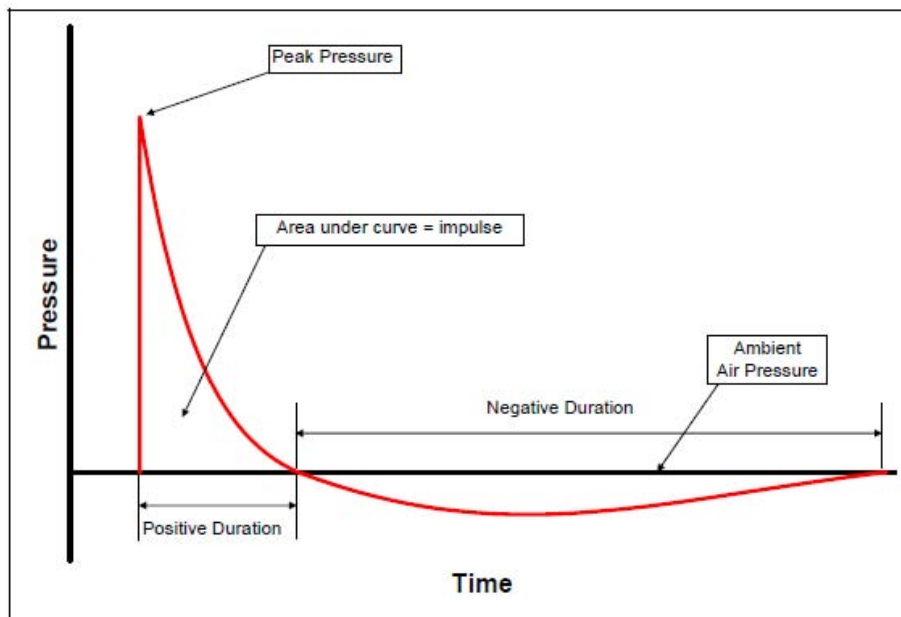

Figure 1. Typical Free-Field Blast Loading on Structure

4

In blast-resistant design, structural components are often termed pressure-sensitive or impulse-sensitive. This is a term that relates the natural dynamic frequency to the duration of the load. Due to the short duration of blast loads, often only a matter of milliseconds, components with high natural frequencies are more sensitive to the peak pressure than to the impulse. In contrast, low-natural-frequency components are more sensitive to the total energy, related to impulse, that is imparted to the component or system. Windows are an example of a component that is pressure-sensitive. Windows are very stiff with low mass. They react very quickly to the imparted load and are more sensitive to a variation in the peak reflected pressure. Concrete components, on the other hand, are very massive with a low modulus. They have a low natural frequency and are slow to react to the blast load (high natural period of oscillation), thus they are more sensitive to impulse loadings. The separator between pressure-sensitive and impulse-sensitive materials is whether they are likely to reach the peak deflection within the positive-phase duration of the loading event. Referring to the examples previously mentioned, windows often vibrate very quickly and have reached their peak deflection within the positive phase duration of the loading, whereas concrete components often don't achieve their peak deflection until after the positive phase duration has expired. The negative phase is often ignored for blast design. This is done because it is conservative to ignore the negative phase in most cases. For pressure-sensitive components, it does not have a great effect. For impulse-sensitive components, including the negative phase reduces the overall impulse imparted to the system. The effect is case dependent and related to the natural frequency of the impulse-sensitive components in question and is generally treated at the discretion of the engineer. In large components, such as concrete tilt-up panels, multi-story cast-in-place concrete structures, etc. the negative phase will greatly increase accuracy of the predictions and reduce the costs of constructing rigid connectors for a more demanding design load. This is the case for components whose natural period of oscillation is sufficiently large that the entire blast load, positive and negative phase, has been applied to the component before the peak deflection has been reached.

The inclusion of blast barrier walls around the perimeter of a facility changes the way that a blast load impacts a structure. As illustrated in Figure 2, the initial shock wave is reflected off the barrier wall. Blast wave propagation is not a linear vector motion. The high energy from the
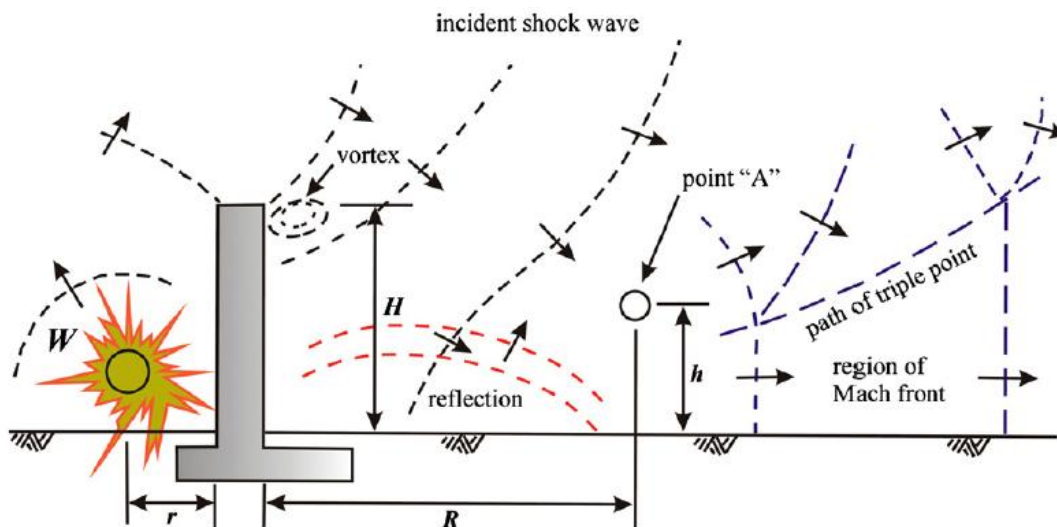
Figure 2. Blast Wave Interaction with Blast Barrier from (Beyer, 1986)

explosive creates high-density air, which expands in every direction possible. This means that the blast wave propagates to the top of the blast wall. There is a small vortex at the top of the blast wall similar to fluid flows. The air then expands in every direction once free of the top of the wall. Referring to point "A" in Figure 2, this point gets a blast pressure from the incident wave propagating in a straight line from the top of the barrier as well as a second peak from the wave that has propagated and reflected off of the ground. This situation is compounded when a structure is present. Depending upon the configuration, if a structure is up very close against a blast wall, the number of spikes in pressure can be two, three or more.

The load that is imparted to a structure that is protected by a blast wall is a non-linear problem to solve. As discussed, the load can have several spikes in pressure. If the barrier-to-structure stand-off is large enough, the blast wave reforms and pressure–time history plots show results similar to the free-field case, for which there is a single spike in pressure followed by an exponential decay as in Figure 1. Figure 3 shows an example of a blast load on a structure protected by a blast barrier wall from an experiment that is presented later in Section 5. Four major spikes in pressure appear in this particular plot. The number of spikes changes above the height of the barrier. Each spike in pressure affects the amount of impulse imparted to the structure.
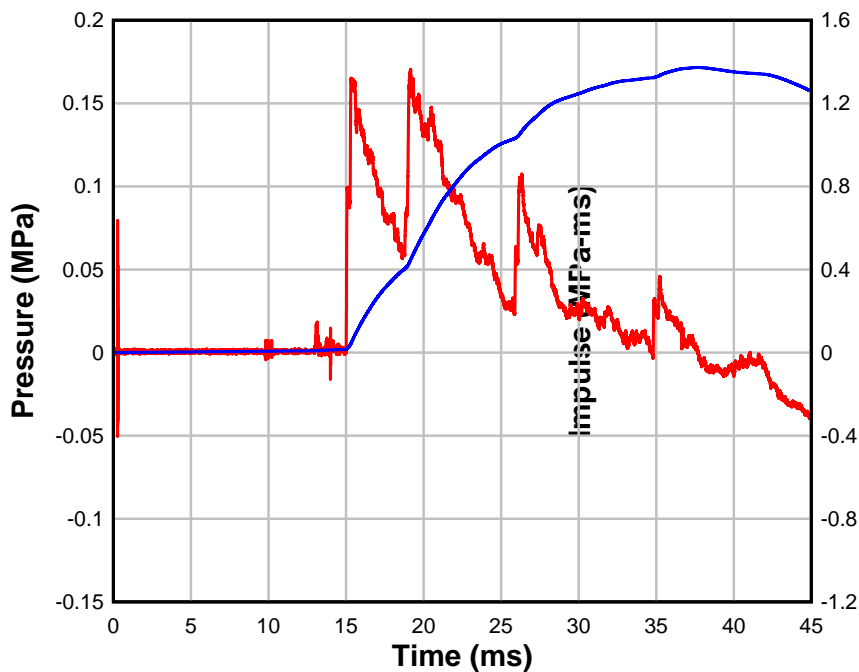
Figure 3. Example Structure Blast Load behind Blast Wall

Blast walls are implemented in several different ways, whether it is in an urban environment or in an expeditionary environment. The most likely implementation of a blast wall is a robust wall, both massive and of strong construction. These designs are intended to be constructed for a permanent facility and are most likely to be used in an urban setting. Examples of a rigid design would be a form-in-place concrete wall, or possibly a concrete masonry unit (CMU) wall. The concept with a robust, rigid design is that the blast wall is designed to be massive enough to withstand high blast loads and absorb some energy from the explosion by being massive. Blast

threats against blast barrier walls are typically located at small standoff distances from the barrier wall. Rigid designs have a high enough natural frequency compared to the duration of the load with small standoff distances that they often do not deflect until late-time, thus the effect of the blast wall is the same as a rigid wall. Even if they are not robust enough to fully take the blast load, the durations are typically short enough that the rigid wall assumption holds.

There are weaker versions of blast walls as well. Examples of this would be metal revetment walls or bastion-type walls that experience large deflections, but their motion is slow enough that the blast shock wave is past the wall before the wall moves to its peak deflection. These types of walls are often soil filled, thus they are very massive with low stiffness. Soil-filled walls are most often used in expeditionary environments and require large thicknesses to provide the stability and mass required to maintain proper levels of protection. Another version that is commonly used in expeditionary environments includes vehicle barriers such as T-walls and Texas barriers. These versions are often implemented more for perimeter security, but can be secured to act as a blast perimeter wall.

Great care must be taken when designing and implementing any type of protective blast wall. If the walls are not designed properly, high loads can cause failures in which the wall fragments and releases flying objects that impact the structure and generate localized impact loads. Energy will be absorbed to a certain degree by the failed wall. However, the impact is that the structure is required to resist both blast and fragmentation loads. Fragmentation threats can be very difficult to predict and design against.

3.2. Methodologies for Analyses of Blast Barrier Performance

Predicting blast loads on structures in an open-air environment is something that is well understood (UFC 3-340-01, 2002; TM5-1300, 1990). For the basic case of free-field blast propagation, the shock front propagates unimpeded and compresses against the structure face, creating a higher peak reflected pressure. The shock wave then reflects and propagates in the opposite direction. Duration of the reflected pressure is affected by the structure size and the amount of the shock front that bleeds around the edges of the structure. These conditions are all well-understood and -described by prediction methodologies, which will be referred to as the TM5-1300 method in this report (UFC 3-340-01, 2002; TM5-1300, 1990; Baker 1973). The solution to prediction of blast loads on structures is greatly complicated by the presence of a blast barrier wall. Blast pressures and impulse are reduced due to the greater distance that the shock front has to travel to propagate over the height of the blast wall. This configuration is a non-linear problem. Depending on the specific configuration of the charge weight, W, the charge to barrier standoff, d_1, the charge to structure standoff, Z, and the barrier height, H, (Figure 4), there are multiple reflections of the blast wave that occur in the problem. For small barrier-to-building standoff configurations, there are at least two spikes in the reflected pressure loading the structure; one for the direct line of the shock front propagating over the barrier wall and directly towards any point on the structure, and a second when the shock front propagates back to the ground and then reflects onto the structure. The effect is lessened at higher locations vertically on the structure. As the barrier-to-structure standoff is increased, the structural loads begin to more closely resemble loads in the free-field blast propagation configuration. This makes for a non-linear problem that requires enhanced tools for analysis.

7

Z (m) $= d_1 + d_2$

d_1 (m)

h_s (m)

H (m) w_s (m)

W (kg TNT)

b (m)
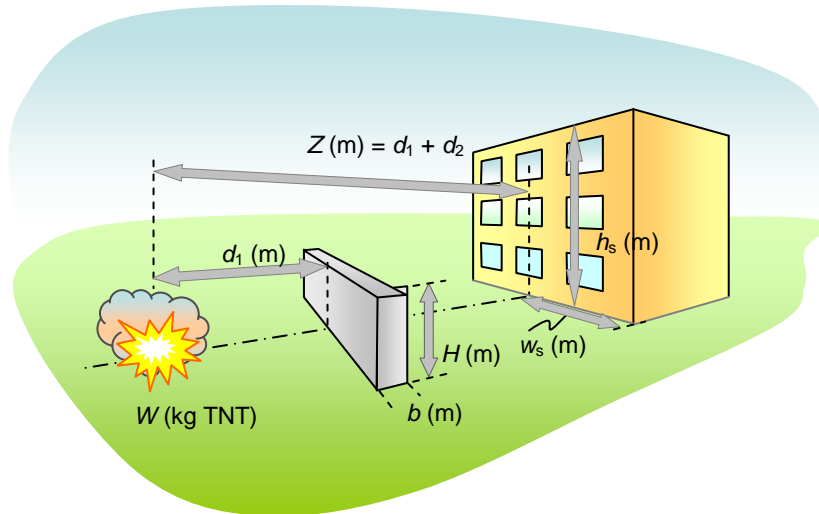
Figure 4. Blast Barrier Wall Configuration

There are four main approaches to analyzing the blast environment for an asset protected by a blast barrier wall. They vary in accuracy and efficiency—two approaches are extremely accurate, but inefficient and expensive, and the other two are efficient and inexpensive, but at the cost of accuracy. The least common is a rare case that occurs only for important facilities. In this case, live blast testing may be used to verify that a certain level of protection is provided for the facility. Live blast tests are expensive and are both time and labor intensive. For that reason, live blast tests are rarely used. The secondary option is the use of high-fidelity modeling, which is accurate, and the more-commonly employed approach. The drawback of computational modeling is that it requires a highly trained professional and can take a long time to analyze a situation for varying configurations of barrier height and standoffs. The third approach is that of applying curve fitting to available data to create a predictive engineering tool. This method has gotten better over the last 15 years, but is still fairly inaccurate. The fourth approach is to train an ANN to model the blast propagation around blast barriers. A background of each approach follows except for a description of live blast testing, which is relatively self-explanatory.

3.2.1. First-Principle Simulation of Impact/Blast Responses
The simulation approach assumes that there is a skilled engineer using internally developed, commercial, or government-owned software that is based on first-principle physics. Popular software commonly used in this approach includes LS-DYNA (Hallquist, 1993), AUTODYN (Century Dynamics, 2003), FEFLO (Lohner, Yang, Baum, Mestreau, 2002), Air3D (Rose T. A., February 22, 2006), SHAMRC (Crepeau, 1998; Crepeau, Needham, Hikida, 2001), CTH (McGlaun, Thompson, Elrick, 1990), and DYSMAS (McKeown, Dengel, Harris, Diekhoff, 2004). Several of these codes have successfully been used to model blast propagation with a blast barrier protective wall. FEFLO was used and compared with experimental results with good correlation (Rice, Giltrud, Luo, Mestreau, Baum, 200), and the same author had done a similar study with SHAMRC (Rice, May 1999). SHAMRC was also utilized in a miniature-scale experimental program and compared favorably to test data (Rickman, Murrell, Armstrong, 2006). AUTODYN was the main tool used by researchers in developing a curve fitting technique for predicting blast–barrier response (Zhou, Hao, 2008). Their work showed favorable results for being able to model the blast environment in the presence of a blast barrier.

The downside to this approach is the logistics of performing such simulations. If an evaluation of an existing facility is required, then there is only one simulation to run and this might be a good approach for an experienced computational modeler. If there are multiple cases to be considered—i.e., differing standoffs, charge sizes, and blast wall heights—then a modeling approach becomes very cumbersome. Computational models can require many processors, up to several thousand depending on the computational domain size and software chosen. The simulations can take hours, days, or weeks to run to completion. If they are large problems that have to be compiled on a large-scale supercomputer, queue times can drive the simulation time out even further. Studies of the ability to use a much coarser mesh for computational assessments performed on computers without large memory or processor capabilities have shown errors as much as 50% (Lohner, Baum, Rice, 2004). Accurate results are attainable, but require a skilled modeler and time for the simulations to be compiled and post-processed.

3.2.2. Adjustment Factors

The adjustment factor approach entails applying curve fitting techniques to data gathered from experiments. In this approach, the data compiled from experiments is compared to the TM5-1300 method of predicting loads on structures in free-field blast configurations through an adjustment factor. The adjustment factor tells the engineer how much to reduce or increase the TM5-1300 predicted loads for the specific barrier problem configuration. Adjustment factors for the pressure load (AF_p) and the impulse load (AF_I) are defined as follows:

$$AF_p = \frac{p_{\text{with barrier}}}{p_{\text{no barrier}}} \text{ and } AF_I = \frac{I_{\text{with barrier}}}{I_{\text{no barrier}}} \tag{1}$$

This approach is defined by a series of look-up charts with best-fit curves defining the adjustment factors for varying ranges of variables. These methodologies are presented in TM5-853-3, the US Army Security Engineering Manual (Security Engineering Manual TM5-853-3, vol. 3) and TM5-1300 (US Department of the Army, 1990). The methods were originally developed using small-scale data from experiments conducted at the US Army Corps of Engineers Waterways Experiment Station (WES) in the 1980s (Dove, Hamilton, Coltharp, 1989). The majority of the research to date has been performed without structures, meaning that the methods are not able to accurately capture multiple jumps in pressure that occur in small barrier-to-structure standoff situations.

Rose et al. (Rose, Smith, Mays, 1995; Rose, Smith, Mays, 1997) applied this technique to data from small scale experiments to generate prediction charts. The set of experiments from these works provides data for specific charge sizes and geometric configurations for the site layout. The small-scale experiments entailed a charge with a blast wall and free-field pressure gauges collecting data behind the blast wall. Based on the small-scale data collected in their experiments, a methodology for design charts was developed. Curve fits were used to predict the adjustment factor based on the geometric configurations. The input variables for their methodology include the barrier height, H, and thickness, b, and the charge-to-barrier standoff, d_1, the charge-to-point of interest standoff, Z, and the charge weight, W. The charge weight is scaled out of the method, leaving four of the five variables as input into the method that returns an adjustment factor. The original research by WES and Rose et al. had limited ranges of applicability and the method is not able to extrapolate beyond these bounds with accuracy.

9

Bogosian et al. expanded on the data of Rose et al. to extend the bounds of the prediction method (Bogosian, Shi, 2003; Bogosian, Shi, 2002). This study also used the blast scaling assumption and added data from 40 live blast tests to expand the bounds of the prediction method. The approach shows ranges of accuracy. A series of curve fits need to be used to capture the behavior accurately. For this reason, the predictions are limited in application and do not extrapolate outside the bounds of the existing data set.

Rickman et al. conducted a series of experiments and computational simulations at approximately 1:18 and 1:30 scales (Rickman, Murrel). The final product from the ERDC experiments was a series of adjustment factors for pressure and impulse loadings with a blast wall present (Rickman, Murrell, Armstrong, 2006; Rickman, Murrell). The aim of this study was to improve accuracy of the existing adjustment factor methodology. The study included 40 small-scale experiments plus supplemental data generated using the hydrocode SHAMRC (Crepeau, 1998). The body of research prior to this effort did not collect data other than at normal incidence to the points of interest. This study sought to capture data at points located at a lateral distance off-axis from the straight line between the charge and perpendicular to the point of interest. The methodology showed good correlation with the data used to develop the method, but there was no independent testing to validate the methodology. The ranges of variables were poorly defined in the effort. The variables are poorly distributed across the domain, which suggests that the model will behave well close to the data points used to train the method, but will likely be poor at data points in between. The poor statistical distribution of the data is represented in Figure 5, which shows the bias of the data.
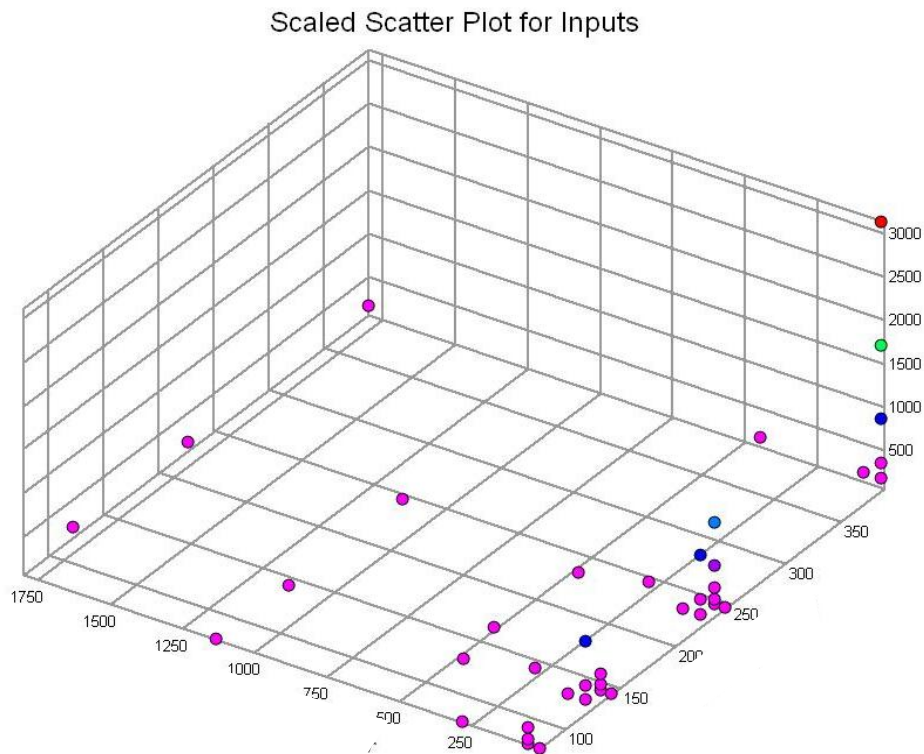
Figure 5. Configuration of 40 Miniature Bomb–Barrier–Building Experiments with TNT-Equivalent (g) Factored-Out by Scaling to 100 g of TNT

Zhou and Hao (Zhou, Hao, 2008) also took a similar approach to the problem. The research prescribes an approximation method for predicting pressure–time histories on structures behind blast walls. The problem configuration is similar to the current study in that they consider charge, distance to barrier, distance to building, height of barrier, height of building and height on building. They do not consider lateral distance from the centerline of the building (the line from the bomb that is perpendicular to the face of the building), nor the top face of the building. They estimate four features:

- peak reflected pressure,
- positive impulse,
- arrival time of shock wave front, and
- positive phase duration.

From this the positive form of the wave is approximated with a triangle.

The model uses an empirically derived model based on computational fluid dynamics (CFD) output using the hydrocode AUTODYN that uses the TM5-1300 free-field model as the baseline for determining the pressures/impulses across a vertical–axial line on the face of the building. It then modifies this to take account of the barrier using (i) a couple of logical rules (that determine the basic form of the pressure/impulse profiles over the face of a building), and (ii) some approximation functions.

The paper fails to validate the model in any meaningful way. In a couple of case studies the new model, a CFD model, and a free-field model are compared graphically for estimations of pressure/impulse over the centerline of the building face; however, in both cases this is for only one bomb–barrier–building configuration, so there is no quantitative assessment of performance/ validity. That is, in contrast to the current study, they do not validate their model for a range of cases, they do not measure and characterize errors, and they do not analyze the errors to look for bias across the problem domain.

3.2.3.   Artificial Neural Network Approach

ANN models have also been shown to have some merit in modeling the blast loads on structures behind a protective blast barrier wall. The ANN approach is a rapid engineering tool that provides a direct mapping of the results based on the required inputs, similar to the adjustment factor approach. The ANN approach also has similar restrictions in that it also requires a large data set to accurately train the models, and the models are not able to extrapolate well beyond the bounds of the data used to train the ANN models. ANNs are very versatile, though. They are capable of handling many variables and capturing nonlinearities in the model with sufficient training data (Flood, Ian; Kartam, Nabil, 1994; Flood, Ian; Kartam, Nabil, 1994). A study has been performed that covered several of the values represented in Figure 4, including d_1, Z, and H as well as the height of burst (HOB) and the height of measuring point behind the barrier wall using data from miniature-scale experiments for free-field propagation behind a barrier without a reflective structure (Remennikov, Rose, 2007). The study had five input variables and output the peak scaled pressure and the peak scaled impulse. The results of the study produced a model which shows good correlation with the data. Similar work has been performed by the authors of this paper exploring the capability of a radial Gaussian (RGIN) neural network using existing data (Flood, Bewick, Dinan, Salim, 2009). The study found that existing data are too scattered

11

and do not provide a good, even distribution over the variable space. The work of this paper is also outlined by Flood, Bewick, Salim, and Dinan (2009).

The previous ANN approach showed very promising results for using ANN technology to predict blast loads on structures behind blast walls (Remmenikov, Rose, 2007). The data used in their study, however, are clustered in very narrow bands. The method was generated using existing data from previous research efforts. Thus the range of applicability is narrow and the limit of the capability for the ANN approach is not fully tested. A small amount of data was used to train the ANN—170 training patterns. The density of the data is not very good as well. There are gaps in the data within the small bands of the range of data. Also, the testing that was performed uses pieces of data that fall within the areas of highly concentrated data points used to train the ANN. A comparison of the clustered data in the Remnikov and Rose (2007) work to the bounds in the present study is shown in
Figure 6. The work also states that there were large discrepancies in the small-scale test data. For this reason, data points from several experiments were omitted. The experiments omitted from the model are not specified. Reviewing the scatter
Figure 6, removal of certain data points would make the range of applicability much smaller than what was reported.

3.3. Blast Loading to Roofs

Blast loads applied to roof structures are predicted by applying an increase factor to the free-field incident pressure based on the standoff, height of the building, and the length of the building to be loaded as shown in
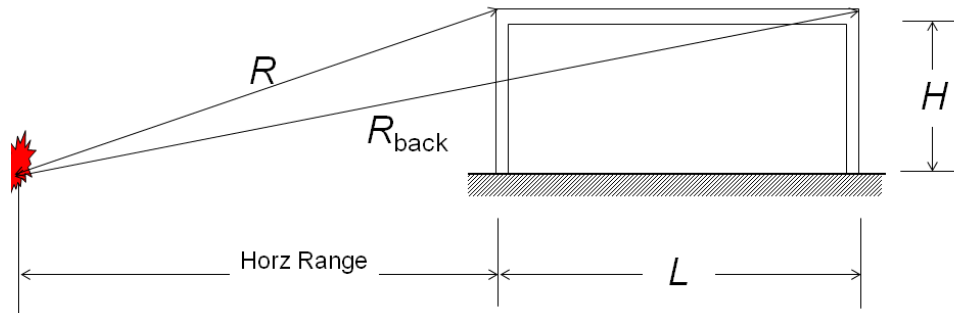
Figure 7 (US Department of the Army, 1990; UFC 3-340-01, 1 June 2002).

In contrast to vertical wall reflected pressures, where the air pressure has a sudden jump from atmospheric pressure up to the peak reflected pressure, roof loads are defined as a rise to the peak pressure over time followed by an unequal decay of the blast pressures. The shape of the roof load is a triangular pulse with uneven rise and decay times. The magnitude of the load is determined by applying load factors. The TM5-1300 methodology

for predicting incident pressures is used with the R_{back} variable from
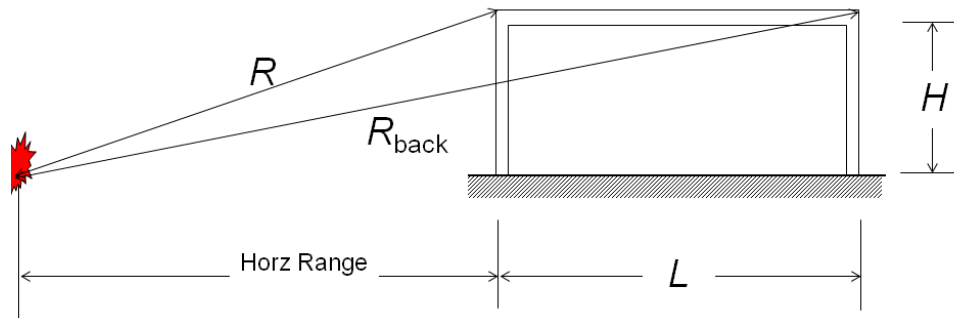
Figure 7 used as the standoff. The resulting load takes the shape in Figure 8. This proves to be an inaccurate way to predict roof blast loads. Blast loads on roofs, like normally reflected pressures or free-field loads, jump from zero pressure up to a peak pressure load.

Blast loading to roofs is a topic that has not had much research. The majority of funding is poured into side wall construction design and retrofits under the tenet that the side wall condition is the most critical. In general, this is the case. However, there are instances, primarily in commercial construction, where roofs are frangible at loads much lower than the design loads of the side wall construction. In 1999, Bogosian et al. recognized the threat posed to lightweight steel joist roofs (Bogosian, Dunn, Baylot, Simmons, 1999). The same research team later studied retrofit designs for this vulnerability (Baylot, Bogosian, Dunn, Simmons, 2000). Blast analyses of airports discovered that metal deck roofs were commonly found to be the most vulnerable piece of construction (Lan, Crawford, 2003). The existing analytical tools for predicting roof loads are often non-conservative and inaccurate (McClendon, 2007)
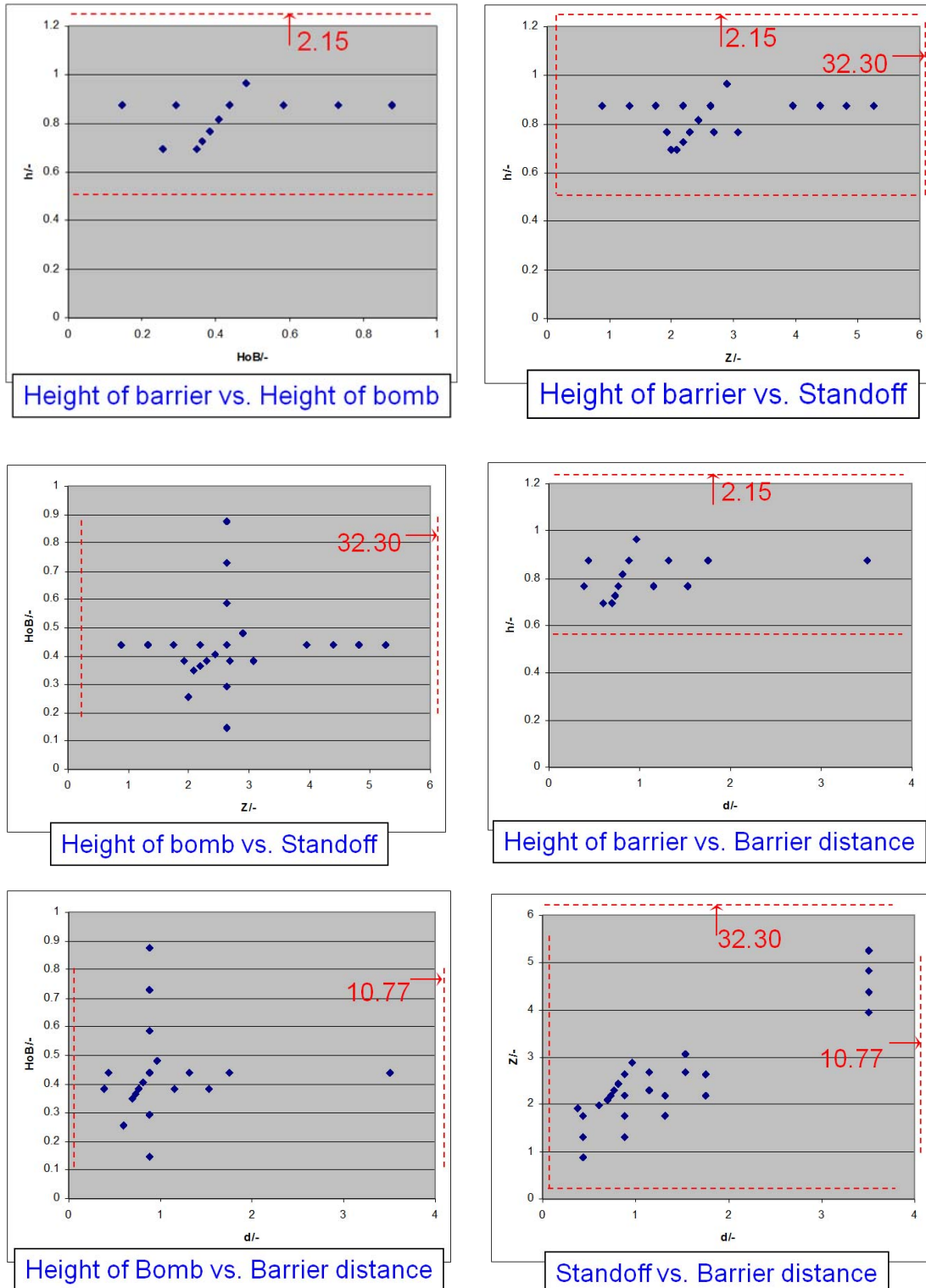
Figure 6. Distribution of Data in the Rose et al. ANN Model, Shown as All Permutations of the Four Variables Plotted against Each Other (red shows limits of currently presented experimental data).
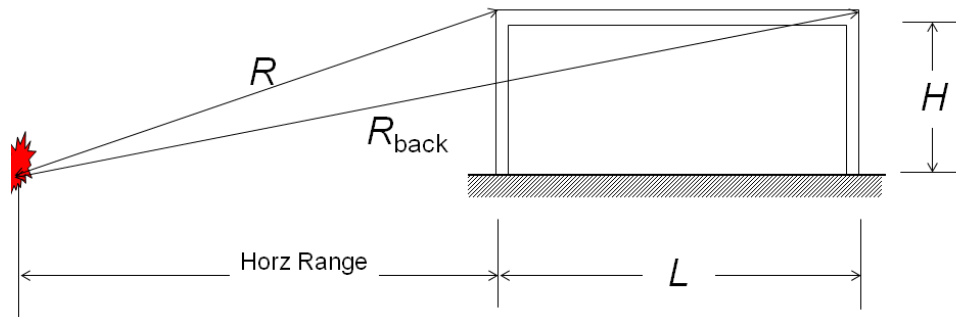
Figure 7. Factors for Predicting Blast Loading to Roofs
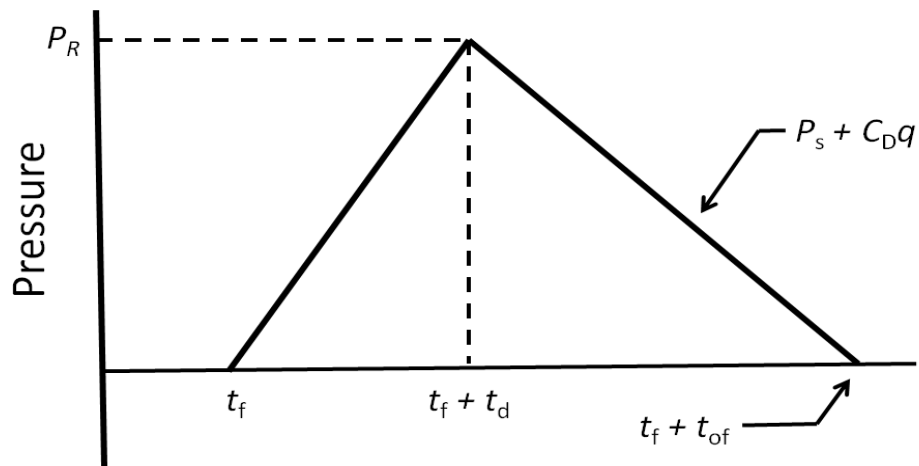
Figure 8. Typical Roof Blast Load Waveform Prediction (TM5-1300)

There are no existing research efforts looking at the effects of blast loading on the roofs of structures which are protected with perimeter blast walls. This study will develop a prediction methodology for this problem. The prediction methodology developed in the current work is independent of any existing prediction methodologies for roof loads, and thus is not bound by the inaccuracies that exist.

4. METHODOLOGY AND SCOPE

The main approach is to populate enough data to generate an accurate and efficient neural network model which is capable of replacing the difficulties in implementing hydrocodes and the limitations of existing methodologies for predicting the blast load of a structure protected by a blast barrier wall. The idea behind a neural network is that it fits a surface (or hypersurface) to a set of observations of the performance of the real system. Neural networks have many benefits. They work well with large numbers of independent variables and highly non-linear problems and can be trained to output a variety of solutions. For example, the neural network can be trained to output maximum values or optimum values. In other words, a neural network could be trained to find the optimum blast barrier wall setup to provide a user-defined loading condition on the structure.

Previous efforts have utilized blast scaling to reduce the amount of data points needed. But blast scaling may not necessarily lend itself well to this type of problem. The reasoning for this is due to the number of variables involved in the problem. Since there is a practical restriction to the number of variables that can be considered, some must remain constant, such as the barrier thickness, b, structure height, h_s, and structure width, w_s, in this case.

4.1.   Methodology

The approach for the current study is to validate the use of the neural network technology for predicting blast loads on structures that are protected by blast walls. Initially, the approach is applied to data generated with the adjustment factor method as outlined in (Bogosian, Shi, 2003). Ultimately, this approach yields results only as good as the methodology used to train the ANN. The purpose of this study was solely to validate that the ANN technology was a good approach that was capable of learning the data needed to produce a prediction in a blast barrier-structure type problem.

Secondly, the approach was applied to the live data that was produced by Rickman et al. (Rickman, Murrell, Armstrong, 2006). The results of the ANN predictions for this approach were not as good due to poor data scatter. This will be addressed in Section 5.

The end approach is to populate a 3x3 grid of the data variable space using computational modeling. The limitation of this approach is the exclusion of certain variables. There are six variables that can be considered as mentioned before and illustrated in Figure 9. Blast Barrier Wall ; W, d_1, d_2, H, b, w_s, and h_s. For this study, it has been determined that there are four independent variables used to define the problem are W, d_1, d_2, and H. There are two dependent variables, w_s, and h_s, which will be input into the ANN, but they do not affect the number of simulations required, as these data points are inherently captured within the confines of each simulation. To completely cover the data space, the number of data points required is determined by the number of data points in the variable space grid raised to the power of the number of independent variables. This means that a data set of 81 (3^4) experiments is required to fully encapsulate the variable space.
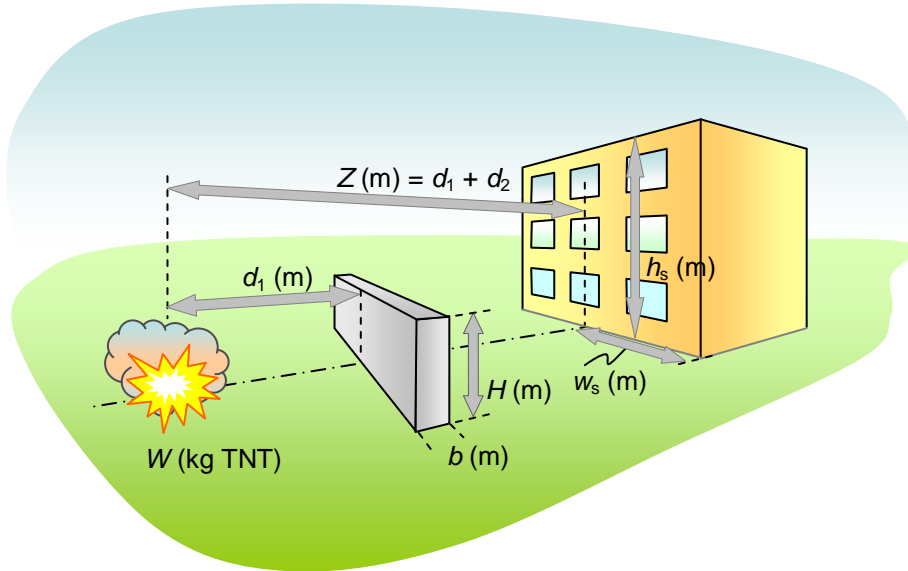
Figure 9. Blast Barrier Wall Configuration

The artificial neural network (ANN) method which is being implemented is a RGIN architecture with an incremental learning paradigm (Flood, Kartam, Nabil, 1994). RGIN networks function as a three-layer feed-forward system. The three layers are the input variables, hidden neurons, and the output value. RGIN networks represent the data as a series of radial-Gaussian functions. The hidden neuron portion of the feed forward system represents the number of radial-Gaussian functions used to fit the data. Each time a hidden neuron is added, a new radial-Gaussian function is added onto the system to capture the data point that represents the largest error. Development of a RGIN ANN progresses one hidden neuron at a time. Each hidden neuron added captures the largest error data point and determines the position, amplitude, and spread of the radial-Gaussian function that reduces the residual as much as possible. The RGIN ANN approach has been shown to work well with large sets of data (Flood, 1999; Flood, Bewick, Dinan, Salim, 2009; Moody, Darken, 1989). The RGIN neural network is illustrated in Figure 10.
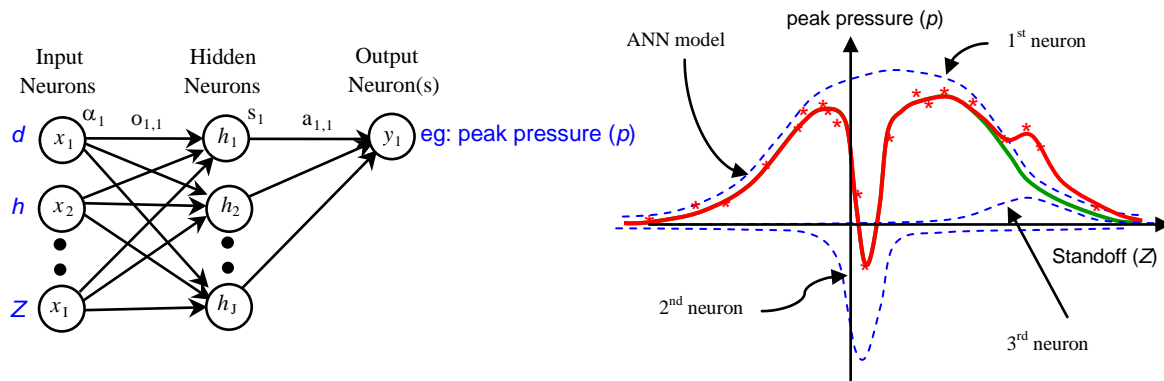
Figure 10. Schematic of RGIN Neural Network

One of the main advantages of this approach is that it is a stand-alone procedure. The results are not reliant upon the accuracy of existing methodologies with inherent errors such as the adjustment factor approach or the techniques for predicting roof loads. The results are all produced using validated numerical simulations. There is a slight bit of error in the computational technique, but the errors are well documented and inherent in each set of data generated. In contrast, most of the techniques developed to date have used available live test data. Each live explosive test has variations and errors inherent in the experiment due to the nature of the explosive event. A live blast experiment repeated several times over with the exact same configuration and charge size will yield slightly different results each time. This is due to the physics involved with the explosives going high order at detonation. Prediction methodologies based solely on live test data have these variations in test built in to the test data. Essentially, a best fit curve running through a series of data may or may not have a low statistical deviation. The variations in live experiments are well known but poorly documented.

4.2.   Scope

The current scope entails a setup of 91 experiments listed in
Table 2. 81 of these experiments will be simulations used to populate data with appropriate blast barrier configurations to create an accurate neural network. Ten simulations will be used to verify and validate the accuracy of the neural network. The problem has been defined by four main variables W, d_1, d_2, and H while holding the structure size, h_s and w_s, and the barrier thickness, b, constant. The ranges for the series of experiment configurations are shown in **Error! Reference source not found.**. The width, w_s, height, h_s, and roof length, l_r, of the tructure are shown as varied values since the neural network will be able to produce loadings at any point on the face and roof of the structure. ANN models will be developed for predicting peak pressure, impulse, time of arrival for the peak pressure, and the positive phase duration of the applied blast loads. The ANN models will be developed for the loads to the structure face as well as to the roof of the structure.

Table 1. Range of Values for the Six Independent Variables

	min	max
W TNT (kg)	22.68	910.42
d_1 (m)	0	7.62
Z (d_1+d_2) (m)	3.048	30.48
H (m)	1.52	6.1
h_s (m)	0	9.144
w_s (m)	0	1.52
b (m)	0.3	0.3
l_r (m)	0	3.048

Each experiment will be collecting a variety of data to be input into the neural network. The neural network data will include a grid of data points on the surfaces where predictions are desired. For the structure face, there will be a 6x31 grid of data points collected in each experiment. For the roof models, there is a 6x11 grid of data points. Each set of grid data points will be set up with the grid data points spaced evenly apart at 1-ft increments. The neural network will then predict the results at any point within the bounds of the defined variable space in **Error! Reference source not found.**. For the roof loading, data will be collected only in the

irst 10 ft of the roof. The barrier wall is considered to be infinitely long, so no wrap-around effects are included.

Table 2. Proposed Simulation Configurations

Simulation #	W (lb-TNT)	H (ft)	d_1 (ft)	Z (ft)
1	50.00	5.00	0.62	10.62
2	50.00	5.00	0.62	35.51
3	50.00	5.00	0.62	75.48
4	50.00	5.00	6.25	16.25
5	50.00	5.00	6.25	41.15
6	50.00	5.00	6.25	81.11
7	50.00	5.00	25.00	35.00
8	50.00	5.00	25.00	59.90
9	50.00	5.00	25.00	99.86
10	50.00	10.00	0.62	10.62
11	50.00	10.00	0.62	35.51
12	50.00	10.00	0.62	75.48
13	50.00	10.00	6.25	16.25
14	50.00	10.00	6.25	41.15
15	50.00	10.00	6.25	81.11
16	50.00	10.00	25.00	35.00
17	50.00	10.00	25.00	59.90
18	50.00	10.00	25.00	99.86
19	50.00	20.00	0.62	10.62
20	50.00	20.00	0.62	35.51
21	50.00	20.00	0.62	75.48
22	50.00	20.00	6.25	16.25
23	50.00	20.00	6.25	41.15
24	50.00	20.00	6.25	81.11
25	50.00	20.00	25.00	35.00
26	50.00	20.00	25.00	59.90
27	50.00	20.00	25.00	99.86
28	541.17	5.00	1.36	11.36
29	541.17	5.00	1.36	36.26
30	541.17	5.00	1.36	76.22
31	541.17	5.00	6.25	16.25
32	541.17	5.00	6.25	41.15
33	541.17	5.00	6.25	81.11
34	541.17	5.00	25.00	35.00
35	541.17	5.00	25.00	59.90
36	541.17	5.00	25.00	99.86
37	541.17	10.00	1.36	11.36
38	541.17	10.00	1.36	36.26
39	541.17	10.00	1.36	76.22
40	541.17	10.00	6.25	16.25
41	541.17	10.00	6.25	41.15
42	541.17	10.00	6.25	81.11
43	541.17	10.00	25.00	35.00
44	541.17	10.00	25.00	59.90
45	541.17	10.00	25.00	99.86

46	541.17	20.00	1.36	11.36
47	541.17	20.00	1.36	36.26
48	541.17	20.00	1.36	76.22
49	541.17	20.00	6.25	16.25
50	541.17	20.00	6.25	41.15
51	541.17	20.00	6.25	81.11
52	541.17	20.00	25.00	35.00
53	541.17	20.00	25.00	59.90
54	541.17	20.00	25.00	99.86
55	2,007.14	5.00	2.11	12.61
56	2,007.14	5.00	2.11	37.01
57	2,007.14	5.00	2.11	76.97
58	2,007.14	5.00	6.25	16.25
59	2,007.14	5.00	6.25	41.15
60	2,007.14	5.00	6.25	81.11
61	2,007.14	5.00	25.00	35.00
62	2,007.14	5.00	25.00	59.90
63	2,007.14	5.00	25.00	99.86
64	2,007.14	10.00	2.11	12.61
65	2,007.14	10.00	2.11	37.01
66	2,007.14	10.00	2.11	76.97
67	2,007.14	10.00	6.25	16.25
68	2,007.14	10.00	6.25	41.15
69	2,007.14	10.00	6.25	81.11
70	2,007.14	10.00	25.00	35.00
71	2,007.14	10.00	25.00	59.90
72	2,007.14	10.00	25.00	99.86
73	2,007.14	20.00	2.11	12.61
74	2,007.14	20.00	2.11	37.01
75	2,007.14	20.00	2.11	76.97
76	2,007.14	20.00	6.25	16.25
77	2,007.14	20.00	6.25	41.15
78	2,007.14	20.00	6.25	81.11
79	2,007.14	20.00	25.00	35.00
80	2,007.14	20.00	25.00	59.90
81	2,007.14	20.00	25.00	99.86
TRN-1	89.85	10.28	23.01	51.44
TRN-2	444.70	6.03	12.56	25.94
TRN-3	1636.21	18.82	9.14	26.95
TRN-4	1281.46	5.84	4.05	36.67
TRN-5	311.86	5.83	10.53	56.39
TEST-1	1501.06	8.67	23.42	95.72
TEST-2	1293.27	7.72	16.92	73.18
TEST-3	1851.43	13.05	16.94	46.91
TEST-4	1236.03	15.11	3.04	24.14
TEST-5	284.38	13.60	24.22	67.80

5. VALIDATION OF ANN APPROACH

5.1. Study 1: Direct Mapping Artificial Neural Networks Trained Using Empirically Derived Data

The first study conducted was a proof of concept that considered the configuration of input parameters shown in Figure 9, where Z is the distance from bomb to building, d is the distance from the bomb to the barrier, H is the height of the barrier, and h_s is the height at the building where the effect of the blast is estimated. The charge, W (lb-TNT), was removed from the problem by scaling all distances by $W^{1/3}$, a scaling parameter that has been shown to work well for a broad range of free field experiments (see, for example,(Mays, Smith, 1995)). The output variable considered in this study was the peak pressure measured at the location y on the face of the target building.

Input values used for training this ANN were obtained using an existing empirical modeling system (Bogosian, Shi, 2003)—the intention was to see if the ANN was capable of reproducing its performance. A total of 1,365 patterns were generated at random for training the ANN and an additional 252 were generated at random for testing its accuracy. The RGIN neural network system was adopted for this study since it has been found to perform well for problems where training uses large data sets (Flood, 1999). Figure 11 shows the progress of training, measured as mean absolute error versus the number of Gauss units—note that in the RGIN system the network is developed one Gauss unit (hidden neuron) at a time. The graph shows separate progress curves for the training patterns and the testing patterns. Training was allowed to proceed until there was little further improvement in performance measured for the testing patterns, which occurred at around 100 Gauss units. The mean absolute error for the testing patterns at this stage was 0.91 psi, about 3%.
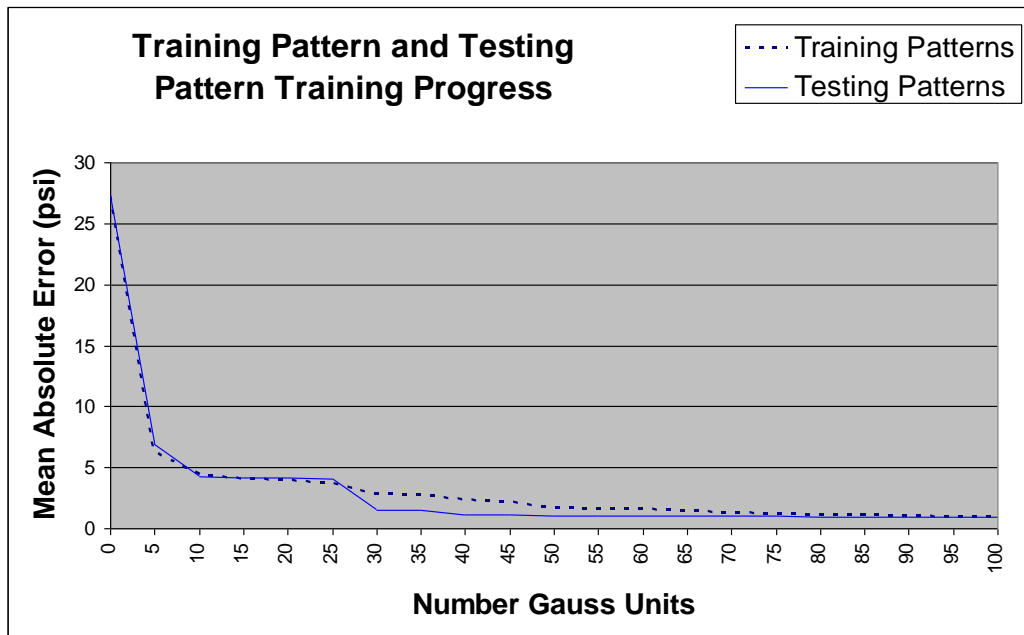
Figure 11. Training Progress for the RGIN-Based Model of Bomb Blast Pressures on Buildings

Figure 12 is a scatter plot of actual versus the ANN predicted peak pressure for the 252 test patterns. If the ANN was a perfect model, all points would fall along the indicated 45° line. Inspection of this plot indicates the model is highly accurate, and performs consistently well across the range of peak pressure values. This is confirmed by the correlation between the predicted and actual peak pressures, which had a value of 0.9959. Remennikov and Rose (2007) found similar performance results in their ANN study trained using scaled live experiments.
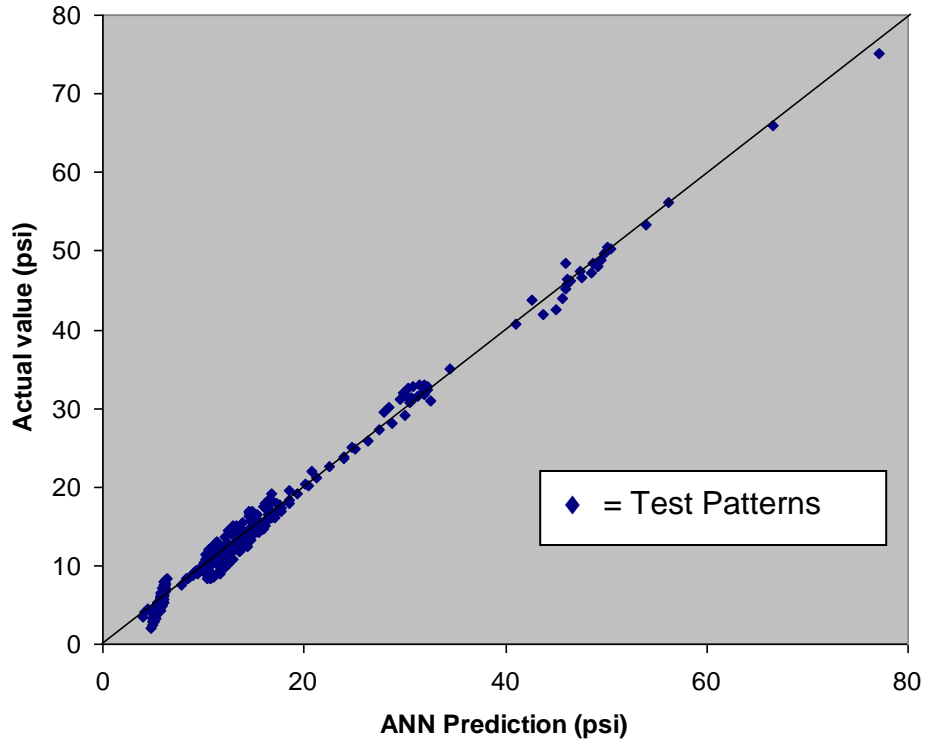
Figure 12. Scatter Plot Validation of the RGIN-Based Model of Bomb Blast Pressures on Buildings

The performance of the model was further analyzed to see if there was any correlation between the magnitude of the errors and the location in the problem domain – that is, whether the errors are dependent on the values of the independent variables. Ideally, the model should perform consistently well across the entire problem domain.

Figure 14 shows the distribution of the errors for the testing patterns plotted against the input variable h (the height of the barrier scaled using the inverse cube method). From this figure it can be seen that the model performed equally well across the entire range for this variable, indicating that the model has no bias in this context. Plots of the distribution of errors for all other input variables yielded similar results, confirming that the ANN performed consistently well across the entire problem domain.

An attempt to refine this ANN was made by training it so that the first unit would act as a linear function (specifically implementing a hyper-plane since there were four input variables) rather than as a Gauss function. The intent was to see if this would allow the ANN to achieve the same

degree of accuracy but with fewer Gauss units, based on the idea that a large part of the function could be explained linearly.
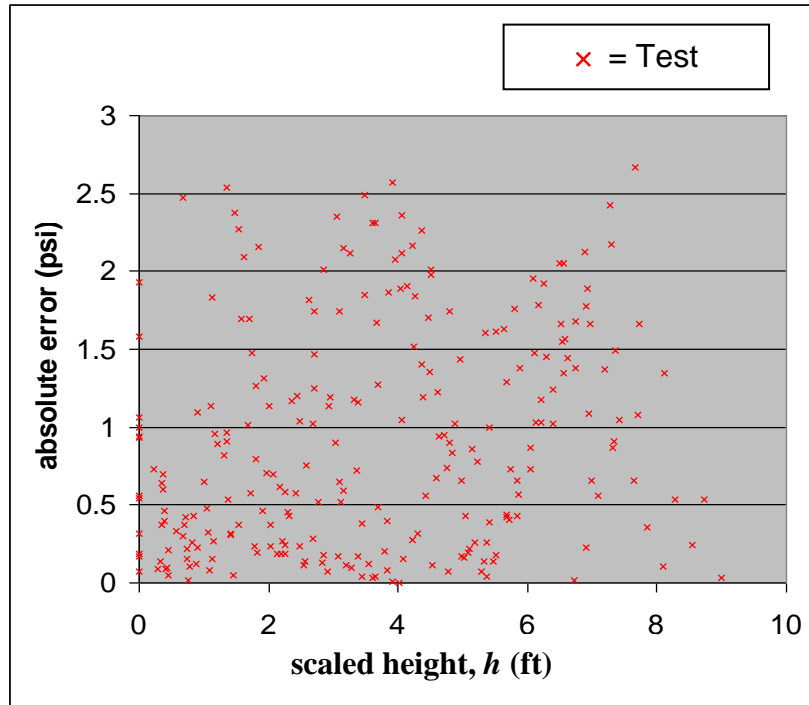
Figure 13. Distribution of Errors for Test Patterns versus Scaled Height of the Barrier, *h*

Figure 14 compares the progress in training for the 252 test patterns, for both the original ANN and the hybrid ANN (containing the linear unit). The graph clearly demonstrates that there is no benefit to including the linear function unit in terms of reducing the size of the network required to achieve the specified level of accuracy. Indeed, the learning for the hybrid ANN lags behind the regular ANN up to the 20th unit, and thereafter learns at a similar rate. This indicates that there is no significant linear component to the problem.
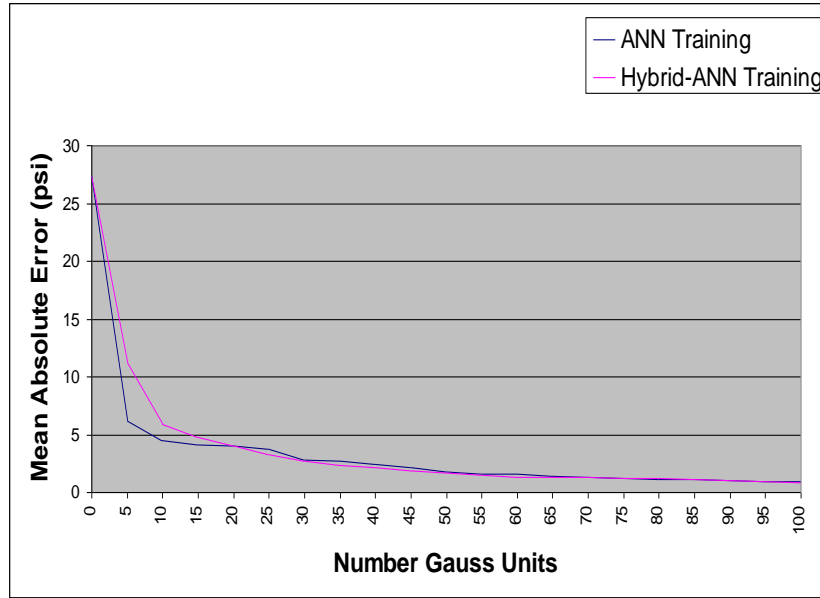
Figure 14. Training Progress for ANN and Hybrid-ANN

5.2. Study 2: Direct Mapping Artificial Neural Networks Trained Using Miniature Live Bomb Blast Experiments

The next set of experiments was concerned with the development and evaluation of a neural network trained and tested using data from a series of miniature-scale bomb–barrier experiments provided by the US Army Engineer Research Development Center (Rickman, Murrell). The independent variables extracted from these data were the charge W, and the following distances: bomb to building, Z; bomb to barrier, d; barrier height, H; and height at the building's front face, y. The dependent variable considered was the peak pressure. Data from 40 scaled experiments were used in this study, each representing a different bomb–barrier–building configuration. These 40 configurations are represented by the points in Figure 5. Each experiment provided five peak pressure readings measured at locations on the front of the scaled building. Thus, it was possible to extract five data patterns (mapping between the independent and dependent variables) from each experiment, giving a total of 200 patterns.

In this trial, the 200 data patterns were divided into two groups: the first group was used for training the neural network and comprised 195 data patterns (selected at random); the second group was used for testing the trained neural network and comprised the remaining five data patterns.

The type of neural network and training system adopted was the same RGIN system used in study 1 above. Figure 15 shows the learning progress for the neural network, measured in terms of the mean absolute error for the training patterns. Training was allowed to occur until there was no improvement in the performance of the neural network measured for the five test patterns; this occurred when around 250 hidden neurons had been added. It can be seen from this figure that the neural network learned the training data sets effectively, bringing the mean absolute error down to just 0.4 kPa.
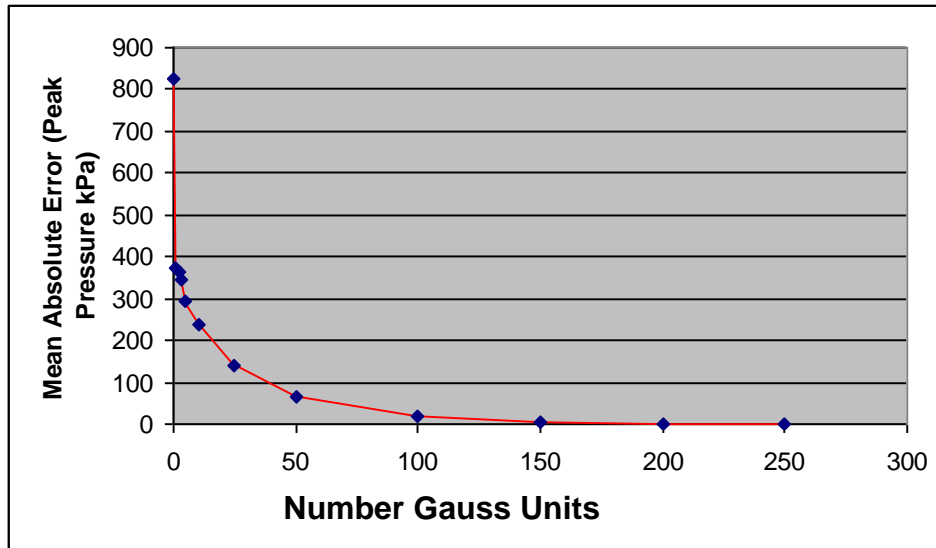
Figure 15. Training Progress for the ANN Developed Using Data from the Miniature Bomb–Barrier–Building Experiments

However, when it came to a validation of the network using the testing data (the set of five patterns not used for training), the performance was found to be relatively poor. This is shown graphically in Figure 16, which plots predicted pressure against actual pressure for the five test patterns. Note, two sets of results are shown in this figure: the first (the test results) represents the case where the test patterns were not used during training; the second set (the training results) represent the case where the test patterns were used during training. The first case, the test patterns, provides the more-accurate measure of validity. If the model were a perfect predictor, these test points would all fall along the diagonal line. Clearly, however, they diverge significantly from the line, implying a relatively poor performance. These results are summarized numerically in Table 3, in which the error is shown to range from 6.4% to 41.8%, having a mean value of 26.1%. The correlation between the predicted values (for the test results) and the actual values indicates a similar conclusion, having a value of 0.83.
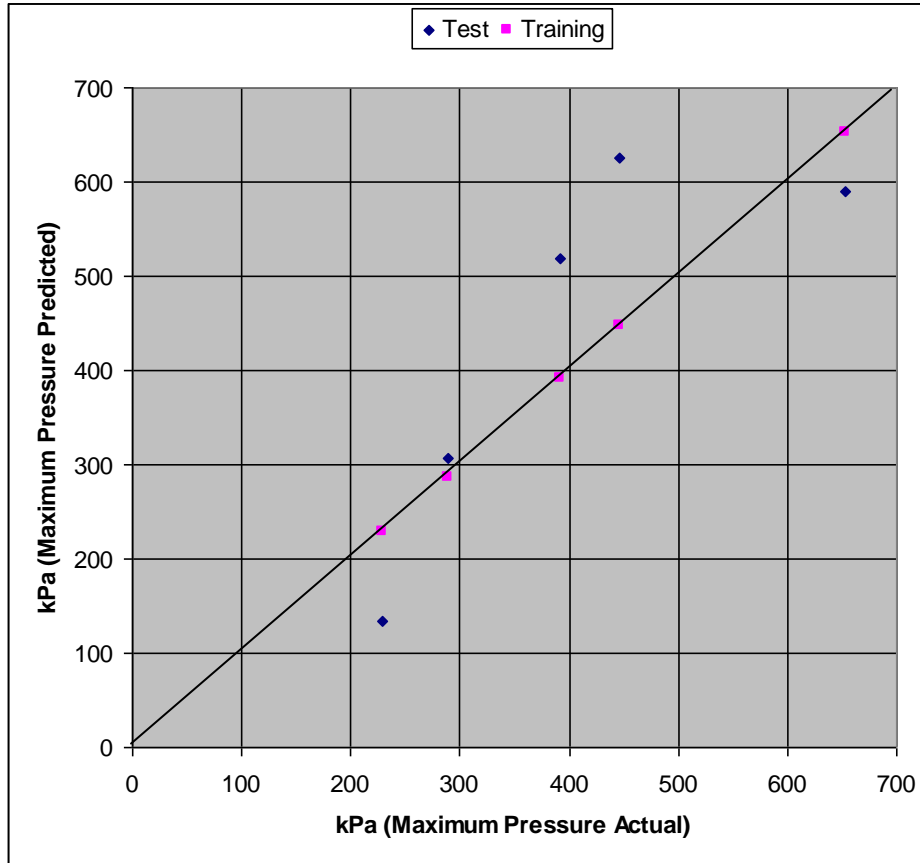
Figure 16. Scatter Plot of Predicted Pressure (by the Neural Network) Versus Actual Pressure, for the Five Test Points.

Table 3. Percentage Error between Predicted (by the Neural Network) Pressure and Actual Pressure for the Five Test Points

Test Point	1	2	3	4	5	Mean
Test Error	41.8%	6.4%	32.7%	39.8%	9.7%	26.1%

The accuracy of the network trained using the scaled data is significantly less than that trained in Study 1 using data extracted from Bogosian & Shi (2003). For the Bogosian & Shi (2003) trained neural network, the average absolute error for a set of test patterns was 3.1% (cf. 26.1% for the current experiments) and the correlation coefficient was 0.996 (cf. 0.83 for the current experiments). One reason for this is that fewer data points were available for training from the miniature-scale experiments. More importantly, however, is the fact that the data points provided by the scaled experiments were very poorly distributed across the problem space, leaving large tracts of the problem space void of examples, as is apparent from Figure 5. In contrast, the training patterns extracted from Bogosian & Shi (2003) were evenly distributed across the entire problem space. Moreover, Remennikov and Rose's study (2007) demonstrated that ANN's can be trained satisfactorily using live data from miniature experiments.

The above neural network training experiment was repeated two more times, each occasion randomly selecting a different group of training and testing patterns from the miniature bomb-barrier-building experimental data set. For both additional experiments, similar results were found to those reported above.

6. COMPUTATIONAL APPROACHES TO BLAST MODELING

Several high-fidelity computational codes have put much effort into the capability to accurately model the blast environment. These codes have stemmed from both commercial and government interests. The available computational tools for modeling the blast environment include shock physics codes and coupled fluid–structure interaction (FSI) codes. The codes considered are first-principle model codes that model the detonation and burn of explosive materials and the energy that is then transferred into a blast wave.

Shock physics codes are commonly used by researchers for problems involving blast propagation. The most common codes in this class of software include CTH, SHAMRC, and FEFLO. DoD researchers have validated the use of CTH (McGlaun, Thompson, Elrick, 1990) for several types of problems involving blast propagation. Mastin et al. (1995) compared CTH simulations to free-field incident pressure as predicted by the Kingery–Bulmash (1984) equations. It is generally a very accurate code, but has high amounts of overhead and memory requirements associated with it. SHAMRC is another code that is commonly used for blast propagation modeling (Crepeau, 1998; Crepeau, Needham, Hikida, 2001; Needham, 2007). FEFLO is a commercial code that has been used for predicting blast loading like the World Trade Center Bombing (Baum, Luo, & Lohner, January 1995) and studies of the effects of coarse meshing for expedient simulation of blast events (Lohner, Baum, & Rice, September 2004).

The other group of codes is the class of codes that have been formulated for coupled fluid–structure interaction. Commonly used codes in this category include LS-DYNA (Hallquist, 1993), AUTODYN (Century Dynamics, 2003), DYSMAS (McKeown, Dengel, Harris, Diekhoff, 2004), ALE3D (Nichols, 2007) and ADINA (ADINA R&D). LS-DYNA, AUTODYN, and ADINA are commercial codes; while DYSMAS and ALE3D are government-owned and -developed codes. DYSMAS is a hydrocode that could fall under both categories described above. DYSMAS is a hydrocode that was developed for underwater explosions. It features a fluid solver, GEMINI (NSWC, 2008), coupled with a US Navy version of DYNA2D. While DYSMAS has been used extensively and validated for underwater explosion events, there has been little work with the code for explosions in air. It has been used with success for modeling a blast event of a field fortification (Roth, Bennet, Heard, & Stinson, October 2006).

Yet another class of codes is particle methods. Particle methods are unique in that continuum flow, or deformation, is not modeled. Rather a finite number of particles is used, with their locations and velocities tracked by Lagrangian kinematics as the particles move through an Eulerian mesh. Some common methods in this class include the Particle-in-Cell method (Harlow), the Smoothed Particle Hydrodynamic (SPH) method (Monaghan, 1988), and the Material Point Method (MPM) (Chen, Brannon, 2002). There is also an entire class of meshfree particle methods (Li, Kam, 2004). Particle methods are generally advantageous for interface problems involving discontinuities. The particles have the ability to carry their own constitutive properties, fluid or solid, as they advect through space.

6.1.   Blast Environment Modeling

FSI is an important class of problems for modeling of the blast environment. There are a large range of computational tools that suit a wide variety of problems under the class of blast environment modeling. These problems include structural dynamics, CFD, FSI, and shock physics. There is often a close overlap between the methods for computational blast modeling. There are trade-offs that have to be weighed when initiating a computational blast-modeling effort.

The structural dynamics class of problems includes issues dealing solely with the design and analysis of structural components. Structural components are typically analyzed with nonlinear explicit finite element solver software such LS-DYNA (Hallquist, 1993), ABAQUS (Sumilia), or AUTODYN (Century Dynamics, 2003). The class of problems that fall under the heading of structural dynamics occurs when there is confidence in the blast load to be applied to the structural components. Assumptions about the distribution of the blast load are made and the blast load is applied to surfaces of the structural components. This could be open-air blast wave propagation, where the TM5-1300 method could be applied to figure out the required blast load applied, or the analyses could be done by applying loads that are derived from engineering models that produce simplified blast loads. Figure 17 illustrates an ungrouted CMU wall subjected to blast loads analyzed with LS-DYNA (Hoemann, Davidson, Dinan, Bewick, 2010). Example engineering tools include tools such as the blast barrier ANN methodology developed in the current research. These analyses are often performed when there is good confidence in the blast load applied to the components.
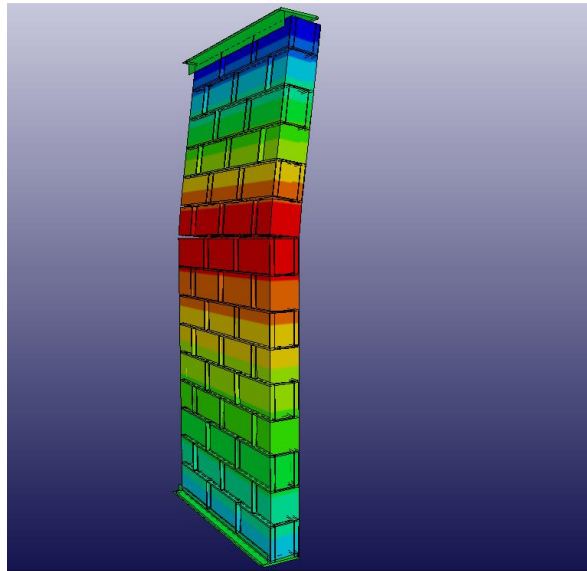
Figure 17. Structural Dynamics Analysis of Ungrouted CMU Wall Subjected to Blast

CFD codes are often implemented for blast wave propagation. A CFD analysis would be performed for cases in which engineering tools are not likely to be able to produce accurate results. Implementation of CFD analyses would entail assuming that all surfaces are rigid, perfectly reflecting surfaces. Blast engineers often employ this technique for complicated

29

environments in which the configuration of the problem requires propagation around edges or through openings, such as windows. The tradeoff of this type of analysis is the rigid component assumption. If the components are frangible, then the blast load could be reduced due to venting. A study has been performed that shows the effect of frangible walls can reduce the exterior blast demand to the structure and increase interior pressures (Baylot, Bevins, 2007). Caution must be exercised when implementing CFD analyses. It must be verified that the components that the CFD analyses are developing loads for are sufficiently rigid such that they can sustain the full blast threat. Otherwise, the blast analysis is not valid.

Fluid–structure interaction is a very broad class of problems in which the combined states of a fluid and a solid need to be determined simultaneously. These problems are especially important for blast environment problems that include frangible structural components. There are four major approaches to fluid-structure interaction problems including Euler–Lagrange coupling, Arbitrary Lagrangian–Eulerian (ALE) method, Eulerian methods, and particle methods. To describe these methods, it is necessary first to define the techniques that are used in these couplings.

Eulerian methods use a mesh fixed in space, where the nodes represent the discretized spatial variable. In Eulerian formulations the governing equations are solved on a fixed grid and the material moves through the mesh. It can be described as a fixed window viewing material that flows in and out of the fixed mesh. Eulerian methods are typically used for modeling fluids as they are well-suited for material flowing in and out of cells.

On the other hand, Lagrangian techniques use the location of material points at a previous step as the spatial variable. The computational grid is inherently tied to the material. The mesh moves and distorts as the material undergoes deformation.

The ALE method is formulated so that the mesh can move with the material, remain fixed in space, or move at an arbitrary velocity. If a problem is simple enough the original ALE mesh will be sufficient to solve the problem. Otherwise, the mesh can be adapted to certain discontinuities such as a shock to improve resolution in areas of interest. The ALE approach requires a skilled engineer to ensure that the proper indicators are used to adapt the mesh in a manner that is correct.

Euler–Lagrange coupling is the most common type of FSI. It typically entails the coupling of two existing codes; one code would be an Eulerian code developed for fluids, and the other a Lagrangian code developed for computational solid dynamics (CSD). The application of the coupling is done by having the components modeled with the Lagrangian solver act as position and velocity boundary conditions for the fluid. Likewise the material modeled by the Eulerian solver imposes a pressure boundary condition on the solid in the Lagrangian code. An algorithm is applied that iterates between the Eulerian and Lagrangian codes until equilibrium between the normal velocity conditions is reached between the solid and fluid boundary conditions.

In the ALE approach to FSI, elements may move with the material, remain fixed, or move at an arbitrary velocity. Elements at the fluid–solid interface can move and be distorted to keep the Eulerian elements in contact with corresponding Lagrangian elements.

A purely Eulerian approach to FSI usually entails the use of a shock physics code. An Eulerian FSI implementation makes sense for problems with very high deformation rates in the solids. The fluids and solids are both modeled using equations of state (EOSs). Deformation rates of the solids in these types of problems are high enough that a jump condition occurs. The solid experiences a shock and can be modeled using Hugoniot EOSs (Cooper, 1996). Example Hugoniot EOSs are Mie–Gruneisen and Johnson–Cook viscoplastic EOSs.

Particle methods accomplish FSI without special algorithms into the methods. Particle methods, in general, solve the governing equations on an Eulerian grid where derivatives can be conveniently defined. Information is transferred back to the particles. The particles carry the constitutive information with them as they advect to a new position for the next time step.

6.2. Material Models

There are a wide variety of materials available in each software suite. For the purposes of this study, only explosives and air are considered. It is assumed that any reflecting surfaces, i.e., blast barrier wall and structure face, are rigid enough to provide a reflective surface for a period of time long enough that the blast load is not affected by a failing structural element.

CTH, SHAMRC, LS-DYNA, AUTODYN, and DYSMAS all employ a version of the Jones–Wilkins–Lee (JWL) EOS for high explosives. The JWL EOS material model requires density, detonation velocity, and the Chapman–Jouget pressure. The general form of the JWL EOS is

$$p = A\left(1 - \frac{\omega}{R_1 V}\right) e^{-R_1 V} + B\left(1 - \frac{\omega}{R_2 V}\right) e^{-R_2 V} + \frac{\omega E_0}{V} \tag{2}$$

where A and B are linear constants, R_1, R_2, and ω are nonlinear coefficients, E_0 is the detonation energy per unit volume, and V is the ratio of the volume of detonation products to the volume of undetonated high explosive. The properties for common explosives are available (Dobratz, Crawford, 1985) and were used in these simulations. The JWL EOS has been implemented into the MPM as well for the current research. CTH uses a slight variation on the common JWL EOS (Bell, Baer, Brannon, Crawford, Elrick, Hertel, 2007). The CTH version is a thermodynamic variation of the form

$$p(\rho, T) = Ae^{-R_1 V} + Be^{-R_2 V} + \omega \rho C_v T \tag{3}$$

where ρ is the density and T is the temperature.

In all studies performed as part of this research, TNT was the explosive modeled. The JWL EOS inputs for TNT are 1.63 g/cm^3, 4.2945 x 10^{10}, 3.712 x 10^{12}, 3.231 x 10^{10}, 4.15, 0.95, and 0.30 for ρ, E_0, A, B, R_1, R_2, and ω, respectively.

The majority of computational codes that are commonly used for air blast calculations use the ideal gas EOS for modeling air. With the exception of CTH, all of the codes mentioned in this work use the ideal gas EOS for modeling air. The ideal gas EOS has the form

$$p = (\gamma - 1)\rho e \tag{4}$$

where γ is the ratio of specific heats, $\gamma = C_p/C_v$, ρ is the air density and e is the specific internal energy. CTH uses a tabular form of EOS for modeling air that was generated from testing (Bell, Baer, Brannon, Crawford, Elrick, & Hertel, November 2007). Properties used for ideal gas EOS modeling of air for all studies in this work are $\rho = 1.3$ kg/m^3, $e = 1.923 \times 10^9$ J/kg, and $\gamma = 1.4$.

The JWL EOS is basically an expansion of the ideal gas EOS with additional terms to handle the high-pressure regions. The first term is a high-pressure term. The second term is an additional term and the third term is the low-pressure term. It can be shown that at large expansion ratios, the first and second terms of the JWL EOS become negligible. In other words, when the explosive becomes compressed so that its volume is lower than its initial volume, the first and second terms of the JWL EOS become null, or it can be said that the relative volume becomes sufficiently important so that the exponential terms vanish. Thus, the remaining term is

$$p = \omega \frac{E_o}{V} \tag{5}$$

This is seen to be the same as the ideal gas law

$$p = (\gamma - 1)\rho e \tag{6}$$

where $\gamma = \omega + 1$.

All structural components of the simulations were modeled as rigid materials. It is assumed that all structural components involved in the simulations have a large enough natural frequency that they do not begin to move until after the full load has already been applied. If there are failing structural components involved, then this assumption is no longer valid and a fluid–structure approach must be utilized. For the simulations in this effort, it is assumed that all walls and structure faces are designed adequately for the rigid material assumption.

6.3.   Blast Wall Computational Approach

Verification of numerical software provides to engineers tools to bound the amount of error that might be expected in a given simulation. A discretization study was performed to compare the accuracy and performance of each code. A two-dimensional (2D)-axisymmetric comparison of CTH, SHAMRC, and DYSMAS was performed. The error and mesh size requirements are presented in comparison using a grid convergence index (GCI), which is a tool used to measure how quickly a CFD method approaches its ideal solution and the error of the most ideal solution produced by the method compared to an exact solution (Roache, 1994; Roache, 1998). The results are also compared against existing work determining a GCI for LS-DYNA, CTH, and AUTODYN (Schwer, Saadeghavaziri, O'Daniel, Madsen, 2008). The codes are then validated against live blast experiment data. Finally, a three-dimensional (3D) mesh convergence study was performed to fully understand the amount of error in the modeling technique.

The concept of a GCI is a commonly used approach to quantify the discretization error of a computational method (Roache, 1994; Roache 1998). There are generally two types of errors in respect to computational methods; discretization errors and modeling errors. Discretization errors are numerical errors due to the grid size of the cells that comprise the computational domain. Modeling errors are due to the choices of materials models, boundary conditions, and

other assumptions that imposed by the modeler. If the discretization errors of a computational method are well-understood, then the modeling choices can be explored in detail to find the most-nearly optimal solution that the modeling approach is able to produce.

The method for determining a GCI entails comparing results from three mesh refinements to estimate the discretization error. Based on this discretization error, a result of the ideal result that the computational method is able to produce for the quantity of interest is obtained along with an interval that will likely contain the numerically exact solution.

The first step in determining the discretization is to compare the three mesh refinements, which is done most efficiently if a constant mesh refinement ratio is kept where the ratio is defined by

$$r_{ji} = \frac{r_j}{r_i} \tag{7}$$

where r_i refers to the coarser grid size and r_j refers to the finer grid size. Comparison of the results produced with the varying mesh sizes produces relative errors for the quantity of interest which can be used to develop a numerical convergence rate. The numerical convergence rate is not always the same as the theoretical convergence rate for the numerical method and methods can have different convergence rates for the desired quantity, such as pressure or impulse as presented in this section. The rate of convergence, p, is defined by

$$p = \frac{\log\left(\frac{f_3 - f_2}{f_2 - f_1}\right)}{\log r_{ji}} \tag{8}$$

where $f_1, f_2,$ and f_3 refer to the numerical result at each mesh refinement level. Eq. 8 is valid only for a constant r_{ji}. Roache (1994, 1998) provides alternate approaches for non-constant mesh refinements. After the observed rate of convergence is obtained, it can then be used to define the GCI. The GCI is given by

$$GCI_{fine}^{21} = \frac{F_s e_a^{21}}{r_{21}^p - 1} \tag{9}$$

The term

$$e_a^{21} = \left|\frac{f_1 - f_2}{f_1}\right| \tag{10}$$

is the relative solution difference between the finest grid solution, f_1, and the next-coarsest grid solution, f_2. F_s factor is a safety factor applied to the GCI. It is an empirically determined constant that is commonly assumed to be 1.25 when three mesh refinements are used. Roache (1998) determined that there is an interval that contains the numerically exact solution based on a 95% confidence level. This interval is defined as

$$I_1[(1 - GCI^{21}), (1 + GCI^{21})] \tag{11}$$

where I_1 is the impulse result from the finest mesh computation. It is also possible to extrapolate an expected value for the computational method based on the observed rate of convergence, p. For example, the extrapolated value for impulse is calculated as

$$I_{ext} = \frac{r_{21}^{p} I_1 - I_2}{r_{21}^{p} - 1} \qquad (12)$$

Eqs. 7–12 represent the GCI convention that has been used for the following studies on the suitability of the modeling approaches.

6.3.1. 2D Axisymmetric Mesh Convergence

To compare codes directly, a mesh convergence study provides a measure of accuracy and efficiency. To provide this direct comparison, a series of 2D-axisymmetric free-field air blast simulations were conducted using CTH, DYSMAS, and SHAMRC. LS-DYNA, FEFLO, AUTODYN, and ADINA were omitted from this study.

The setup for the study is a free-air explosion of a 226.8-kg bare TNT explosive charge. Data were recorded at a standoff of 4.572 m, and a GCI for both pressure readings and impulse readings was developed. Table 4 shows the results of the study in regards to pressure and Table 5 shows the results in regards to impulse.

Table 4. Grid Convergence Index for Pressure

Prediction Tool	p_1 (MPa)	p_2 (MPa)	p_3 (MPa)	p_{ext} (MPa)	p	GCI^{21}	Asymptotic Range	Interval (MPa)	
CTH	2.55	2.49	2.34	2.58	1.53	0.01	0.978	2.51	2.58
DYSMAS	2.64	2.59	2.37	2.65	2.14	0.01	0.980	2.62	2.66
SHAMRC	3.09	3.02	2.83	3.28	N/A*	0.08	0.802	2.84	3.33
TM5-1300				2.419					

* - Calculation produces a value below 1.0.

Table 5. Grid Convergence Index for Impulse

	I_1	I_2	I_3 (MPa-ms)	I_{ext}	p	GCI^{21}	Asymptotic Range	Interval (MPa-ms)	
CTH	1.071	1.070	1.039	1.071	4.701	0.000	0.998	1.071	1.071
DYSMAS	1.254	1.258	1.291	1.253	3.044	0.001	1.003	1.253	1.255
SHAMRC	1.124	1.150	1.194	1.123	3.843	0.001	127.172	1.123	1.125
TM 5-1300				1.169					

p_1, p_2, p_3, I_1, I_2, I_3 refer to the values produced by the simulations. The subscript refers to the refinement of the mesh, 3 being the coarsest and 1 being the finest mesh. For CTH and DYSMAS the three levels of mesh refinement correlate to 2-cm, 4-cm, and 8-cm mesh sizes (r_{ji}=2.0). For SHAMRC, the mesh sizes considered are 0.2 cm, 0.5 cm, and 4 cm. The asymptotic range is a check to see if the solution is asymptotically converging to the expected values for an appropriately refined computational model, p_{ext} and I_{ext}. If the value is close to 1.0, then the solution is close to convergence to the extrapolated values meaning that the mesh is appropriately refined. The *interval* is the 95% confidence range of solutions for a well-refined mesh. As a comparison, the expected value as predicted by the TM5-1300 (US Department of the Army, 1990) methodology has been presented.

All three of the codes over-predict the peak pressure for a well-refined mesh. All start with a low value and converge to a higher peak pressure value—as would be expected. SHAMRC over-predicts the peak pressure at the coarsest level. For the impulse, SHAMRC and DYSMAS converge from a large impulse number down to their ideal impulse solution, whereas CTH, by comparison, converges upward from an under-predicted value to the ideal solution. All three over-predict the expected TM5-1300 pressure, CTH being the closest. In contrast, for the impulse CTH under-predicts the impulse while SHAMRC and DYSMAS over-predict. The TM5-1300 expected values for pressure and impulse do not fall within any of the confidence intervals. A similar study by Schwer et al. (2008) found a similar result for CTH under-predicting the impulse. Schwer et al. (2008) also found that LS-DYNA and AUTODYN over-predicted the expected impulse. All of the codes were stable and converged asymptotically to their ideal solution with the exception of SHAMRC's impulse solution.

According to the current study and the work by Schwer et al. (2008), LS-DYNA, CTH, and DYSMAS appear to be good options. Due to the volume of data required to train the desired neural networks, an efficient scalable code is desired. Originally CTH was chosen for this effort, but the logistical overhead of the memory requirements and the efficiency of the code made it a poor choice for multiple pure blast propagation simulations. DYSMAS was ultimately chosen due to its availability to be utilized on the DoD high-performance supercomputers at the Air Force Research Laboratory (AFRL) and the trade-offs between efficiency and accuracy.

6.3.2. Live Experiment Verification

To increase confidence in the simulation results, verification of predicting the results from a live blast experiment is considered. The problem is a live blast experiment that was performed by the Air Force Research Laboratory at Tyndall AFB, FL. The experiment setup includes a metal revetment blast barrier wall in front of a rigid-faced structure. The goal of the experiment was to measure the effectiveness of metal revetments and assess the effectiveness to reduce the structural loads to the rigid face behind the barrier wall. Eight reflective pressure gauges were placed on the structure, five along the centerline of the structure and three placed a horizontal distance of 2.45 m from the vertical centerline of the structure (Figure 18). During the experiment, all data were captured. There was a gauge failure, however, and there were no data from gauge R4 (Figure 18). The explosive threat is a 216-kg TNT charge. The charge-to-barrier standoff is 5.8 m, and the charge–to-structure standoff is 11.5 m (Figure 19).
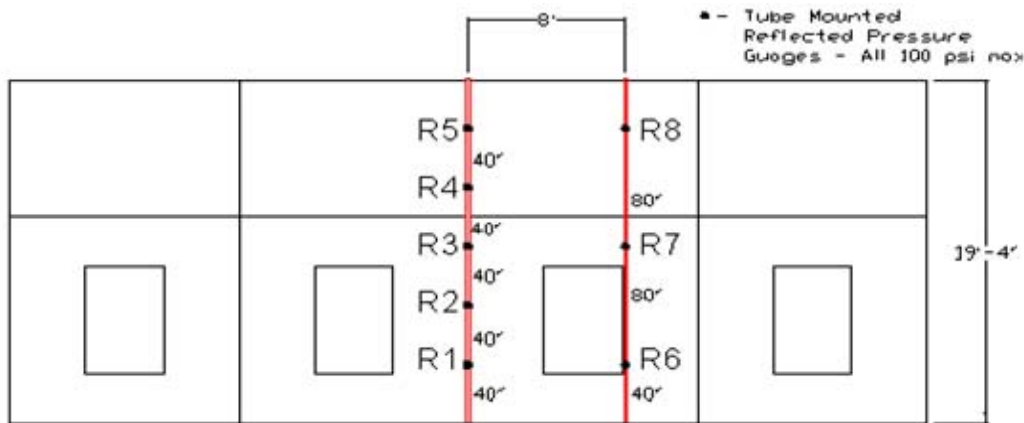
Figure 18. Gauge Placement for Live Blast Experiment
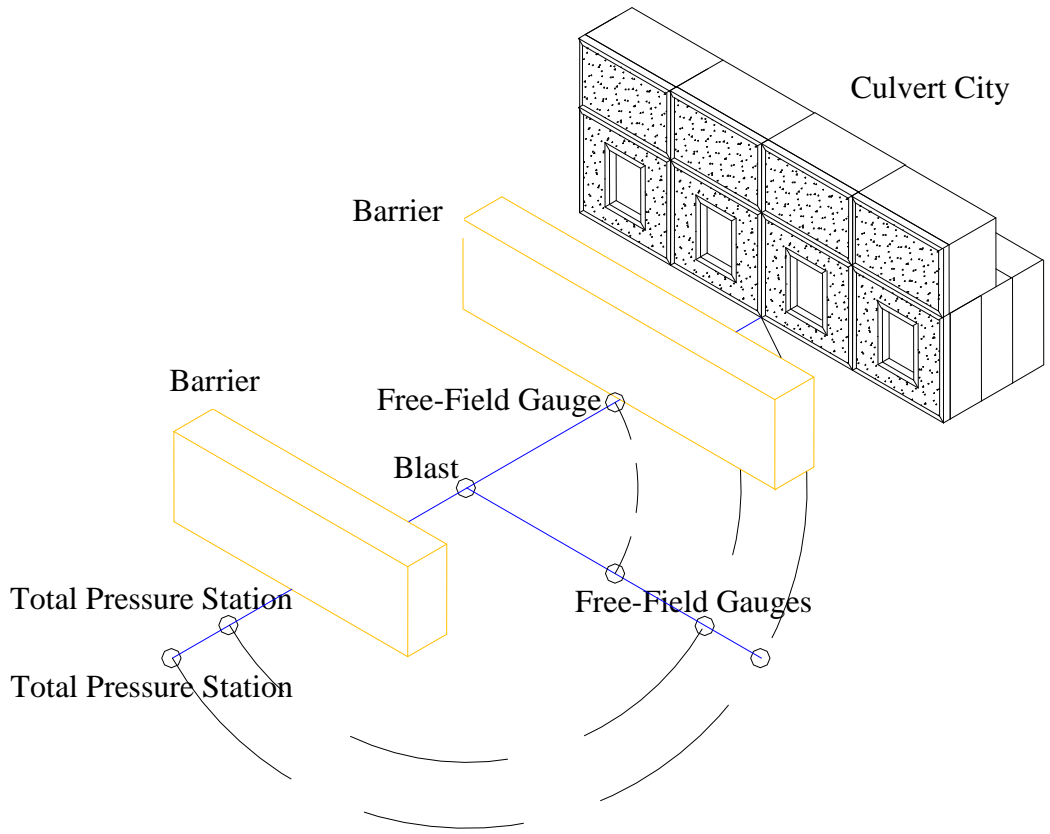
Figure 19. Live Experiment Configuration

The metal revetment is approximately 3 m tall and 1.52 m thick. The revetment performed well during the experiment. The peak deflection which occurred at the top of the wall in line with the charge was about 54.6 cm. The pre- and post-test results are shown in Figure 20.

(a)   (b)
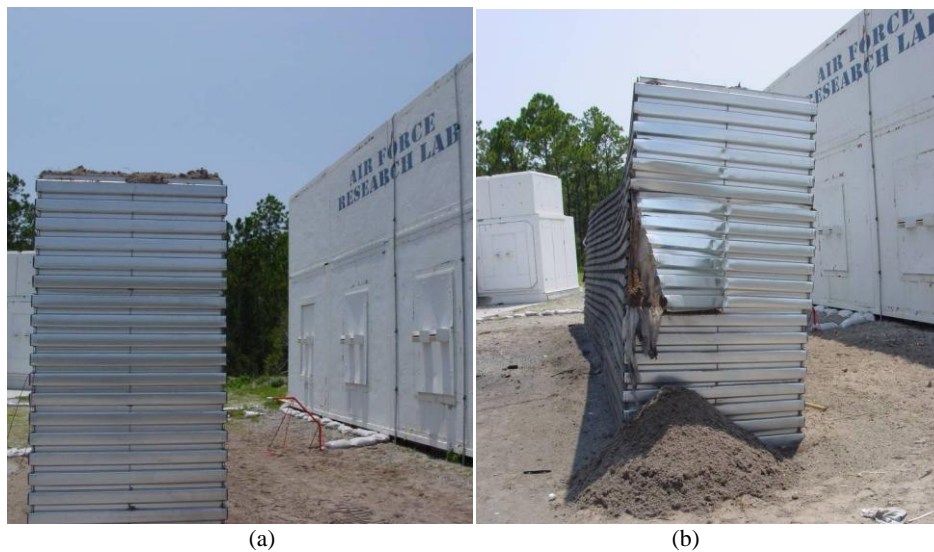
Figure 20. Metal Revetment Blast Wall (a) Pre-Test, (b) Post-Test

To help ascertain which code is the best choice, the experiment is modeled using both CTH and DYSMAS. The CTH simulation is performed using a 2D axisymmetric model. The DYSMAS model is performed using a full 3D model and is performed using multiple mesh discretizations. In both cases, both the metal revetment and the structure are modeled as rigid surfaces. While the metal revetment had a deflection of 54.6 cm, the assumption is that the low-stiffness, high-mass system was slow to react and so the interaction with the blast wave is relatively unaffected. Both codes performed well in modeling the full-scale live blast event.

The CTH 2D axisymmetric approach is presented first. The 2D axisymmetric setup is chosen with the assumption that the data are captured fully before any erroneous reflections. As in the 2D convergence study, the explosives are modeled using the JWL EOS, and the air is modeled using the tabular EOS for air (Bell, Baer, Brannon, Crawford, Elrick, Hertel, 2007). The domain is discretized using 2-cm cells, as the 2D GCI study showed that CTH converges to its most accurate solution with approximately 2-cm cell size dimensions. Figure 21 shows the time-history progression of the pressure contour maps during the 2D axisymmetric simulation. A reflective boundary condition is used at the end of the x-axis as preliminary studies showed accuracy was decreased when outflow conditions were specified. Figure 21 (f) shows the erroneous reflective wave that occurred as a result of this boundary condition. Figure 22 shows the numerical results of the simulation. CTH performs quite well and captures the waveform excellently. The model was attempted in a 3D version of CTH, but the model stalled out due to high sound speeds in which the program was not able to regulate the timestep. The timestep was too low for the simulation to progress forward.

The experiment is also modeled using the DYSMAS software suite. The DYSMAS model is performed using the full 3D model space since the 3D computational domain is required for certain blast barrier–structure configurations. The computational domain of the blast barrier configuration is simulated with a half symmetry model. The half symmetry model is required to avoid erroneous reflections. The bare explosive charge is placed as a hemispherical charge on the ground level, with an outflow boundary condition on all boundaries except for the ground, the x–y plane, and the axis of symmetry, the x–z plane, which are modeled as perfectly reflective surfaces. The simulation is performed with multiple discretizations. The discretizations used were 1-cm, 2-cm, 3-cm, and 4-cm cell sizes. Figure 23 shows the progression of the incident shock wave expanding after propagating over the blast wall and then reflecting off of the structure and the ground in between the blast wall and the structure for the simulation with the 3-cm cell size discretization.

Plots (d) – (h) in Figure 23 illustrate the shock wave reflecting between the structure and the barrier several times which produces the multiple spikes in pressure. The results show good correlation with the live test data. As shown in the convergence study, the peak pressures are predicted very well. The impulse shows a little more variation in accuracy, which was also depicted in the grid convergence study.
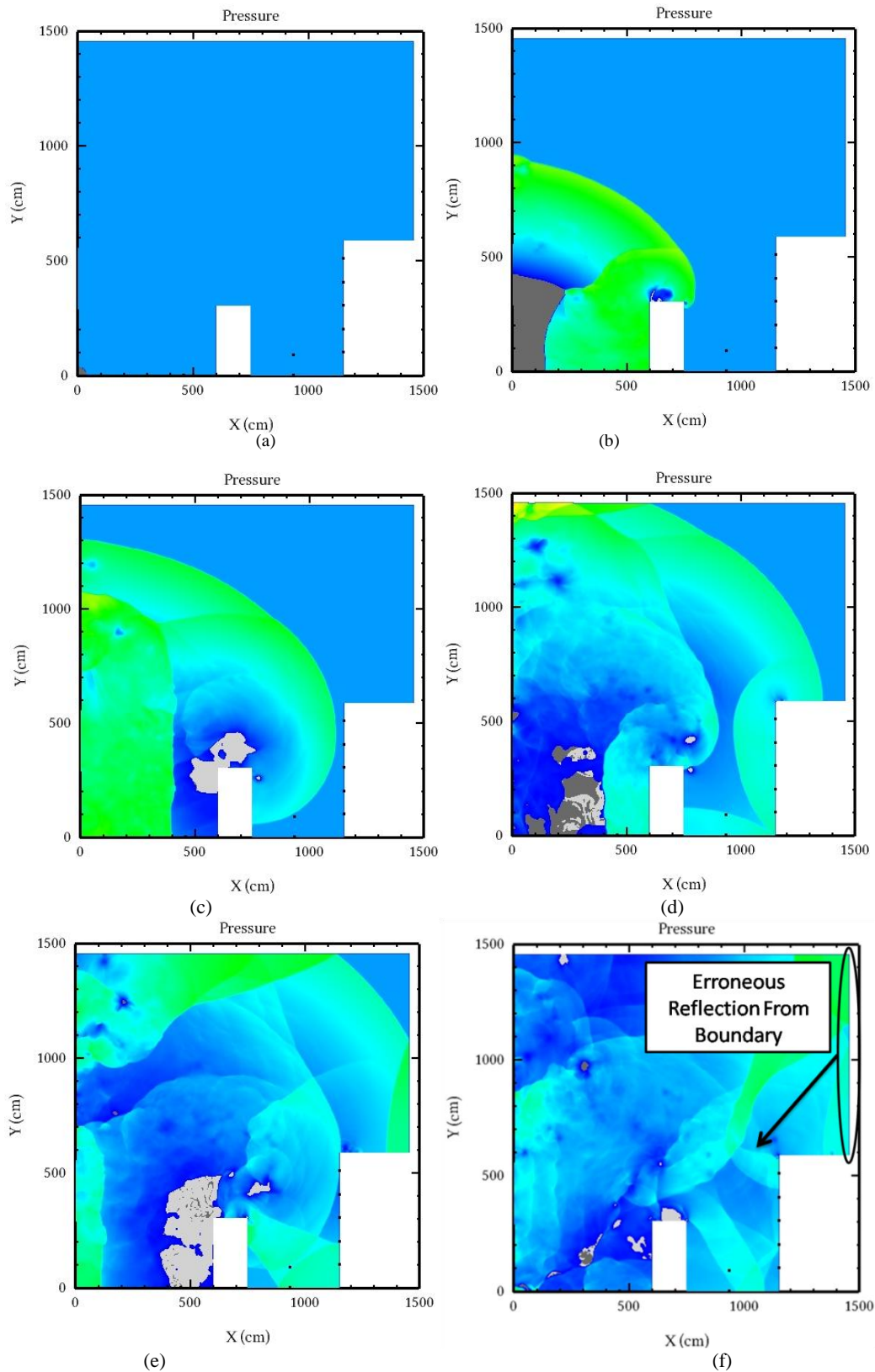
Figure 21. 2D Axisymmetric CTH Simulation Pressure Contours at (a) 0 ms, (b) 5 ms, (c) 10 ms, (d) 15 ms, (e) 20 ms, and (f) 30 ms
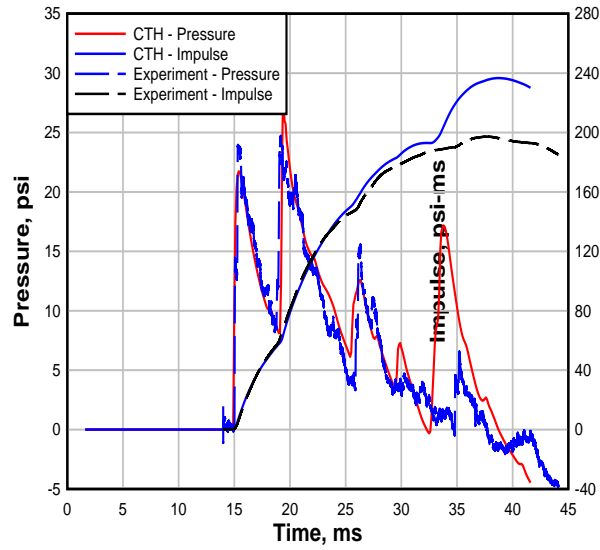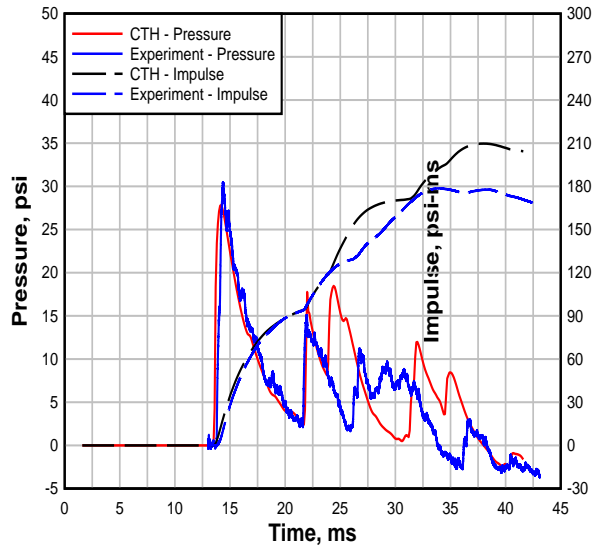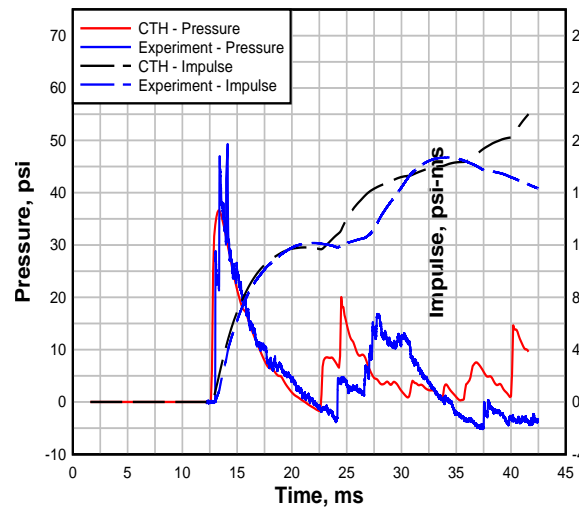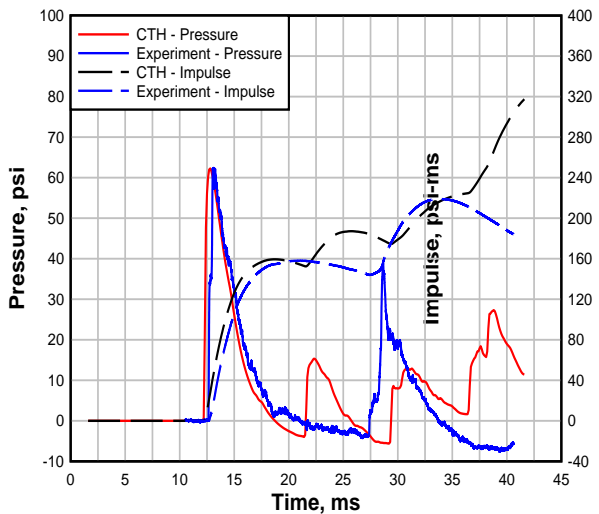
Figure 22. CTH-2D Axisymmetric Experiment Overlays (a) R1, (b) R2, (c) R3, (d) R5
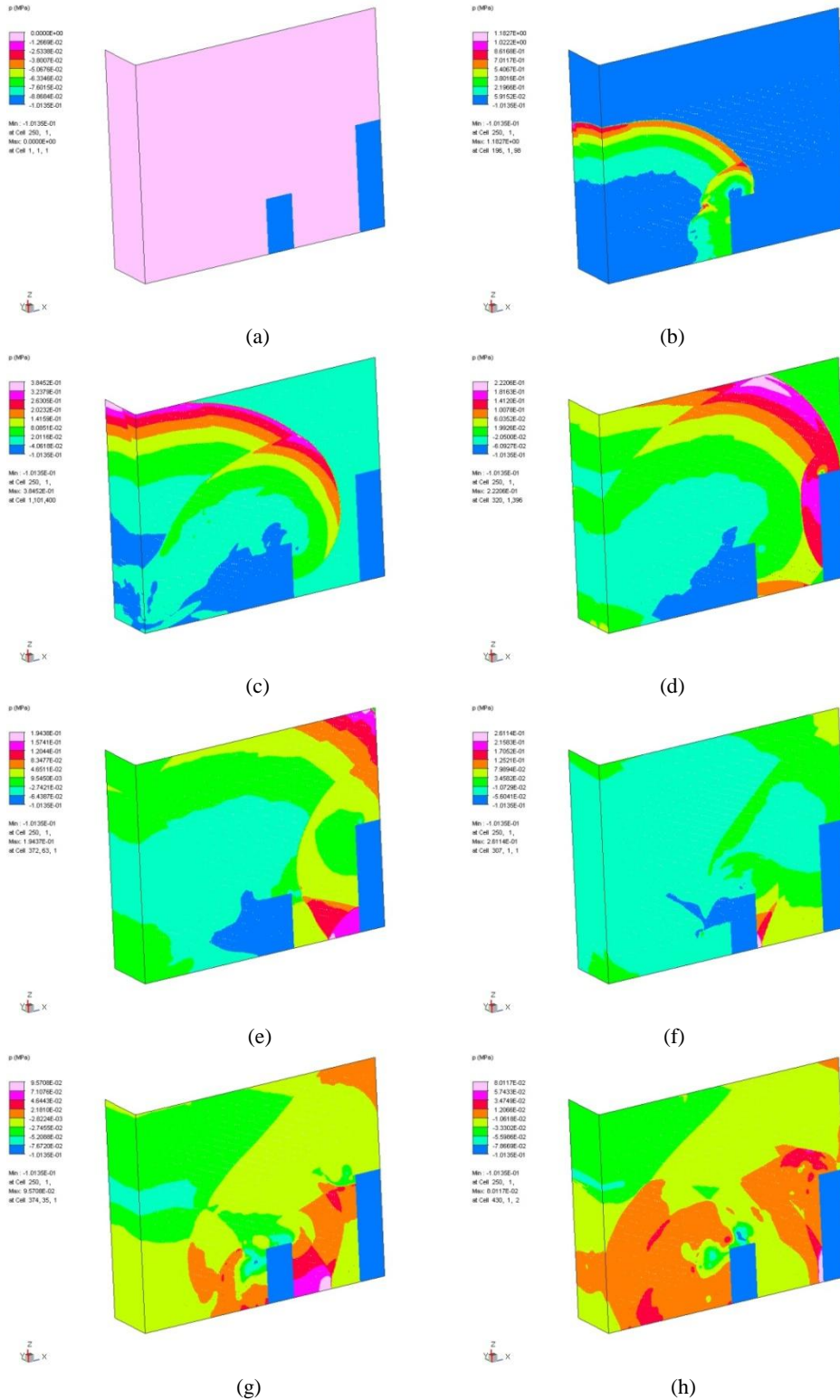
Figure 23. Blast Wave Propagation of DYSMAS Simulation at (a) 0 ms, (b) 5 ms, (c) 10 ms, (d) 15 ms, (e) 20 ms, (f) 25 ms, (g) 30 ms, (h) 35 ms

Figure 24 illustrates the behavior of the DYSMAS models as the mesh is refined. As indicated previously, the pressure is quite good, and the impulse is a little bit low. Figure 25 shows the overlay of the simulation results compared to live blast data gathered from the experiment reflection gauges as illustrated in Figure 18.

(a)

(b)
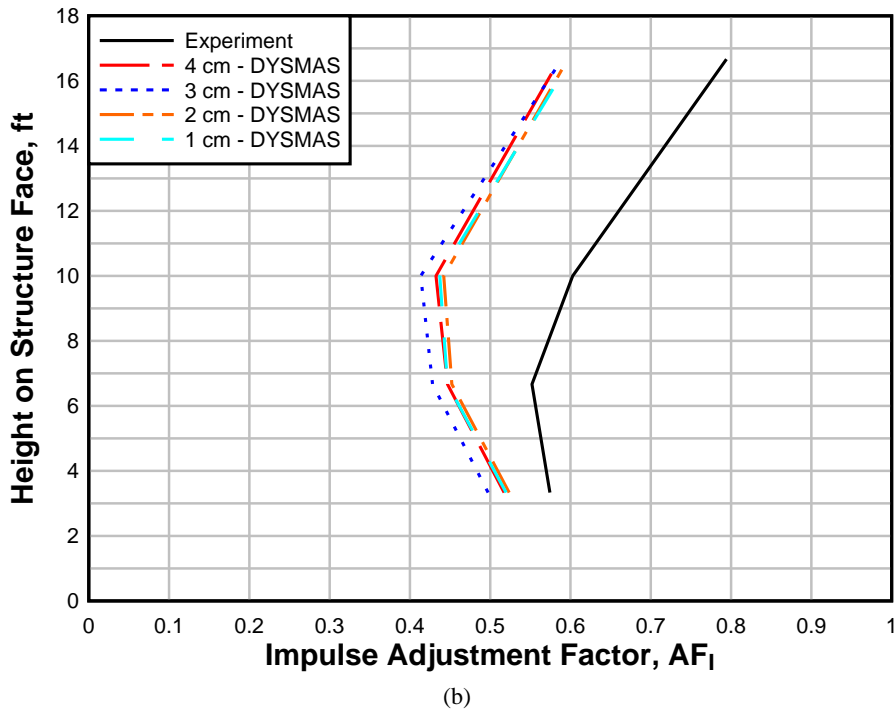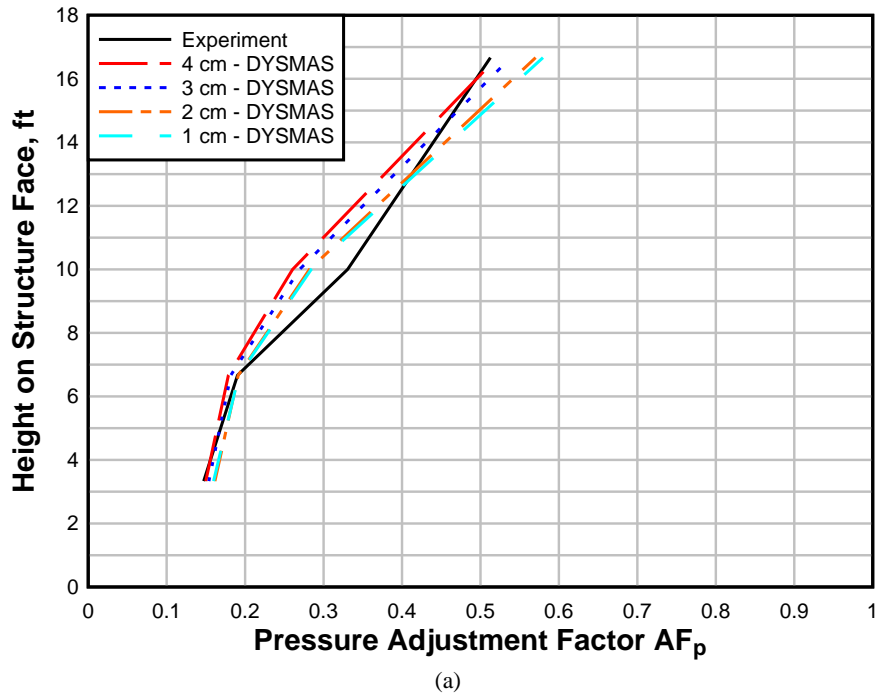
Figure 24. DYSMAS Mesh Refinement Accuracy of Live Blast Event (a) AF_p and (b) AF_I
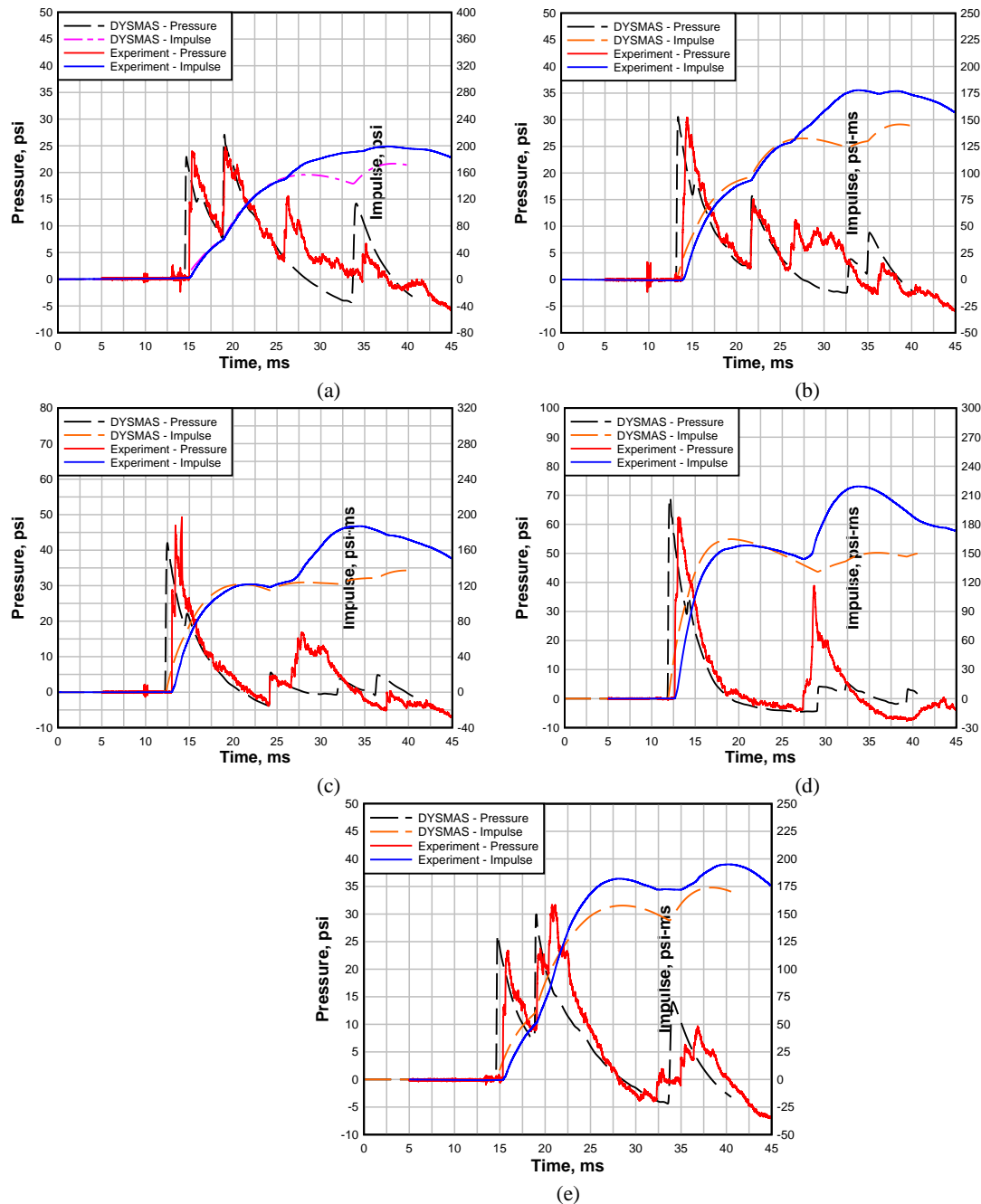
Figure 25. Overlay of Reflective Pressure Gauges (a) R1, (b) R2, (c) R3, (d) R5 and (e) R6

A close look at the overlay data presented in Figure 25 reveals that there is a tertiary spike in the experimental data in the 25- to 30-ms time range that is not captured very well by the simulation. This additional spike accounts for the impulse's being recorded as lower later in the event. Before the 25-ms point, the simulation and experimental data are nearly exact overlays of each other. The additional spike is not shown in the off-center gauge, R6. In the live blast experiment, there was an additional blast wall on the opposite side of the arena from the explosive charge. A quick analysis using the TM5-1300 method shows that the time of arrival

for a free-field threat to propagate the length from the charge to the opposite side barrier and reflect back to the structure would be 21 ms. It is hypothesized that the additional spike not captured by the simulation data is caused by a reflective wave from the barrier wall on the opposite side of the arena that then has to propagate over the barrier towards the structure.

It is apparent that the accuracy of DYSMAS changes little within the range of discretizations explored in this study. There are benefits had with the finer mesh sizes up to the 2-cm mesh size. The difference between the 2-cm and 1-cm mesh size is very little. The 1-cm mesh size is slightly more accurate in pressure, while the 2-cm mesh size is slightly better with the impulse prediction. Table 6 and

Table 7 compare the accuracy of CTH and DYSMAS for modeling the full-scale live blast experiment. The tables also show the adjustment factors (*AF*) calculated based on Eq. 1.

Table 6. Pressure Predictions of Full-Scale Experiment

Gauge	AFRL			CTH 2D Predictions		DYSMAS 3D Predictions	
	TM5-1300 Pressure (no wall)	Measured Pressure (psi)	AF_p	Predicted Pressure (psi)	AF_p	Predicted Pressure (psi)	AF_p
R1	167.7	24.7	0.15	30.1	0.18	27.1	0.16
R2	159.7	30.4	0.19	27.8	0.17	30.5	0.19
R3	148.7	49.3	0.33	36.6	0.24	42.1	0.28
R4	135.1	N/A*		49.4	0.36	N/A**	
R5	121.7	62.3	0.51	62.2	0.49	69.4	0.57
R6	153	31.6	0.21	N/A**		30.0	0.18
R7	137	N/A*		N/A**			
R8	114.4	N/A*		N/A**			

* - Instrumented Gauges Failed
** - Data Not Collected

Table 7. Impulse Predictions of Full-Scale Experiment

Gauge	Predicted (no wall)	AFRL Experiment		CTH 2D Predictions		DYSMAS 3D Predictions	
		Measured Impulse (psi-ms)	AF_I	Predicted Impulse (psi-ms)	AF_I	Predicted Impulse (psi-ms)	AF_I
R1	330.9	190.1	0.44	192.9	0.45	173.3	0.52
R2	322.1	178.6	0.42	170.6	0.40	145.7	0.45
R3	310.2	187.0	0.45	118.2	0.29	137.2	0.44
R4	NA*	N/A**		179.2	0.47	NA**	
R5	276	158.1	0.47	159.4	0.47	164.7	0.60
R6	329.8	NA*		NA**		174.0	0.53
R7	NA*	NA*	NA*	NA**		NA**	
R8	NA*	NA*	NA*	NA**		NA**	

* - Instrumented Gauges Failed
** - Data Not Collected

Both codes perform exceptionally well with very similar results. DYSMAS is slight more accurate predicting the peak pressure. CTH appears to be slightly more accurate on the impulse, but is non-conservative at gauges R2 and R3. Both codes appear to be excellent tools for modeling the blast environment.

6.3.3. Code Selection

The GCI study indicated that there were several codes available which could predict the blast environment with fairly good accuracy. CTH and DYSMAS were both able to converge to results that were within 10% of values predicted by TM5-1300 for peak pressure and impulse. For SHAMRC, the converged peak pressure prediction was quite high (35% error). The impulse had very good results (3.9% error), but the mesh size required was very small for convergence, making the logistics of accurate solutions very problematic.

Schwer et al. (2008) showed the convergence of LS-DYNA and AUTODYN compared with CTH. A comparison of those results with the results presented here shows some interesting trends. For the hydrocodes, CTH, DYSMAS, and SHAMRC, the trend is that the pressure and impulse both converge up to the most accurate to be expected results; meaning that the predictions are low for coarse meshes and a higher number is predicted for finer meshes. What is seen with the finite element codes that have been formulated for fluid–structure interaction, i.e., LS-DYNA and AUTODYN, is that the pressure converges from below, but the impulse converges from above. These codes tend to have waveforms that plateau before reaching the negative phase of the blast load scenario as illustrated by the free-field propagation model in Figure 26. Observation shows that the accuracy is dependent upon the standoff as well.

Incident Overpressures at Various Standoff Distances
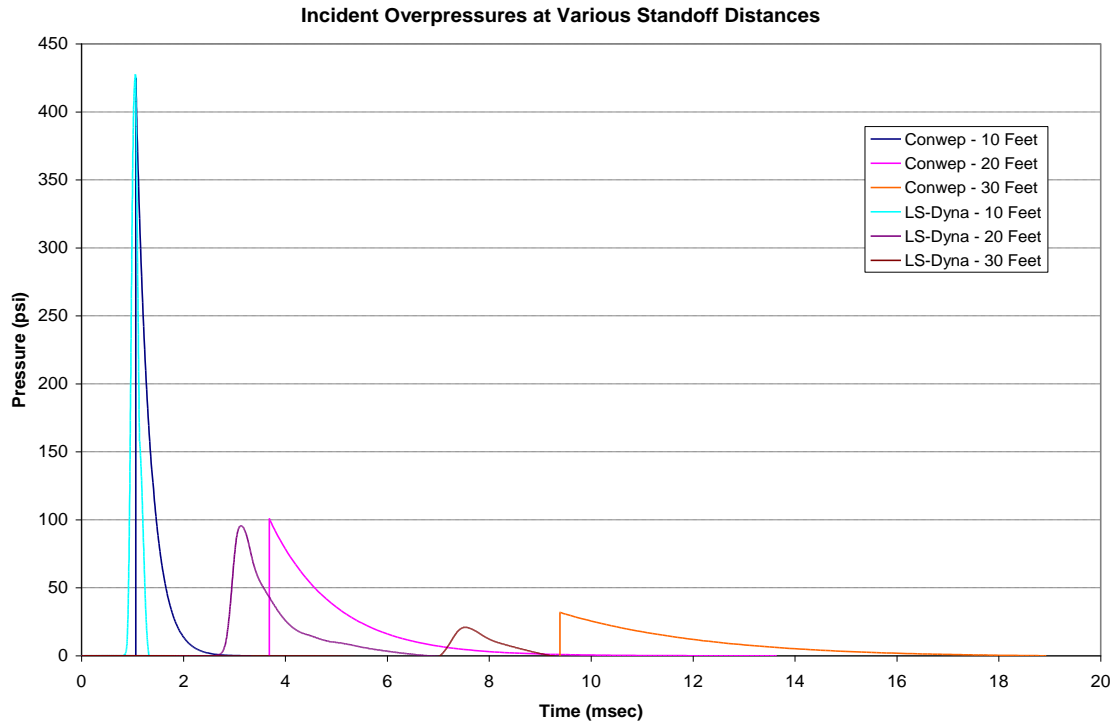
Figure 26. LS-DYNA Simulation of Free-Field Blast

Given the lessons learned, CTH and DYSMAS were determined to be the best choices for the effort. Initially, the research effort was performed using CTH. However, several simulations into the effort, it became evident that CTH is a very powerful and robust tool, but is not suited well for this type of research program. CTH is very accurate as shown here and by Mastin, Armstrong, and Welch (1995), but the overhead is too high for populating large sets of data. CTH is strongly suited for impact and penetration problems. The accuracy of this code makes it a good choice for efforts where one simulation is required. The large memory, processor, and wall clock times required for CTH make it too cumbersome for this type of research.

DYSMAS is proposed as the code to be used to populate the set required for training the neural network. DYSMAS showed to be very accurate and efficient as well. It requires roughly the same memory as CTH, but is more efficient in its use of the memory. It is also much more stable with regard to limiting the timesteps in a manner that produces accurate results, but does not compress the timestep to an impractical level such that no progress is made in the simulation. DYSMAS was chosen as the best balance between accuracy and efficiency.

6.3.4. 3D Mesh Convergence

To further study the mesh sensitivity and determine the accuracy of DYSMAS, a series of 3D free-field air blast simulations are considered. The results are compared to the widely accepted TM5-1300 method of predicting blast pressures in free-field blasts. Blast propagation is a problem with a spherically exact solution, which is discretized in a rectilinear fashion. It is expected that there will be errors and directional dependencies that occur due to this. The purpose of the 3D grid convergence study is to verify that DYSMAS has stable solutions, show

45

that the directional dependencies decrease as the mesh is refined, validate the accuracy against different charge size to see if there is an energy loss error tied to the explosive energy, and validate that the accuracy has the same grid convergence rate towards accuracy as was found in the study presented in section 6.3.1.

The 3D study includes three mesh sizes simulating four different charge sizes. The four charge sizes studied are W = 99.8 kg, 226.8 kg, 907.18 kg, and 2,267.96 kg. Each case was simulated with 1/8 symmetry using 2-cm, 4-cm, and 8-cm mesh sizes. Data were collected at 0.75-m increments in five directions. Tracers were placed along the x-axis, the y-axis, at a 45° angle up the x–z plane, at a 45° angle up the y–z plane, and at a 45°angle in the x–y–z direction. The results have been compared against the predictions of the TM5-1300 methodology. Figure 27 compares the results to the prediction from the TM5-1300 method for the 99.8-kg charge size.
Figure 28 shows the comparison of the results and the prediction from the TM 5-1300 for the 2,267.96-kg charge size. The results are reported in the 45° x–y–z direction, but should be considered typical of the results.

As shown in both figures, there is an effect of the charge size on the accuracy. The predictions of the peak pressure are very accurate in both cases. The impulse is more accurate for the larger charge size. This is a trend that is typical through all of the experiments.
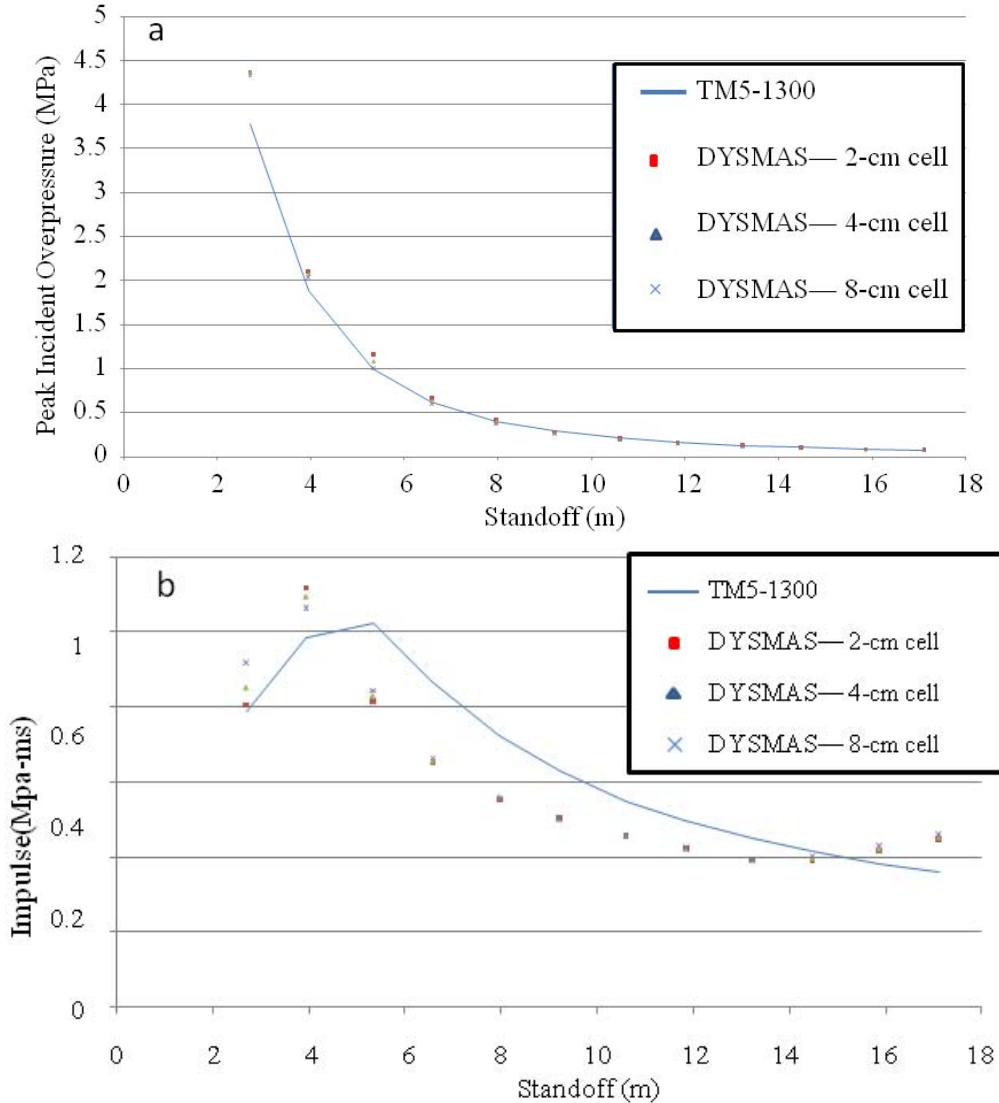
Figure 27. (a) Peak Incident Pressure and (b) Impulse Comparison for 99.8-kg TNT Charge

The convergence study also looked at the effect of direction in the accuracy. Blast propagation is, by nature, a spherical problem. Because of this, there will be errors due to rectangular discretization of a spherical problem. Figure 29 shows the correlation between the predicted pressures and impulses with the expected TM5-1300 values for the finest mesh condition, 2-cm cell sizes. There is a good correlation between the two sets of data. The biggest sources of errors occur along the *x*-axis and the *y*-axis.

Errors range from 1% in the best case up to 42% in the worst case. The correlation factor for the set of data is 0.987 for the pressure predictions with a mean absolute error of 437 kPa, and 0.9628 for the impulse predictions with a mean absolute error of 0.165 MPa-ms. The scatter of the error is consistent, meaning that there are no specific directional dependencies.
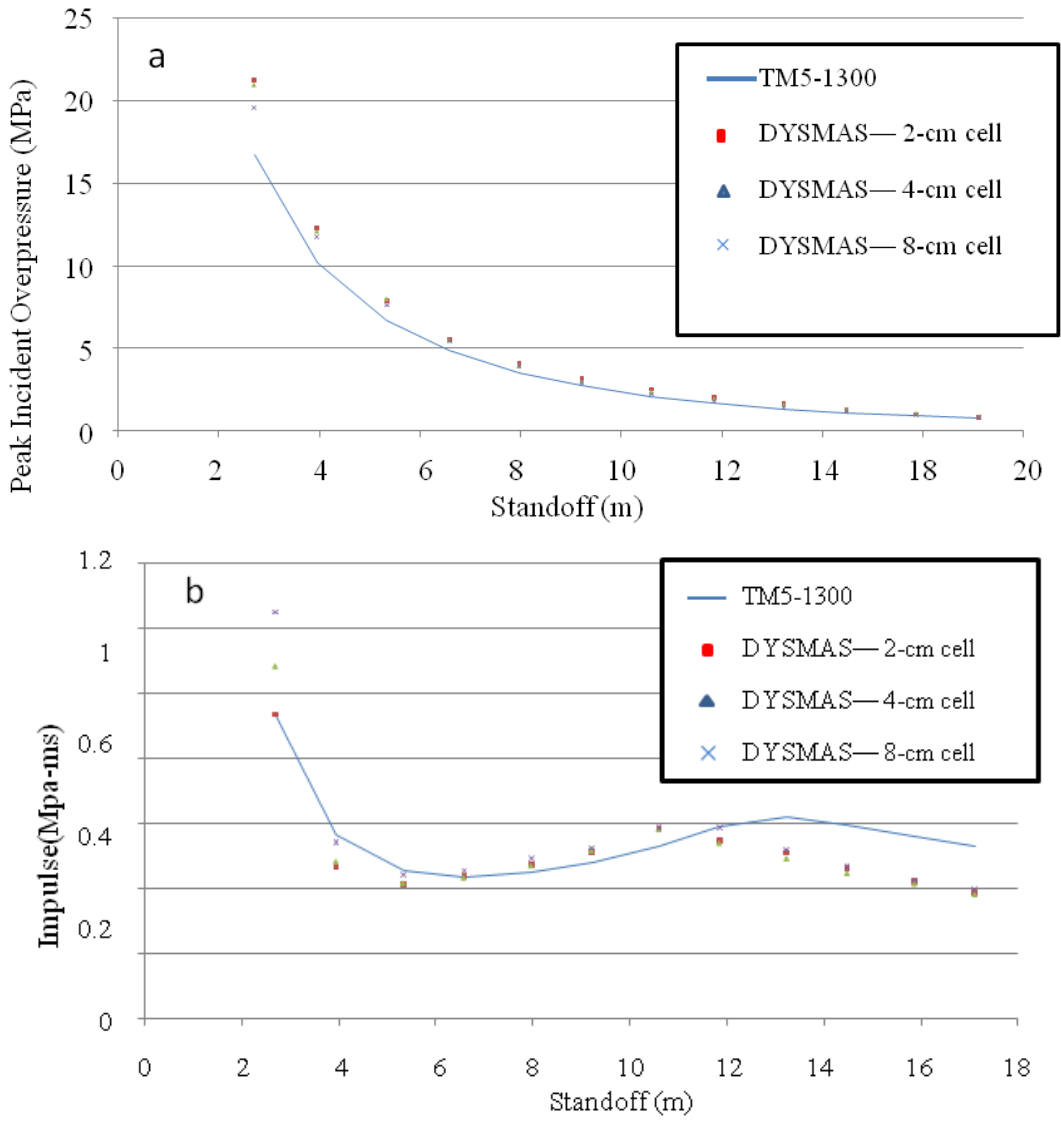
Figure 28. (a) Peak Incident Pressure and (b) Impulse Comparison for 2,267-kg TNT Charge

For each of the four threats, the pressure is very accurately predicted by the DYSMAS simulations. As mentioned before, the impulse predictions are less accurate. A review of the data reveals a trend to these errors. According to the TM5-1300 methodology, the blast pressure decays exponentially as illustrated in Figure 27 (a) and
Figure 28 (a). The general trend for the impulse predictions is a curve that takes the shape of a cubic line. Using
Figure 28 (b) as a reference, the impulse starts at a high value and drops as the standoff is decreased. At a certain standoff, there is a trough in the impulse value and the slope changes towards an increase in impulse prediction up to a maximum where the slope again changes and slopes down towards zero as the standoff goes to infinity. These can be seen in Figure 28 (b) with the trough in the curve occurring at about a 6-m standoff and the secondary max in the curve occurring at a standoff of about 14 m. The importance of this phenomenon is that it represents a problem error

(a)

(b)

49
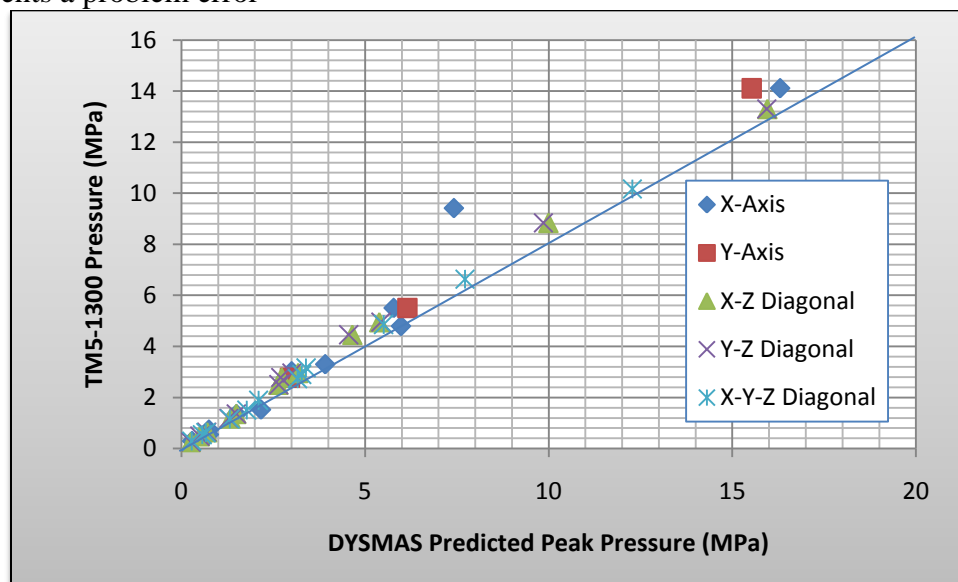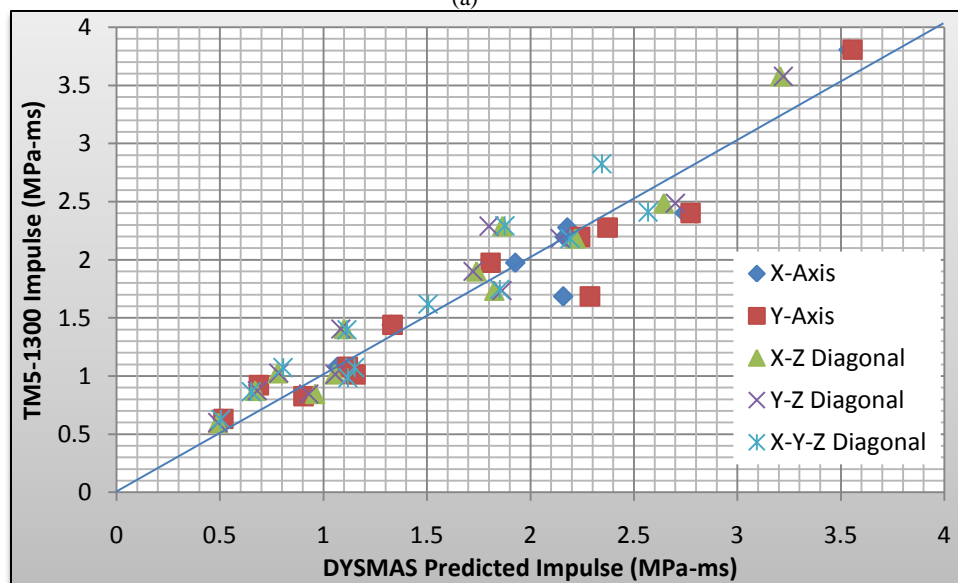
Figure 29. Directional Errors — Correlation of (a) Pressure and (b) Impulse

for the simulations to capture properly. A survey of the data shows that the impulse predictions are good up until the point of the secondary maximum. For all discretizations, charge sizes, and directional dependencies, the simulations under predict the impulse at this secondary peak. As the standoff increases, the impulse prediction from the simulation approaches back to better accuracy in line with the engineering model. A trend line of the simulation data shows this secondary peak in the impulse–standoff curve as well. It is typically under predicted, however. A compilation of all of the figures illustrating the error versus direction and the error over the standoff for all four charges and the three discretizations has been placed in 0.

7. APPLICATION OF THE PROPOSED PROCEDURE

7.1. Blast Barrier Simulation Problem Setup

The convergence studies and live blast data validation experiments provide confidence in the accuracy of DYSMAS for modeling blast shock wave propagation. For this reason, the research program was carried out using DYSMAS. For each simulation completed in the current study, a common format is used. The material properties are set to the values as used in the computational studies of Section 6.

Initial attempts at modeling the blast environment were performed using a 2D axisymmetric analysis. It was quickly realized that the 2D axisymmetric analysis was insufficient. The reason for this is that there are certain configurations for which the blast wave expands into the space between the barrier and the structure and there are erroneous reflections off the axis of symmetry before the initial load has cleared the structure. Due to this problem, the approach moved to a full 3D modeling approach.

The blast wall simulations are all set up as half symmetry. For each simulation, there is a set standoff behind the bare hemispherical surface charge opposite the blast wall that was set to 1.524 m with an outflow boundary condition. The width of the simulation is also set to 1.524 m due to memory restrictions of performing large numbers of memory intensive simulations. The structure height is set to 9.144 m. While variances in the structure height would be beneficial, this variable is held constant due to the restrictions of the number of independent input variables into the ANN methodology. The thickness of the blast barrier is set to 30.48 cm. This is again due to the limitations of the input variables for the ANN technology. Additionally, Zhou and Hao (2008) have reported in a sensitivity study that the barrier thickness does not have a large effect on the behavior of the blast loads. Figure 30 displays the typical setup. Outflow boundary
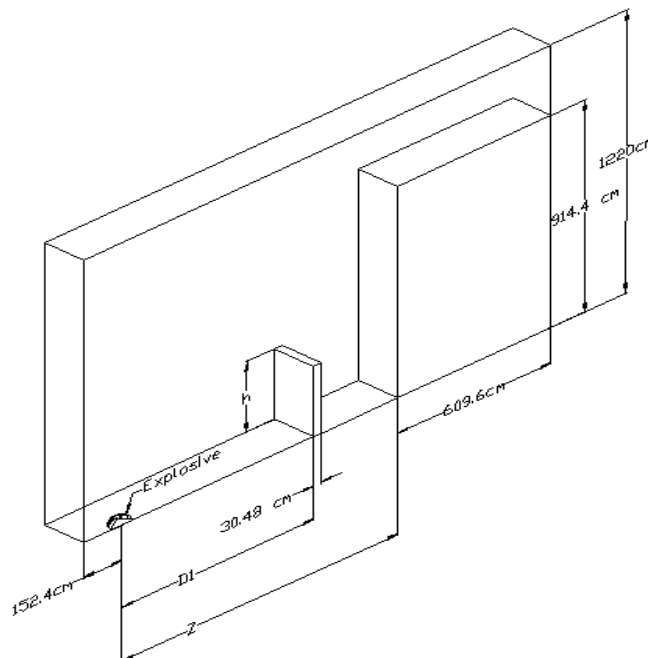
Figure 30. Neural Network Training Patterns: Typical Simulation Configuration

conditions were defined at the extents of the computational domain. The x–y plane simulates the ground and is modeled as a perfectly reflective surface. Likewise, the x–z plane acts as an axis of symmetry and is modeled as a perfectly reflective surface.

Tracer data collection points were placed at evenly spaced increments on the face of the barrier, the face of the structure, and on the first 1.524 m of the roof of the structure. The data tracer points were placed at 30.48-cm increments on each face. On the structure face, there are 31 tracer points over the height of the structure and six tracer points over the width for a total of 186 tracer points collecting data on the structure face for each simulation. On the roof structure, the evenly spaced grid of tracer points includes six tracer points over the length, and six tracer points over the width for a total of 36 tracer points.

To get good correlation with an ANN approach, it is important to train the ANN model with data that cover all regions of the variable space. As outlined in **Error! Reference source not found.**, here are six variables to be considered as input into the ANN model. There are four independent variables considering two of the variables, the locations on the structure face l_s and w_s, are inherent in each simulation and, thus, do not require extra simulations to fill that part of the variable space. Generally, experience shows that collecting data that cover a 3 x 3 grid of the data space is required at a minimum to get accurate results from an ANN model. If available, moving to a 5 x 5 grid of the variable space can give even better results as there are more training patterns for the ANN to learn. However, this can be quite cumbersome. The number of data points required to completely cover the data space is determined by the number of data points in the variable space grid raised to the power of the number of independent variables. For the current study, there are four independent variables. Thus, for a 3 x 3 grid, $3^4 = 81$ simulations are required. To collect enough data for a 5 x 5 grid, $5^4 = 625$ simulations are required. Due to the sheer volume of computational memory and wall clock time required, this study focused on developing the 3 x 3 grid with 81 simulations. Ten additional simulations were completed; five as test conditions, and five simulations intended to show the effect of filling in the variable space with additional simulations.

Four main focus areas are presented for this study. Training of the ANN models was performed using a sample of the data collected from each simulation. For the structure face, 36 of the 186 tracer points were used to train the ANN. In the first approach presented, an evenly spaced 6 x 6 grid of the tracer points on the structure face was used to train the ANN model. The effects of using blast scaling were also explored. The second approach shows the effect of biasing the collection of data from the grid on the structure faces to collect more data in the ranges that showed the greatest amount of error from approach 1. In approach 3, a case is made for the effect of using additional simulations to fill in more areas of the variable space. Five additional randomly generated simulations were completed and added into the ANN model. The fourth focus area is using the data generated to examine the effect of blast walls on the roof loads. For the roof portion, nine of the 36 tracer points collected in each simulation on the surface of the roof were used for training purposes.

7.2.   Discussion of Simulation Results Trends

Analysis of the numerical simulation data generated with the DYSMAS code allowed several general trends to be readily observed. First, the best results are obtained when the charge-to-wall

standoff, d_1, is at a minimum. The largest reduction factors are found toward the bottom of the structure. When the effectiveness is at its optimal, the reduction factor is the largest at the base of the structure. As the standoffs increase, there is often a kink point found slightly above the base of the structure. The location of this kink point moves to higher locations on the structure face as the standoff increases. Figure 33–33 illustrate the phenomenon with representative plots of the pressure adjustment factors over the height of the structure for differing values of barrier height and charge to structure standoff. The pressure adjustment factor over the height of the structure is plotted. For the small standoff, Z, Figure 33, the AF_p is at a maximum at the base of the structure. At the interim standoff, there is a kink point just slightly above the base. At the largest standoff, in general, the kink point is towards the top of the structure. The largest standoff actually creates an increased load for the barrier heights of 1.52 m and 3.05 m.
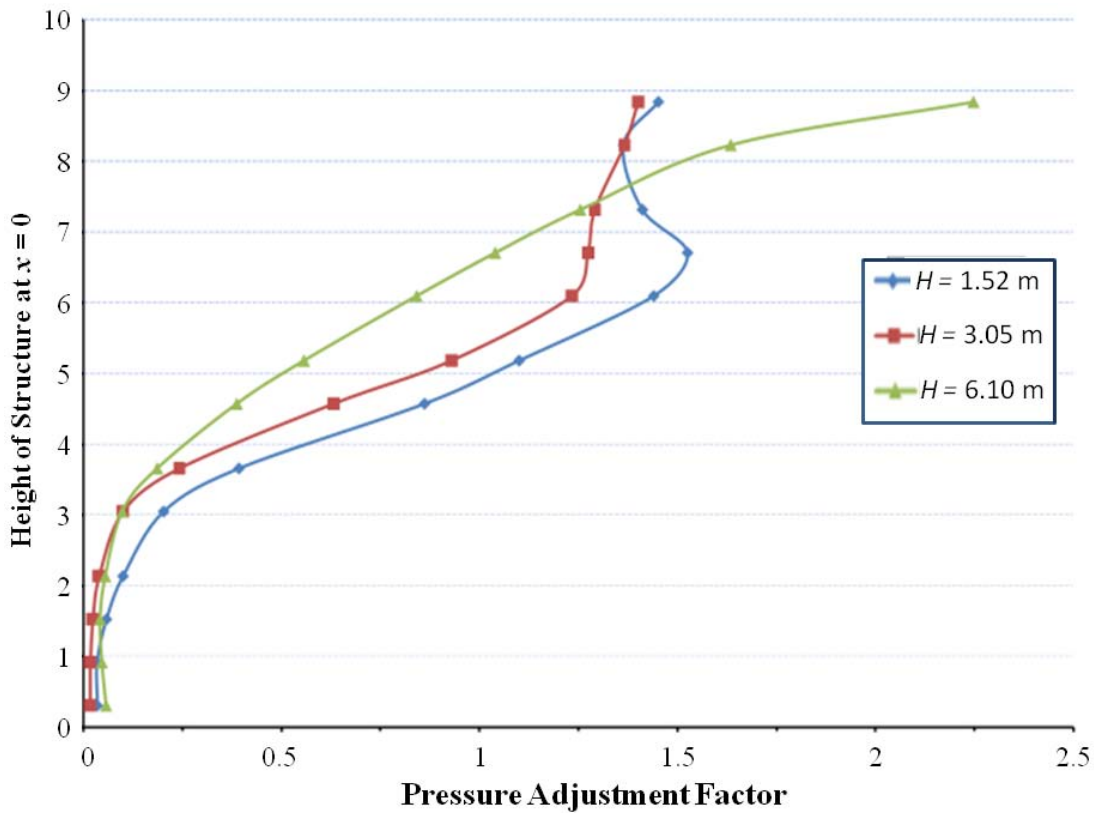
Figure 31. Effect of Barrier Height on Pressure Factors, W= 22.68 kg-TNT, d_1 = 0.19 m, Z = 3.24 m

For the same set of configurations, there is a different behavior with the impulse adjustment factors. Comparing the impulse reduction factors (Figure 34–Figure 36) with the pressure adjustment factors (Figure 31–Figure 33) shows that the effect of the barrier height is more pronounced. For the pressure adjustment factors, the reduction over the height of the structure is near identical for each barrier height at the smallest configuration of Z. At each of the next two increments of Z, there is a distinct increase in the effectiveness of the barrier as the height is increased. The impulse reduction factors are increased for all of the scenarios in this particular

illustration for the 1.52-m barrier height. However, the reduction factors are quite large for the 3.05-m and 6.10-m heights.
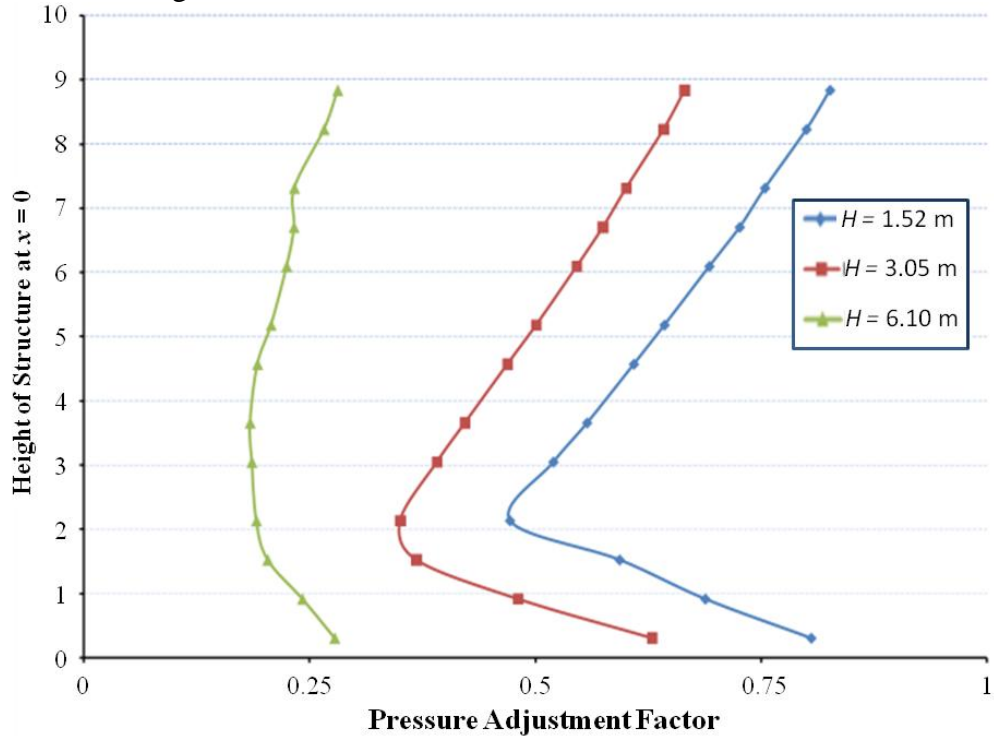
Figure 32. Effect of Barrier Height on Pressure Factors, W =22.68 kg-TNT, d_1 =0.19 m, Z =10.82 m
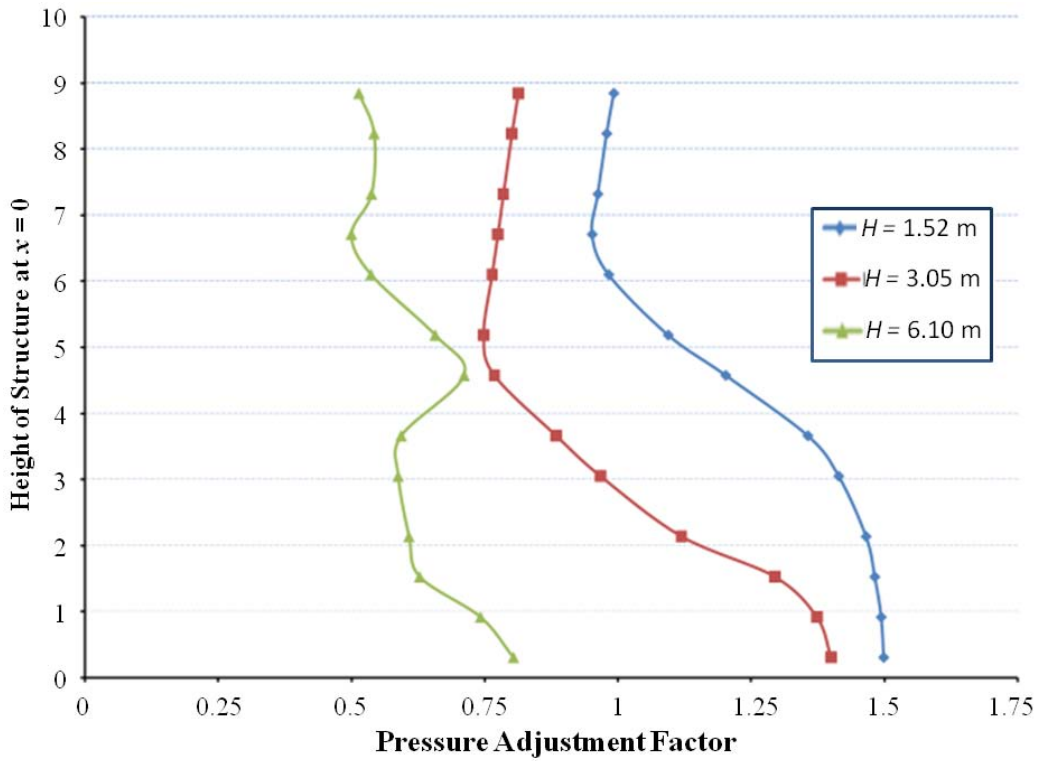
Figure 33. Effect of Barrier Height on Pressure Factors, W =22.68 kg-TNT, d_1 =0.19 m, Z =23.01 m
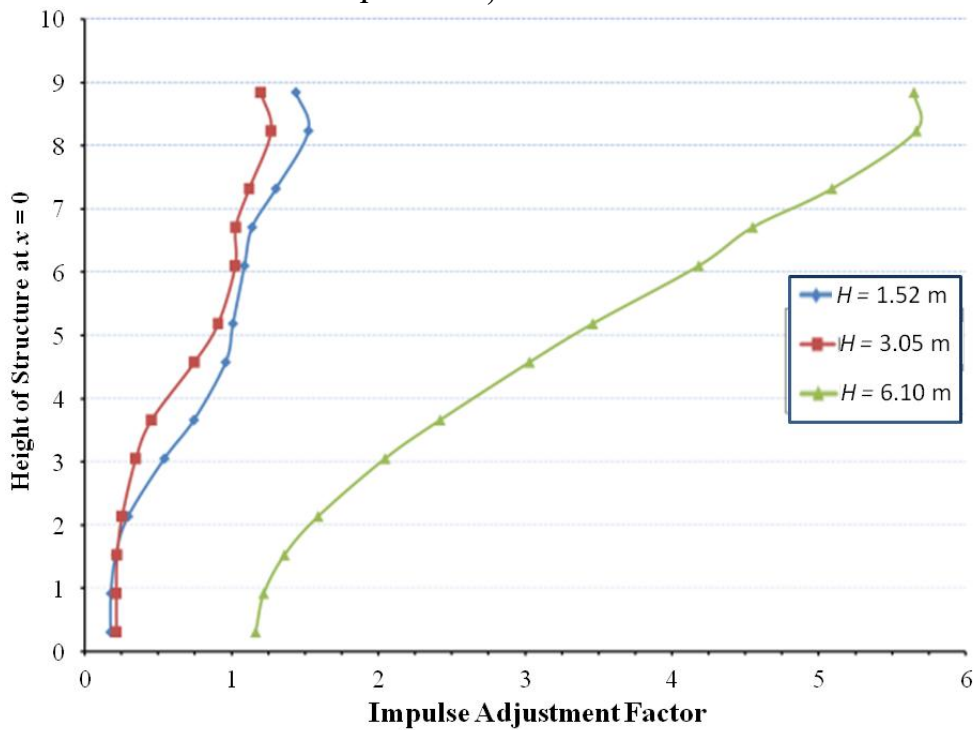
Figure 34. Effect of Barrier Height on Impulse Factor, W = 22.68 kg-TNT, d_1 = Contact Charge, Z = 3.24 m
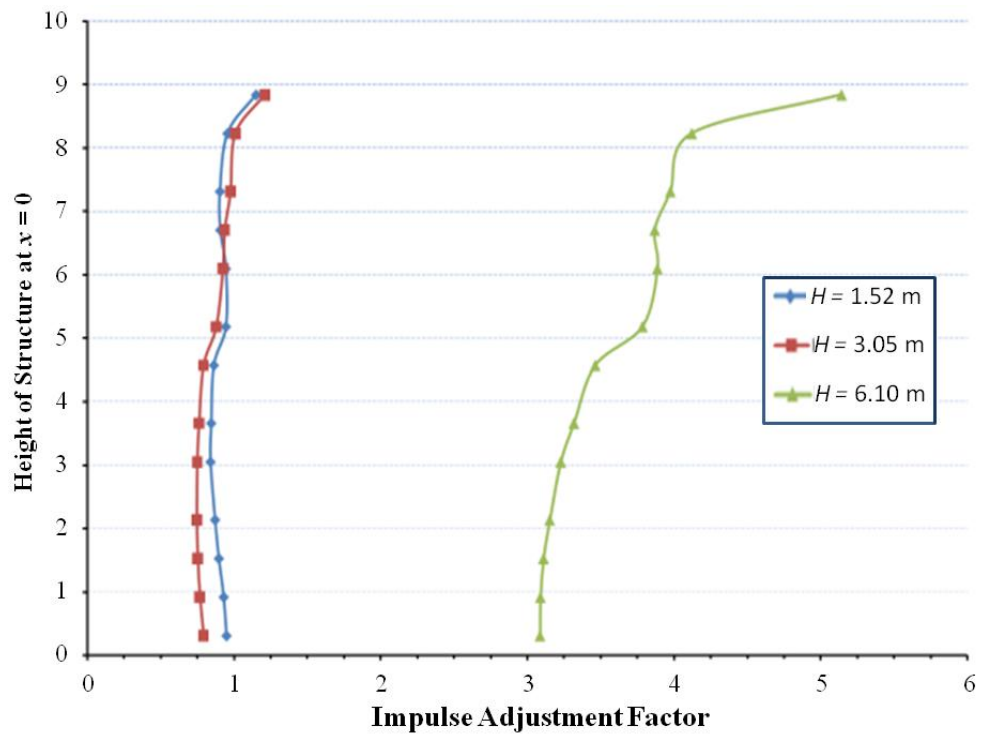
Figure 35. Effect of Barrier Height on Impulse Factor, W = 22.68 kg-TNT, d_1 = Contact Charge, Z = 10.82 m
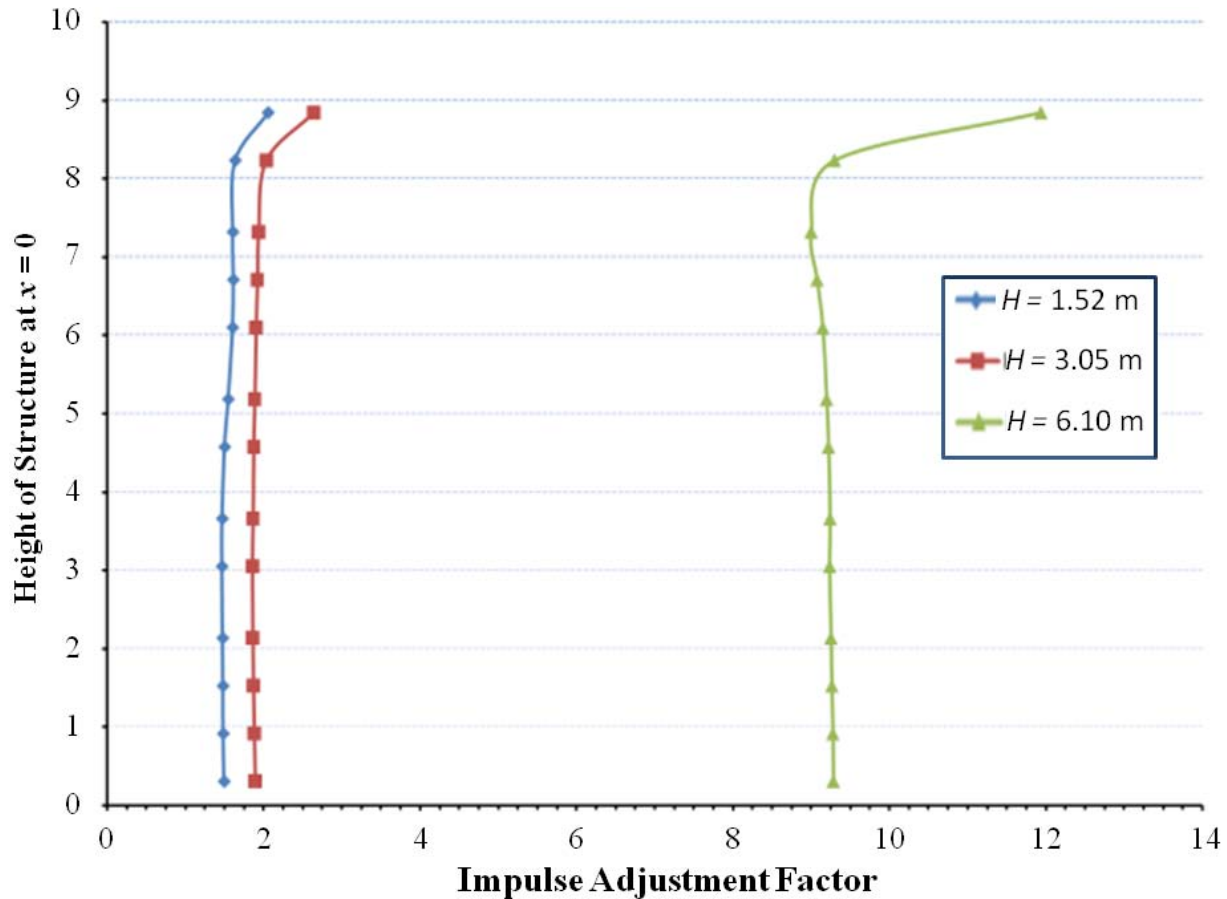
Figure 36. Effect of Barrier Height on Impulse Factor, W = 22.68 kg-TNT, d_1 = Contact Charge, Z = 23.01 m

Results were also collected at locations at lateral locations away from the axis of symmetry. Figure 37–Figure 39 are results of the data off-center correlating to the centerline results in Figure 31–Figure 33. The trends that are seen in the case along the centerline are, in general, also found at locations at lateral distances from the axis of symmetry for the barrier problem.

The effectiveness realized in the form of the reduction factors decreases as the height on the structure face is increased. In general the effectiveness of the blast barrier provides increased protection over the entire height of the 9.14-m-tall structure. The enhancement of the pressure and impulse loads (reduction factors > 1) is a significant finding. This situation occurs in general at locations on the structure at a height above the height of the protective blast wall. The worst configurations for these enhancement scenarios are those of large barrier-to-structure standoffs with short barrier heights.
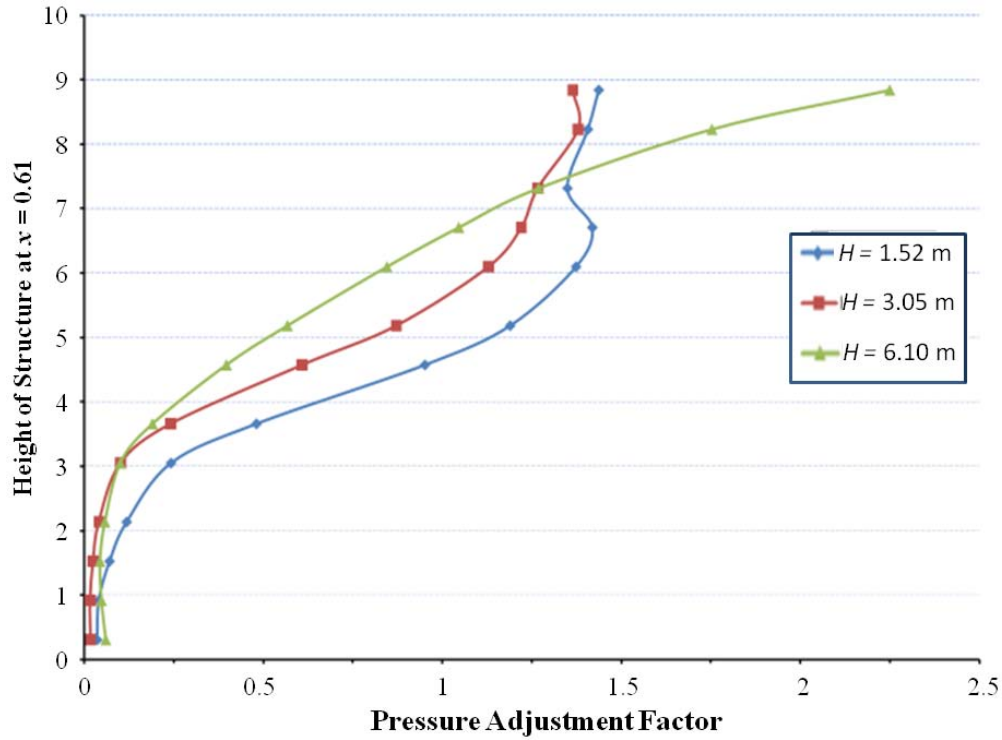
Figure 37. Effect of Barrier Height on Pressure Factor, W = 22.68 kg-TNT, d_1 = 0.19 m, Z = 3.24 m
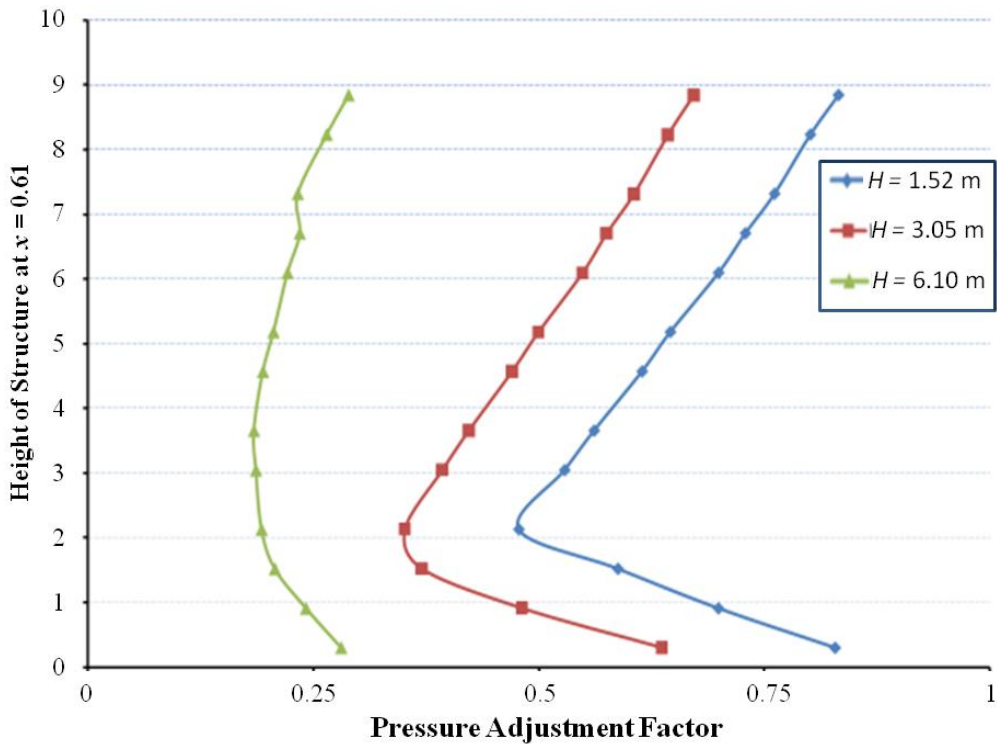
Figure 38. Effect of Barrier Height on Pressure Factor, W = 22.68 kg-TNT, d_1 = 0.19 m, Z = 10.82 m
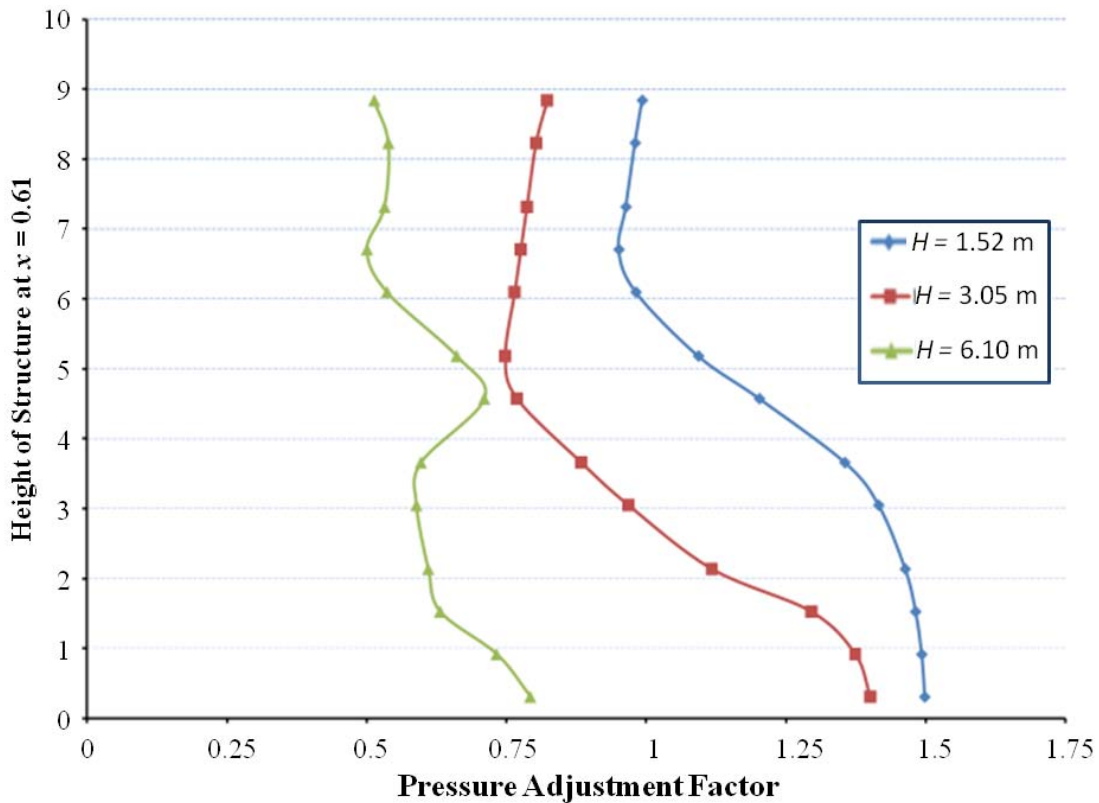
Figure 39. Effect of Barrier Height on Pressure Factor, $W = 22.68$ kg-TNT, $d_1 = 0.19$ m, $Z = 23.01$ m

The above illustrations exhibit the non-linearity of the problem at hand. They also raise alarm about the importance of having an effective design tool for blast barrier effectiveness. There are certain configurations that actually exacerbate the blast loading on structural components. This adjusted load may not particularly be at the ground floor level. The amount of effectiveness is not equivalent for both the pressure and impulse reduction factors.

Reduction factor plots have been generated for eight different cases to explore the effects of different configurations on the reduction factors for pressure and impulse loadings. The first set of four cases includes plots such as figures discussed in this section in which all the variables of the configuration are held constant except for the charge–to-structure standoff and the barrier height. In this way, the effect of the barrier height is illustrated for a set configuration. This is done for the pressure reduction factor along the center line (Appendix B.1), and for the pressure reduction factor over the height of the structure at a lateral distance of 0.61 m away from the axis of symmetry of the problem (Appendix B.2). The same plots are generated for the impulse reduction factors as well (Appendix B.3 and Appendix B.4). Similarly, a set of plots have been generated for investigating the effect of barrier height to pressure reduction factors for configurations where the barrier-to-structure standoff is held (Appendix B.5). The same plots at a lateral distance of 0.61 m from the axis of symmetry are in Appendix B.6. Likewise, the effect of the barrier height plotted for varying configurations of the barrier to structure standoff (Appendix B.7 and Appendix B.8).

7.3.   Approach 1: Evenly Spaced Training Grid

The first approach entails training four ANNs for predicting peak pressure, impulse, time of arrival, and positive-phase duration, respectively, using training data based on an evenly spaced grid on the structure face. As discussed in section 7.1, a 6 x 31 grid of data tracer points (186 total) was used to collect data on the structure face for each experiment. For the training data, only 30 data points were used. The 30 points chosen include a 6 x 5 evenly distributed grid of the data points. The independent input variables are d_1 (m), Z (m), H (m), and W (kg-TNT). The other variables are the height h_s (m) and width, w_s (m) on the structure face, but these are not considered independent variables since the variables are inherent in every configuration. The dependent variables for each ANN is peak pressure, p (MPa), impulse, i (MPa-ms), time of arrival, t_{oa} (ms), and positive-phase duration, t_{dur} (ms). The ANNs were trained using results from the primary 81 simulations performed.
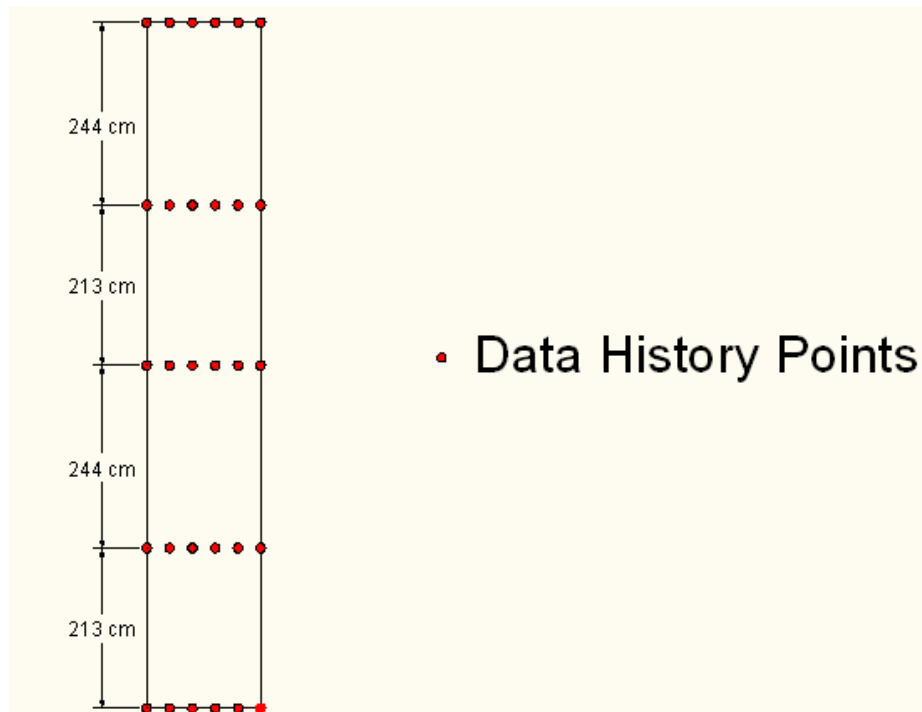
Figure 40. Layout of Data Points used for Training Evenly Distributed ANNs

Initial testing of ANN models was conducted with results from tracer points in between the tracer points used for training. These points are data points anywhere on the lateral position and vertically in between the lines of data points used to train the ANNs. This is not a complete and accurate depiction of the validity for the ANN models since the test data is only partially independent of the training data, but this approach provides a qualitative comparison of the different approaches to the ANN models. Figure 41 shows the training progress of the RGIN ANN approach to predicting the impulse loading to the structure face. It is typical of the results for the other three ANN models for the impulse, time of arrival, and positive-phase duration. The mean absolute error is 40 kPa-ms, which correlates to about 6% error. The correlation factor
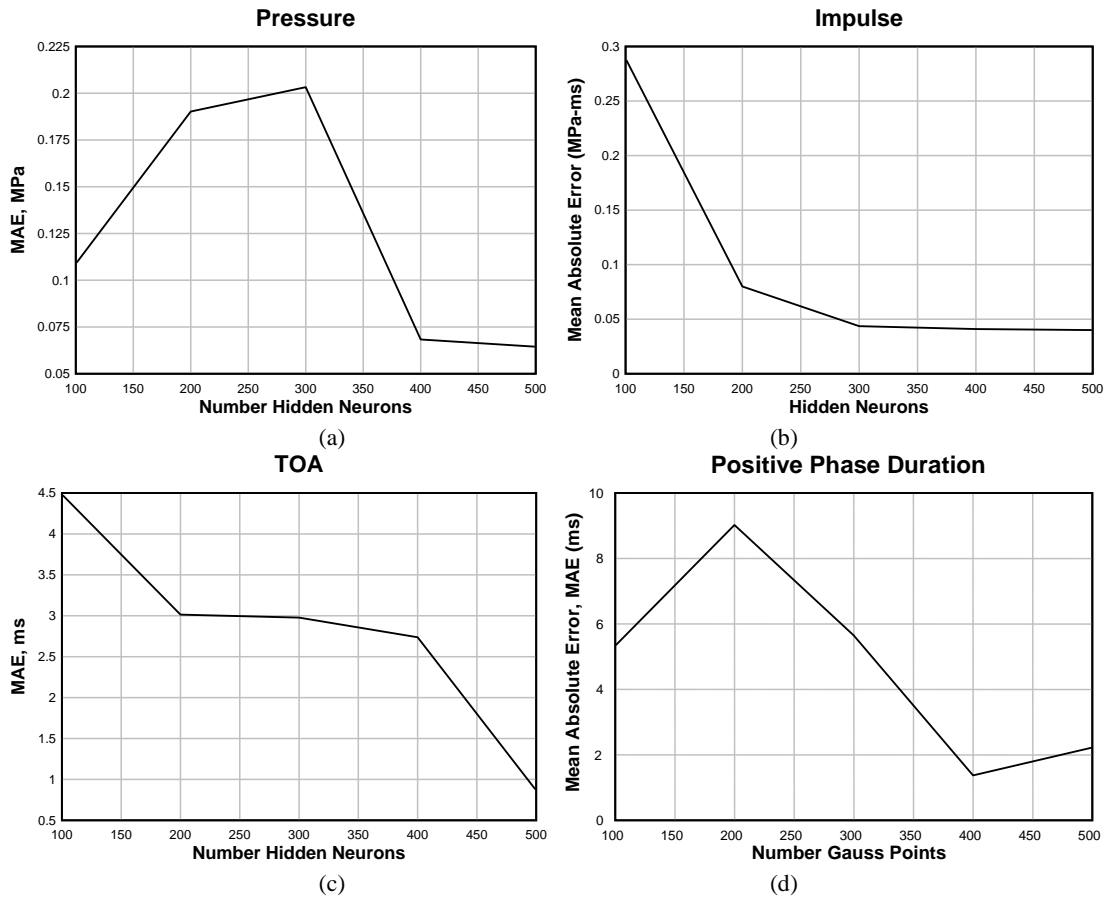
Figure 41. Training progress for RGIN ANN of (a) Pressure, (b) Impulse, (c) TOA, and (d) Duration

for each ANN is 0.9814, 0.9938, 0.9681, and 0.9806 for the peak pressure prediction, impulse prediction, positive-phase duration prediction, and time of arrival prediction respectively. The mean absolute error for each ANN is 0.644 MPa, 0.040 MPa-ms, 2.22 ms, and 0.864 ms for the predictions of peak pressure, impulse, positive-phase duration, and time of arrival, respectively. Scatter plots of the predicted versus actual values for each progression of the ANN models are provided in Appendix C.

The initial ANN development showed very good correlation with the sample training inputs. One point of interest to be considered is the effect of using blast scaling. Blast scaling is a common practice for reducing the number of input variables and simplifying blast problems (Baker, 1973). It is also commonly used to compress full-scale experiments into small-scale experiments. This practice helps cut costs for construction, and avoids the difficulty of having range space to perform large-scale detonations. The blast scaling concept relates all dimensions of a blast configuration through the charge weight by scaling the distances by $W^{1/3}$. Cube-root scaling removes the charge weight as a variable. This concept has been used with good correlation for several other blast wall effectiveness efforts (Bogosian, Shi, 2003; Rickman, Murrell, Armstrong, 2006; Rose, Smith, Mays, 1997; Zhou, Hao, 2008; Rice, Giltrud, Luo, Mestreau, Baum, 2000). The expectation is that with fewer input variables, the ANN might be

able to converge with fewer Gaussian points required. Figure 42 shows the results with 500 Gaussian points. While both results show good correlation, the scaled version has more errors in the mid and low range. This does not show in the correlation coefficient, because most of the errors are in the low and mid range, biasing the measure of the correlation coefficient. Also, the non-scaled version has a higher kurtosis, meaning that the errors are a factor of a few outlier data points as opposed to many moderate-sized errors as in the scaled version.
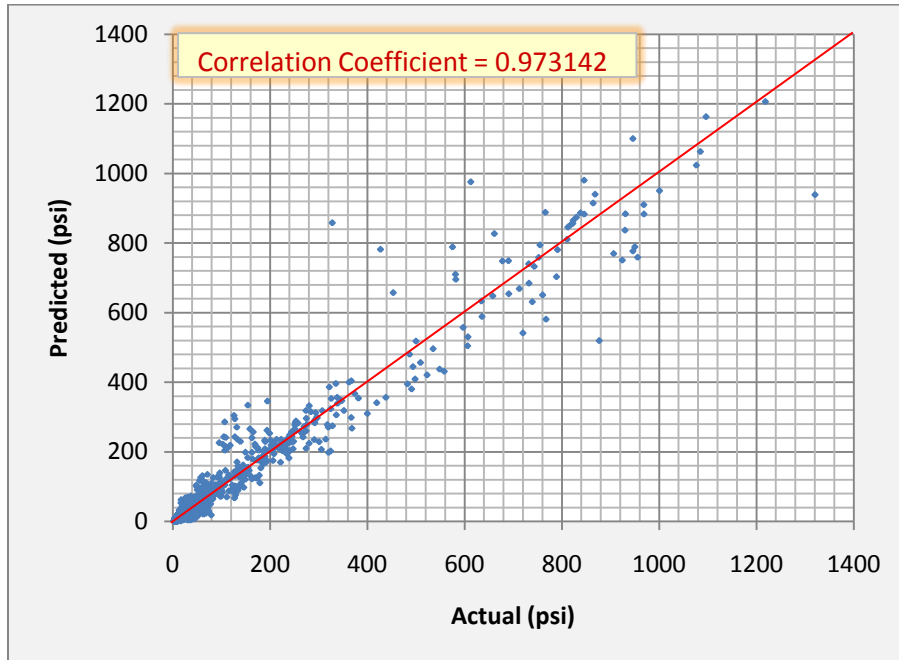
(a)
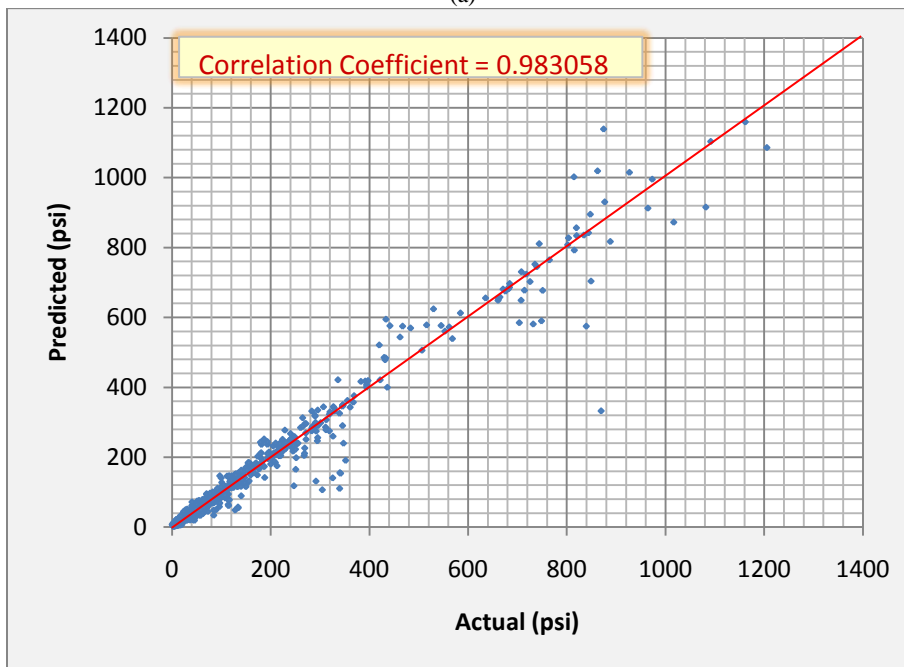
(b)

Figure 42. Results for (a) <u>Scaled</u> Input (Five Input Variables) and (b) <u>Non-scaled</u> Input (Six Input Variables)

The non-scaled version produces better results than the scaled version. This is not an implication of the validity of the practice of cube-root scaling, but rather a depiction of the ability of the ANN to learn the training patterns. When cube-root scaling is applied, the errors due to the charge size are hidden in the other variables. With six variables instead of five, the ANN is able to learn the patterns better. Therefore, all following work was performed without the use of cube-root scaling.

7.4. Approach 2: Biased Spacing of Training Grid

Analysis of the results from approach one showed a bias for errors to be toward the base of the structure. Investigation of the data shows a bias toward errors of points below the height of the barrier as depicted in Figure 43. For the second approach, values from the tracer points on the face of the structure were biased toward the bottom of the structure to include several near the base of the structure. Tracers chosen on the width of the structure remained in the same place, however. By biasing the location of the tracer points used in training, the training set includes more values in the areas that have been shown to cause the most error in the ANN predictions.
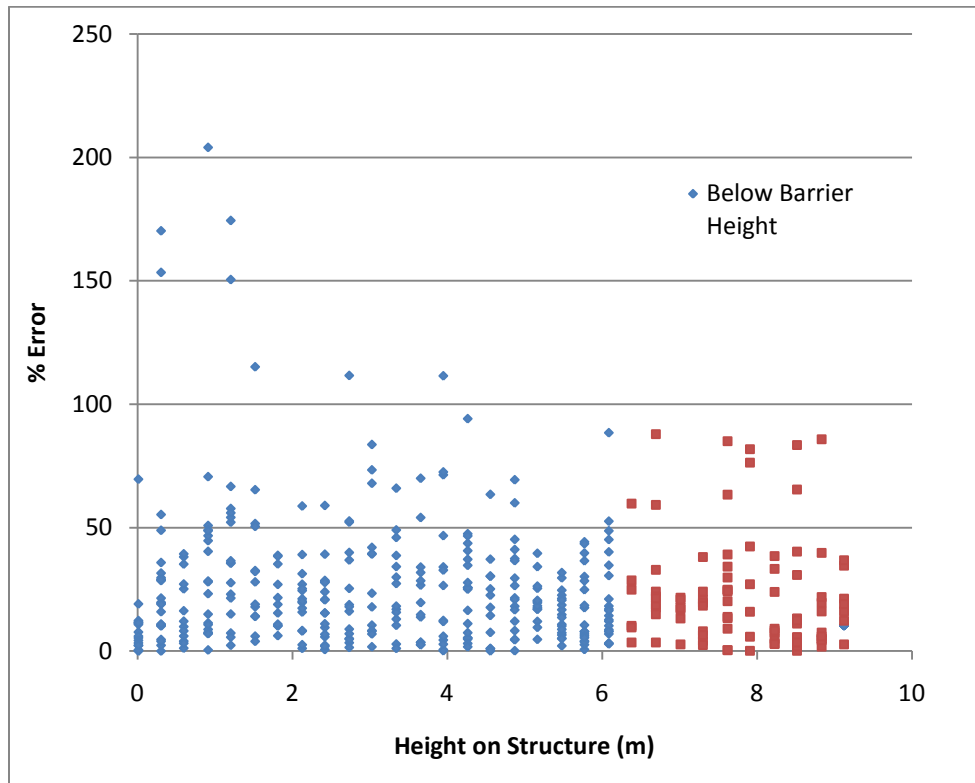
Figure 43. Bias of Errors Toward Heights on the Structure Face below the Height of the Blast Wall

The structure is 914.4 cm tall in every numerical simulation. For the evenly spaced grid, input points used for training are arranged in an evenly distributed 6 x 5 grid. All six data points in the lateral direction are used at five different elevations, 0 cm, 228.6 cm, 457.2 cm, 685.8 cm, and 914.4 cm. By biasing the grid training points used by the ANN, more inputs are used in the areas

Distribution A. Approved for public release; distribution unlimited.

that are shown to cause a larger amount of errors. For every possible value for the barrier height, there are at least two rows of data below the barrier height. The multiple reflections that occur below the height of the barrier make the lower levels of the structure more prone to errors than locations higher on the structure. The approach using the biased grid uses data collected as illustrated in Figure 44.
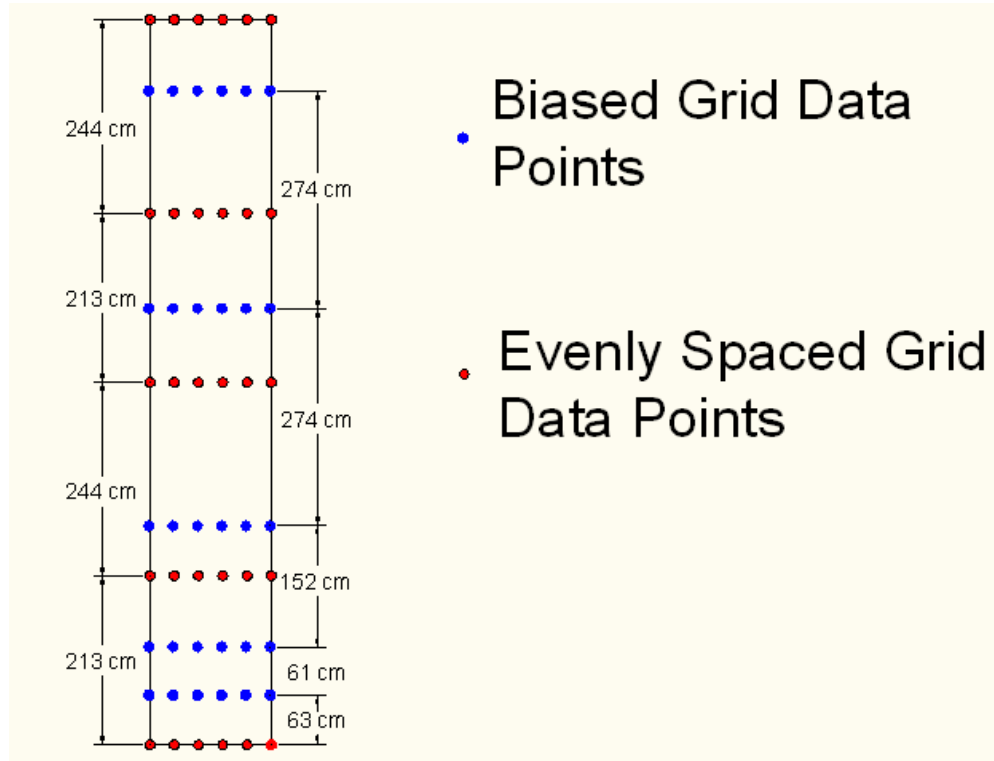
Figure 44. Training Grid Locations for Evenly Spaced and Biased Grid Approaches

Table 8 compares the behavior of the evenly spaced grid with the biased grid with 500 Gaussian points.

Table 8. Statistical Comparison of an Evenly Distributed Grid of Training Points and a Biased Grid

	Statistical Measure									
	Correlation Factor		Mean Absolute Error		RMSE		Std Deviation		Kurtosis	
ANN Model	Even	Bias	Even	Bias	Even	Bias	Even	Bias	Even	Bias
Peak Pressure (MPa)	0.981	0.987	0.064	0.040	0.209	0.173	1.086	1.061	15.07	14.78
Impulse (MPa-ms)	0.993	0.995	0.040	0.080	0.417	0.355	3.793	3.775	4.13	3.74
Time of Arrival (ms)	0.980	0.979	0.864	1.414	5.247	5.356	26.86	26.72	3.76	3.40
Duration (ms)	0.968	0.961	2.222	1.918	7.959	8.781	31.61	31.81	-0.31	-0.24

The analysis of biasing the grid of training points lower on the structure face produces some interesting results. The peak pressure ANN is improved by all accounts when using the biased grid. The correlation is better, the mean absolute error (MAE) is reduced and it shows a more linear behavior with fewer occurrences of large error. The impulse ANN is improved by biasing the grid with the exception of the MAE, which doubles as a result of the biased grid. Despite the MAE increase, it shows a more-linear distribution with fewer occurrences of large errors. There are more occurrences of small errors, but the general fit is better. The time-of-arrival ANN has better correlation, MAE, and root mean square error (RMSE) for the evenly spaced grid. The standard deviation and kurtosis are better with the biased grid, however. The evenly spaced grid shows better correlation in general, but the biased grid shows better results for high values of the time of arrival. The duration ANN shows better results for the evenly spaced grid despite a lower MAE with the biased grid.
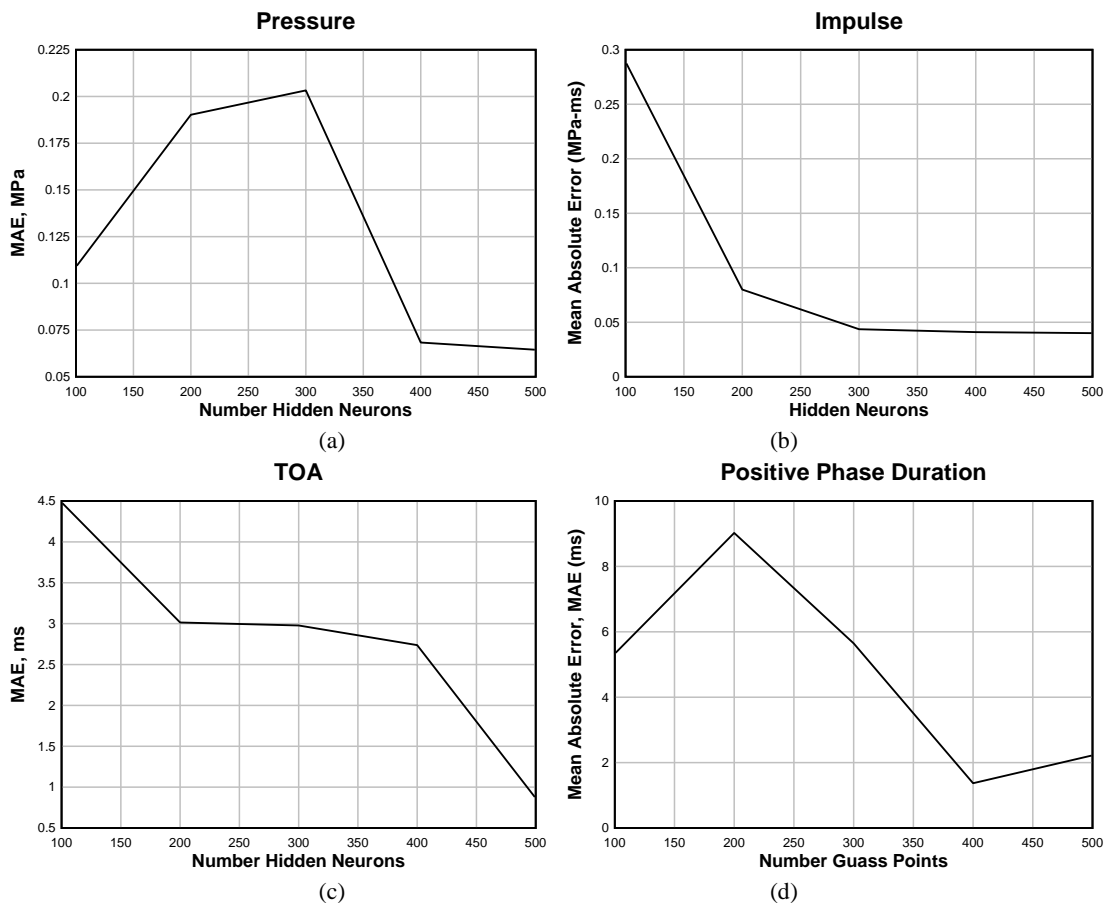
Figure 45. Training Progress for RGIN ANN of (a) Pressure, (b) Impulse, (c) TOA and (d) Duration

The training progression of the ANNs for the biased-grid approach provides interesting results. The training progression of the impulse ANN is very clean. The impulse ANN converges in the amount of error produced. The pressure and positive-phase duration ANNs increase in MAE before the RGIN methodology is able to hone in on decreased errors. The time-of-arrival ANN continually improves along the progression, but plateaus between 200 and 400 neurons before

65

again improving at 500 neurons. However, despite the odd behavior, each of the four ANNs has improved correlation factors and RMSE, meaning that, although it is not evident through the MAE, the correlation of the data and the RMSE improve throughout the progression. The significance of the RMSE is that it represents the average distance of the training results from the ANN predicted results. In this case, that would mean a straight line comparing the predicted to the actual values. Thus, even though the MAE does not clearly represent the progression in some of the cases, the improvement of the correlation factor and the RMSE means that the models are improving. Despite the improving progression of the ANN models, the ill-mannered behavior is a concerning indicator that the ANN model is having trouble learning the data set. These issues were also seen with the evenly spaced grid.

Table 9–Table 12 show the statistical improvement of the ANN progressions. The predicted values compared to the actual values of the ANN models for each increment of additional increments of hidden neurons are shown in Appendix C.2.

Table 9. Statistical Progression of Pressure ANN – Biased Grid

Hidden Neurons	Correlation Factor	Mean Absolute Error (MPa)	RMSE (MPa)	Standard Deviation (MPa)	Kurtosis (MPa)
100	0.9615	0.1088	0.298	1.063	15.120
200	0.9773	0.1902	0.229	1.080	14.978
300	0.9807	0.2032	0.212	1.084	15.068
400	0.9814	0.0683	0.208	1.085	15.087
500	0.9814	0.0644	0.209	1.086	15.070

Table 10. Statistical Progression of Impulse ANN –Biased Grid

Hidden Neurons	Correlation Factor	Mean Absolute Error (MPa)	RMSE (MPa)	Standard Deviation	Kurtosis
100	0.9796	0.2890	0.760	3.740	4.154
200	0.9892	0.0800	0.551	3.777	4.117
300	0.9922	0.0436	0.468	3.785	4.141
400	0.9935	0.0410	0.430	3.790	4.103
500	0.9938	0.0400	0.417	3.793	4.126

Table 11. Statistical Progression of Time of Arrival ANN – Biased Grid

Hidden Neurons	Correlation Factor	Mean Absolute Error (ms)	RMSE (ms)	Standard Deviation (ms)	Kurtosis
100	0.9649	4.4841	7.018	26.434	3.775511
200	0.9768	3.0142	5.718	26.628	3.689
300	0.9790	2.9779	5.439	26.661	3.739
400	0.9799	2.7375	5.335	26.776	3.759
500	0.9806	0.8643	5.247	26.862	3.762

Table 12. Statistical Progression of Duration ANN – Biased Grid

Hidden Neurons	Correlation Factor	Mean Absolute Error (MPa)	RMSE (MPa)	Standard Deviation	Kurtosis
100	0.8925	5.330	14.418	30.064	-0.19073
200	0.9382	9.023	11.076	30.726	-0.244
300	0.9531	5.647	9.663	31.172	-0.272
400	0.9635	1.370	8.555	31.385	-0.303
500	0.9681	2.222	7.959	31.618	-0.314

7.5.   Approach 3: Effect of Additional Training Patterns

The current results are produced using a 3 x 3 grid covering the variable data space. The 3 x 3 grid represents 81 experiments (3^4) with 30 data points embedded in each experiment for a total of 2,430 training patterns. Increasing to a 5 x 5 grid of the variable data space would increase the number of experiments to 625 (5^4) with 30 data points embedded in each experiment for a total of 18,750 training patterns.

The cost of increasing the density of the grid of training data is the difficulty in generating the amount of training input required. The problem is magnified when the bounds of the model are to be expanded from the current range. By examining the charge weight variable, the implications can be demonstrated. The current range for the charge weight is 22.68 kg to 910.42 kg. Assuming an evenly-distributed grid spacing, the density for a 3 x 3 grid would require experiments with the charge weight incremented 443.87 kg. Increasing to the 5 x 5 grid would have the charge weight incremented by 221.935 kg. After the 5 x 5 grid is established, the bounds of the model can be extended by maintaining a consistent density of the data in the grid of training data. Thus, for each 221.35-kg incremental increase in the range of the charge weight, 256 (4^4) experiments will be required to maintain a consistent density.

The computational modeling used to produce the simulations for the 3 x 3 grid was completed using DoD supercomputers. The simulations ranged from 12 processors up to 164 processors with an average wall clock time of 60 hours. The total number of processor hours required for the simulations populating the 3 x 3 grid of data was approximately 1.5 million hours. This reveals both the large investment required to produce accurate numerical simulations and the need for a quick engineering tool for efficient and accurate predictions. The limitations of applying a neural network modeling technique reside mostly in the investment to produce the training results required for training the ANN model.

The aim of the third approach is to explore the value of expanding the amount of data within the variable space used to train the ANN models. As described prior, increasing from a 3 x 3 grid to a 5 x 5 grid will increase the accuracy of the ANN model. In addition to the primary 81 simulations that were generated, five additional randomly generated simulations were completed to use for the study of the effect of the number of training patterns as outlined in Table 2.

Table 13 indicates that the ANN models are improved in most every aspect with the addition of the five extra training patterns. The standard deviation and kurtosis are slightly higher for the

impulse ANN, but all other measures are less. The time-of-arrival ANN model is the only one of the four models that shows little or no improvement with the addition of extra training patterns. The pressure ANN shows a 70% improvement in the MAE. Figure 46 indicates that the impulse ANN is learning better with the extra training patterns. All measures suggest that expanding to a 5 x 5 grid, if possible; will continue to yield improved results.

Table 13. Statistical Comparison of Biased Grid Models and the Biased Grid Models with Five Extra Simulations

	Statistical Measure									
	Correlation Factor		Mean Absolute Error		RMSE		Std Deviation		Kurtosis	
ANN Model	Extra	Bias	Extra	Bias	Extra	Bias	Extra	Bias	Extra	Bias
Peak Pressure (MPa)	0.990	0.987	0.012	0.040	0.154	0.173	1.065	1.061	14.74	14.78
Impulse (MPa-ms)	0.996	0.995	0.053	0.080	0.339	0.355	3.782	3.775	3.87	3.74
Time of Arrival (ms)	0.979	0.979	1.414	1.414	5.356	5.356	26.72	26.72	3.40	3.40
Duration (ms)	0.963	0.961	0.337	1.918	8.549	8.781	31.73	31.81	-0.23	-0.24
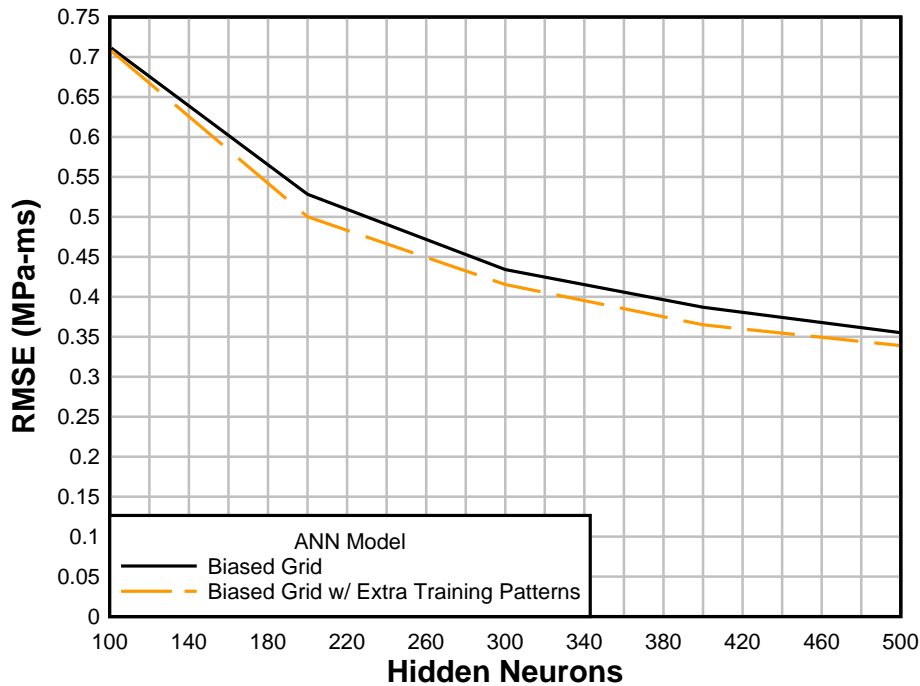
Figure 46. Training Progression of Impulse ANN Compared to the Model with Extra Training Patterns

7.6. Testing

The approaches presented to this point have been compared qualitatively using values that exist in between the tracers used for training the ANN models. It is important to gauge the behavior

of the ANN models against a blind set of results that exist in the variable space between the blast wall and structure configurations used in training the ANN models. To this end, five additional, randomly generated test simulations were completed to gauge the ability of the ANN models to reproduce the test values. The configurations of the test simulations (Table 14) can be compared against the ranges for the variables in the training sets in **Error! Reference source not found.**.

Table 14. Test Simulation Configurations

W (kg-TNT)	H (m)	d_1 (m)	Z (m)
680.87	2.64	7.14	29.17
586.62	2.35	5.16	22.31
839.80	3.98	5.16	14.30
560.65	4.60	0.93	7.36
128.99	4.14	7.38	20.67

The test produced mixed results. The peak pressure is the most accurate followed by the time of arrival, impulse, and the positive phase duration, in turn. Table 15 displays the behavior and Figure 48 show the performance of the four ANN models.

Table 15. Comparison of ANN Model Correlation with Test Results

ANN Model	Correlation Factor	MAE	RMSE	Standard Deviation	Kurtosis
Peak Pressure (MPa)	0.942	0.044	0.117	0.343	1.229
Impulse (MPa-ms)	0.784	1.486	1.743	2.495	-0.999
Time of Arrival (ms)	0.851	2.010	5.820	15.555	-1.430
Duration (ms)	0.504	24.984	27.067	17.534	-0.633
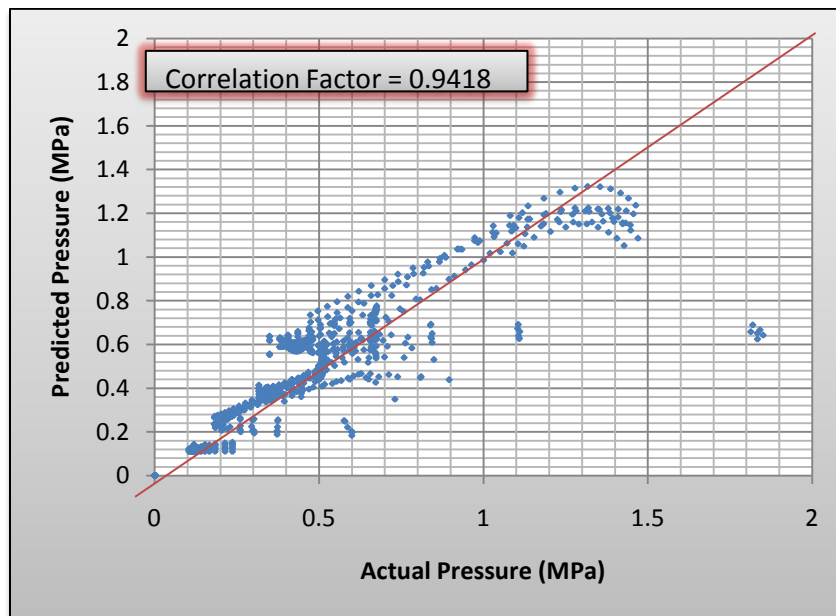
Figure 47. Correlation of Peak Pressure ANN with Test Results
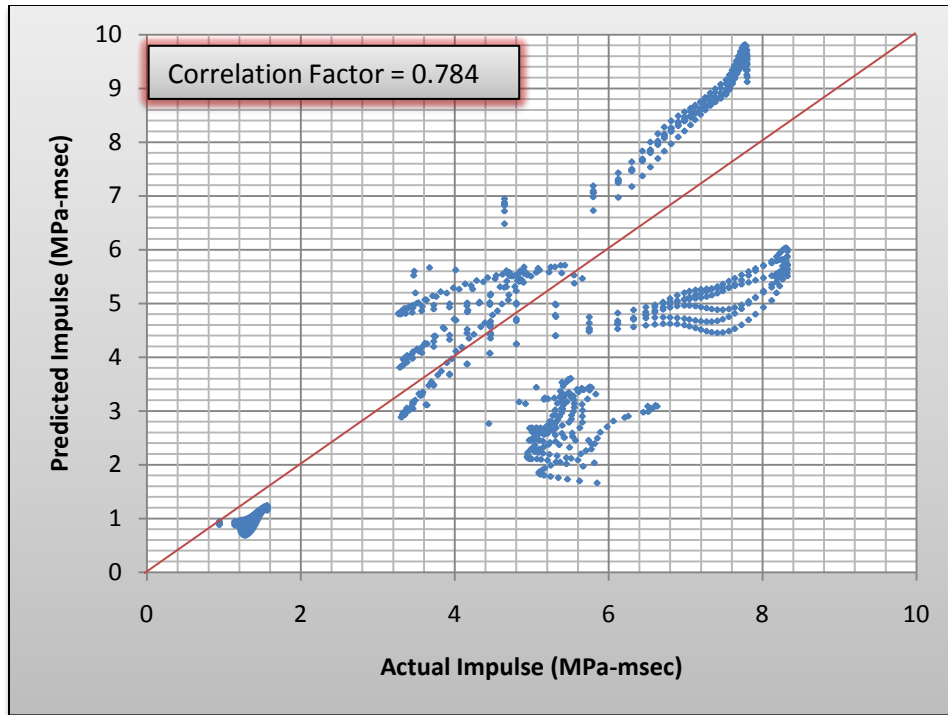
Figure 48. Correlation of Impulse ANN Model with Test Results
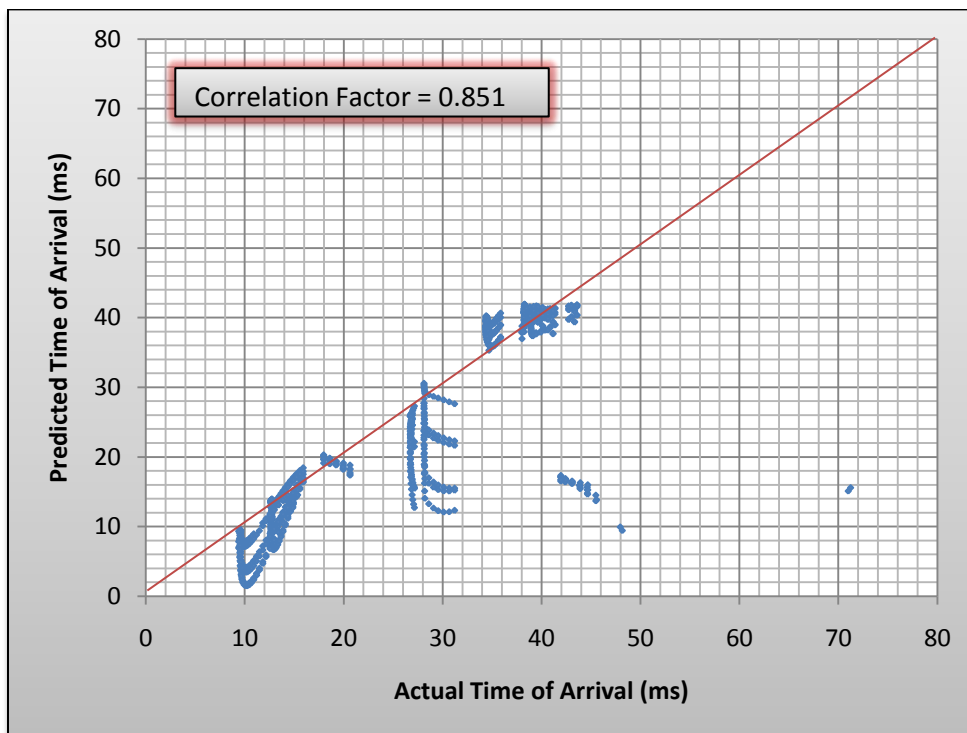
Figure 49. Correlation of Time of Arrival ANN Model with Test Results

70
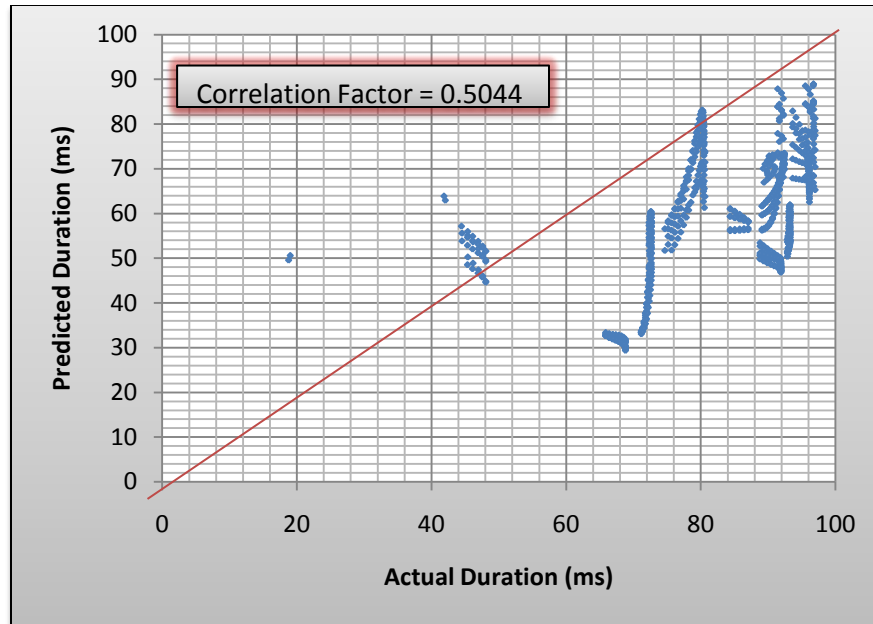
Figure 50. Correlation of Positive-Phase Duration ANN Model with Test Results

The results tend to be in line with what might be expected. The peak pressure and the time of arrival are the most accurate, which is intuitive because these values are not as likely to be affected by multiple reflections. The peak pressure and time of arrival often can be correlated to the longest distance the blast wave has to travel to get to the point of interest. For the most part, there are clusters of values that represent each of the five test experiments. That is a good indicator that the ANN models are fairly stable in their predictions and that the computational training results are fairly well conditioned. The couple of outlier points in the pressure ANN model correspond with the same behavior in the TOA ANN model, which further illustrates the commonality of the pressure and TOA ANN models.

The impulse and duration ANN models are not as accurate. It is postulated that this is due to the increased difficulty of capturing the multiple spikes in pressure that adjust the waveform and increase the nonlinearity of the predicted values. For the impulse ANN model, there is a set of training patterns from one experiment with low impulse values, where all of the data points fall just below the line of unity. The other four sets of training patterns are split above and below the line of unity. The results show that the predictions that fall below the line of unity are the experiments with a small charge-to-structure-standoff, Z. The experiments with larger values of Z are above the line of unity. From these observations, it is apparent that the accuracy of the ANN model is directly related to Z. This is intuitive from the previous observations that the smaller standoff values are prone to more variation in the amount of reflections and the magnitude. These scenarios are less difficult to capture as the standoffs increase.

7.7. Prediction of Roof Loads

To study the effects of protective blast walls on the blast loading of roofs, values for the first 10 ft of the structures were collected during all of the simulations generated for the structure loading ANNs formulated in this work. For the roof load ANN models, a similar approach as the

structure loads was applied. Initial ANN models for the peak pressure, the impulse, time of arrival, and positive phase duration were trained and compared against data from history points that are in between the data points used to train the ANN models.

A pragmatic evaluation of the variables provides insight into the effects on the properties that define a blast loading. In general, similar to the structure loads, the peak pressure and time of arrival are less affected by the presence of a blast wall than are the impulse and duration. This is seen in the results from the roof load ANN development (Table 16, Figs. 51–54). The training progression of the pressure ANN model was ill-behaved. MAE was actually slightly increased by the addition of five experiments. The other irregularity that is seen is an increased MAE for the duration ANN model. Both the 81-experiment-trained ANN and the 86-experiment-trained ANN for the duration models were well-behaved in the training progression. The RMSE, standard deviation and kurtosis all improved. Within the 500 hidden neurons used for training, the impulse and TOA ANN models never reached a stable lower bound of error with the addition of the extra five experiments. The impulse ANN does not show very good correlation, however, likely because there are more reflective waves that propagate onto the roof of the structure. As the duration of roof loads is often longer than typical structure loads, multiple reflections propagating up onto the roof have a greater effect on the accuracy of roof ANN impulse predictions.

Table 16. Comparison of Statistical Progression of ANN Model Predictions

ANN Model	Correlation Factor		MAE		RMSE		Std. Deviation		Kurtosis	
	Even	Extra	Even	Extra	Even	Extra	Even	Extra	Even	Extra
Peak Pressure (MPa)	0.984	0.984	0.000	0.004	0.014	0.014	0.080	0.080	20.61	20.20
Impulse (MPa)	0.627	0.601	0.009	0.031	1.191	1.214	1.099	1.094	156.8	159.8
Time of Arrival (ms)	0.942	0.948	9.629	0.501	3.785	3.548	21.05	21.20	3.693	3.617
Duration (ms)	0.886	0.903	3.18	9.46	7.28	6.76	34.06	33.24	-0.46	-0.42
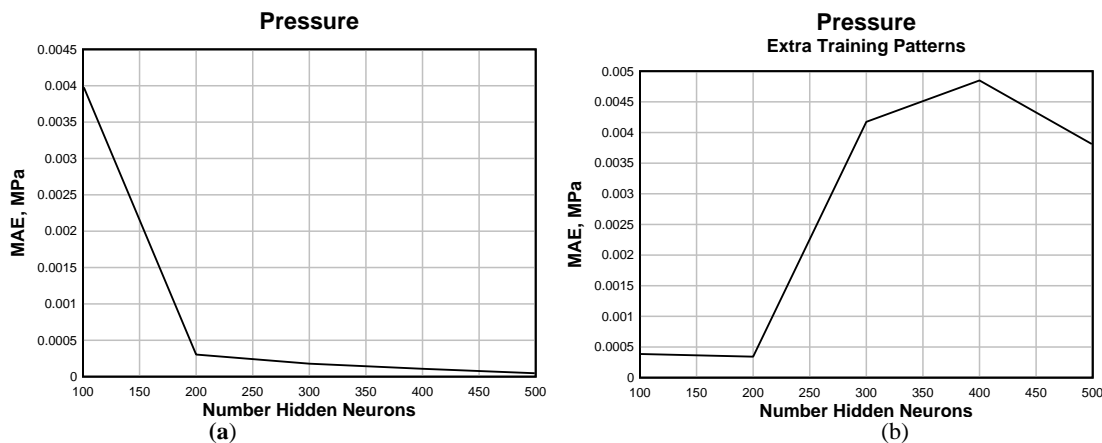
Figure 51. Training Progression of Roof Pressure ANN for (a) 81 and (b) 86 Experiments

72
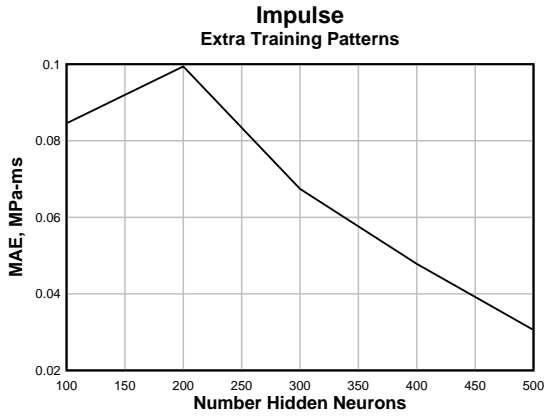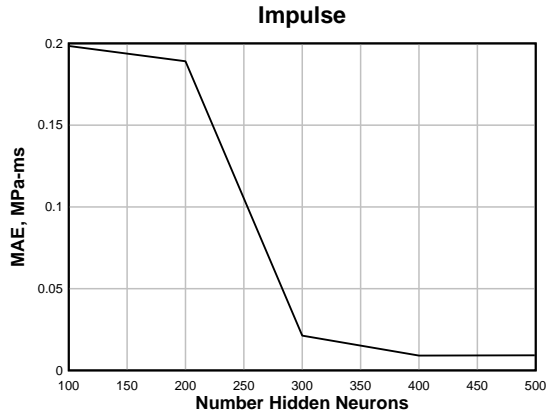
Figure 52. Training Progression of Roof Impulse ANN for (a) 81 and (b) 86 Experiments
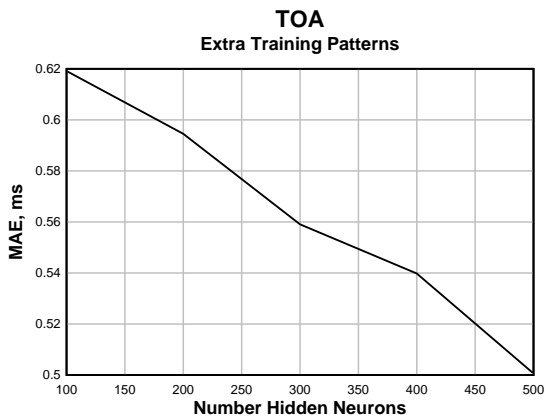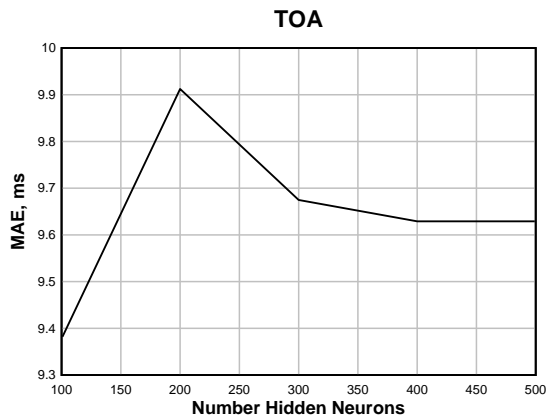
Figure 53. Training Progression of Roof TOA ANN for (a) 81 and (b) 86 Experiments
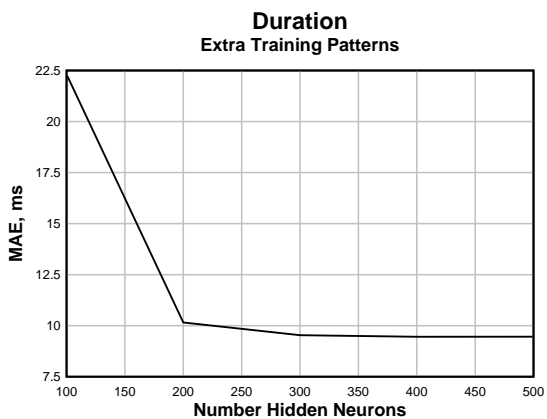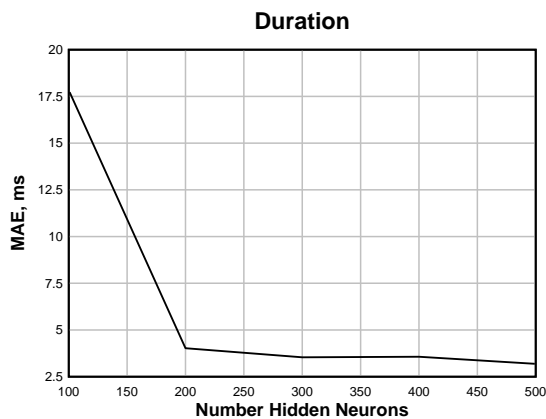
Figure 54. Training Progression of Roof Duration ANN for (a) 81 and (b) 86 Experiments

Table 17 shows the results of applying the ANN models to the test patterns. The peak pressure ANN shows little change with the addition of the extra five computational training experiments. The correlation factor and the RMSE remained the same. The MAE is better by 4 kPa and the kurtosis slightly improved. The pressure ANN for roof loads is slightly better behaved than for structure loads.

Table 17. Comparison of ANN Model Predictions with Test Data

ANN Model	Correlation Factor		MAE		RMSE		Std. Deviation		Kurtosis	
	Even	Extra	Even	Extra	Even	Extra	Even	Extra	Even	Extra
Peak Pressure (MPa)	0.989	0.989	0.038	0.034	0.014	0.014	0.071	0.07	9.20	9.06
Impulse (MPa)	0.959	0.949	0.286	0.202	0.336	0.376	0.820	0.81	8.97	9.42
Time of Arrival (ms)	0.958	0.956	0.263	1.777	1.892	1.939	12.11	12.27	3.27	3.35
Duration (ms)	0.431	0.496	15.341	17.759	7.704	8.313	14.81	15.32	-1.08	-1.10

For the impulse ANN, the correlation factor was actually reduced by adding training patterns from the five additional computational training experiments. RMSE and kurtosis were also slightly worse with the additional training patterns, but MAE and standard deviation did go down slightly. In this particular case, the additional five training patterns decreased the accuracy of the ANN model. This is evident in the comparison of the predicted to actual values in

Figure 55. Correlation of Impulse ANN Trained with (a) 81 and (b) 86 Experiments.
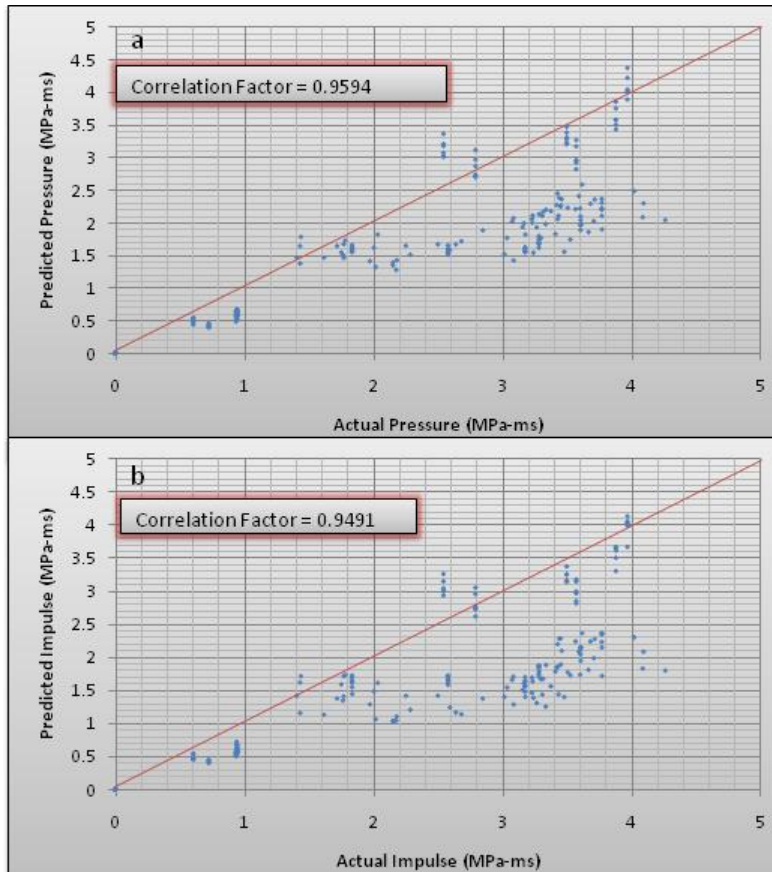
Figure 55. Correlation of Impulse ANN Trained with (a) 81 and (b) 86 Experiments

The TOA ANN was worse by all statistical accounts with the addition of the five extra training patterns. The ANN model with the original 3 x 3 grid of training trials shows good correlation with the training set. The MAE of 0.263 ms indicates good accuracy and a low amount of error.

The duration ANN shows very poor correlation in comparison with the other three ANN models. This is likely due to reasons similar to the problems seen with the training of the roof impulse ANN. The difficulties in predicting the multiple spikes in pressure that occur due to multiple blast wave reflections are likely the main cause for the poor performance. This is seen when referring to a plot of the actual against the predicted values, in which the predicted values are all low compared to the actual values in Figure 56.
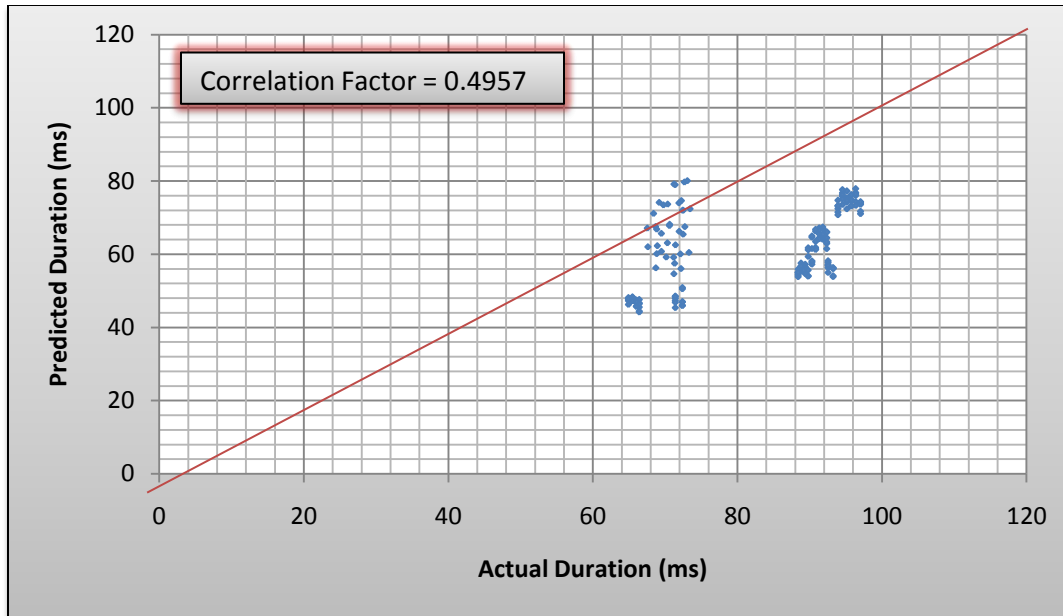
Figure 56. Correlation of ANN Predicted Durations with Test Values

7.8. Load Characterization

One of the main advantages of the ANN approach is that it is a stand-alone, direct-mapping technique for predicting the output variables. Each variable is directly mapped from the input parameters to the output variables. The only error in the methodology arises from the ANN learning the data incorrectly, which can be controlled by having the proper distribution and the amount of training set to produce an accurate ANN model.

The results from the ANN model development provide a tool for predicting blast loads on structures protected by blast barriers. Based on six input variables, charge weight, W, charge-to-barrier standoff, d_1, charge-to-structure standoff, Z, barrier height, H, and location on the structure face, w_s and h_s, a fast-running tool is able to give graphical representation (Figure 57) and an idealized blast load to structural components. This engineering tool is capable of providing results in a very efficient manner so that the engineer can explore the effects of varying blast wall site layout configurations.
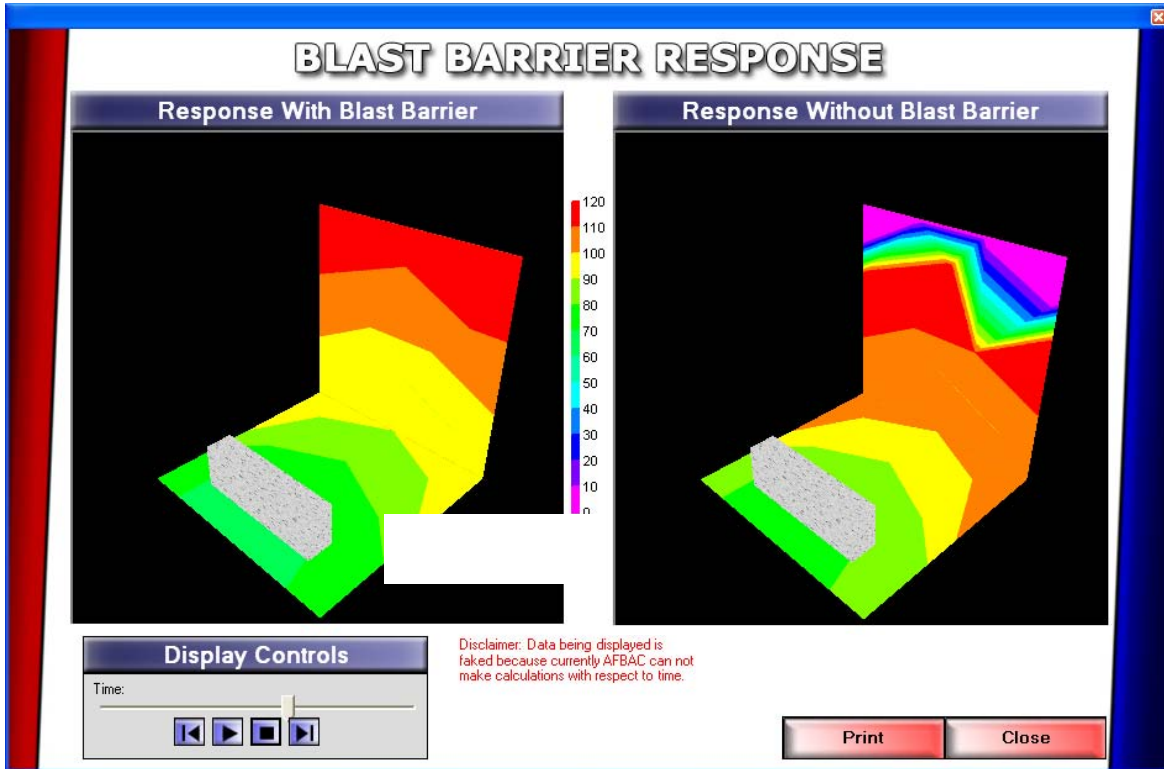
Figure 57. Graphical Representation of Blast Wave Pressure Loading on Structure Face

It is important for the output of the ANN to produce a simplified load that can be utilized by structural blast engineers for blast-resistant design. Given the output variables, a simplified pressure–time history curve can be developed to be used as a tool for blast-resistant design of the structure to be protected by the blast wall. The training of the ANN model determined that the duration model is the least accurate. Thus, the waveform of the blast load can be determined from the peak pressure and the impulse. This is done by assuming a triangular pulse load that jumps from zero up to the value of the peak pressure and then decreases with a slop that provides an area under the curve equal to the predicted impulse.

Applying the input variables into the ANN models, outputs predict the blast load for the point in question. Due to the inaccuracy of the duration ANN model, only the time of arrival, pressure, and the impulse ANN models are used to develop the load characterizations. The time arrival ANN produces the time at which the pressure load on the point of interest jumps from zero up to the peak pressure value, which is output by the pressure ANN model. The waveform is then defined as a triangle with a linear decrease in pressure down to zero. The positive phase duration is replaced with a fictitious duration for development of design loads. The fictitious duration used to develop the design loads uses the impulse ANN model output to define the area under the pressure–time history curve and calculate the positive phase duration as

$$t_{\text{dur}} = \frac{2i}{p} \qquad (13)$$

77

where t_{dur} is the positive-phase duration, i is the impulse, and p is the peak reflected pressure. Since the duration ANN models have been shown to be inaccurate, the second option is implemented as the method to produce the waveform of the blast loads.

The method is illustrated through predicting the load at a point on the structure and a point on the roof. This is done using an input point from one of the randomly generated test experiments with the configuration as listed in Table 18. The numerical experiment was chosen based on the results from the ANN testing showing good correlation with the test data. The results shown are good results, but the errors of methods developed in the current study are well documented in the previous sections. It is prudent to expect that other variations of the configuration input variables might produce either better or worse results depending on how closely the input variables lie to data used to train the ANN models. The data points on the structure face and on the roof surface were chosen at random.

Table 18. Test Parameters for Load Characterization

W (kg-TNT)	H (m)	d_1 (m)	Z (m)	w_s (m)	h_s (m)	w_r (m)	l_r (m)
680.87	2.64	7.14	29.17	0.3048	2.74	0.3048	0.6096

The inputs listed in Table 18 provide the following outputs from the structure load ANN models:

Table 19. ANN Model Structure Load Outputs

Condition	Pressure, p (MPa)	Impulse, i (MPa-ms)	TOA, t_{oa} (ms)	Duration, t_{dur} (ms)
With Barrier	0.501215	4.7143035	39.86	72.8
W/O Barrier	36.16	252.8	37.39	26.98

The duration value does not fall in line with the other output values. The duration output for this scenario is erroneous. The duration for the problem is determined using Equation **Error! eference source not found.**, which provides a positive phase duration of 18.8115 ms. The output variables are then applied to developing the waveform. The load jumps from zero to 0.501215 MPa at $t = 39.86$ ms. It then linearly decays to zero at $t = 58.67$ ms based on Equation **Error! Reference source not found.**. The resulting structure load is compared to the actual oad from the numerical experiment in Figure 58.

The predicted load shows good correlation. The errors are 1.39%, 7.03%, 2.2% and 58.1% for the predicted pressure, impulse, time of arrival and the positive-phase duration, respectively.
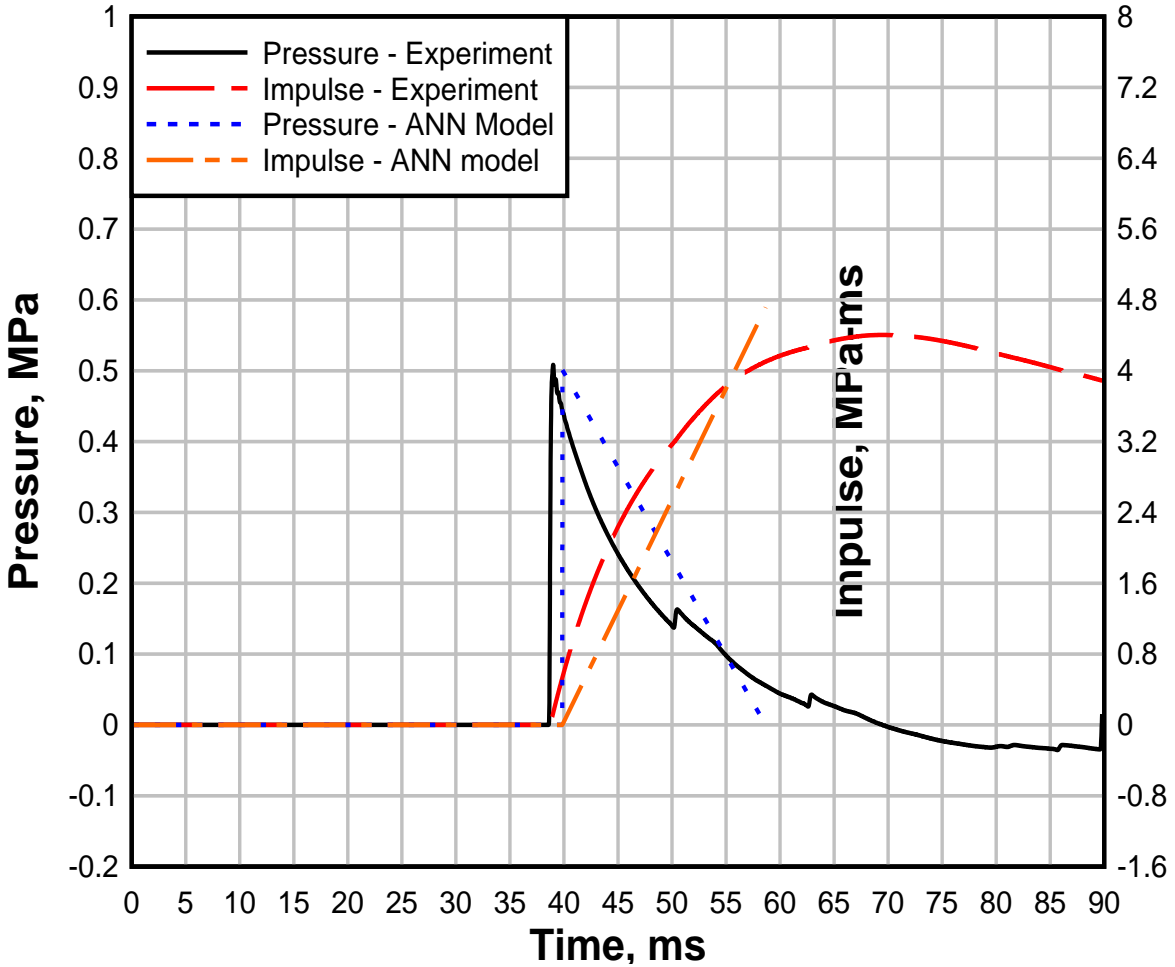
Figure 58. Structure Load Development from ANN Outputs

The inputs listed in Table 18 provide the following outputs from the roof load ANN models:

Table 20. ANN Model Structure Roof Load Outputs

Pressure, p (MPa)	Impulse, i (MPa-ms)	TOA, t_{oa} (ms)	Duration, t_{dur} (ms)
0.157256	1.8883	37.805	36.36

Using Equation 7 to develop a more accurate value, increased the positive-phase duration to 24.01 ms. The waveform is then defined as a triangular load that jumps from zero pressure up to a peak value of 0.157256 MPa at $t = 37.805$ ms. The pressure then linearly returns to zero over a duration of 24.01 ms, which means the time at which the blast load is over is $t = 61.82$ ms. The resulting roof load is compared to the actual load from the numerical experiment in Figure 59.
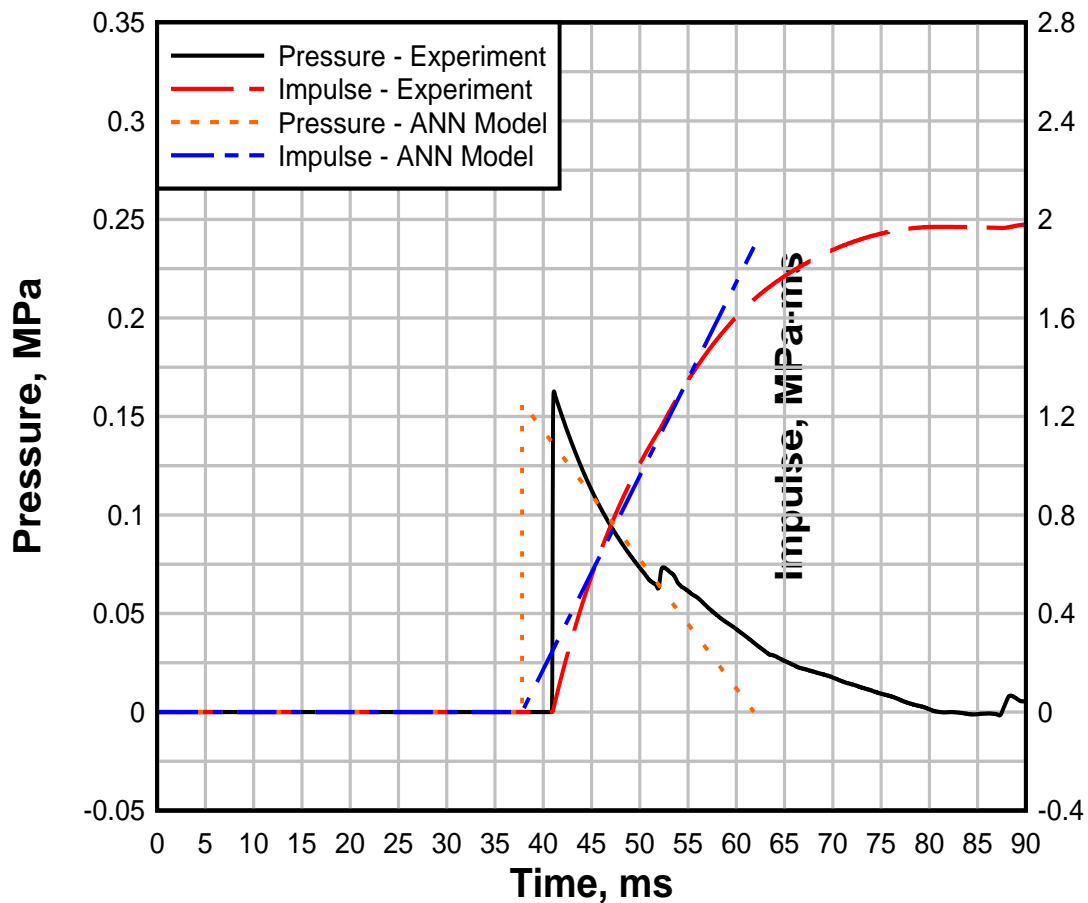
Figure 59. Roof Load Development from ANN Outputs

The predicted load shows good correlation. The errors of the ANN's predictions are 3.33%, 4.63%, 8.05% and 9.14% for the peak reflected pressure, impulse, time of arrival and positive phase duration, respectively.

The examples illustrated above show the ability to generate structural side wall and roof component loads. The design engineer can also reverse engineer the site layout to find if there are blast wall configurations which will produce a desired level of loading for the structural components. This is a powerful tool that can be used in two ways. The first advantage is that in pre-construction design, the design engineer can develop a blast wall configuration that reduces loads to a point that an alternate type of construction might be able to save considerable amounts of money in construction. For instance, a concrete or steel framed structure with CMU infill walls might be able to switch to light-gauge steel stud or wood stud infill walls and maintain an equivalent level of protection. The switch in construction type can save considerable amounts of money.

An additional application is for vulnerability studies. Existing structures with inadequate levels of protection can use blast walls to increase the level of protection, which might have a cost-advantage over blast retrofits. Or likewise, the tool can be used to evaluate the level of protection of a facility with a blast wall already in place.

8. CONCLUSION

8.1. Overview

Blast design and assessment of structures protected by blast barrier walls require aids to develop beneficial configurations. CFD modeling, as demonstrated, can be a very accurate approach to developing blast wave and structure interaction. To produce those accurate results, there is a very large overhead of hardware requirements and wall clock time. ANNs provide an efficient tool to aid in optimizing site layout and structural design for terrorist-type threats. The advantage is that the ANN model approach has been shown to provide good results. It is an independent approach that is closed off from exterior sources of error. The weakness in the approach resides in the ANN's ability to learn the data set. Thus, the errors from experimental duplication or previous data fitting efforts as seen in the curve-fitting engineering models currently used by the blast community are alleviated. The downside is that ANNs require a large training set of data relevant to the problem at hand to become very accurate.

The results of this study show the development of an ANN methodology for a range of values for the variables of charge weight, charge-to-barrier standoff, barrier-to-structure standoff, barrier height, and location on the structure face—as well as roof loads. The development was performed on a 3 x 3 grid of the variable data space. Experience and the results of this study show that moving to a 5 x 5 grid of the variable space will provide improved results. The significance of this study is that it displays the ANN technology at the edge of its applicability. 81 simulations were required for the 3 x 3 grid, 625 are required for the 5 x 5. The 5 x 5 grid will provide improved results for the bounds of the current problem. However, the current study has limited the ranges of the variables. This means that to practically expand the ranges of the values in the models, it will be necessary to examine the variable space carefully to ensure that the same density of data points within the variable space is maintained to keep the same level of accuracy for the models. This implies that a large number of data points will be required to expand the variable range as desired.

The ANN technology shows the capability to model the results for the non-linear results that arise in the blast environment with a blast barrier protective wall. For a 3 x 3 grid of the variable space, the ANN behavior has been presented. ANNs were developed for peak pressure, impulse, time of arrival and duration. There are differing degrees of non-linearity for the predicted values of each variable. Peak pressure and time of arrival show the most predictable responses. Impulse and positive-phase duration have a higher degree of non-linearity that proves more difficult for the RGIN ANN approach to learn the training patterns.

8.2. Future Work

The results of this dissertation show the limits of applying the ANN technology to the problem of predicting blast loads on structures protected by blast barrier walls. Possible future work includes, but is not limited to, the following aspects.
1) The current models are developed using a 3 x 3 grid density for the variable space. Increasing to a higher density grid of the variable space was shown to be of benefit. Thus, increasing the grid density from a 3 x 3 to a 5 x 5 spacing of the variables in the grid density would be beneficial to the accuracy of the ANN models.

2) Practical limits were chosen to explore the effectiveness of the ANN approach. It is possible that higher limits would be desired for certain configurations, or higher threats. An extension of the range covered by the ANN models would allow for a more robust engineering tool.   Extension of the bounds of the variable space would be performed by maintaining a consistent grid density with the existing ANN models depending on whether the extension is built upon 3 x 3 grid density or 5 x 5 grid density.
3) Addition of input parameters would make the approach more robust. Input variables to be added include height of charge, thickness of barrier and the height of the structure.

9. REFERENCES

1998 United States Embassy Bombings. (n.d.). Retrieved April 2010, from Wikipedia: http://en.wikipedia.org/wiki/1998_United_States_embassy_bombings

2008 Danish Embassy Bombing in Islamabad. (n.d.). Retrieved April 2010, from Wikipedia: http://en.wikipedia.org/wiki/2008_Danish_embassy_bombing_in_Islamabad

ADINA R&D. *ADINA User's Manual.* Watertown, MA.

Baker, W. (1973). *Explosions in Air.* Austin, TX, USA: University of Texas Press.

Bardenhagen, S. G. (2002). Energy Conservation Error in the Material Point Method for Solid Mechanics. *Journal of Computational Physics* , 180:383-403.

Baum, J. D., Luo, H., Lohner, R. (January 1995). Numerical Simulation of Blast in World Trade Center. Reno, NV: AIAA-95-0085, AIAA, 33rd Aerospace Sciences Meeting.

Baylot, J. T., & Bevins, T. L. (2007). Effect of Responding and Failing Structural Components on the Airblast Pressures and Loads On and Inside of the Structure. *Computers & Structures* (85), 891-910.

Baylot, J. T., Bogosian, D. D., Dunn, B. W., Simmons, L. (May 2000). Retrofits for Steel Joist Roofs Exposed to Blast Loads. *ASCE 2000 Structures Congress.* Philadelphia, PA, USA.

Bell, R. L., Baer, M. R., Brannon, R. M., Crawford, D. A., Elrick, M. G., Hertel, E. S. (November 2007). *CTH User's Manual and Input Instructions, Version 8.1.* Albuquerque, NM, USA: Sandia National Laboratories.

Berzins, M., Tran, L.-T., Kim, J. (2007). Solving Time-Dependent PDEs using the Material Point Method, Error and Stability Analysis of a Gas Dynamics Case Study. *3rd Material Point Method Workshop.* Albuquerque, NM.

Bewick, B., Chen, Z. (2010). Evaluation of Existing Codes for Air Blast Modeling. *Journal of Critical Technologies , (Submitted)*.

Bewick, B., Flood, I., Chen, Z. (2010). A Neural-Network Model-Based Simulation Tool for Blast Wall Protection of Structures. *International Journal of Protective Structures , (Submitted)*.

Beyer, M. E. (1986). Blast Loads behind Vertical Walls. *22nd Explosives Safety Seminar.* Anaheim, CA, USA: DoD Explosives Safety Board.

Bogosian, D. D., Dunn, B. W., Baylot, J. T., Simmons, L. (November 1999). Response of a Lightweight Steel Roof to Blast Loads. *70th Shock and Vibration Symposium.* Albuquerque, NM, USA.

Bogosian, D., Shi, Y. (October 2003). An Enhanced Methodology for Predicting Loads Behind Blast Barriers. *74th Shock and Vibration Symposium.* San Diego, CA, USA: 74th Shock & Vibration Symposium.

Bogosian, David; Shi, Yongjiang. (January 2002). *Assessment of a predictive methodology for blast barrier effectiveness.* Karagozian & Case, TR-01-34.

Brackbill, J. U., Ruppel, H. M. (1986). FLIP: A Method for Adaptively Zoned, Particle-in-Cell Calculations of Fluid Flows in Two Dimensions. *Journal of Computational Physics* , 314-343.

Century Dynamics. (2003). *AUTODYN 2-D & 3-D User's Manual.*

Chen, Z., Brannon, R. (February 2002). *An Evaluation of the Material Point Method.* Albuqeurqe, New Mexico 87185: Sandia National Laboratories.

Cooper, P. (1996). *Explosives Engineering.* Wiley.

Crepeau, J. (1998). *SHAMRC Second-Order Hyrdynamic Automatic Mesh Refinement Code. User's Manual, Vol. 2.* Albuquerque, NM: Applied Research Associates, Inc.

Crepeau, J; Needham, C; Hikida, S. (2001). *SHAMRC Second-Order Hydrodynamic Automatic Mesh Refinement Code. Methodology, Vol. 1.* Albuquerque, NM: Applied Research Associates, Inc.

Dobratz, B. M., Crawford, P. C. (1985). *LLNL Explosives Handbook, Properties and Explosive Simulants.* Livermore, CA, USA: Lawrence Livermore Laboratory, UCRL-52997.

Dove, R., Hamilton, J., Coltharp, D. (1989). Perimeter Walls for Blast Reduction. *ASCE Specialty Conference on Structures for Enhanced Safety and Physical Security*, (pp. 142-153).

Flood, I. (1999). Modeling Dynamic Engineering Processes Using Radial–Gaussian Neural Networks. (7: 373-385).

Flood, I., Bewick, B., Dinan, R., & Salim, H. (2009). Modeling Blast Wave Propagation Using Artificial Neural Network Methods. *Journal of Advanced Informatics* (23: 418-423).

Flood, Ian; Kartam, Nabil. (1994). Neural Networks in Civil Engineering I: Principals and Understanding. (8(8): 131-148).

Flood, Ian; Kartam, Nabil. (1994). Neural Networks in Civil Engineering II: Systems and Application. (8(8): 149-162).

Hallquist, J. (July 1993). *LS-DYNA3D Theoretical Manual.* Livermore, CA: Livermore Software Technology Corp., LSTC Report 1018 Rev 2.

Harlow, F. H. (n.d.). Hydrodynamic Problems Involving Large Fluid Distortions.

Hoemann, J., Davidson, J., Dinan, R., Bewick, B. (2010). Boundary Condition Behavior and Connection Design for Retrofitted Unreinforced Masonry Walls Subjected to Blast Loads. *ASCE Structures Congress.* Orlando, FL, USA.

Hu, W., Chen, Z. (2006). Model-based Simulation of the Synergistic Effects of Blast and Fragmentation on a Concrete Wall Using the MPM. *Int. J. of Impact Engng* , 32:2066-2096.

Islamabad Marriott Hotel Bombing. (n.d.). Retrieved from Wikipedia: http://en.wikipedia.org/wiki/Islamabad_Marriott_Hotel_bombing

Kingery, C. N., Bulmash, G. (1984). *Airblast Parameters from TNT Spherical Air Burst and Hemispherical Surface Burst.* Aberdeen, MD, USA: ARBRL-TR-0255, Ballistic Research Laboratory.

Lan, S., Crawford, J. E. (12-14 November 2003). Evaluation of the Blast Resistance of Metal Deck Roofs. *5th Asia–Pacific Conference on Shock & Impact Loads on Strcutures.* Changsha, Hunan, China.

Li, S., Kam, W. (2004). *Meshfree Particle Methods.* Springer.

Lohner, R., Baum, J. D., Rice, D. (September 2004). Comparison of Coarse and Fine Mesh 3-D Euler Predictions for Blast Loads on Generic Building Configurations. Bad Reichenhall, Germany: Proceedings of Military Aspects of Blast and Shock (MABS) 18.

Lohner, R., Yang, C., Baum, J. D., Mestreau, E. (2002). Advances in FEFLO. (AIAA-02-1024).

Mastin, C. W., Armstrong, B. J., Welch, C. W. (1995). Verification of the CTH Hydrocode Against the Kingery and Bulmash Data Sets. 66th S&V Symposium.

Mays, G C; Smith, P D; (Eds.). (1995). *Blast Effects on Buildings.* Thomas Telford.

McClendon, M. (December 2007). *Blast Resistant Design for Roof Systems.* Columbia, MO, USA: University of Missouri-Columbia.

McGlaun, J. M., Thompson, S. L., Elrick, M. G. (1990). CTH: A Three-Dimensional Shock Wave Physics Code. *Int. J. Impact Engng* , 10:351-360.

McKeown, R., Dengel, O., Harris, G., Diekhoff, H. J. (February 2004). *Development and Evaluation of DYSMAS Hydrocode for Predicting Underwater Explosion Effects. Executive Summary, Vol. I.* Indian Head, MD, USA: IHTR 2492, Naval Surface Warfare Center (NSWC).

Monaghan, J. J. (1988). An Introduction to SPH. *Computer Physics Communications , 48*, 88-96.

Moody, J., Darken, C. J. (1989). Fast Learning in Networks of Locally-Tuned Processing Units. *Neural Computation* (1), 281-294.

Needham, C. E. (July 2007). Blast Loads and Propagation around and over a Building. Gottingen, Germany: 26th International Symposium on Shock Waves.

Nichols, A. (2007). *Users Manual for ALE3D: An Arbritrary Lagrange/Eulerian 3D Code System.* LLNL Technical Report, UCRL-MA-152204 Rev 6.

NSWC-Indian Head, MD. (15 April 2008). *GEMINI: the DYSMAS Euler Solver User's Manual (Release 4.46).*

Oklahoma City National Memorial & Museum History. (n.d.). Retrieved April 2010, from Oklahoma City National Memorial & Museum: http://www.oklahomacitynationalmemorial.org/secondary.php?section=1&catid=193

Remennikov, A. M., Rose, T. (2007). Predicting the Effectiveness of Blast Barrier Walls Using Neural Networks. (34: 1907-1923).

Rice, D. L. (May 1999). A Study of Blast Wall Effectiveness Using Small-Scale Experiments and Hydrocode Simulations. *9th International Symposium on the Interaction of the Effects of Munitions with Structures*, (pp. 87-94). Berlin-Straussberg.

Rice, D. L., Giltrud, M. E., Luo, H., Mestreau, E., Baum, J. D. (2000). Experimental and Numerical Investigation of Shock Diffraction about Blast Walls. *16th International Symposium on the Military Aspects of Blast and Shock (MABS-16).* Oxford, UK.

Rickman, D. D., Murrell, D., Armstrong, B. (May 2006). Improved Predictive Methods for Airblast Shielding by Barrier Walls. St. Louis, MO, USA: ASCE Structures Congress.

Rickman, Denis D; Murrell, Donald. *Miniature-Scale Experiments of Airblast Diffraction Over Barrier Walls: Results and Analysis.* Vicksburg, MS: USACE Engineering Research and Development Center.

Roache, P J. (1998). *Verificatoin and Validation in Computational Science and Engineering.* Hermosa Publishers.

Roache, P. J. (1994). Perspective: A Method for Uniform Reporting of Grid Refinement Studies. (116: 405-413).

Rose, T. A. (February 22, 2006). *Air3D User's Guide 9.0.* Shrivenham, UK: Cranfield University.

Rose, T. A., Smith, P. D., Mays, G. C. (1997). Design Charts Relating to Protection of Structures Against Airblast from High Explosives. (123: 186-192).

Rose, T. A., Smith, P. D., Mays, G. C. (1995). The Effectiveness of Walls Designed for the Protection of Structures Against Airblast From High Explosives. (110: 78-85).

Roth, M., Bennet, J., Heard, W., Stinson, R. (October 2006). CFD Modeling of Blast Intrusion into Field Fortifications. 77th Shock & Vibration Symposium.

Schwer, L., Saadeghvaziri, M., O'Daniel, J., Madsen, T. (2008). Free-Air Blast Simulation: Engineering Model and MM-ALE Calculations. Oslo, Norway: Military Aspects of Blast and Shock (MABS) 20.

Sod, G. A. (1978). A Survey of Several Finite Difference Methods for Systems of Nonlinear Hyperbolic Conservation Laws. *Journal of Computational Physics , 27*, 1-31.

Steffen, M., Berzins, M., Kirby, M. (2007). Effects of Higher_Order Basis Functions on Spatial Convergence in the Material Point Method. *3rd Material Point Method Workshop.* Albuquerque, NM.

Sulsky, D., Schreyer, H. (1996). Axisymmetric Form of the Material Point Method with Applications to Upsetting and Taylor Impact Problems. *Comput. Methods Appl. Mech. Engrg. , 139*, 409-429.

Sulsky, D., Zhou, S.-J., Schreyer, H. L. (1995). Application of a Particle-in-cell Method to Solid Mechanics. *Computer Physics Communications* (87), 236-252.

Sulsky, Deborah; Chen, Zhen; Schreyer, Howard L. (1994). A Particle Method for History-Dependent Materials. *Comput. Methods Appl. Mech. Engrg.* (118), 179-196.

Sumilia. *ABAQUS Analysis Users Manual.*

UFC 3-340-01. (1 June 2002). *Design and Analysis of Hardened Structures to Conventional Weapons Effects.* US Army Corps of Engineers, Naval Facilities Engineering Command, Air Force Civil Engineering Support Agency.

US Army. (1994). *Security Engineering Manual TM5-853-3, vol. 3.* Washington, DC: Department of the Army.

US Department of the Army. (1990). *TM5-1300, Structures to Resist the Effects of Accidental Explosions.*

Wallstedt, P. C., Guilkey, J. E. (2007). Improved Velocity Projection for the Material Point Method. *CMES ,* 19(3):223-232.

York II, A. R., Sulsky, D., Schreyer, H. L. (2000). Fluid-Membrane Interaction Based on the Material Point Method. *Int. J. Numer. Meth. Engng ,* 48:901-924.

Zhou, X. Q., Hao, H. (2008). Prediction of Airblast Loads on Structures Behind a Protective Barrier. (35: 363-375).

APPENDIX TABLE OF CONTENTS

LIST OF APPENDIX FIGURES

Appendix A: 3D CONVERGENCE STUDY FIGURES

A.1. Error versus Direction Bar Charts
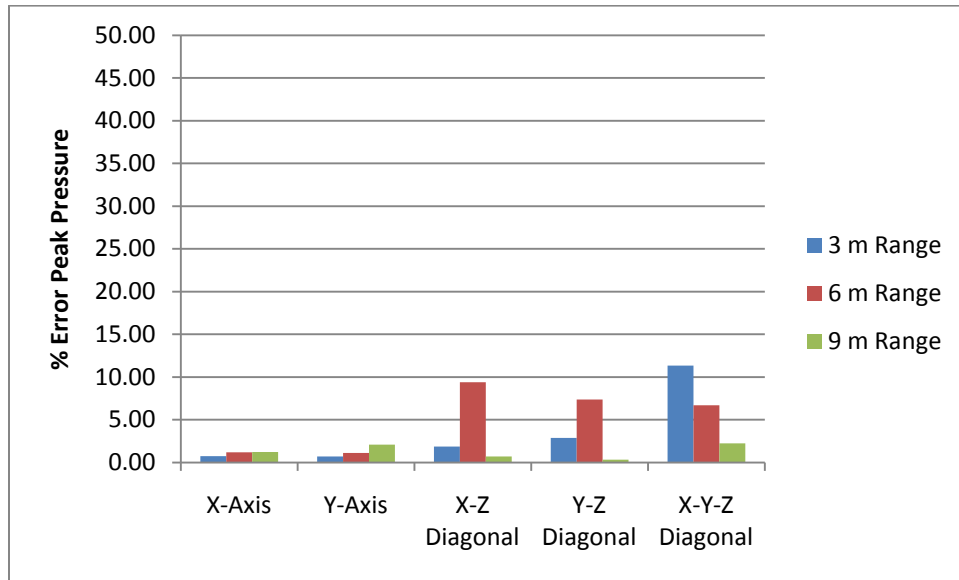
(a)
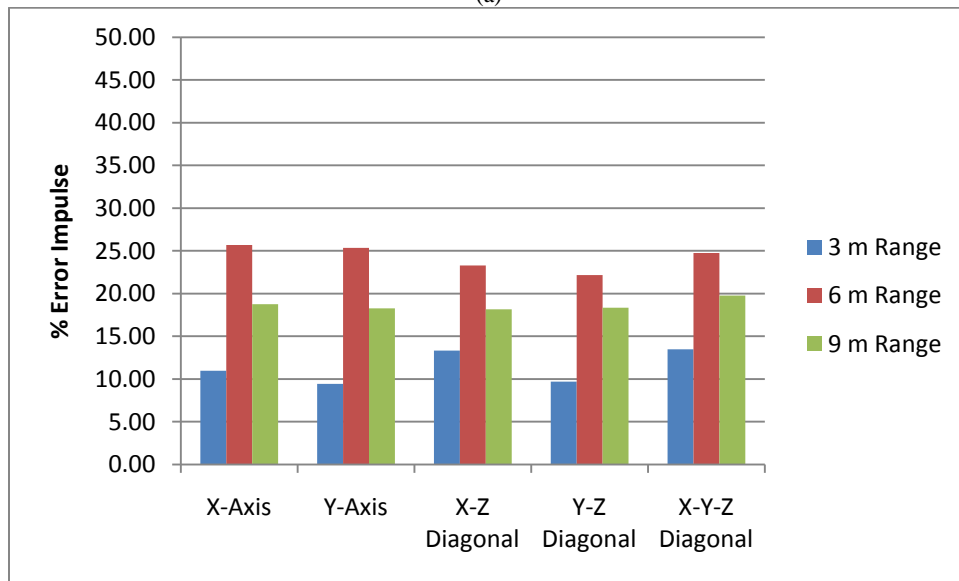
(b)

Figure A-1. DYSMAS Directional Error, $W = 99.8$ kg (a) Pressure and (b) Impulse
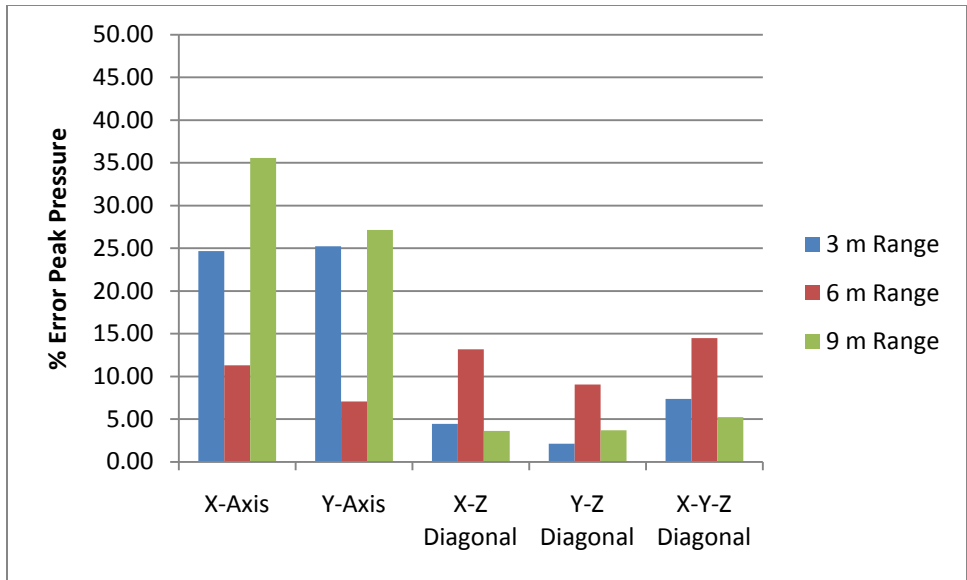
(a)
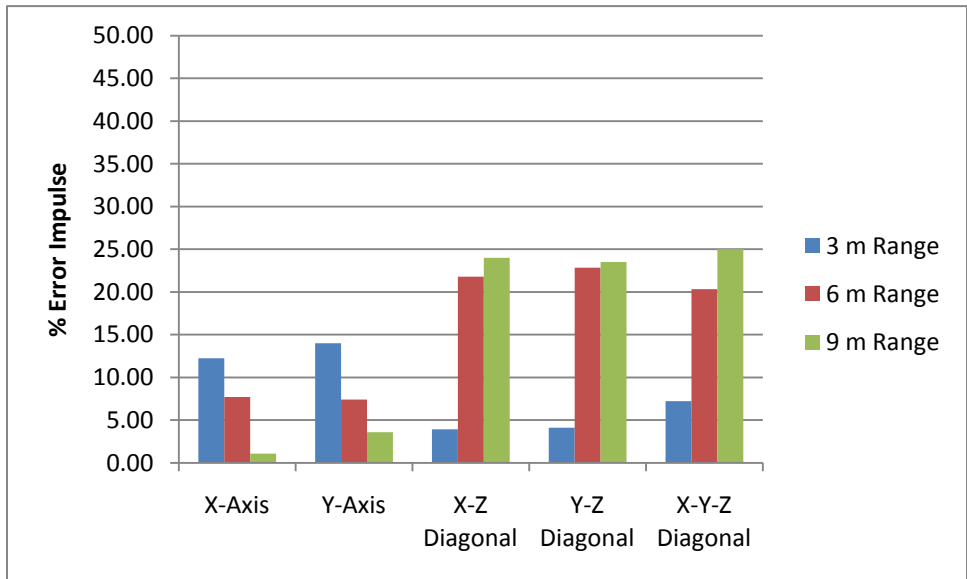
(b)

Figure A-2. DYSMAS Directional Error, W = 226.8 kg (a) Pressure and (b) Impulse
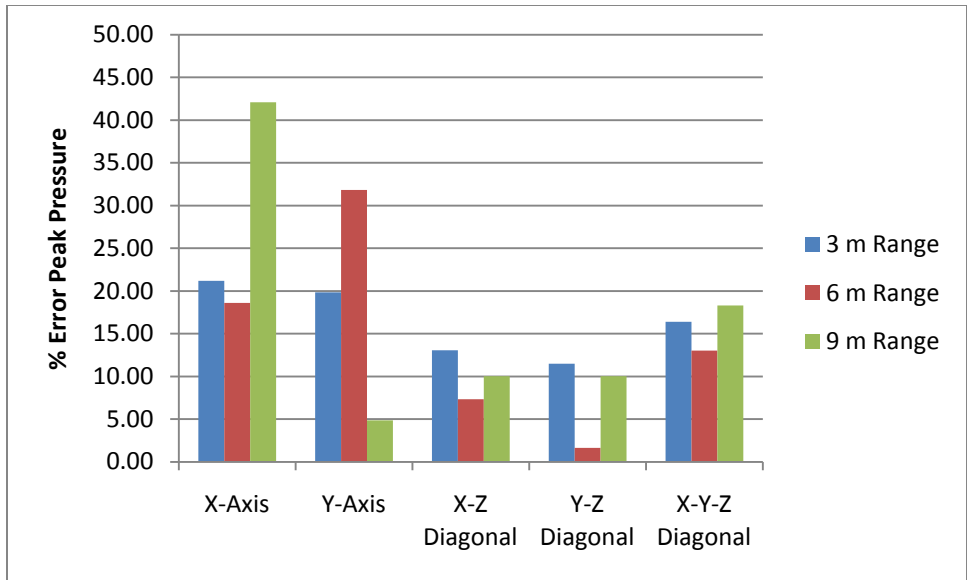
(a)
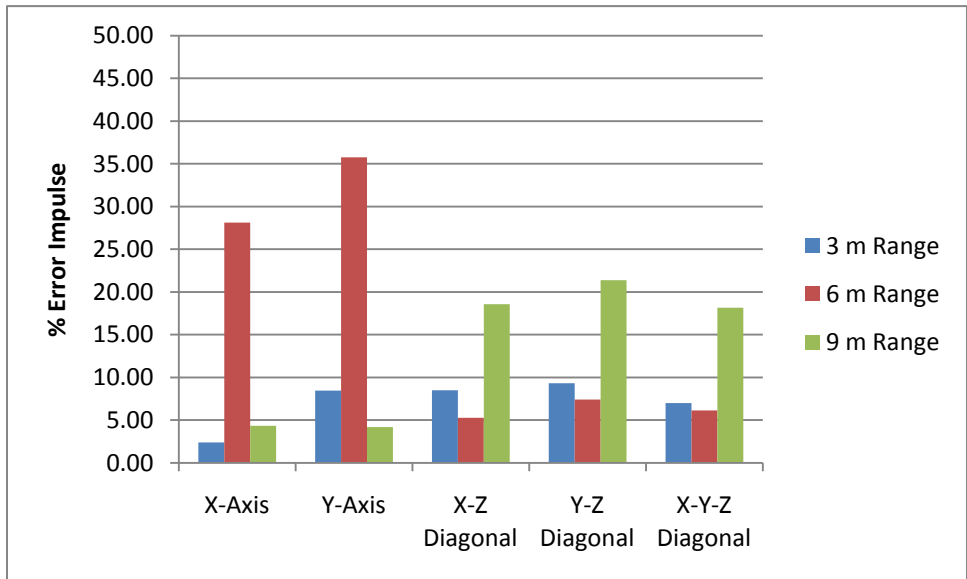
(b)

Figure A-3. DYSMAS Directional Error, W = 907.28 kg for (a) Pressure and (b) Impulse
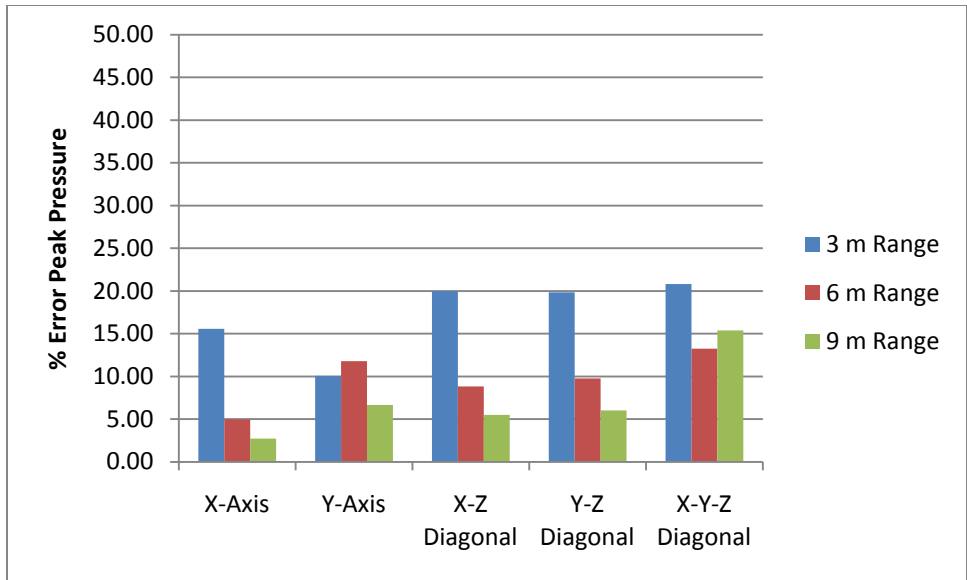
(a)
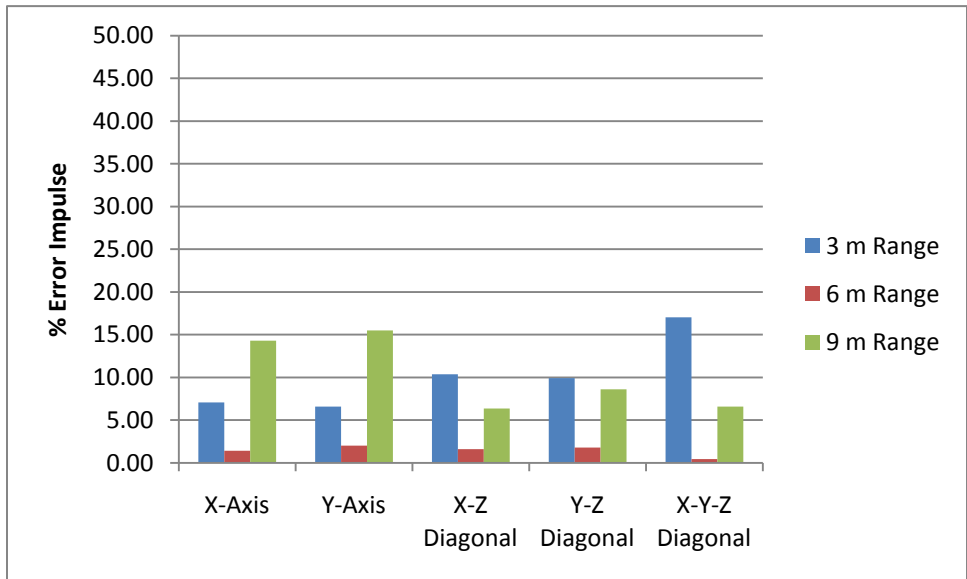
(b)

Figure A-4. DYSMAS Directional Error, $W = 2{,}267.96$ kg for (a) Pressure and (b) Impulse

A.2. Predicted Loads over Standoff

A.2.1. 99.8-kg TNT Charge
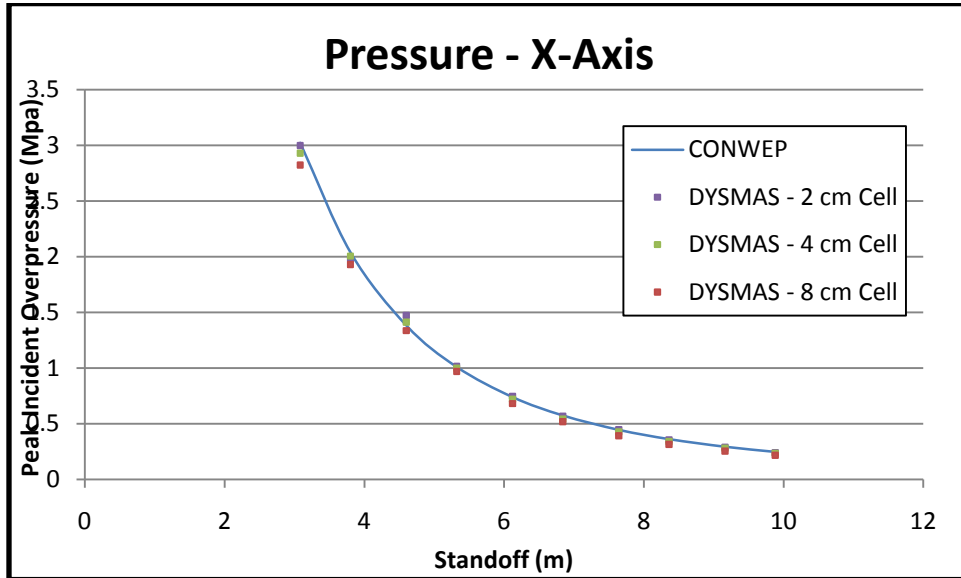
Figure A-5. Predicted Pressure along X-Axis,
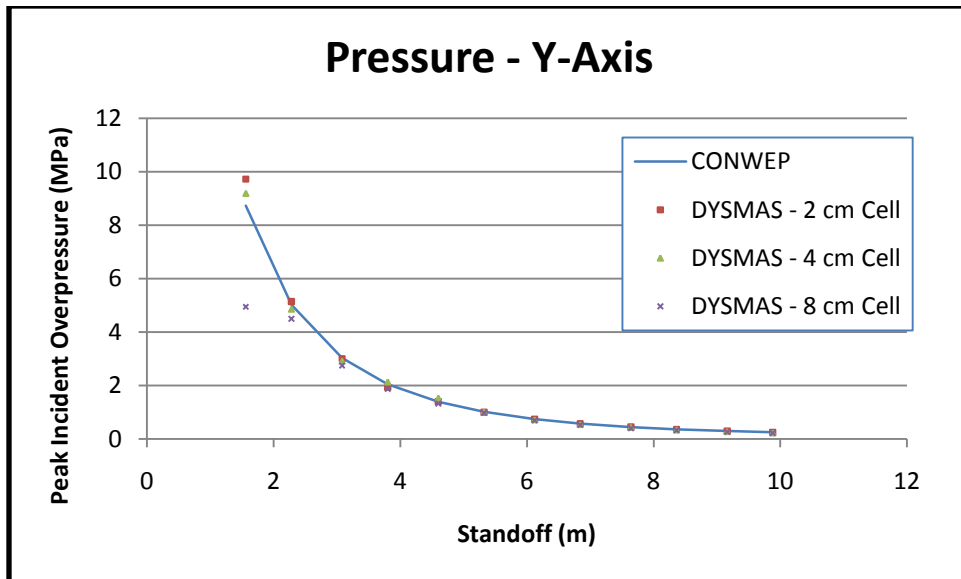
Figure A-6. Predicted Pressure along *y*-Axis,
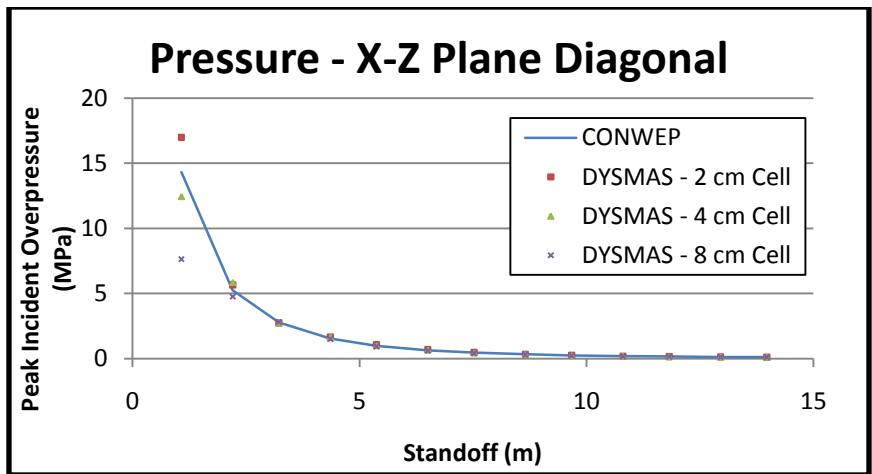
Figure A-7. Predicted Pressure along *x–z* Plane,
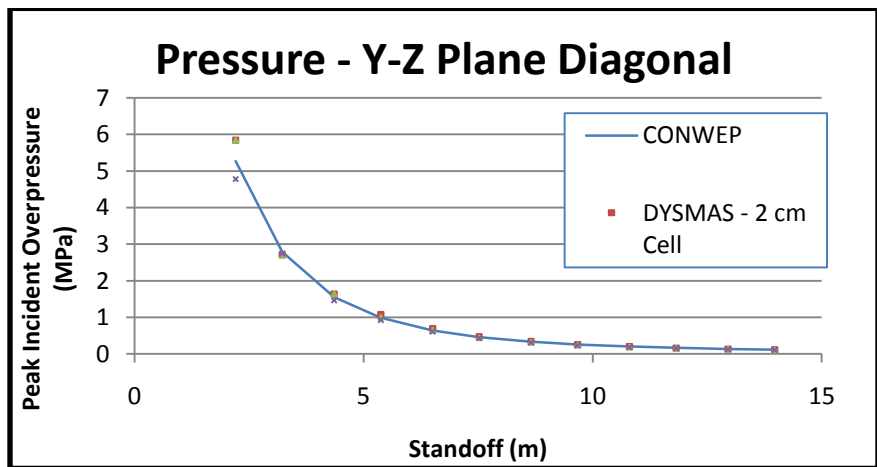
Figure A-8. Predicted Pressure along *y–z* Plane,
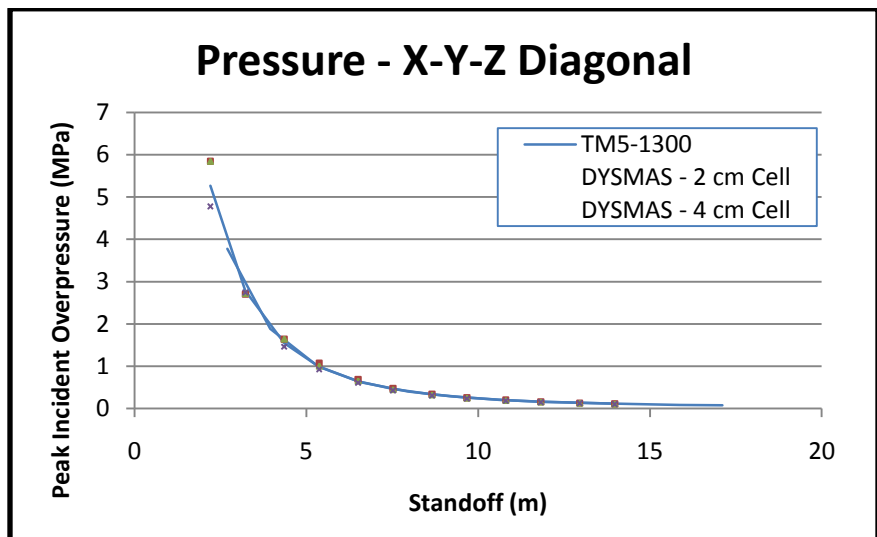
Figure A-9. Predicted Pressure along *x–y–z* Diagonal

99
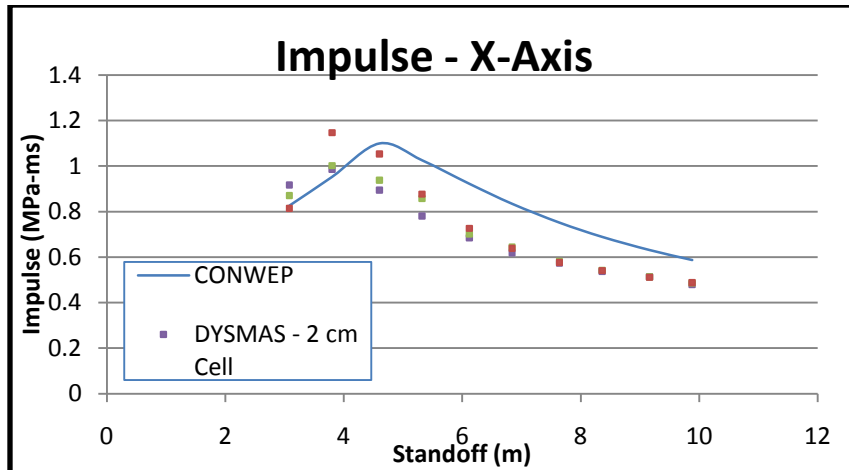
Figure A-10. Predicted Impulse along *x*-Axis
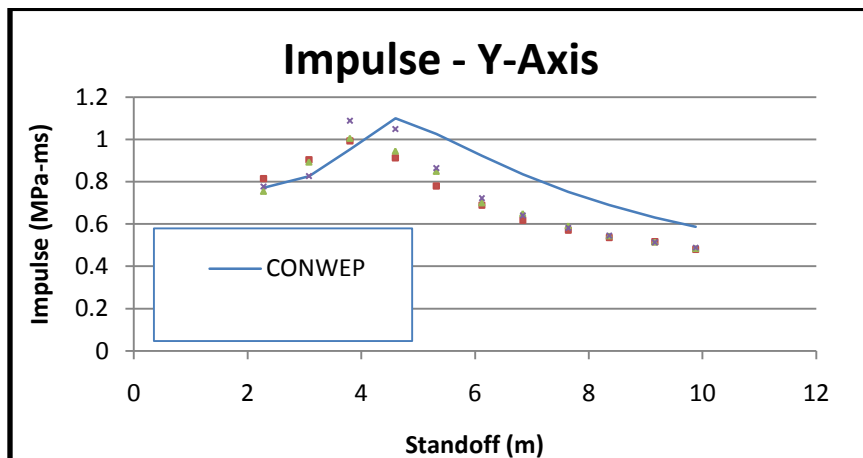
Figure A-11. Predicted Impulse along *y*-Axis
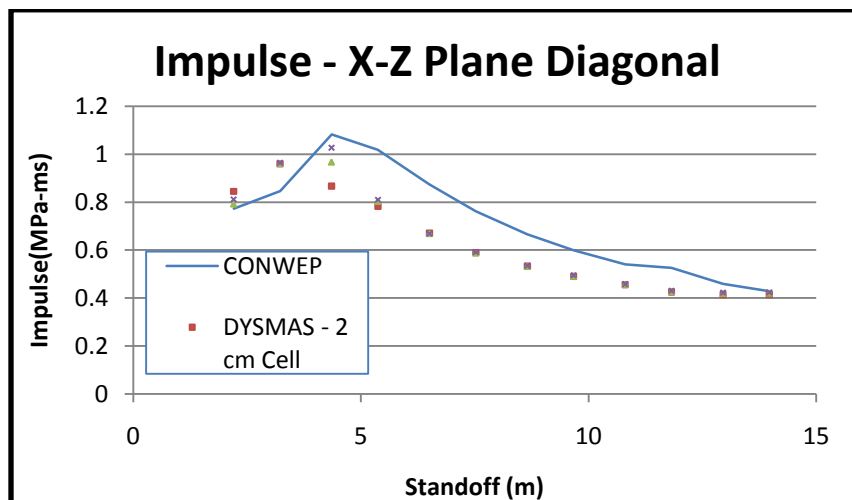
Figure A-12. Predicted Impulse along *x–z* Plane
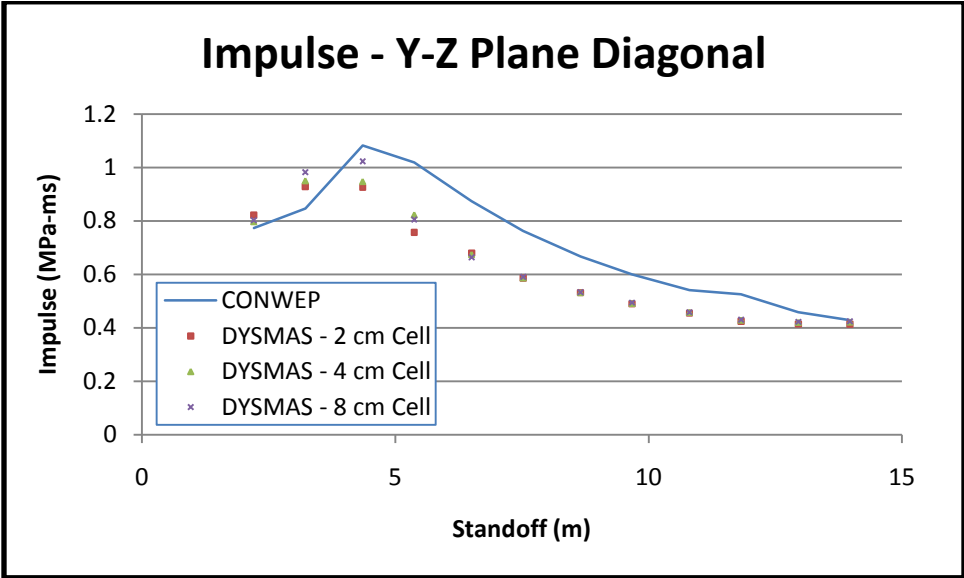
Figure A-13. Predicted Impulse along *y–z* Plane
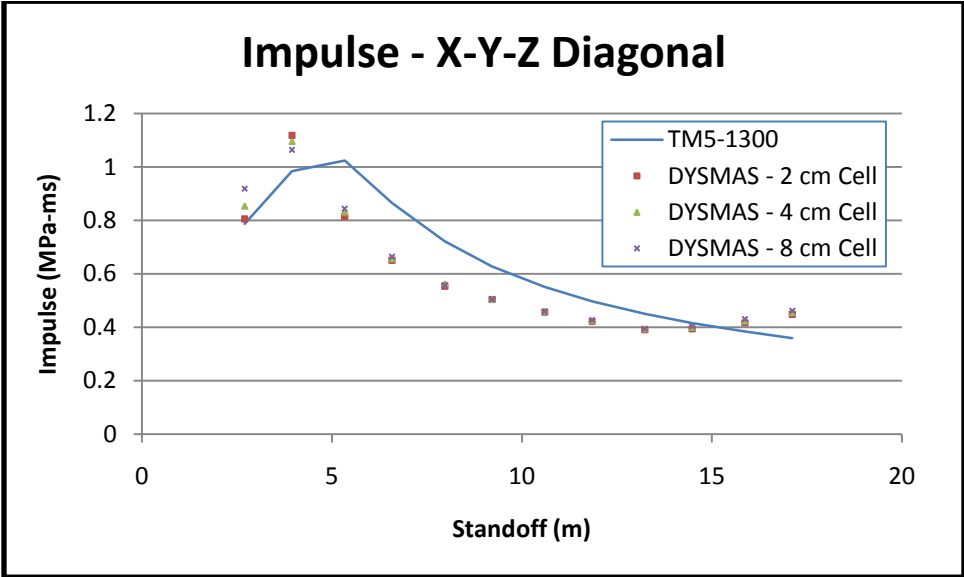
Figure A-14. Predicted Impulse along *x–y–z* Diagonal

A.2.2. 226.8-kg TNT Charge
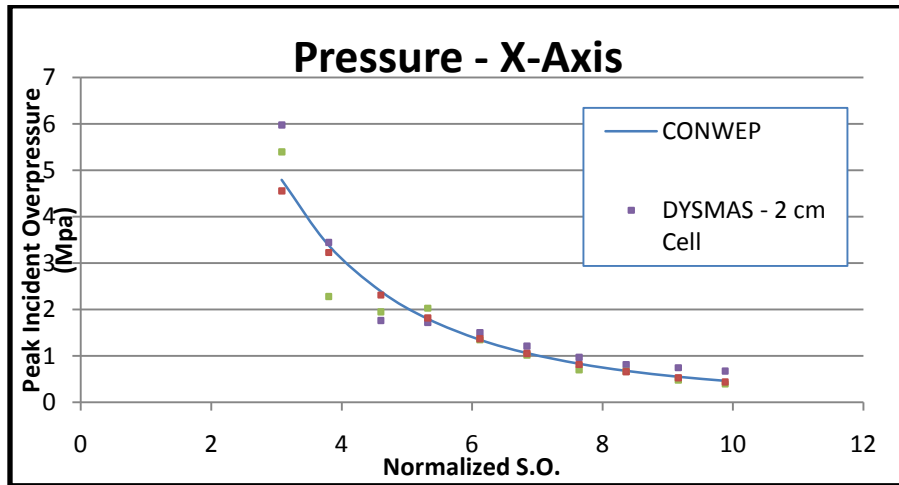
Figure A-15. Predicted Pressure along *x*-Axis
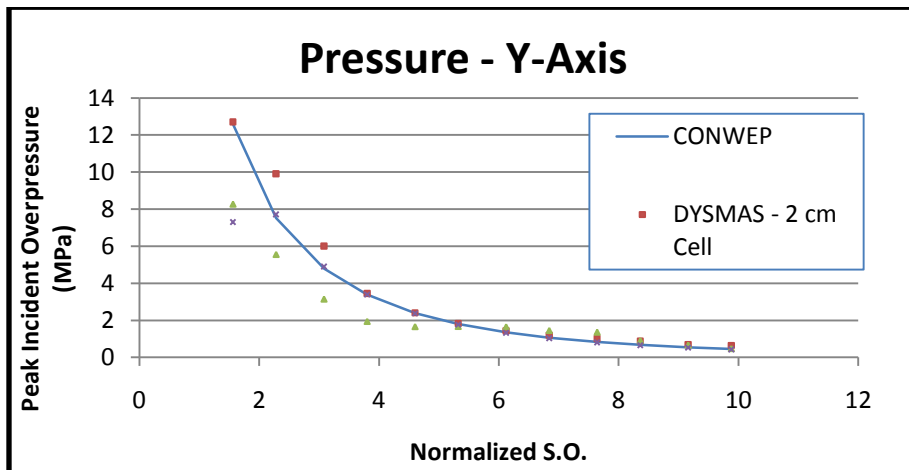
Figure A-16. Predicted Pressure along *y*-Axis
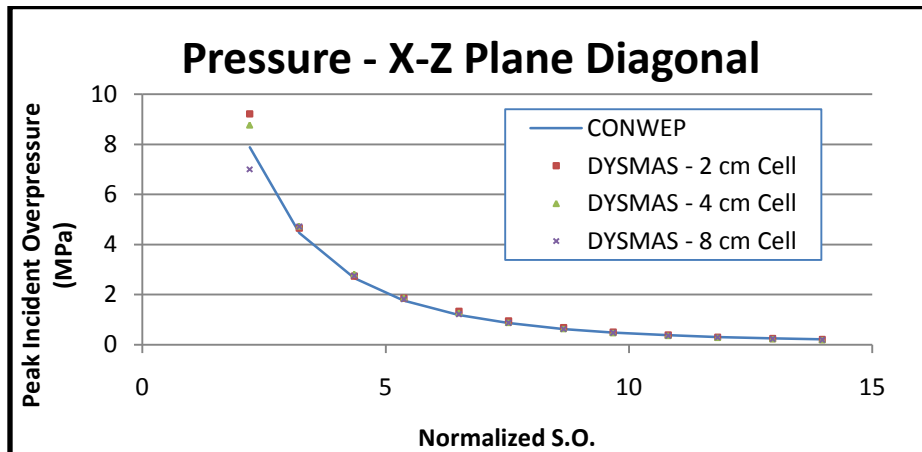
Figure A-17. Predicted Pressure along *y–z* Plane
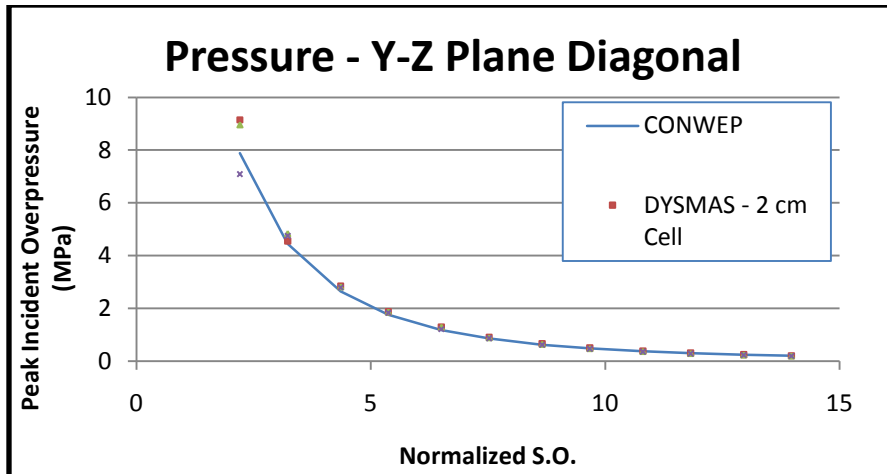
Figure A-18. Predicted Pressure along _y–z_ Plane
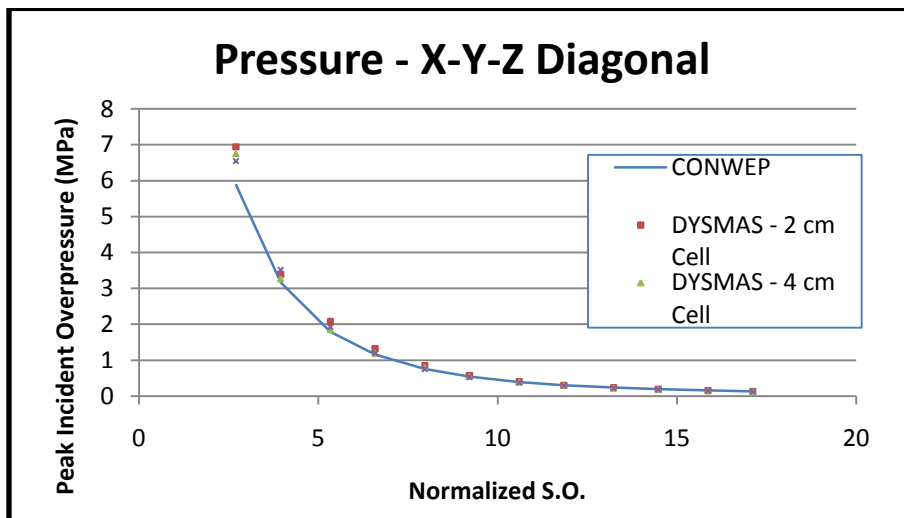
Figure A-19. Predicted Pressure along _x–y–z_ Diagonal
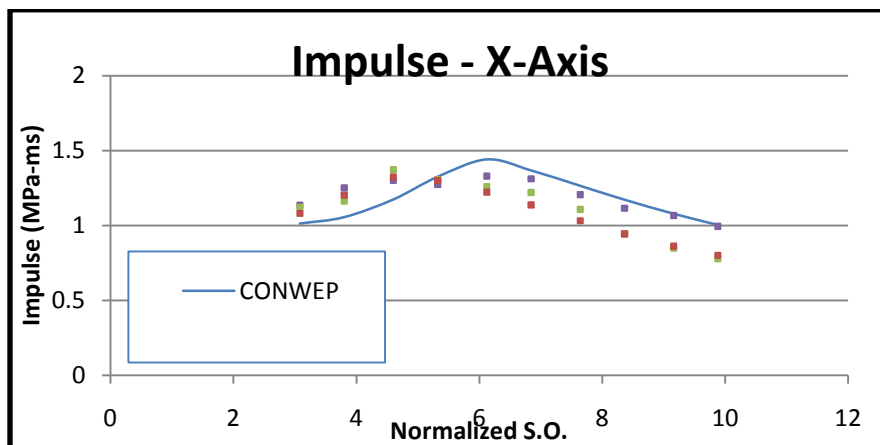
Figure A-20. Predicted Impulse along _x_-Axis

103
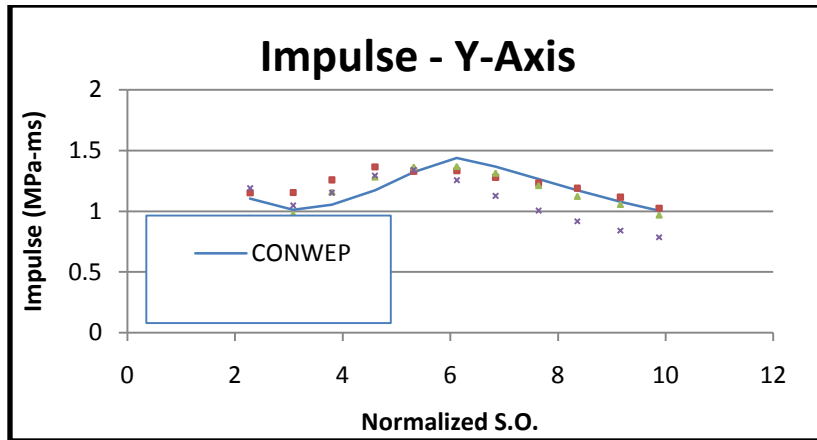
Figure A-21. Predicted Impulse along *y*-Axis
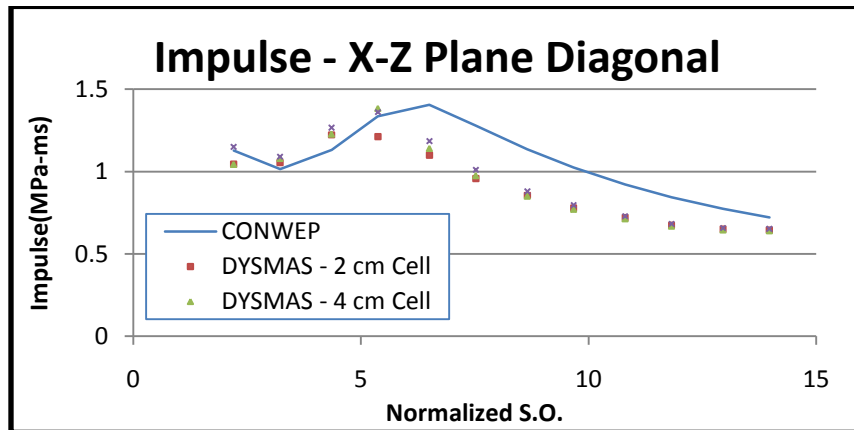
Figure A-22. Predicted Impulse along *x–z* Plane
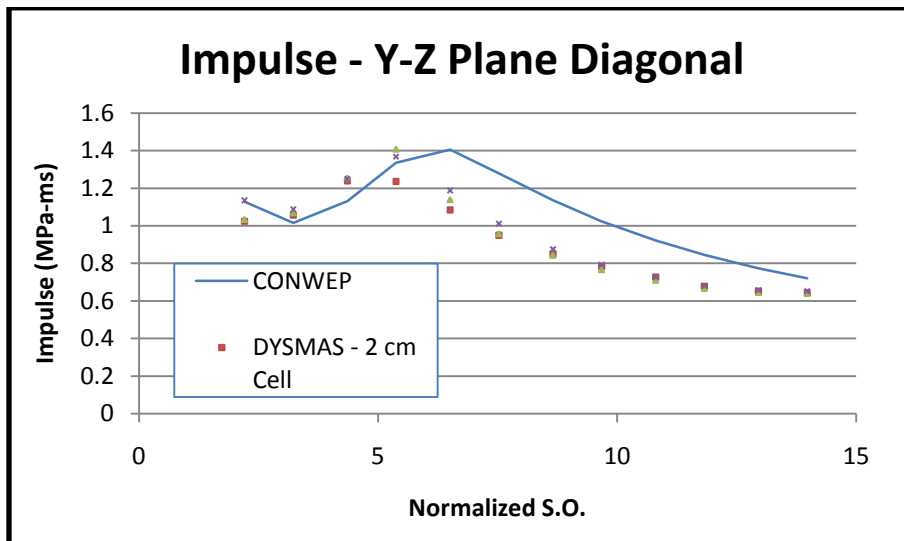
Figure A-23. Predicted Impulse along *y–z* Plane

104
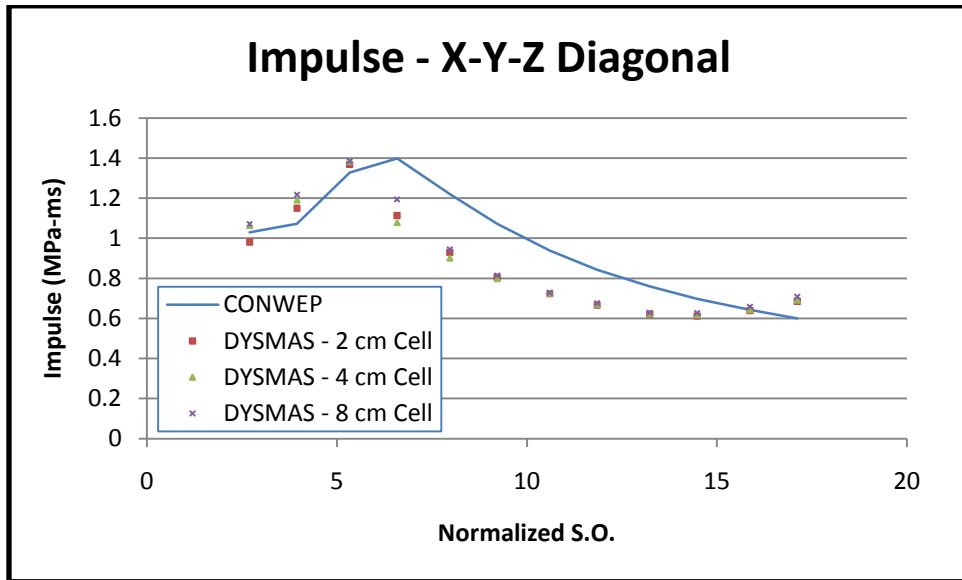
Figure A-24. Predicted Impulse along *x–y–z* Diagonal

A.2.3 907.18-kg TNT Charge
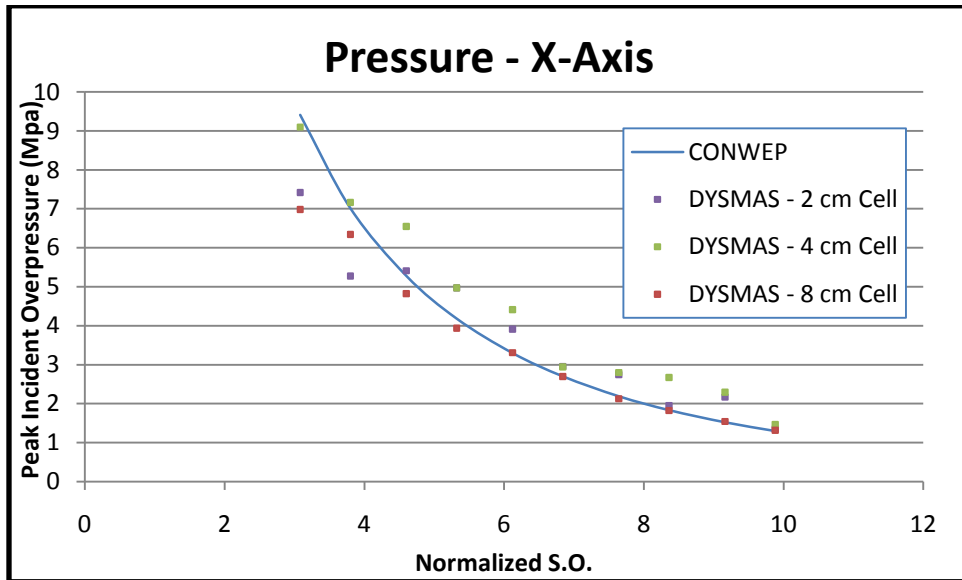
Figure A-25. Predicted Pressure along *x*-Axis
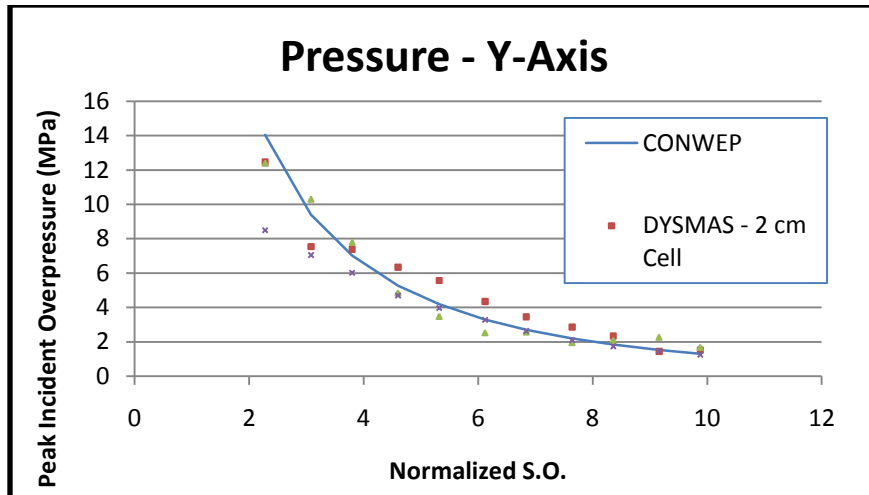
Figure A-26. Predicted Pressure along *y*--Axis
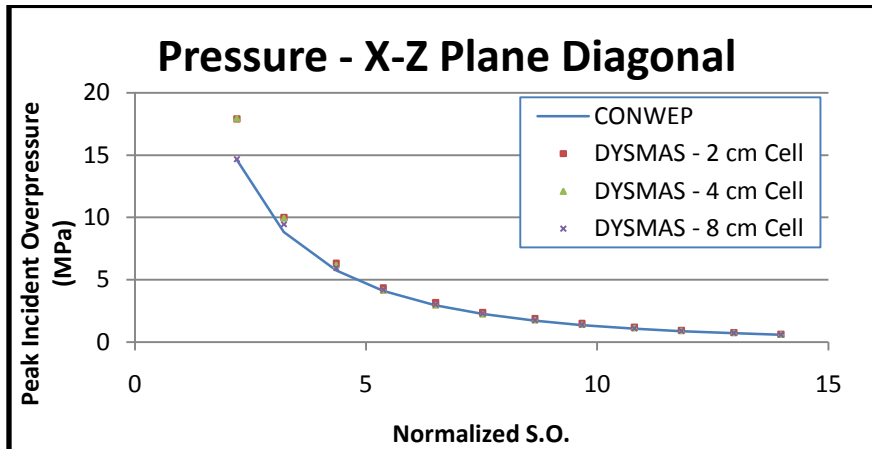
Figure A-27. Predicted Pressure along *x–z* Plane
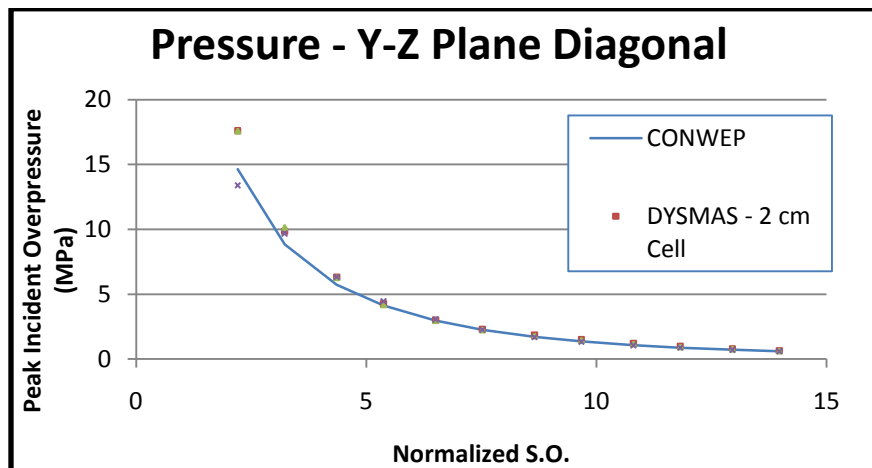
Figure A-28. Predicted Pressure along *y–z* Plane
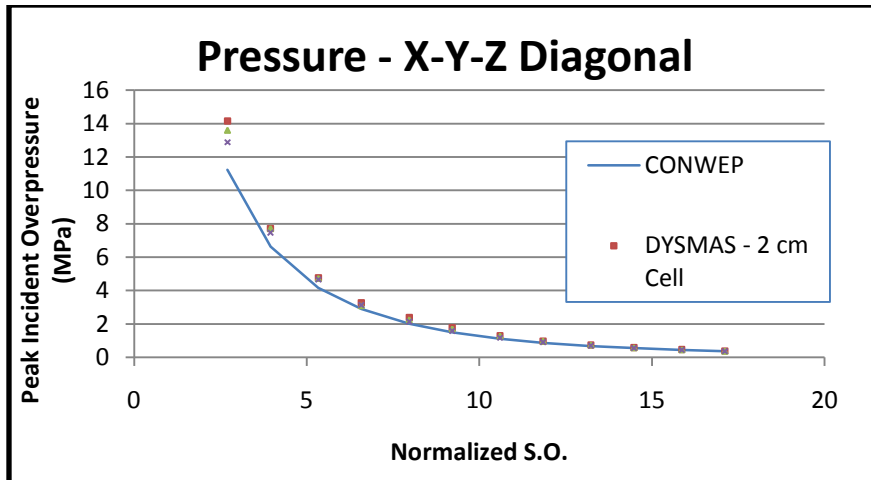
Figure A-29. Predicted Pressure along *x–y–z* Diagonal
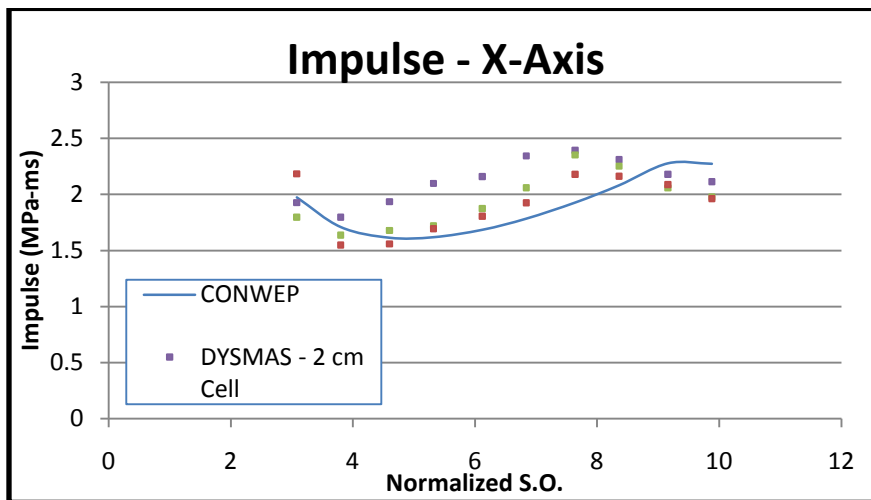
Figure A-30. Predicted Impulse along *x*-Axis
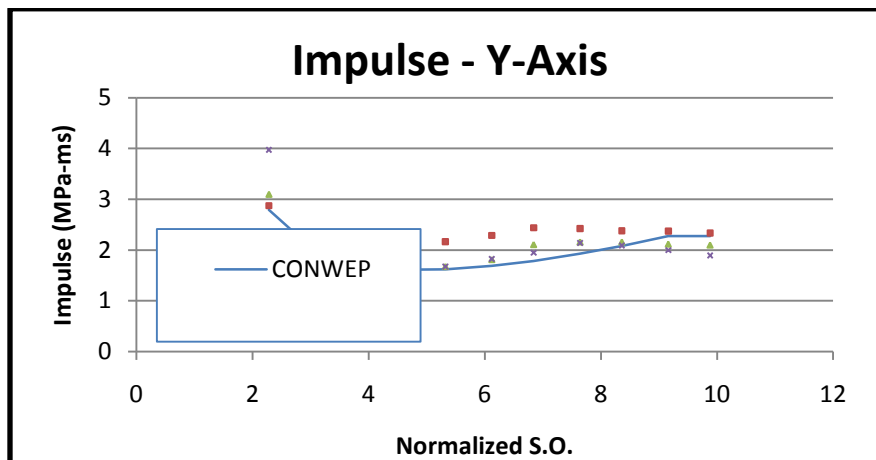
Figure A-31. Predicted Impulse along *y*-Axis
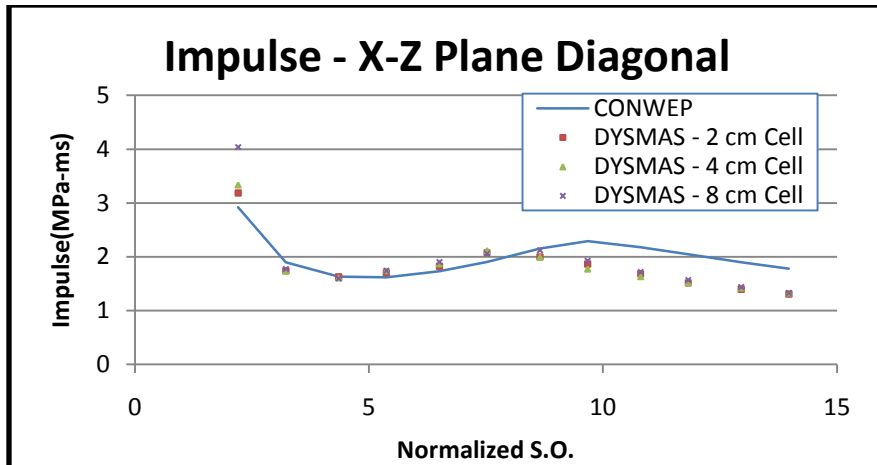
Figure A-32. Predicted Impulse along *x–z* Plane
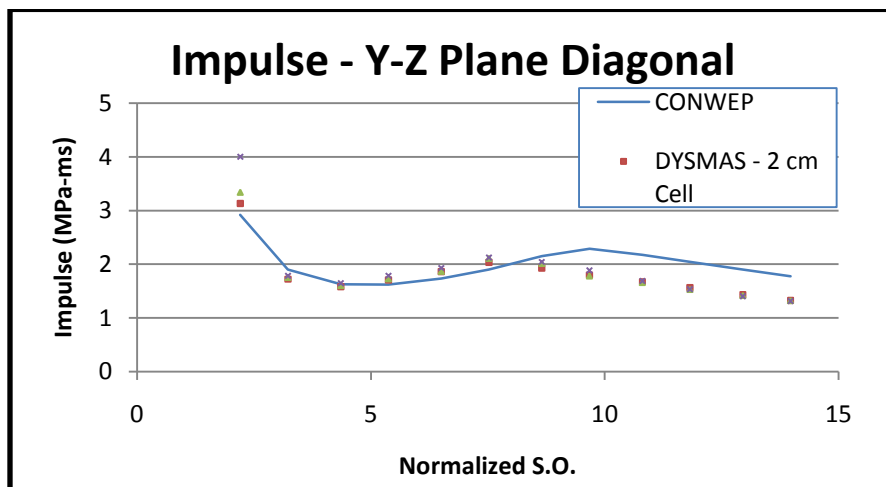
Figure A-33. Predicted Impulse along *y–z* Plane,
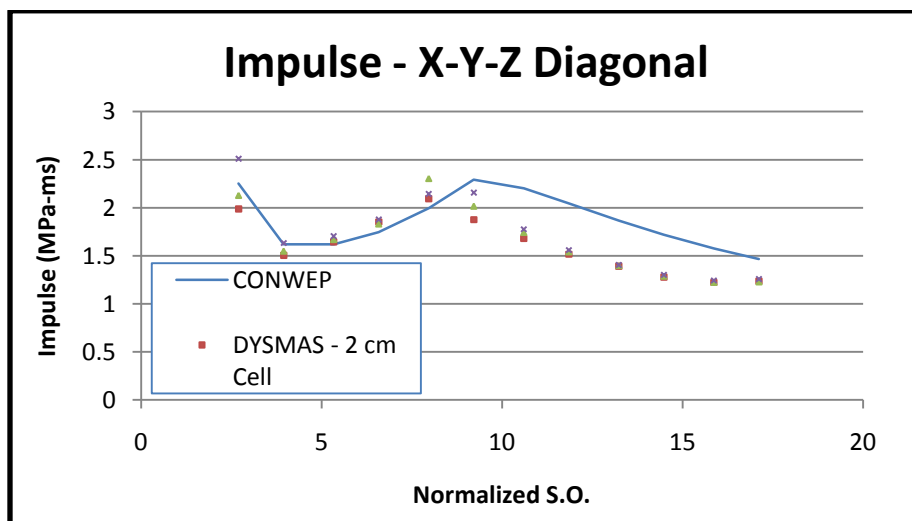
Figure A-34. Predicted Impulse along *x–y–z* Diagonal

A.2.3. 2,267.96-kg TNT Charge
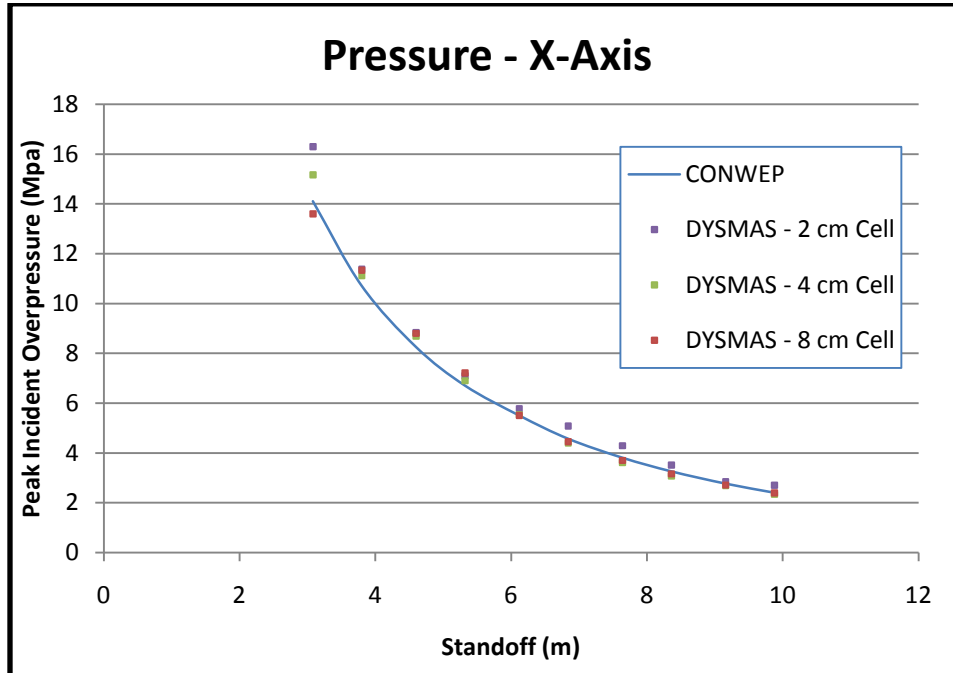
Figure A-35. Predicted Pressure along *x*-Axis
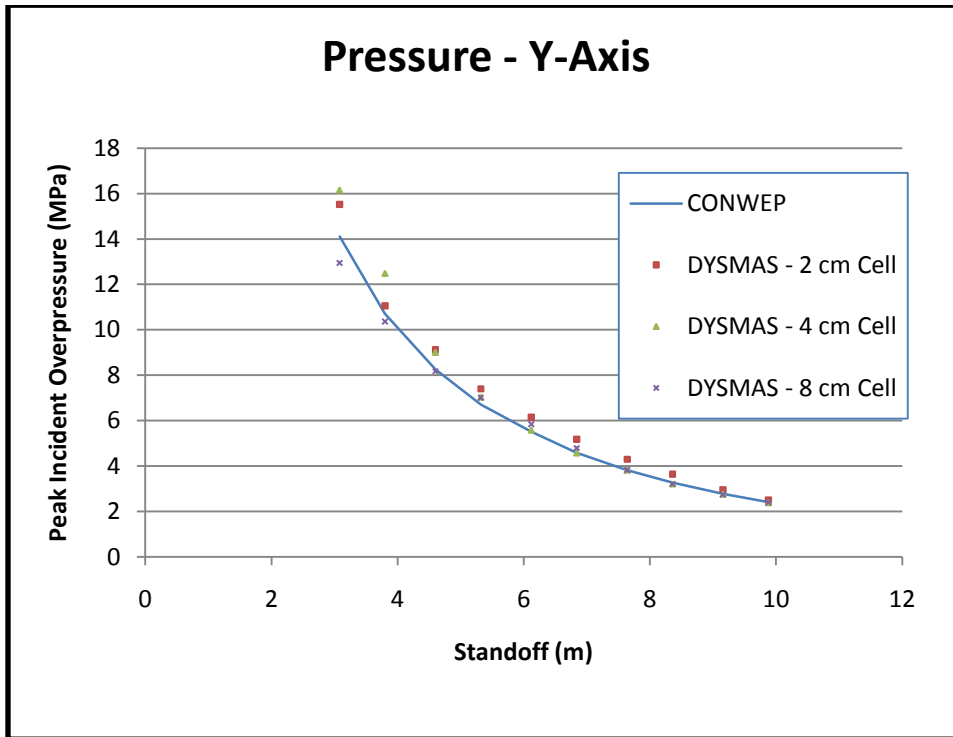
Figure A-36. Predicted Pressure along *y*-Axis
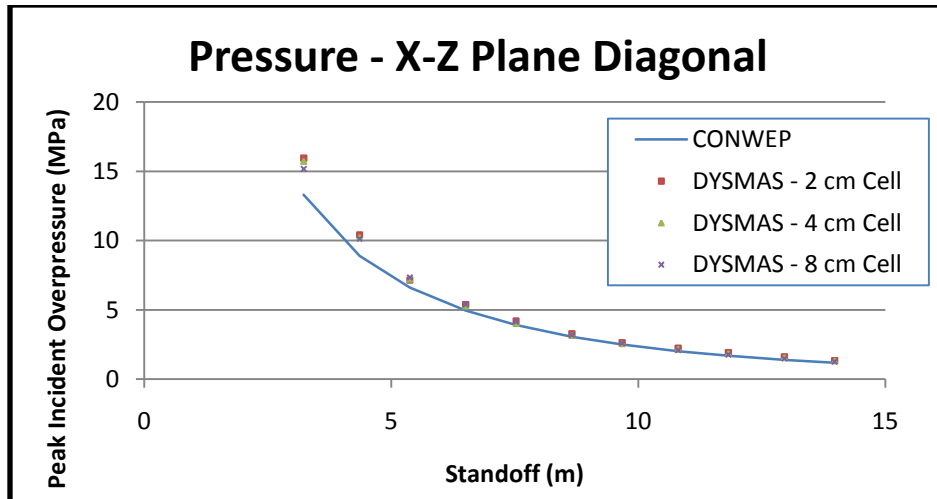
Figure A-37. Predicted Pressure along *x–z* Plane
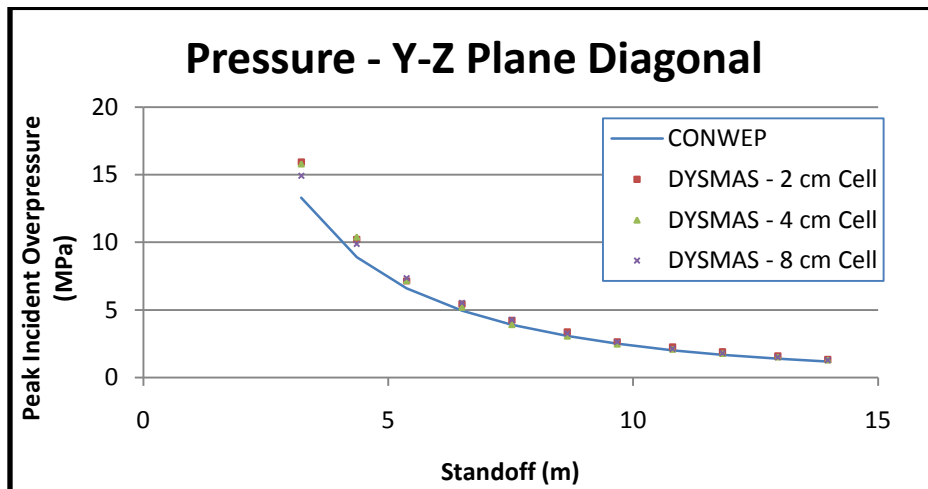
Figure A-38. Predicted Pressure along *y–z* Plane
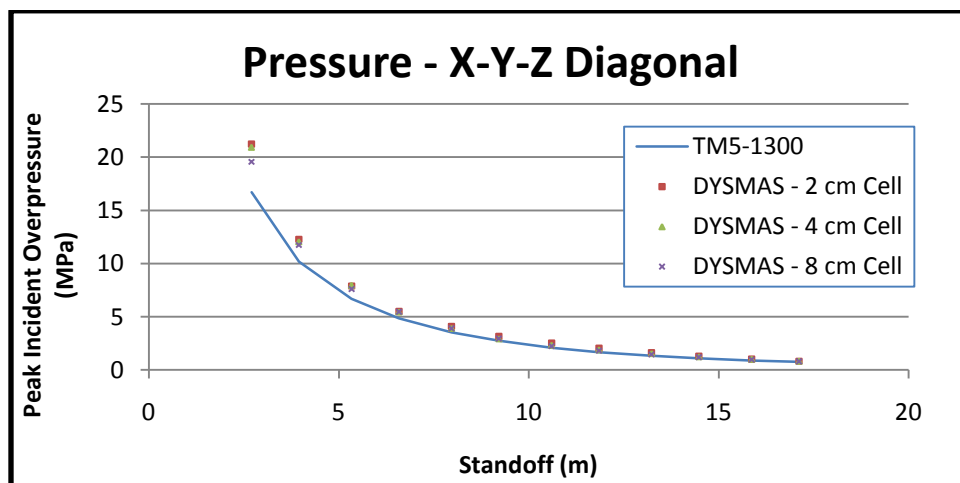
Figure A-39. Predicted Pressure along *x–y–z* Diagonal
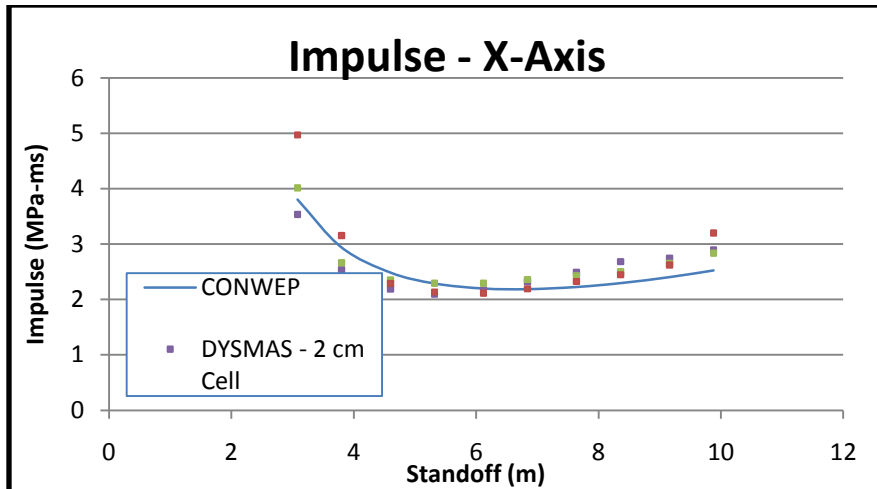
Figure A-40. Predicted Impulse along *x*-Axis
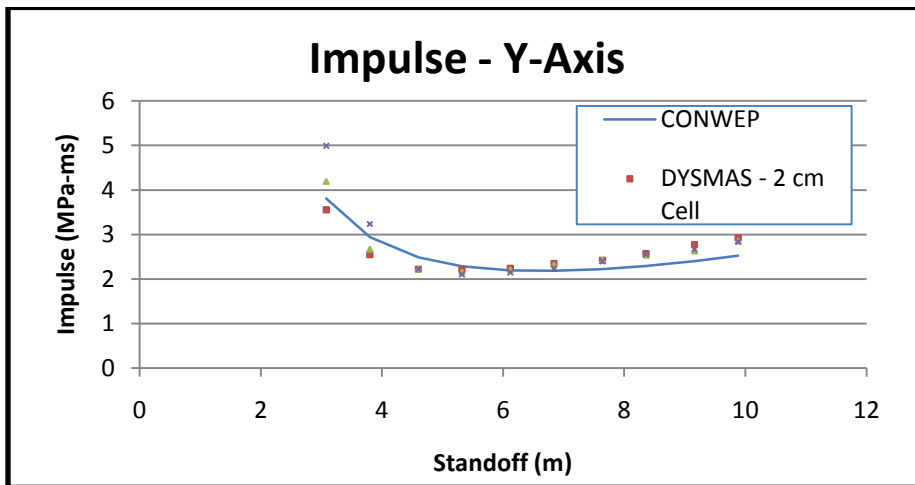
Figure A-41. Predicted Impulse along *y*-Axis
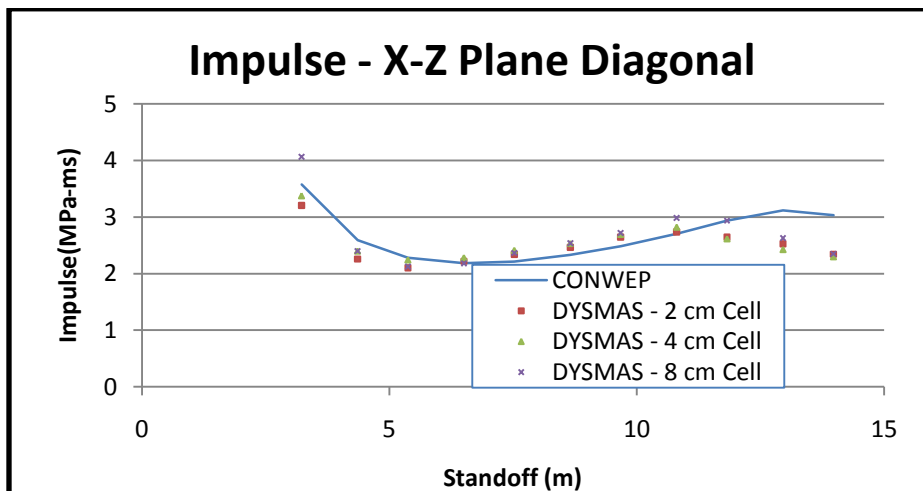
Figure A-42. Predicted Impulse along *x–z* Plane

111
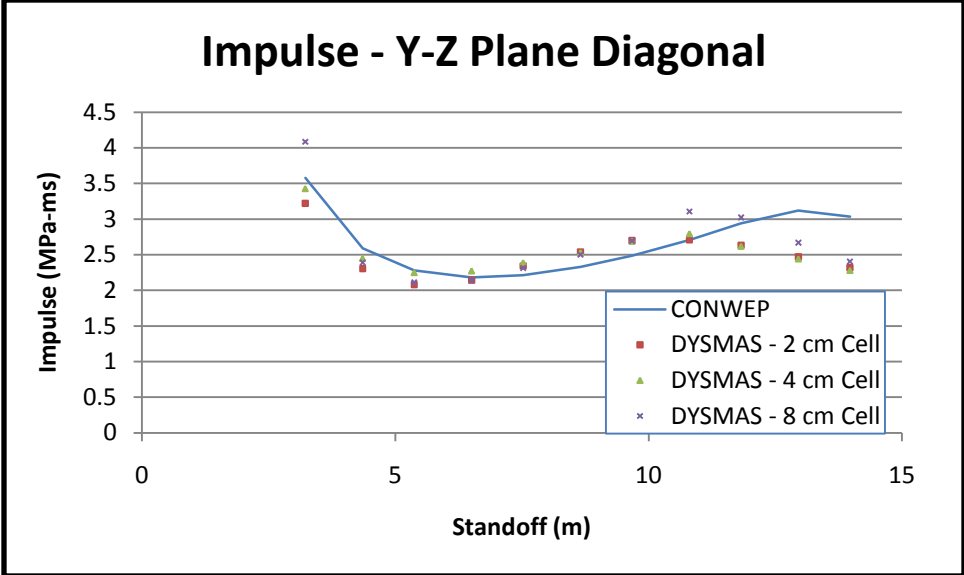
Figure A-43. Predicted Impulse along *y–z* Plane
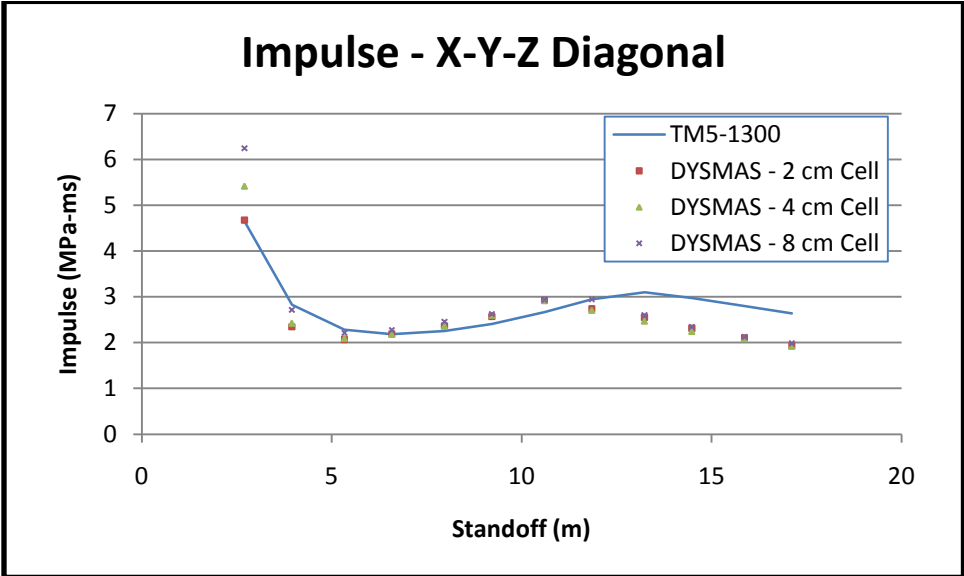
Figure A-44. Predicted Impulse along *x–y–z* Diagonal

Appendix B: BLAST BARRIER REDUCTION FACTORS

B.1. Effect of Blast Barrier Height to Pressure Adjustment Factors along Vertical Centerline of Structure

(a)

(b)

(c)
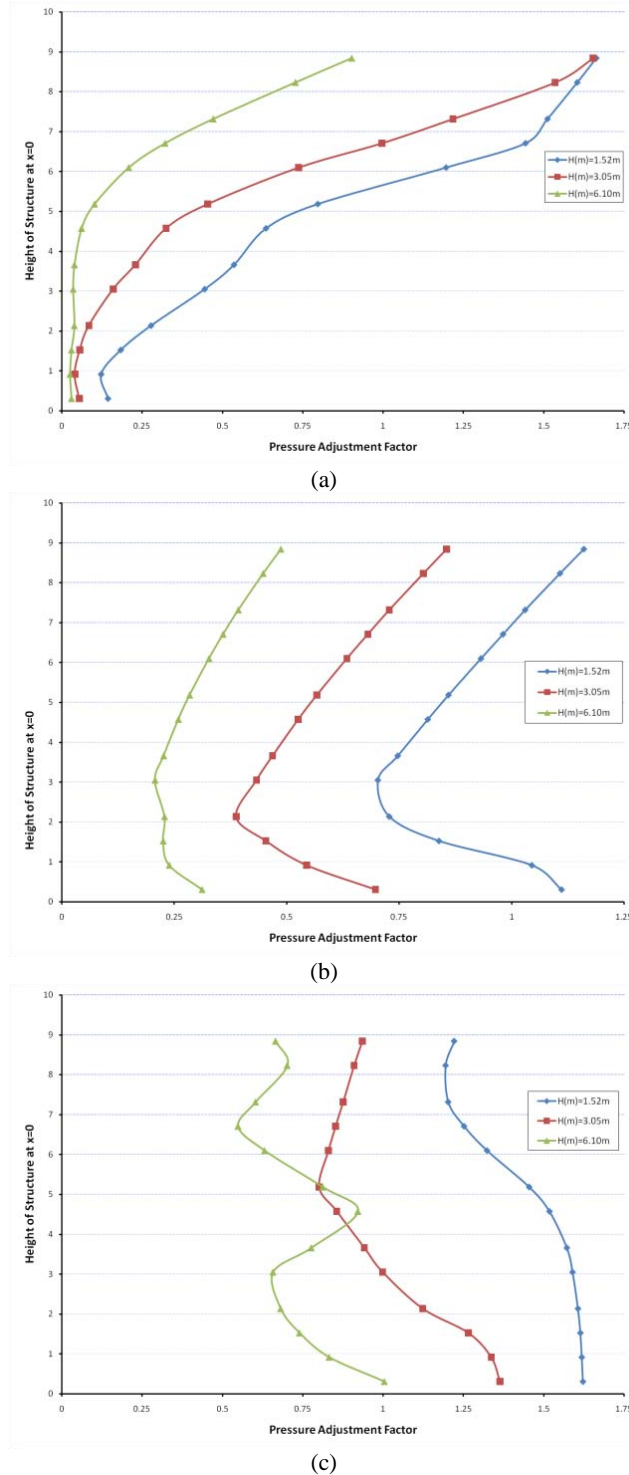
Figure B-1. Effect of Barrier Height on Pressure Factor, W = 22.68 kg-TNT, d_1 = 1.91 m, (a) Z = 4.95 m, (b) Z = 12.54 m, (c) Z = 24.72 m
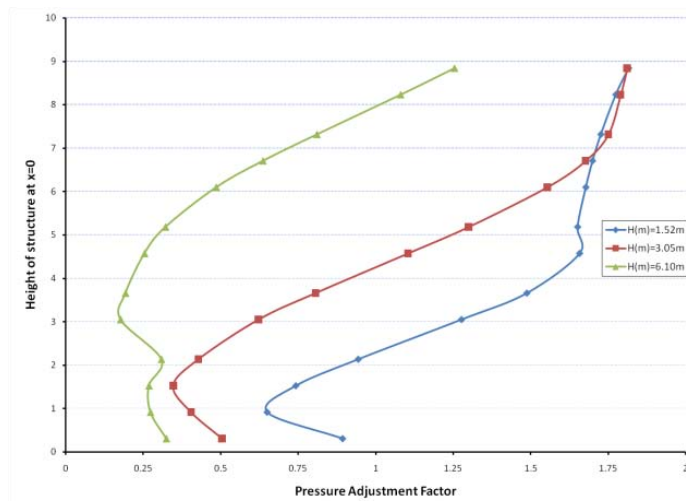
(a)
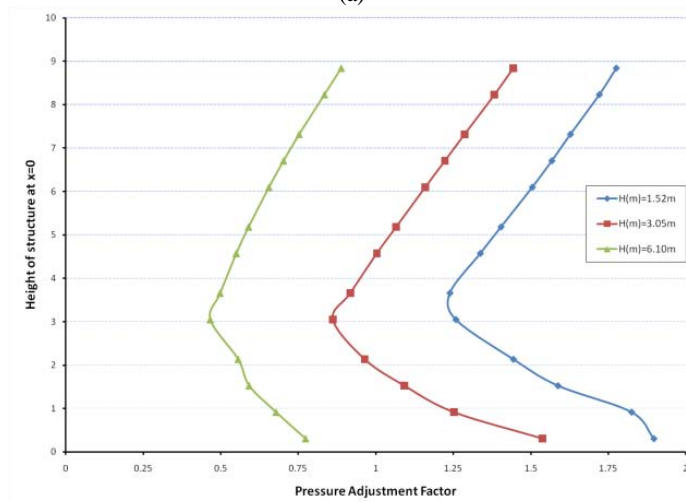
(b)
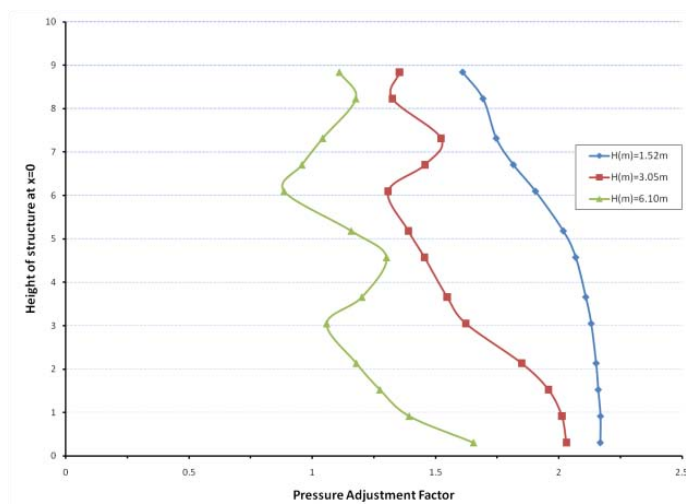
(c)

Figure B-2. Effect of Barrier Height on Pressure Factor, W = 22.68 kg-TNT, d_1 = 7.62 m, (a) Z = 10.67 m, (b) Z = 18.26 m, (c) Z = 30.44 m

114
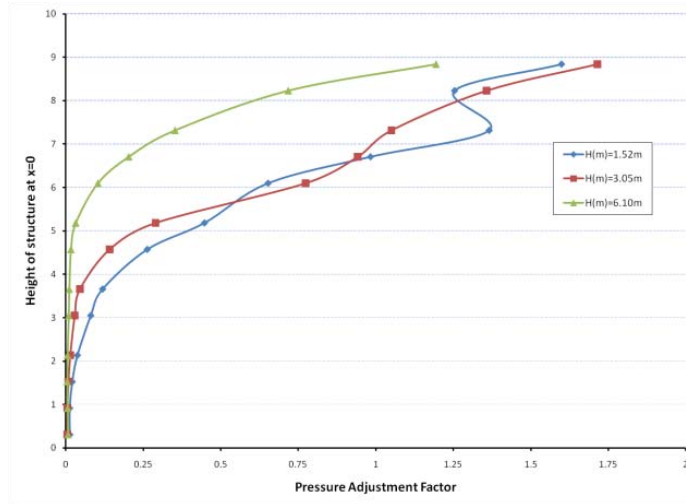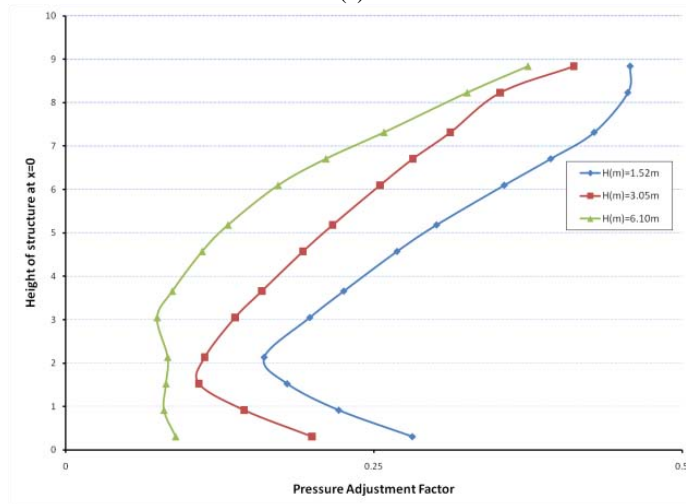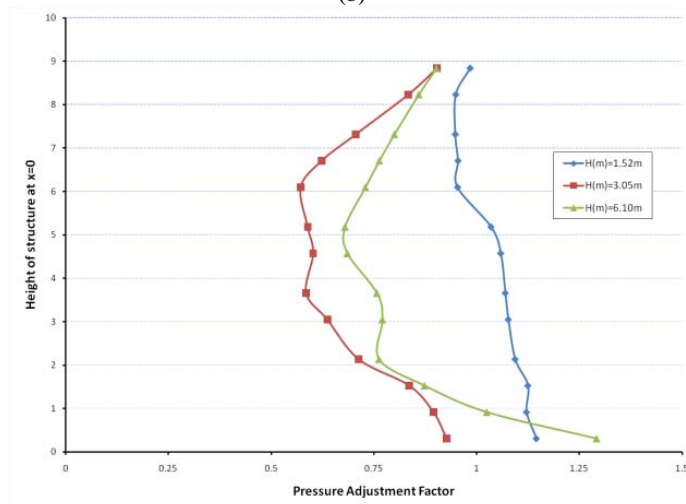
Figure B-3. Effect of Barrier Height on Pressure Factor, W = 245.47 kg-TNT, d_1 = 0.42 m, (a) Z = 3.46 m, (b) Z = 11.05 m, (c) Z = 23.23 m

115
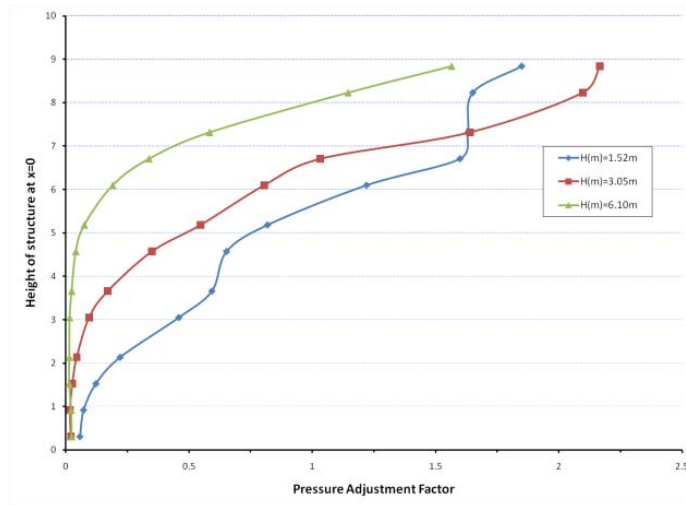
(a)
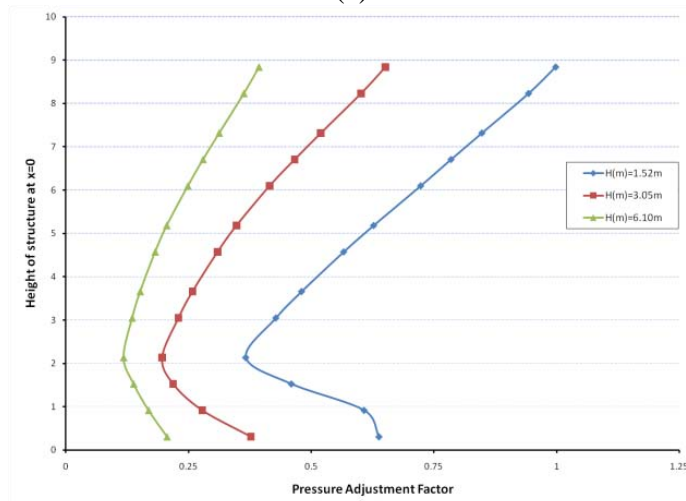
(b)
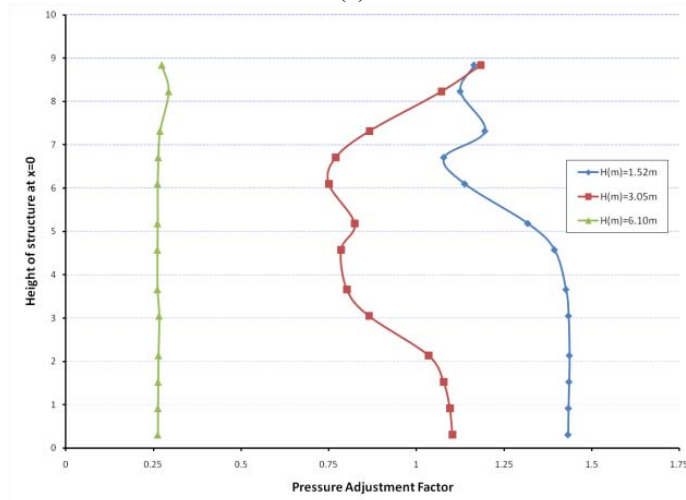
(c)

Figure B-4. Effect of Barrier Height on Pressure Factor, $W = 245.47$ kg-TNT, $d_1 = 1.91$ m, (a) $Z = 4.95$ m, (b) $Z = 12.54$ m, (c) $Z = 24.72$ m
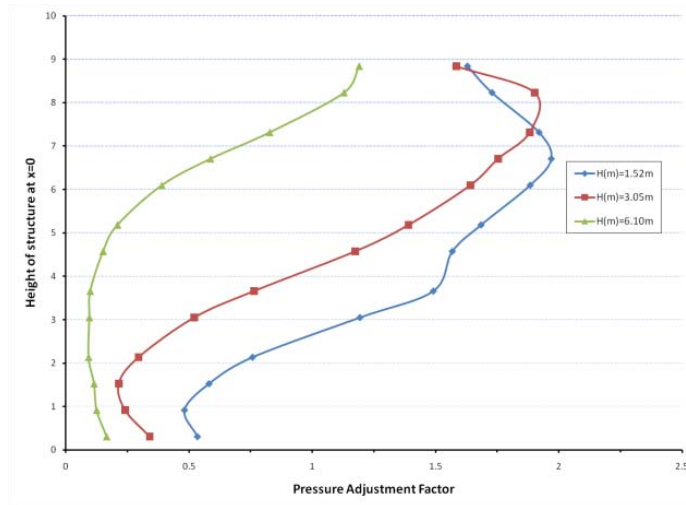
(a)
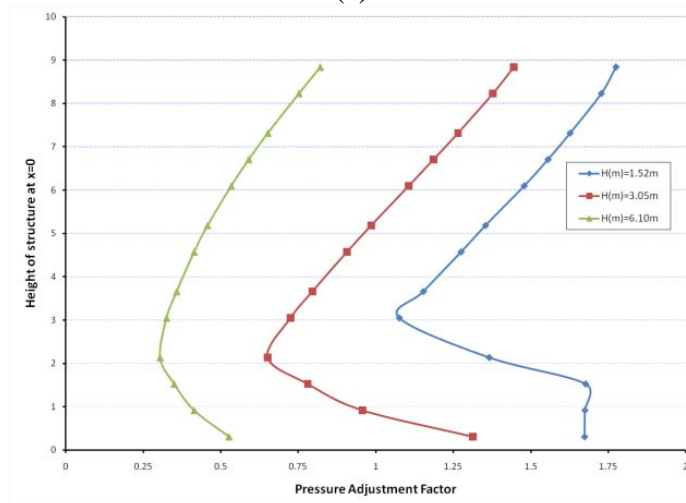
(b)
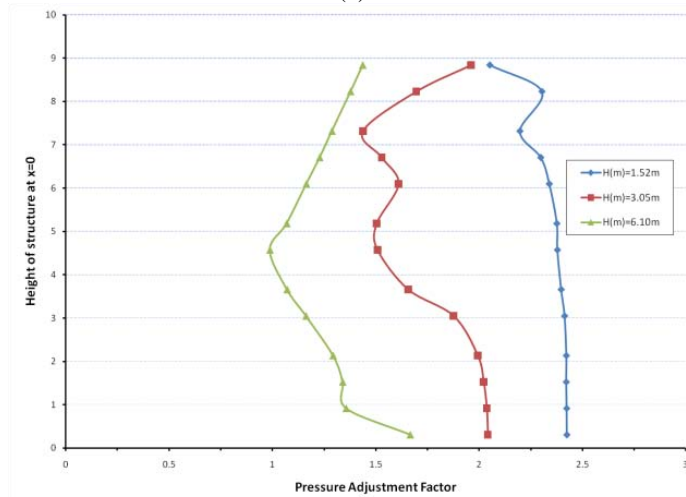
(c)

Figure B-5. Effect of Barrier Height on Pressure Factor, W = 245.47 kg-TNT, d_1 = 7.62 m, (a) Z = 10.67 m, (b) Z = 18.26 m, (c) Z = 30.44 m
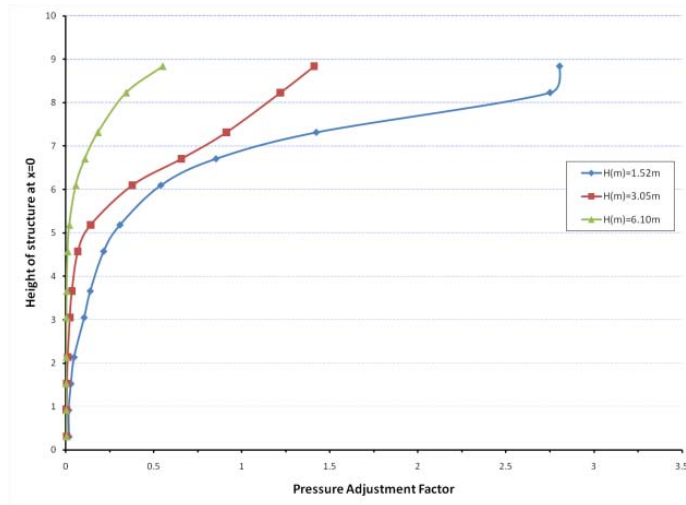
(a)
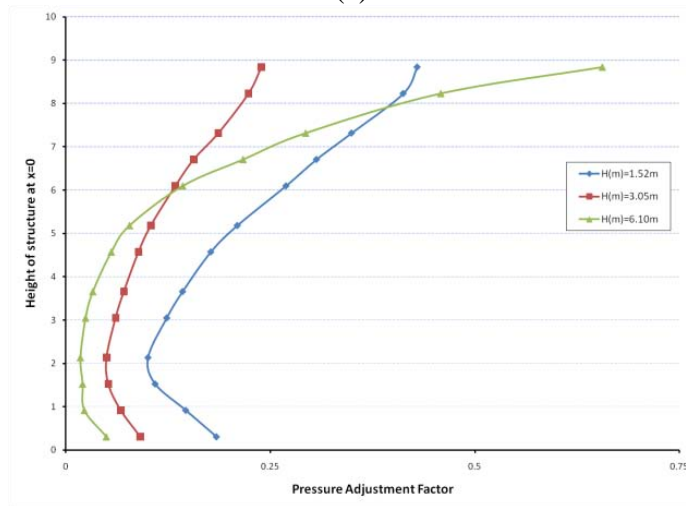
(b)
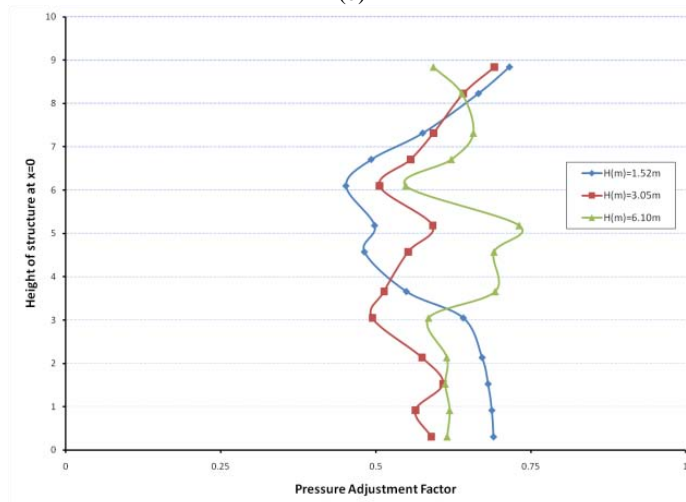
(c)

Figure B-6. Effect of Barrier Height on Pressure Factor, W = 910.42 kg-TNT, d_1 = 0.64 m, (a) Z = 3.84 m, (b) Z = 11.28 m, (c) Z = 23.46 m
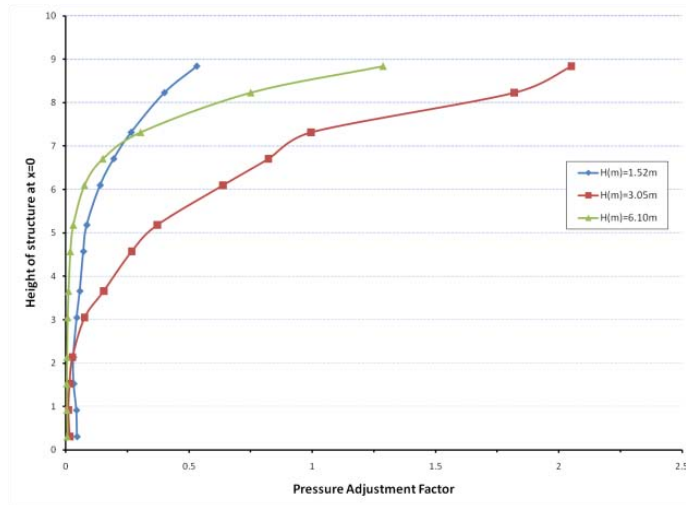
(a)
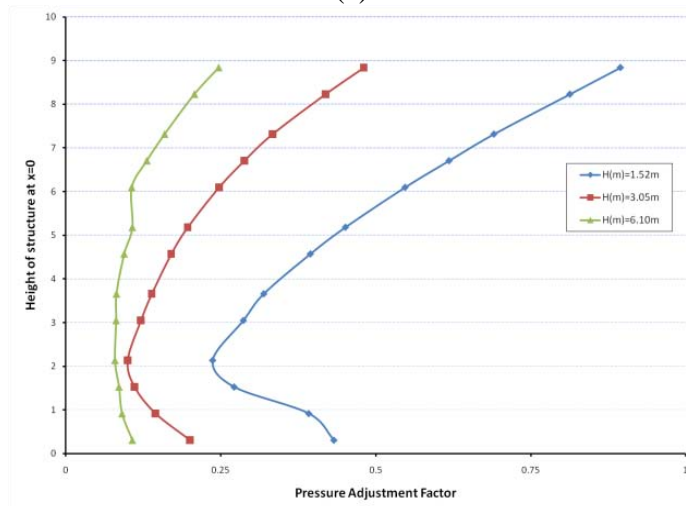
(b)
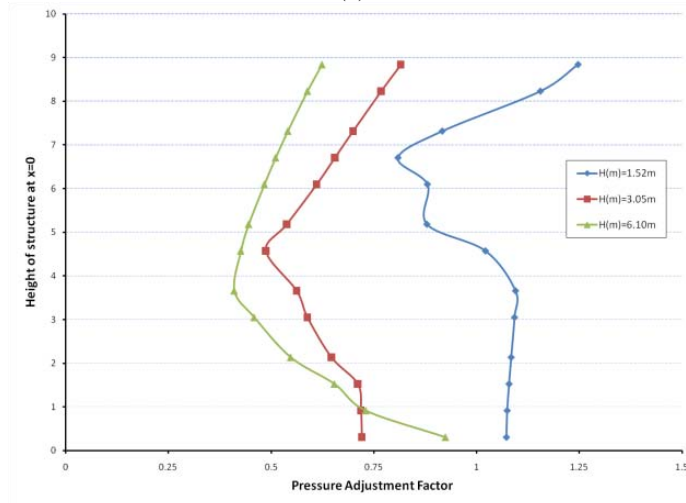
(c)

Figure B-7. Effect of Barrier Height on Pressure Factor, W = 910.42 kg-TNT, d_1 = 1.91 m, (a) Z = 495 m, (b) Z = 12.54 m, (c) Z = 24.72 m
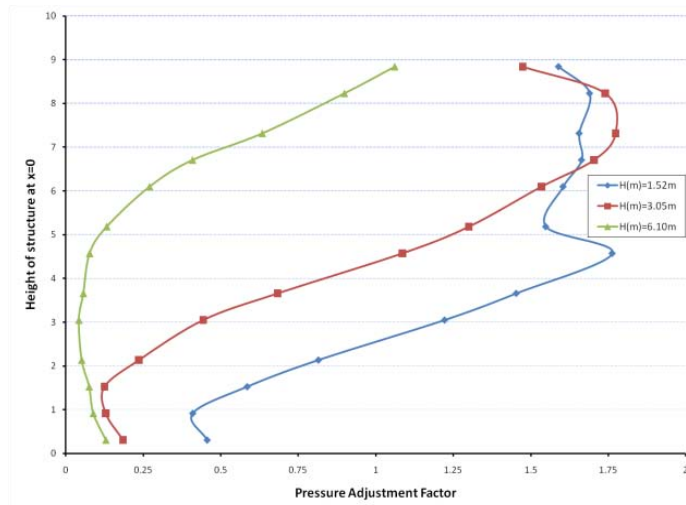
(a)
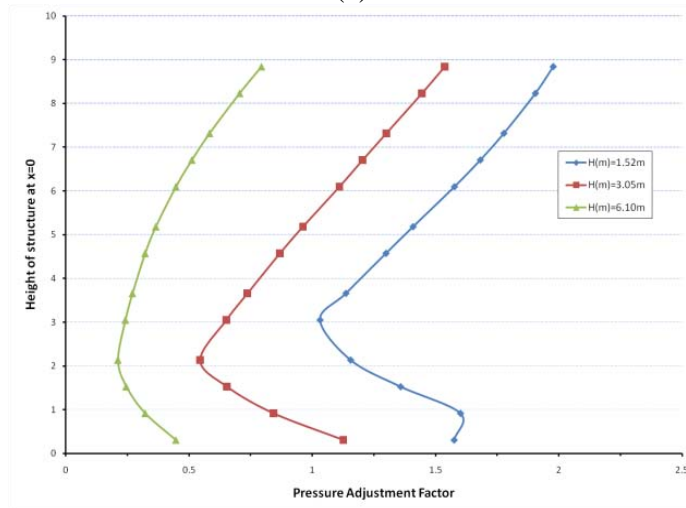
(b)
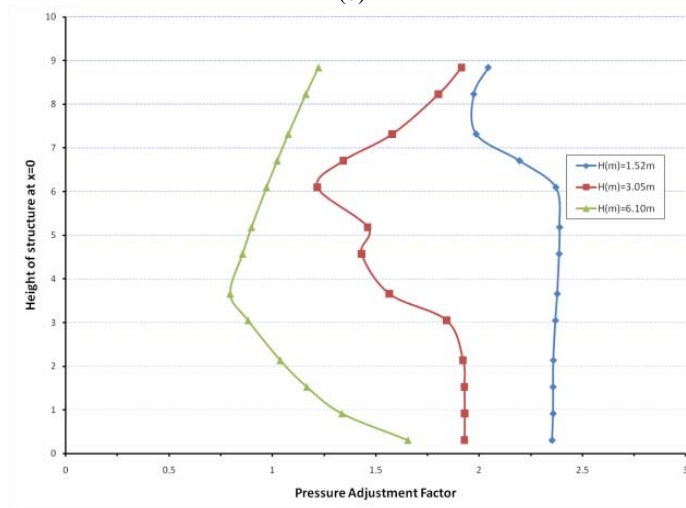
(c)

Figure B-8. Effect of Barrier Height on Pressure Factor, W = 910.42 kg-TNT, d_1 = 7.62 m, (a) Z = 10.67 m, (b) Z = 18.26 m, (c) Z = 30.44 m

120

B.2. Effect of Blast Barrier Height to Pressure Adjustment Factors along Vertical Line 0.61 m from Center of Structure

(a)

(b)

(c)
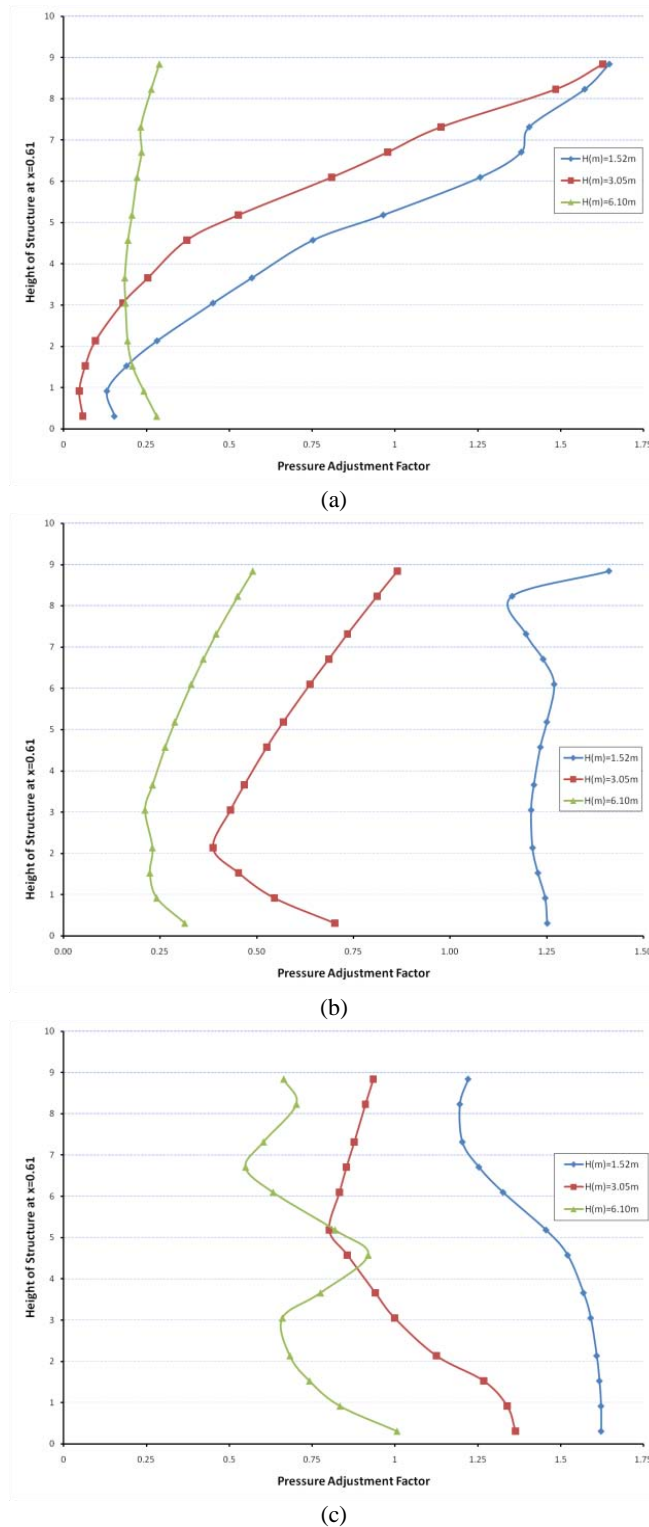
Figure B-9. Effect of Barrier Height on Pressure Factor, W = 22.68 kg-TNT, d_1 = 1.91 m, (a) Z = 4.95 m, (b) Z = 12.54 m, (c) Z = 24.72 m
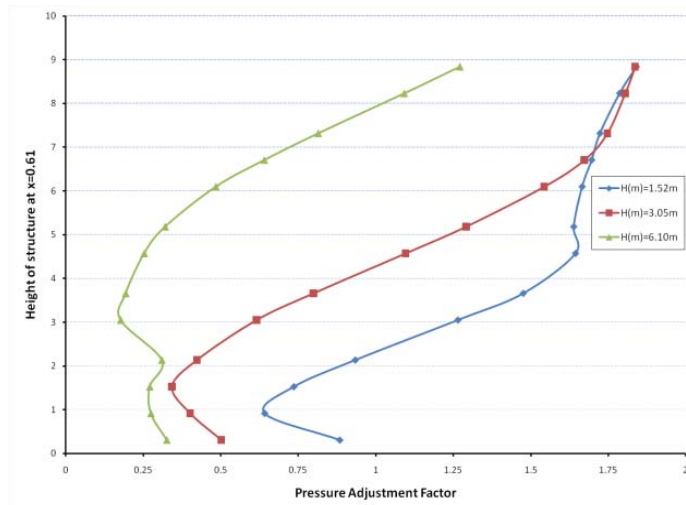
(a)
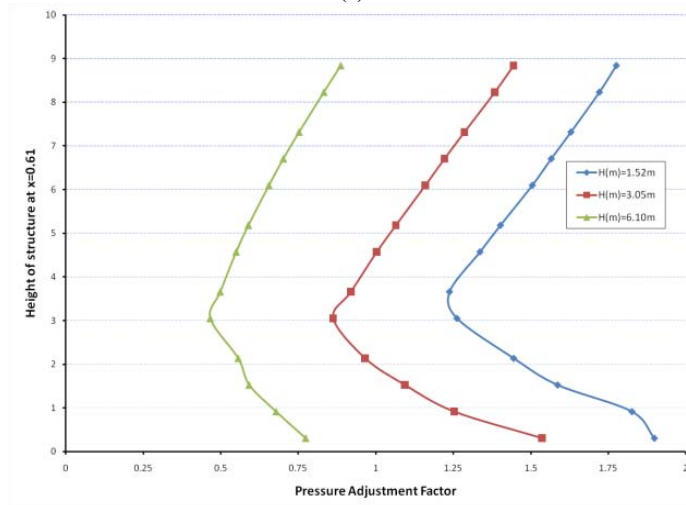
(b)
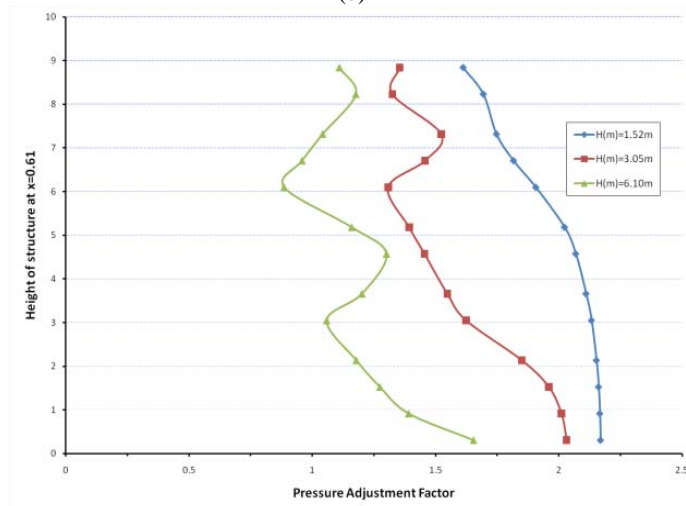
(c)

Figure B-10. Effect of Barrier Height on Pressure Factor, W = 22.68 kg-TNT, d_1 = 7.62 m, (a) Z = 10.67 m, (b) Z = 18.26 m, (c) Z = 30.44 m
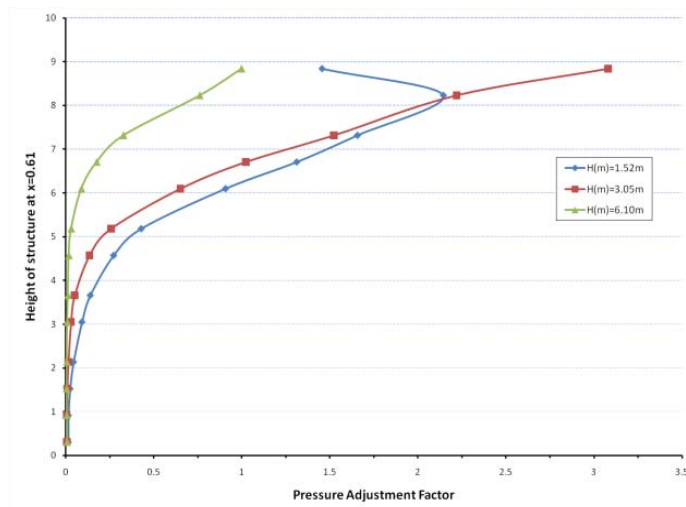
(a)
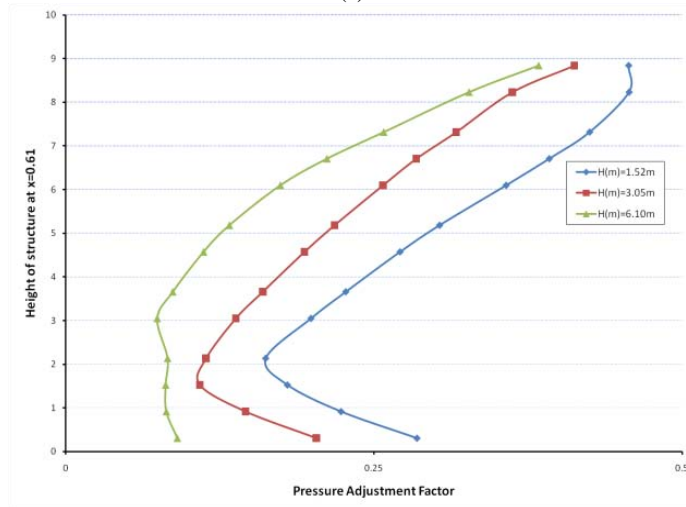
(b)
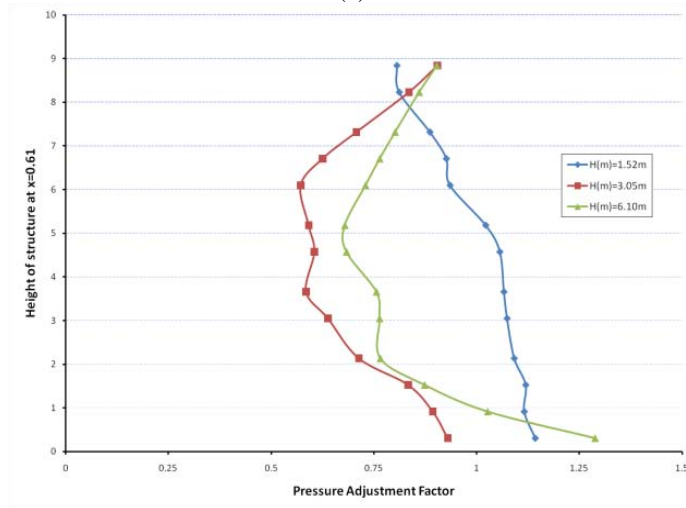
(c)

Figure B-11. Effect of Barrier Height on Pressure Factor, W = 245.47 kg-TNT, d_1 = 0.42 m, (a) Z = 3.46 m, (b) Z = 11.05 m, (c) Z = 23.23 m

123
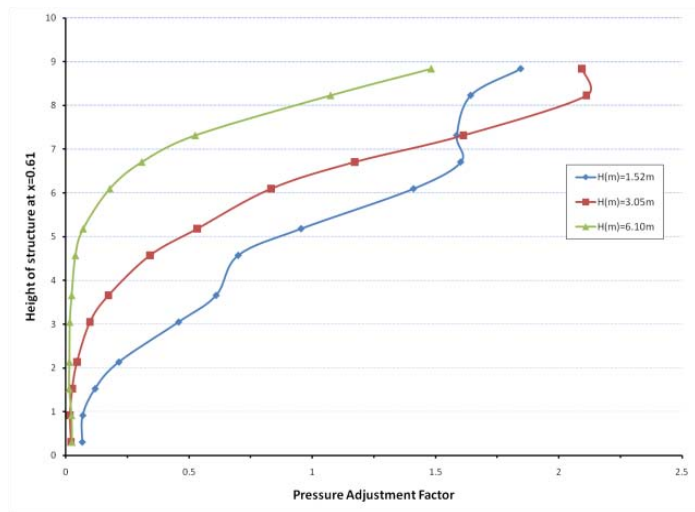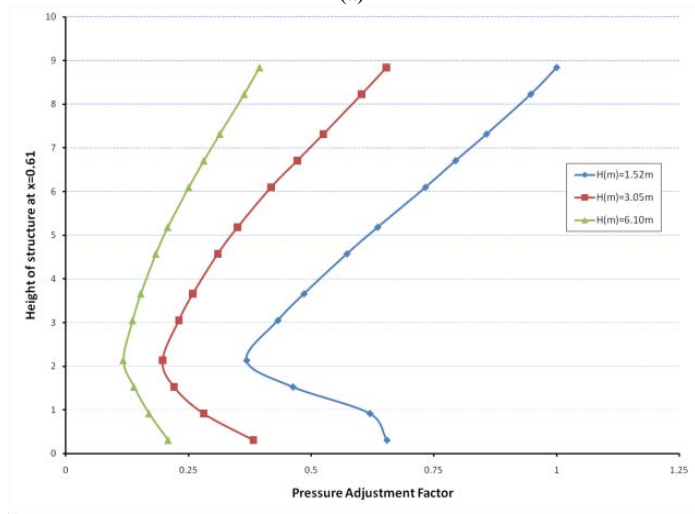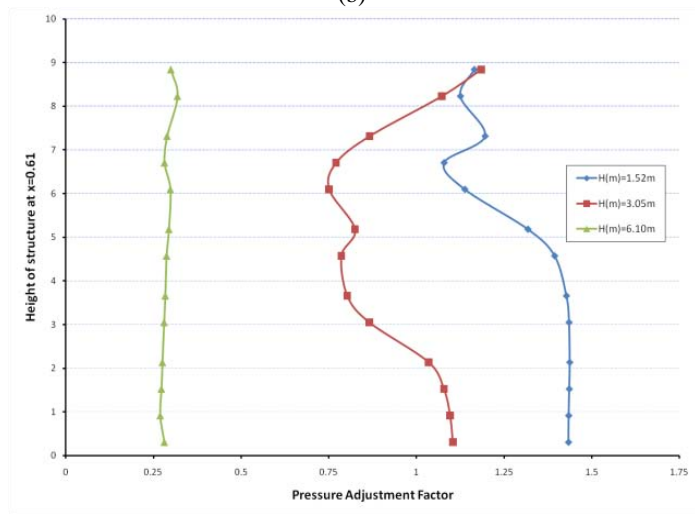
Figure B-12. Effect of Barrier Height on Pressure Factor, $W = 245.47$ kg-TNT, $d_1 = 1.91$ m, (a) $Z = 4.85$ m, (b) $Z = 12.54$ m, (c) $Z = 24.72$ m
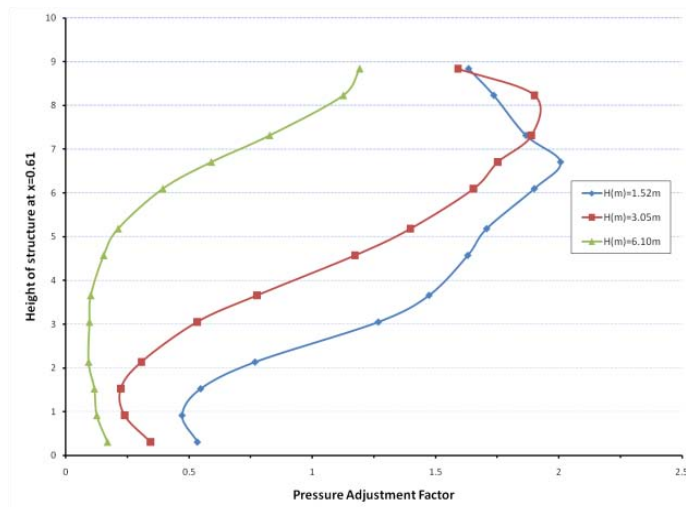
(a)
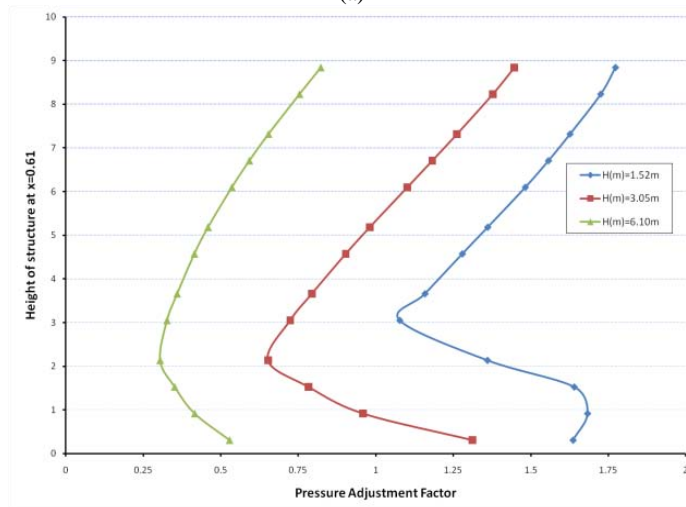
(b)
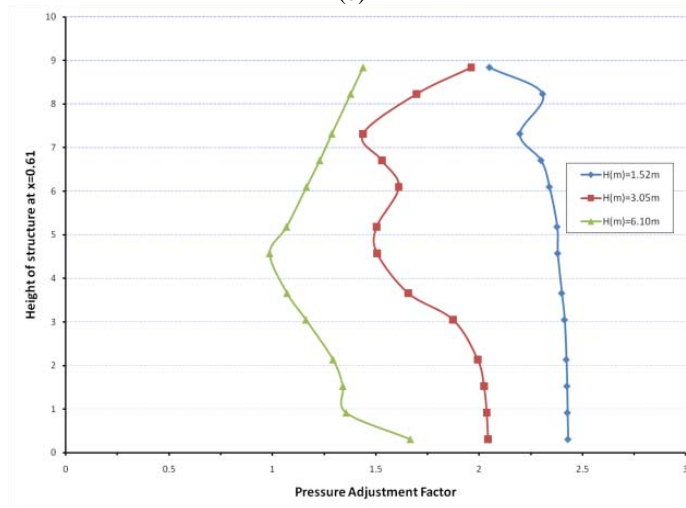
(c)

Figure B-13. Effect of Barrier Height on Pressure Factor, $W = 245.47$ kg-TNT, $d_1 = 7.62$ m, (a) $Z = 10.67$ m, (b) $Z = 18.26$ m, (c) $Z = 30.44$ m

125
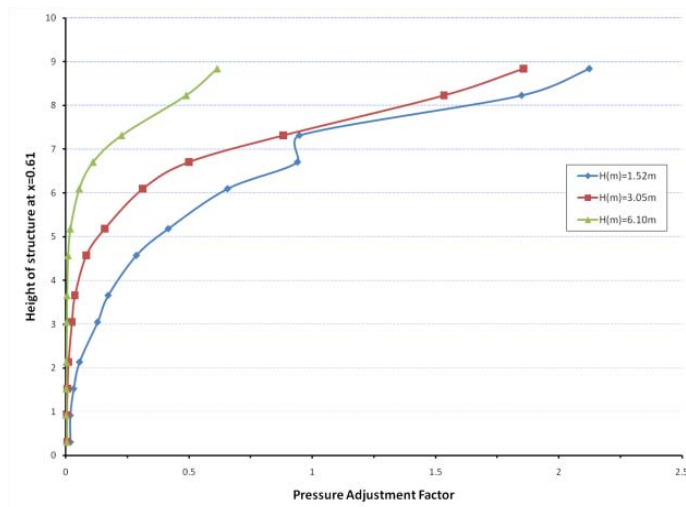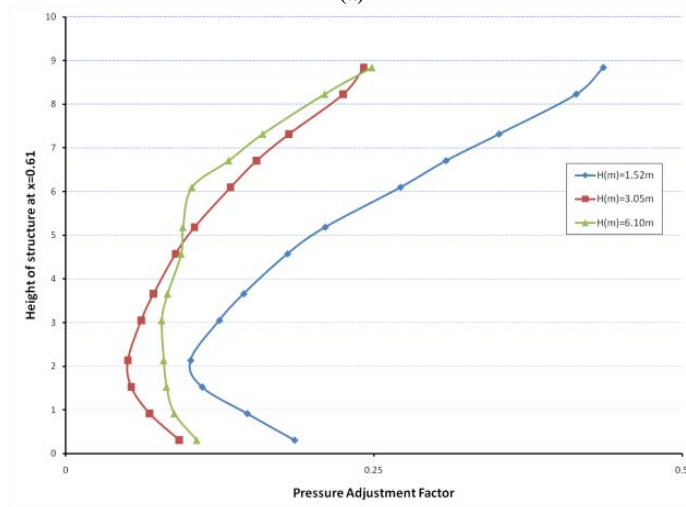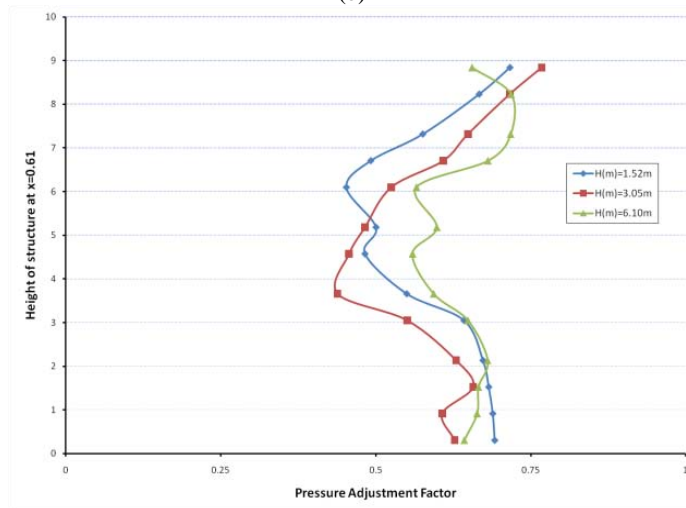
Figure B-14. Effect of Barrier Height on Pressure Factor, W = 910.42 kg-TNT, d_1 = 0.64 m, (a) Z = 3.84 m, (b) Z = 11.28 m, (c) Z = 23.46 m
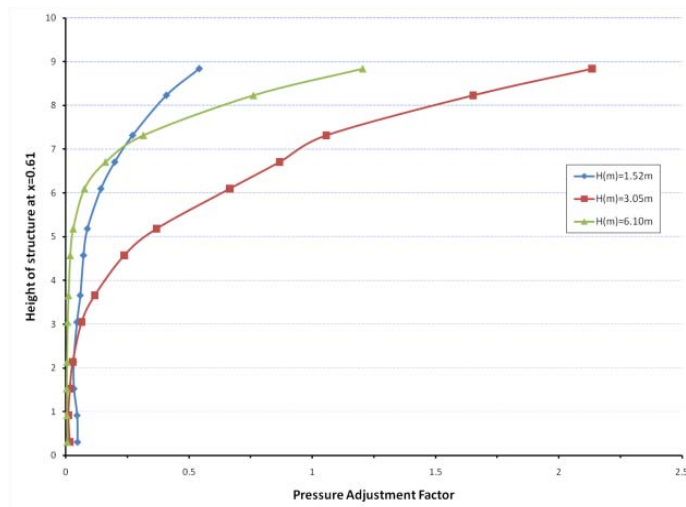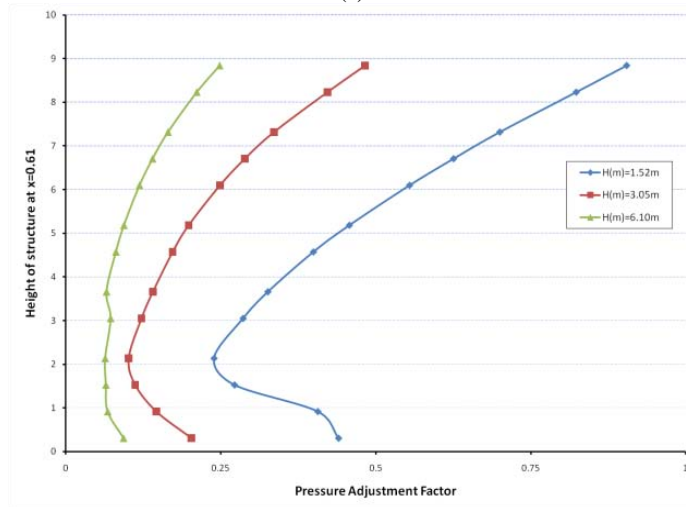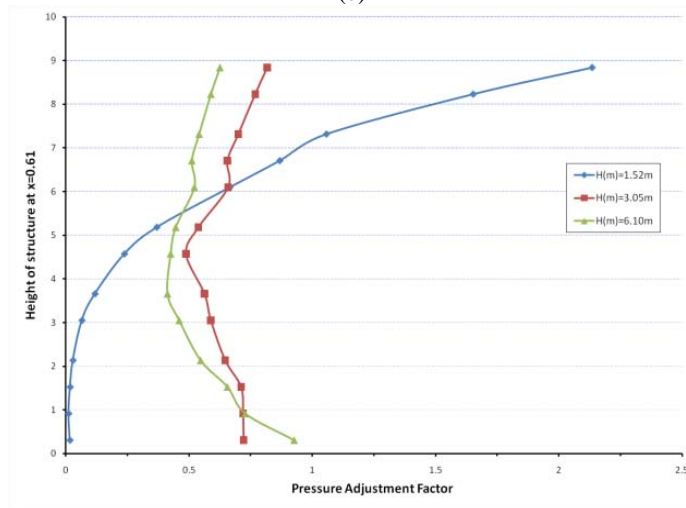
Figure B-15. Effect of Barrier Height on Pressure Factor, $W = 910.42$ kg-TNT, $d_1 = 1.91$ m, (a) $Z = 4.95$ m, (b) $Z = 12.54$ m, (c) $Z = 24.72$ m

127
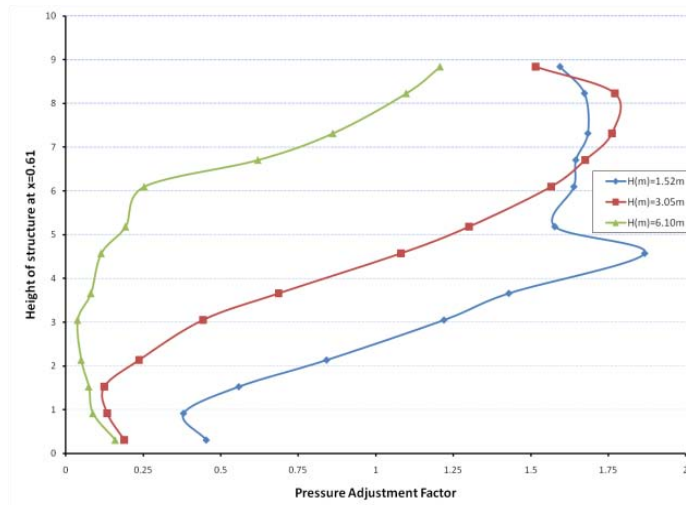
(a)
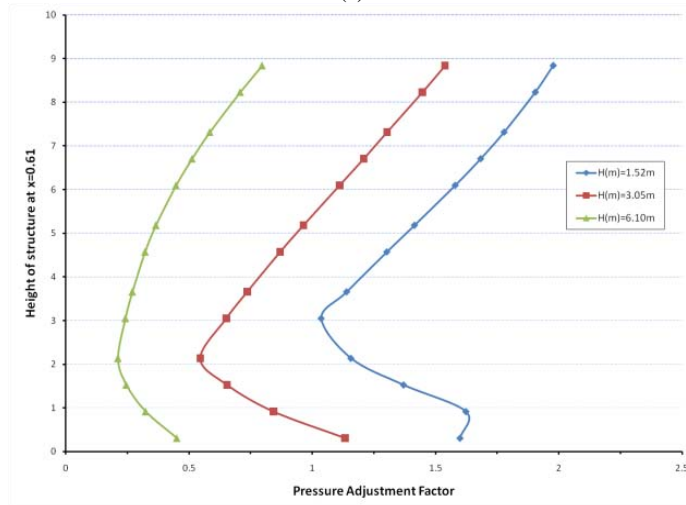
(b)
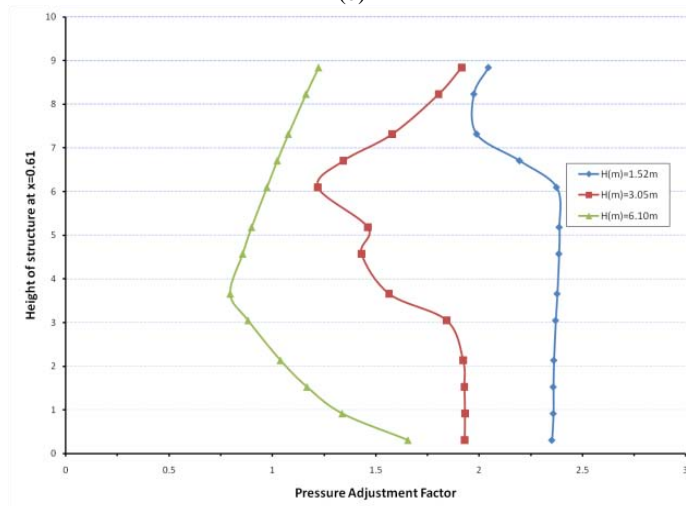
(c)

Figure B-16. Effect of Barrier Height on Pressure Factor, W = 910.42 kg-TNT, d_1 = 7.62 m, (a) Z = 10.67 m, (b) Z = 18.26 m, (c) Z = 30.44 m

128

B.3. Effect of Blast Barrier Height to Impulse Adjustment Factors along Vertical Centerline of Structure
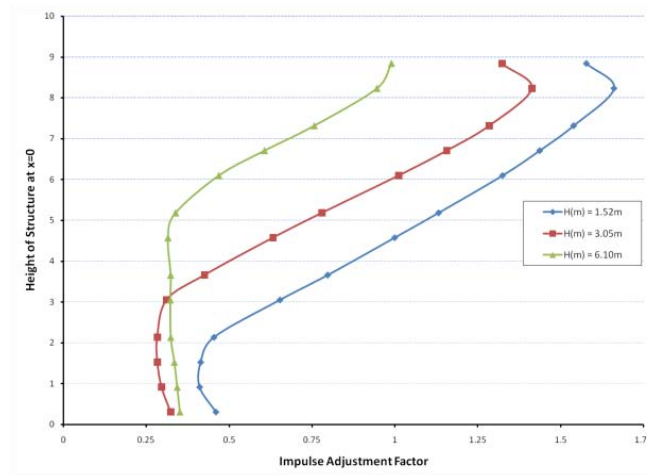
(a)
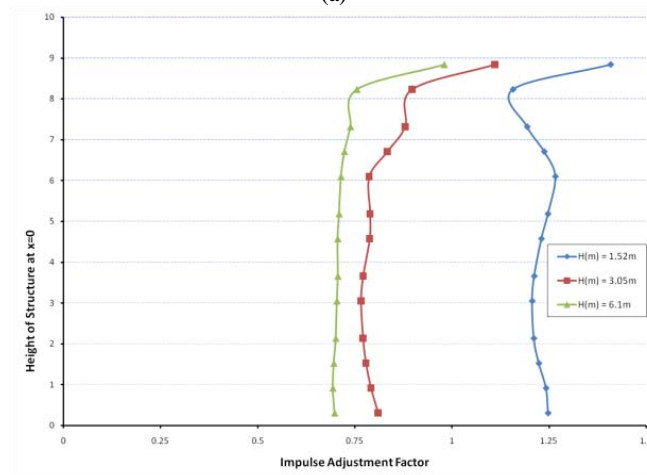
(b)
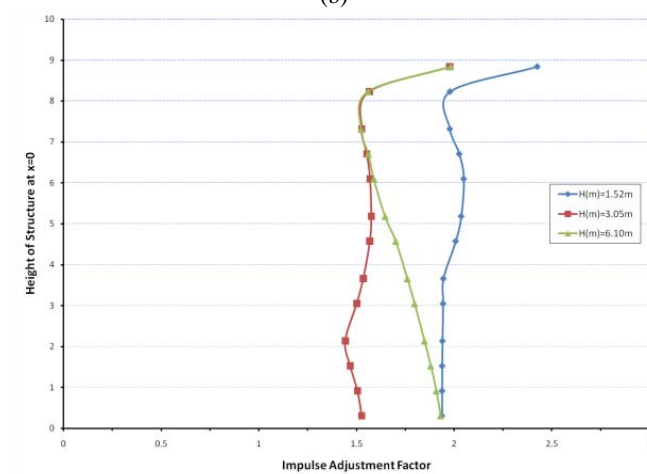
(c)

Figure B-17. Effect of Barrier Height and Building Standoff on Impulse Factor, *W* = 22.68 kg-TNT, *d₁* = 1.91 m, (a) *Z* = 4.95 m, (b) *Z* = 12.54 m, (c) *Z* = 24.72 m
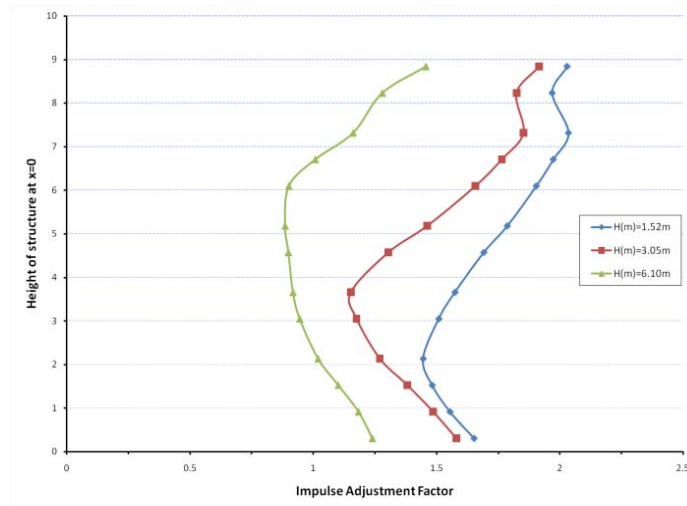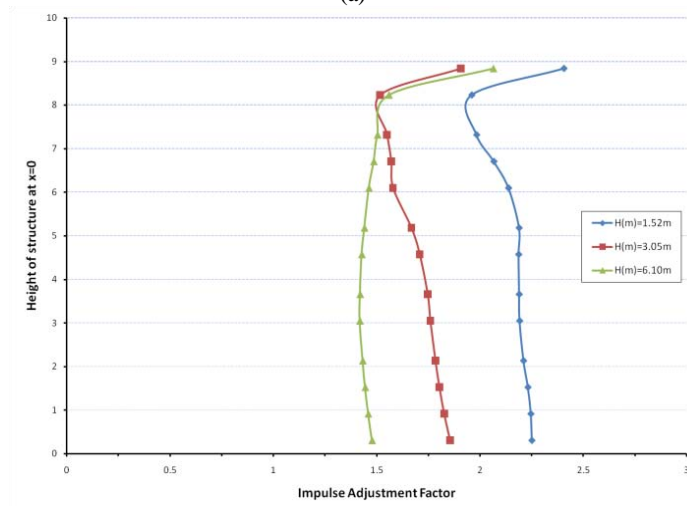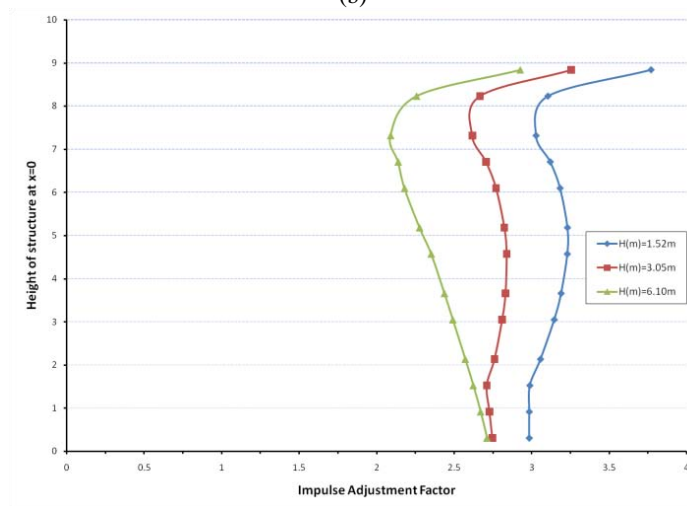
Figure B-18. Effect of Barrier Height and Building Standoff on Impulse Factor, $W = 22.68$ **kg-TNT,** $d_1 = 7.63$ **m, (a)** $Z = 10.67$ **m, (b)** $Z = 18.26$ **m, (c)** $Z = 30.44$ **m**

Distribution A. Approved for public release; distribution unlimited.
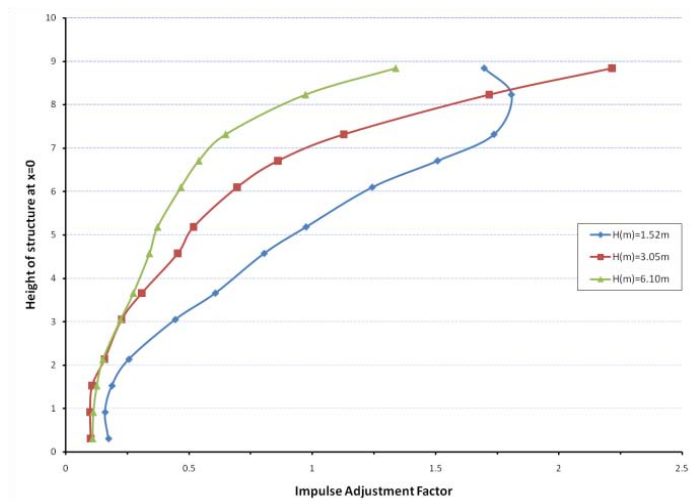
(a)
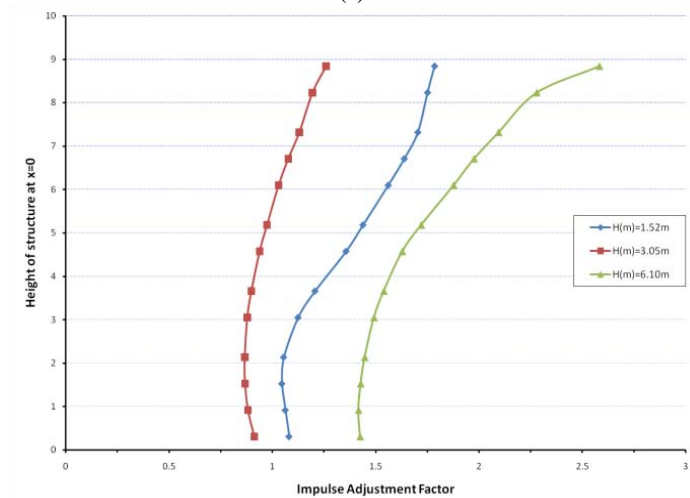
(b)
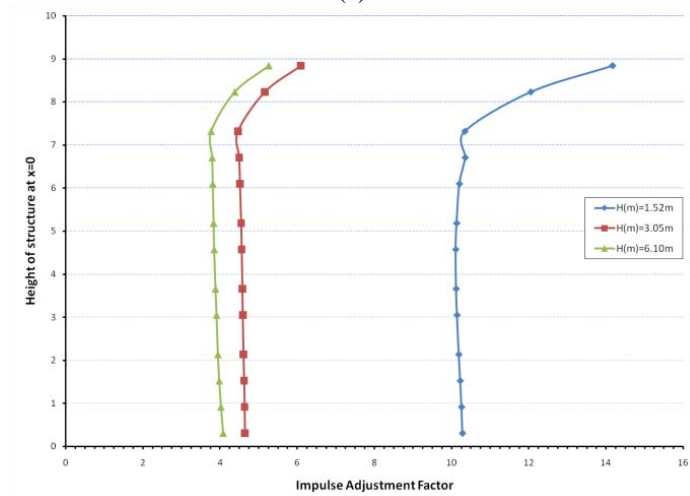
(c)

Figure B-19. Effect of Barrier Height and Building Standoff on Impulse Factor, *W* = 245.47 kg-TNT, *d₁* = Contact Charge, (a) *Z* = 3.46 m, (b) *Z* = 11.05 m, (c) *Z* = 23.23 m
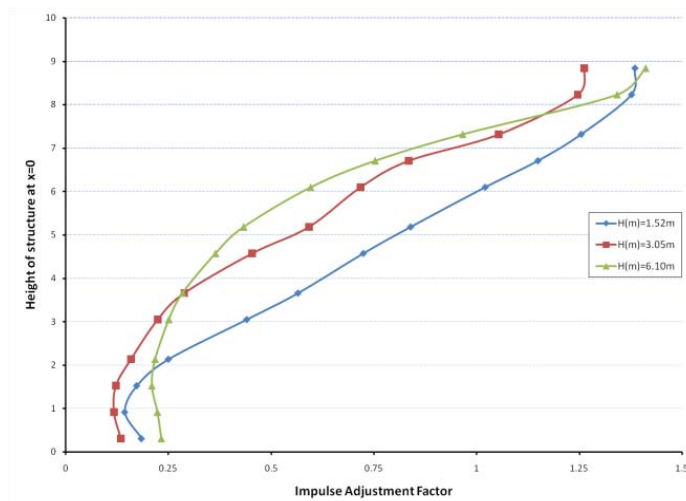
(a)
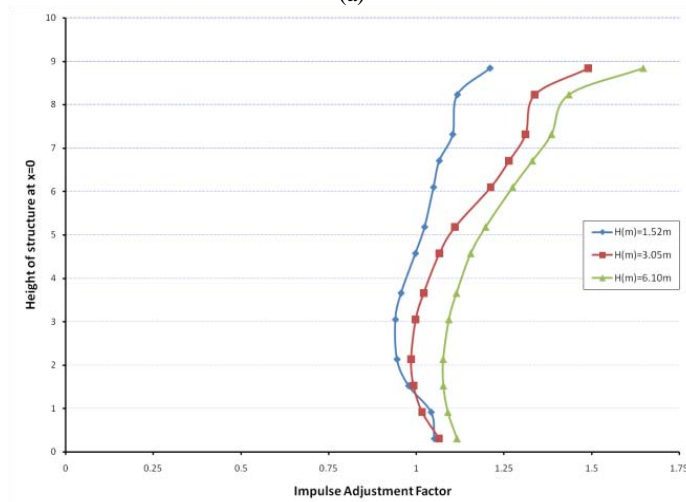
(b)
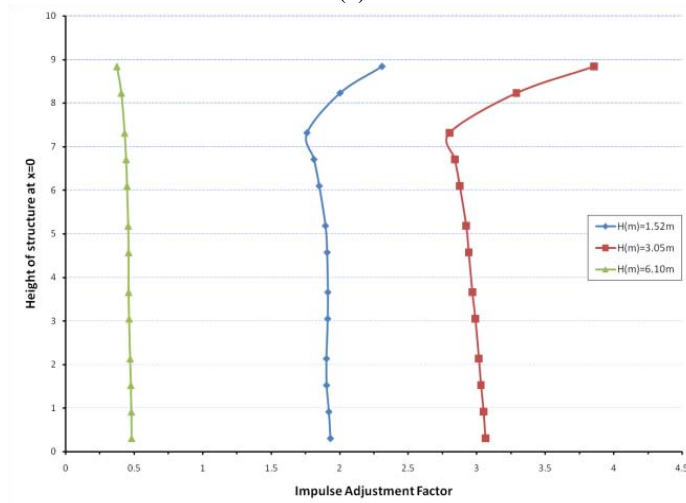
(c)

Figure B-20. Effect of Barrier Height and Building Standoff on Impulse Factor, $W =$ **245.47 kg-TNT,** $d_1 = 1.91$ **m, (a)** $Z = 4.95$ **m, (b)** $Z = 12.544$**m, (c)** $Z = 24.72$ **m**
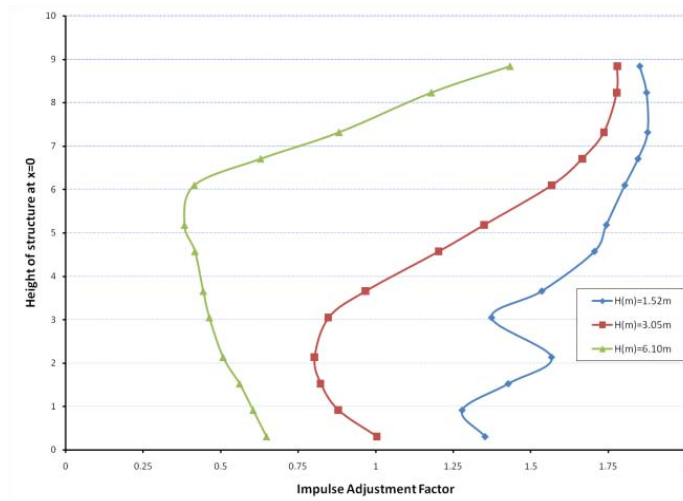
(a)
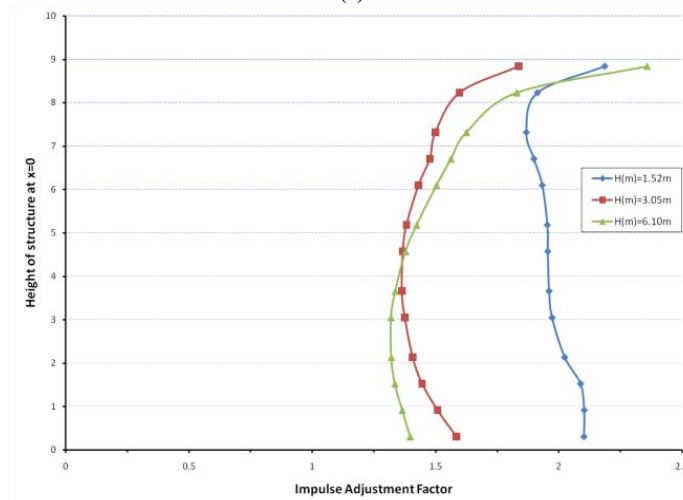
(b)
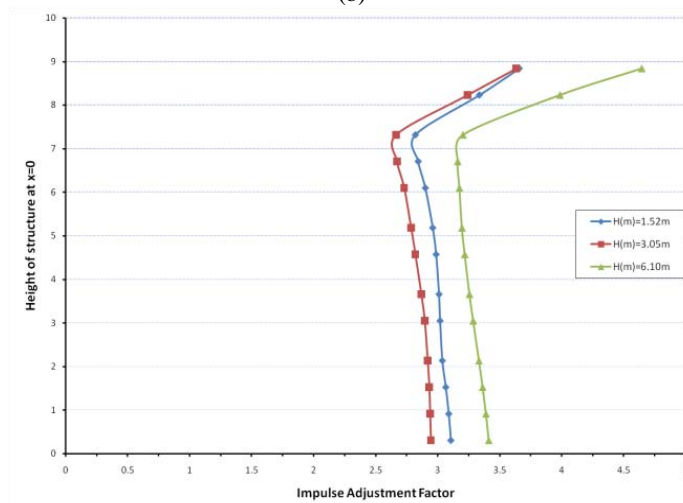
(c)

Figure B-21. Effect of Barrier Height and Building Standoff on Impulse Factor, $W =$ **245.47 kg-TNT,** $d_1 = 7.62$ **m, (a)** $Z = 10.67$ **m, (b)** $Z = 18.26$ **m, (c)** $Z = 30.44$ **m**
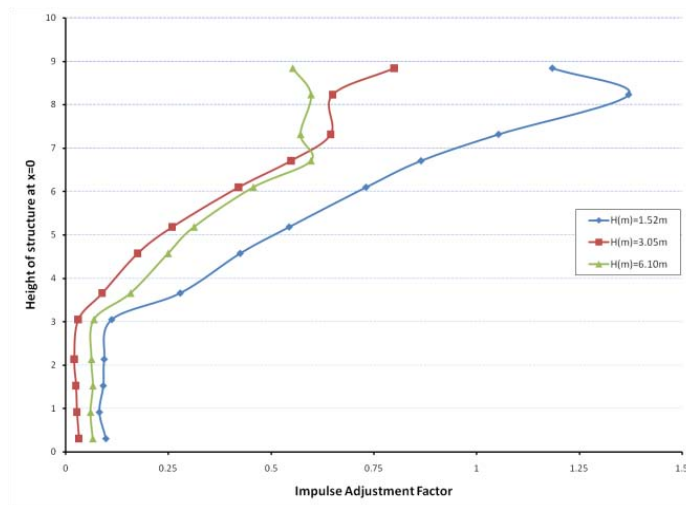
(a)
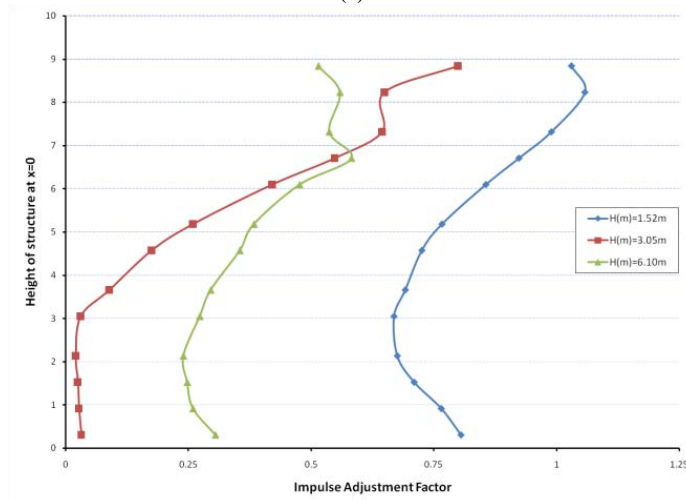
(b)
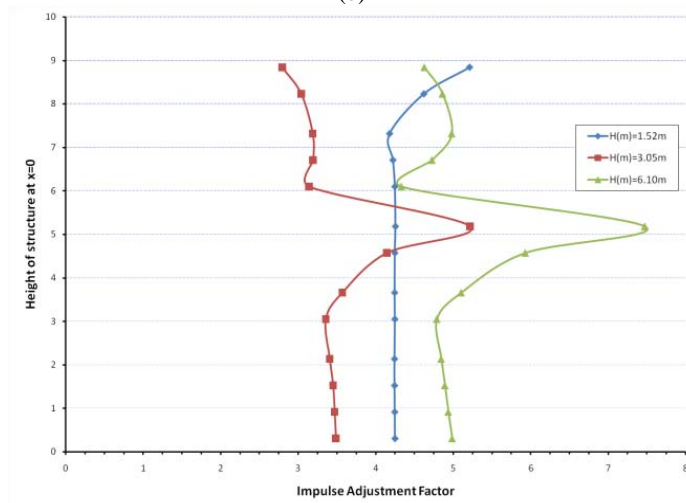
(c)

Figure B-22. Effect of Barrier Height and Building Standoff on Impulse Factor, $W =$ **910.42 kg-TNT,** $d_1 =$ **Contact Charge, (a)** $Z = 3.84$ **m, (b)** $Z = 11.28$ **m, (c)** $Z = 23.46$ **m**
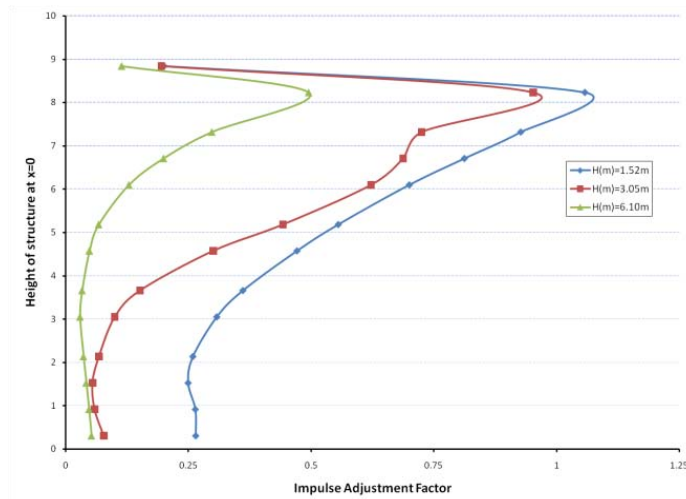
(a)
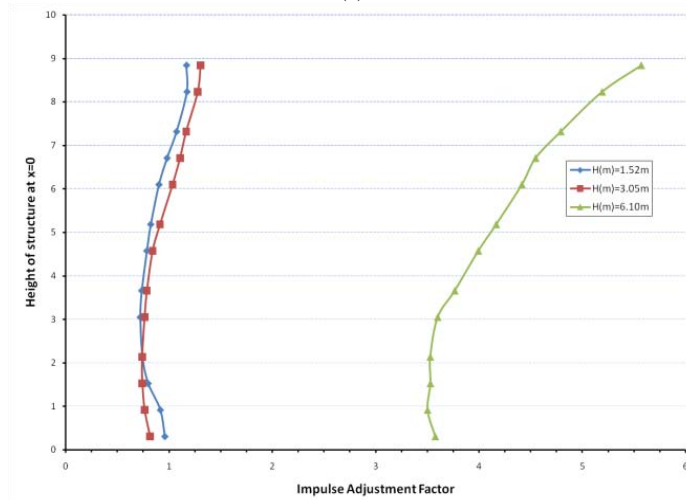
(b)
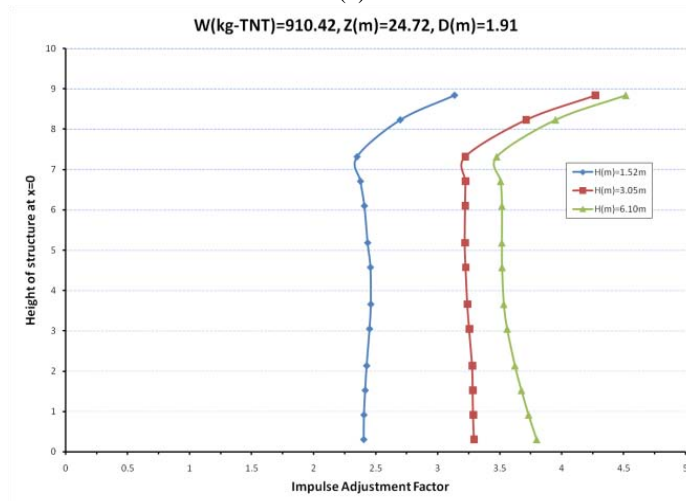
(c)

Figure B-23. Effect of Barrier Height and Building Standoff on Impulse Factor, $W = 910.42$ kg-TNT, $d_1 = 1.91$ m, (a) $Z = 4.95$ m, (b) $Z = 12.54$ m, (c) $Z = 24.72$ m

135
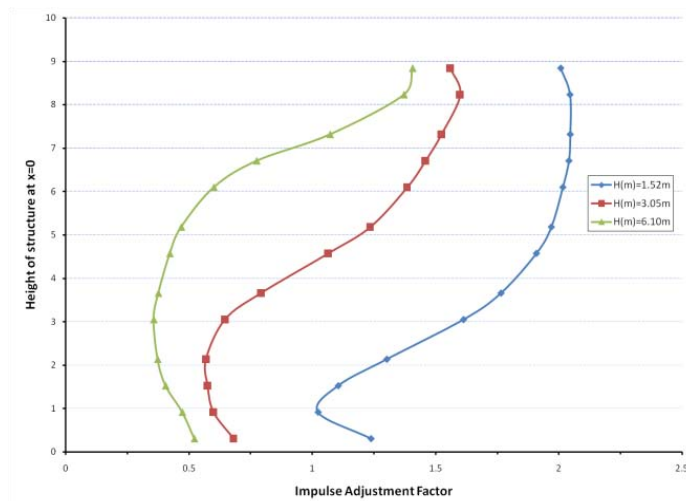
(a)
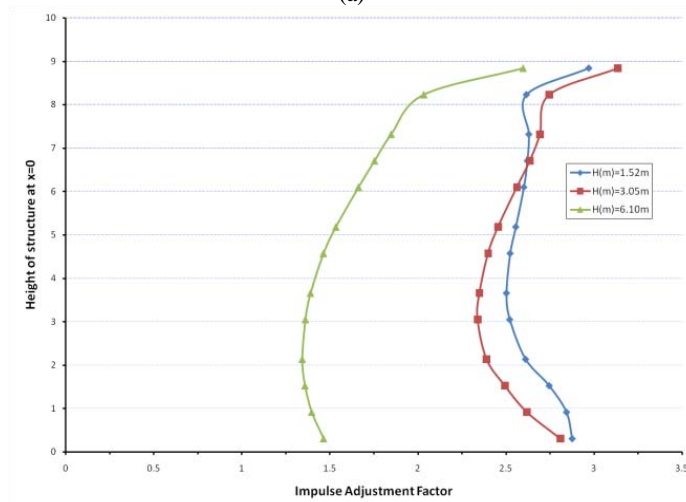
(b)
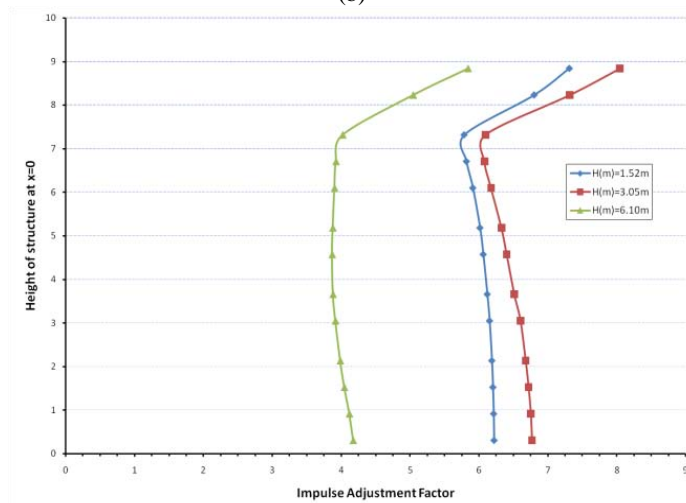
(c)

Figure B-24. Effect of Barrier Height and Building Standoff on Impulse Factor, $W =$ 910.42 kg-TNT, $d_1 = 7.62$ m, (a) $Z = 10.67$ m, (b) $Z = 18.26$ m, (c) $Z = 30.44$ m

B.4. Effect Blast Barrier Height to Pressure Adjustment Factors along Vertical Line 0.61 m from Center of Structure
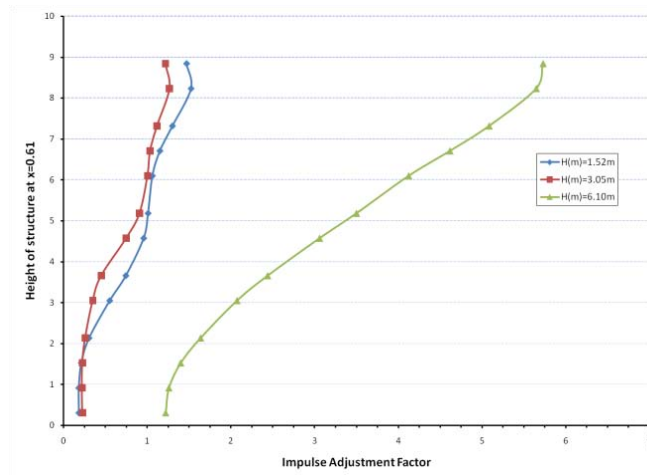
(a)
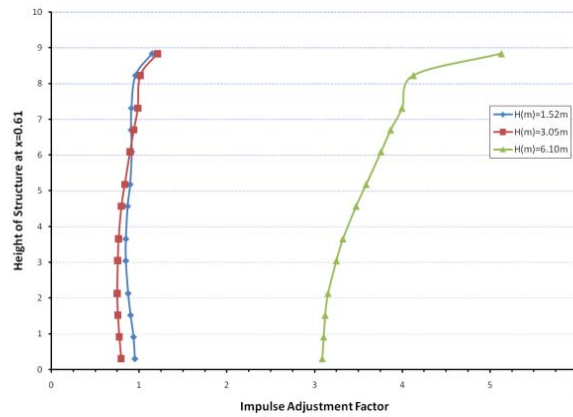
(b)
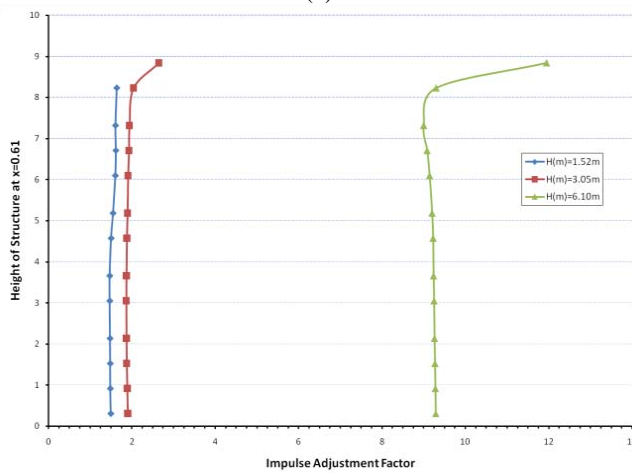
(c)

Figure B-25. Effect of Barrier Height and Building Standoff on Impulse Factor 0.61 m off Vertical Centerline of Structure, W = 22.68 kg-TNT, d_1 = 0.19 m, (a) Z = 3.24 m, (b) Z = 12.54 m, (c) Z = 24.72 m
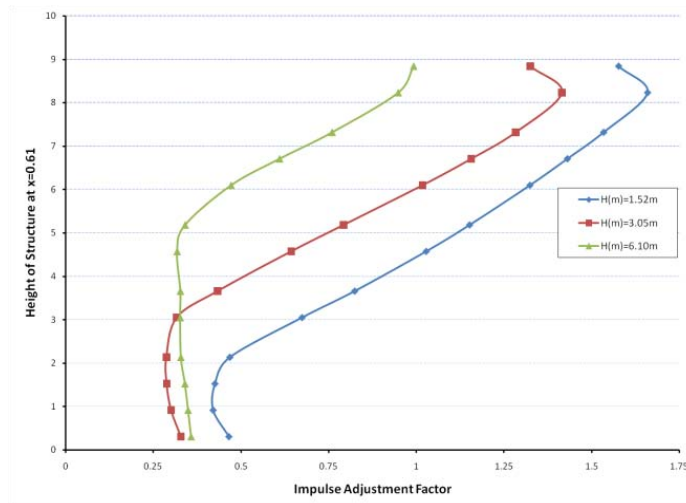
(a)
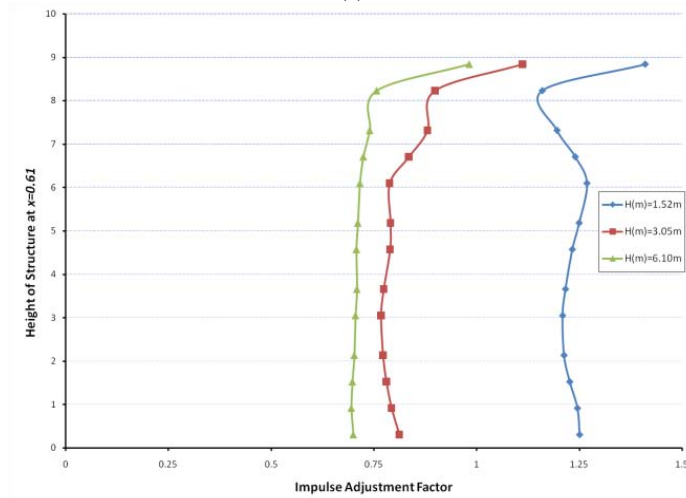
(b)
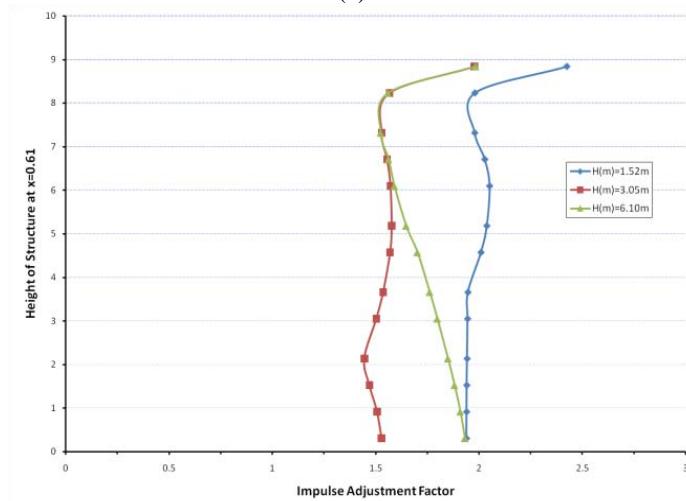
(c)

Figure B-26. Effect of Barrier Height and Building Standoff on Impulse Factor 0.61 m off Vertical Centerline of Structure, W = 22.68 kg-TNT, d_1 = 1.91 m, (a) Z = 4.95 m, (b) Z = 12.54 m, (c) Z = 24.72 m

138
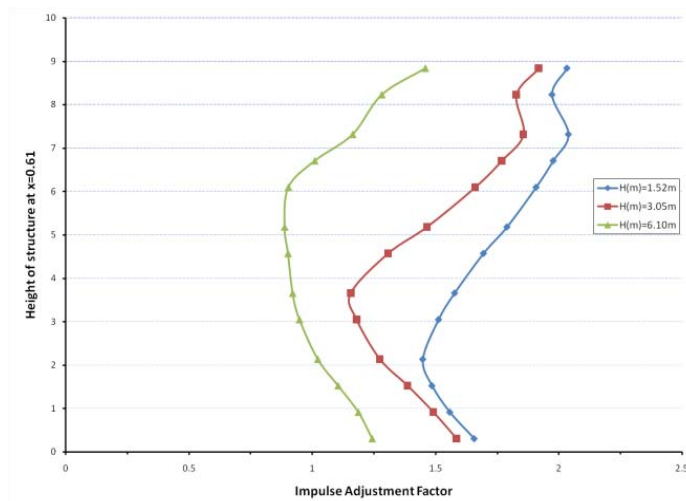
(a)
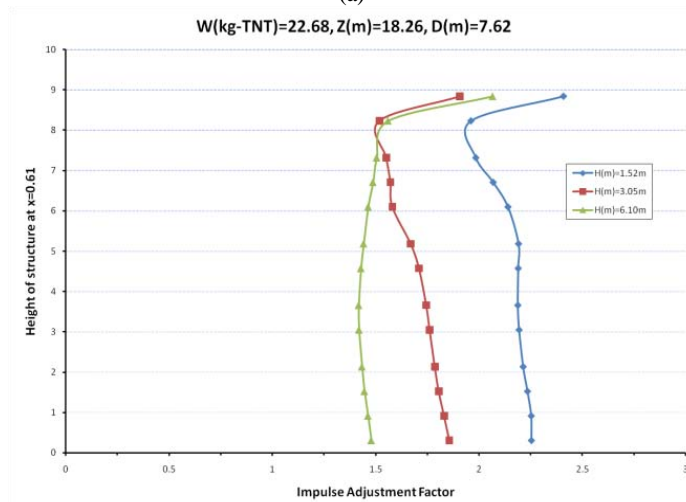
(b)
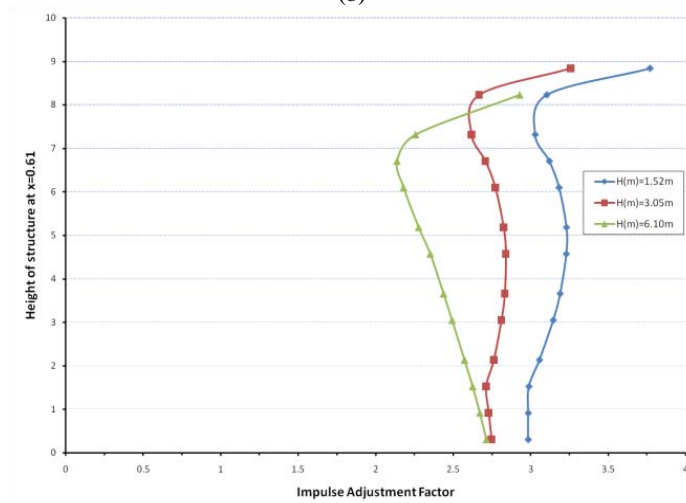
(c)

Figure B-27. Effect of Barrier Height and Building Standoff on Impulse Factor 0.61 m off of Vertical Centerline of Structure, W = 22.68 kg-TNT, d_1 = 7.62 m, (a) Z = 10.67 m, (b) Z = 18.26 m, (c) Z = 30.44 m

139
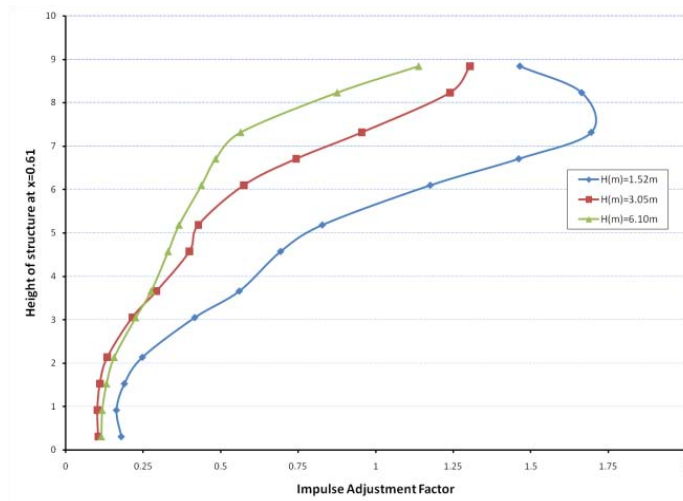
(a)
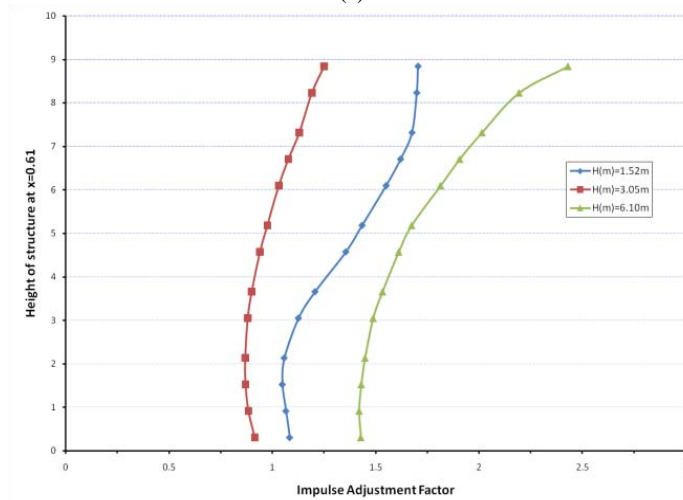
(b)
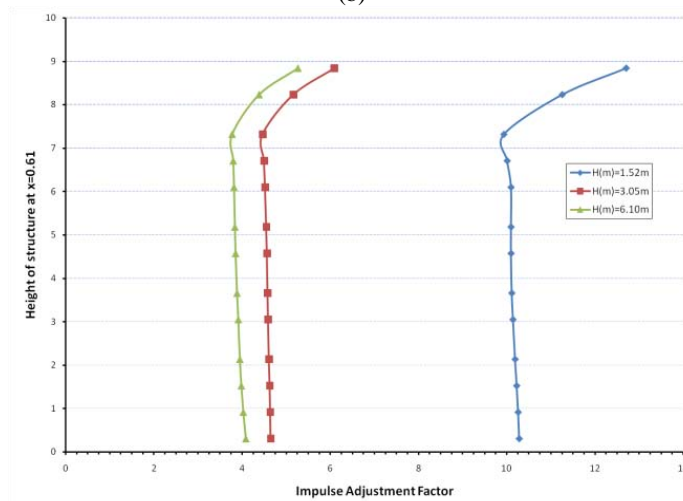
(c)

Figure B-28. Effect of Barrier Height and Building Standoff on Impulse Factor 0.61 m off Vertical Centerline of Structure, W = 245.47 kg-TNT, d_1 = 0.42 m, (a) Z = 3.46 m, (b) Z = 11.05 m, (c) Z = 23.23 m

140
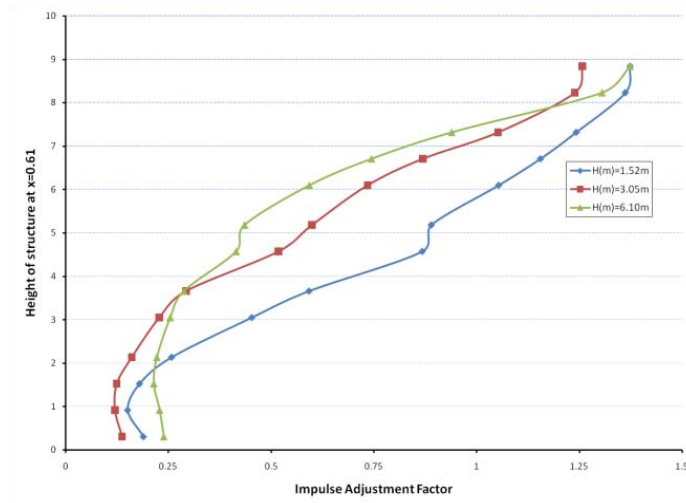
(a)
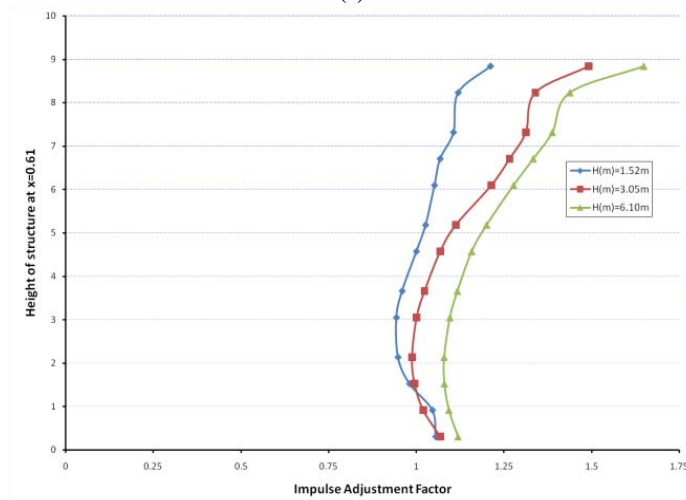
(b)
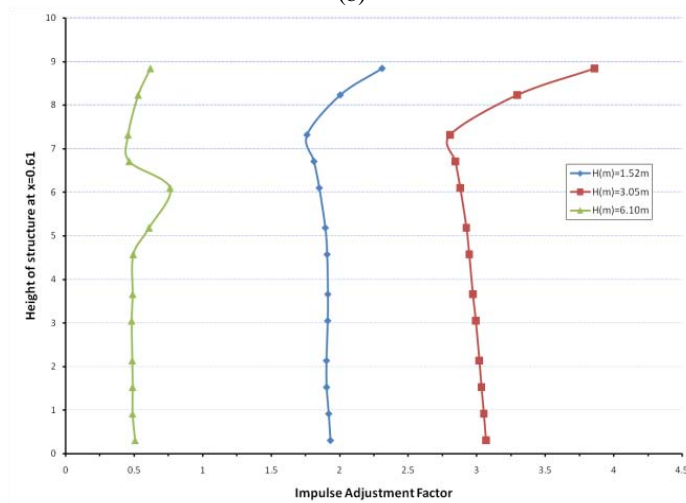
(c)

Figure B-29. Effect of Barrier Height and Building Standoff on Impulse Factor 0.61 m off Vertical Centerline of Structure, W = 245.47 kg-TNT, d_1 = 1.91 m, (a) Z = 4.95 m, (b) Z = 12.54 m, (c) Z = 24.72 m
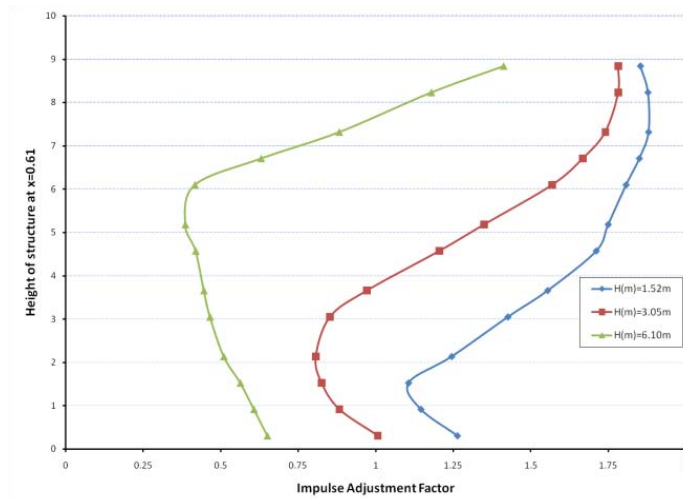
(a)
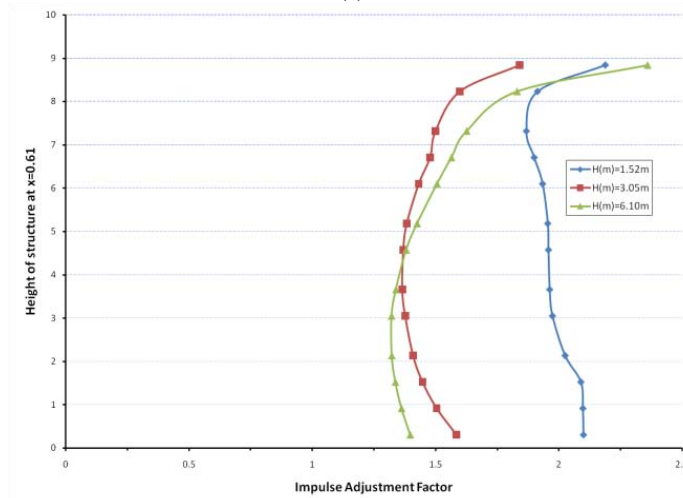
(b)
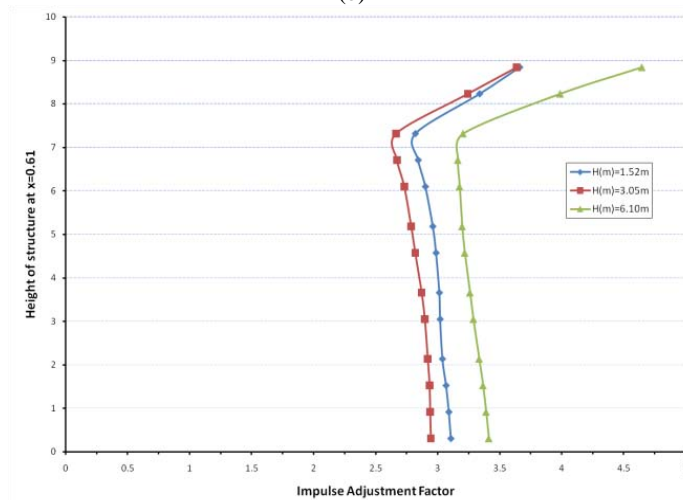
(c)

Figure B-30. Effect of Barrier Height and Building Standoff on Impulse Factor 0.61 m off Vertical Centerline of Structure, $W = 245.47$ kg-TNT, $d_1 = 7.62$ m, (a) $Z = 10.67$ m, (b) $Z = 18.26$ m, (c) $Z = 30.44$ m

142
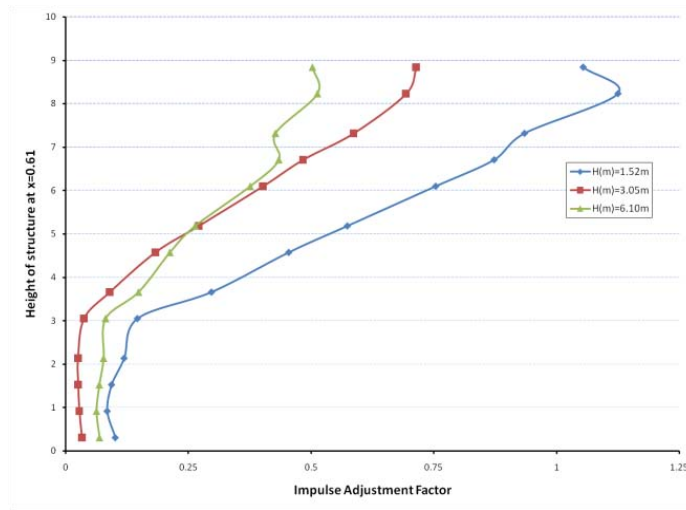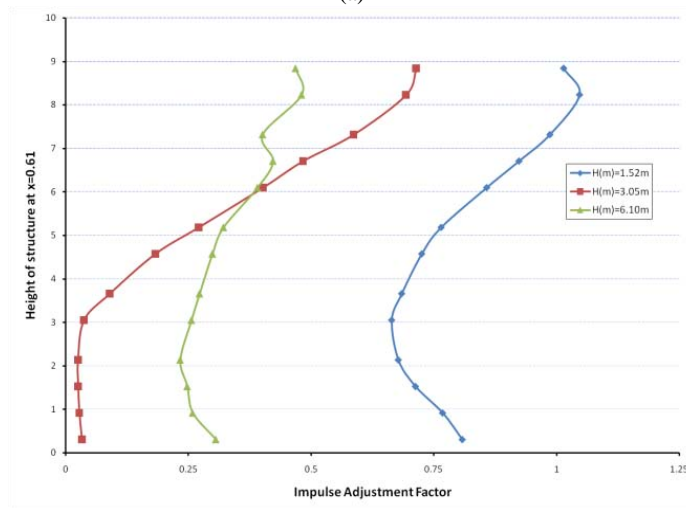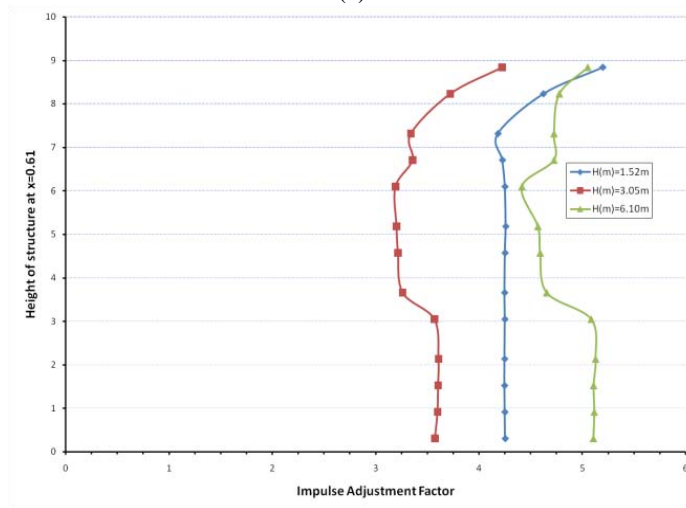
Figure B-31. Effect of Barrier Height on Impulse Factor, $W = 910.42$ kg-TNT, $d_1 = 0.64$ m, (a) $Z = 3.84$ m, (b) $Z = 11.28$ m, (c) $Z = 23.46$ m
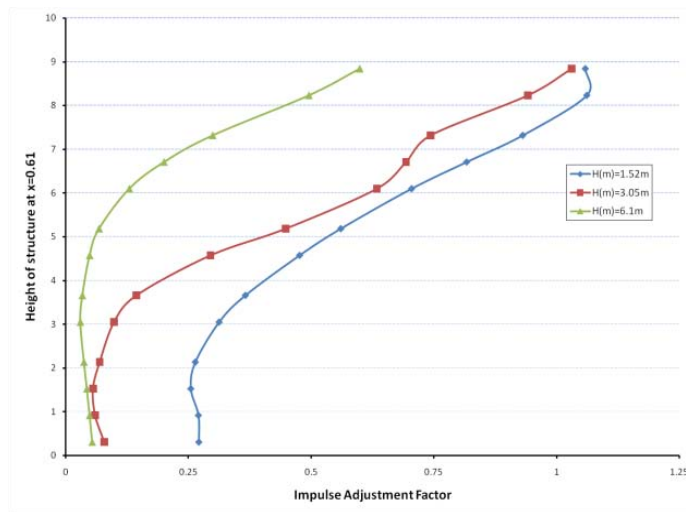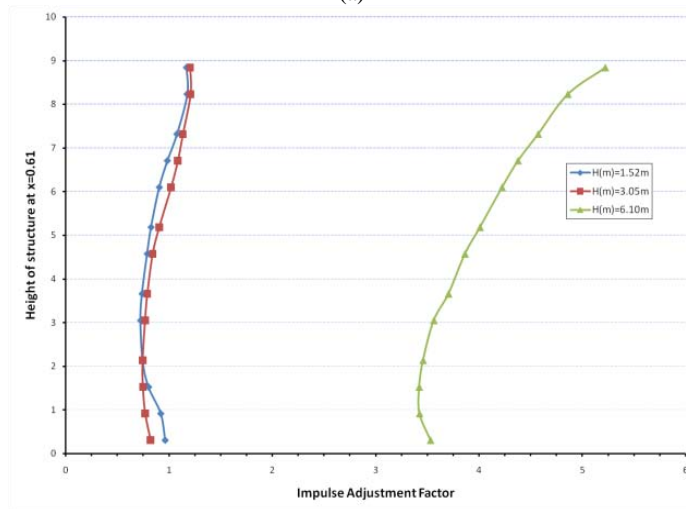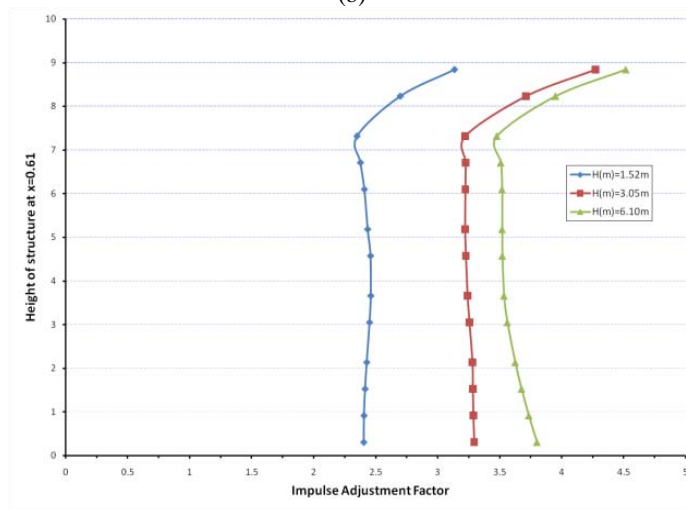
Figure B-32. Effect of Barrier Height on Impulse Factor, W = 910.42 kg-TNT, d_1 = 1.91 m, (a) Z = 4.95 m, (b) Z = 12.54 m, (c) Z = 24.72 m

Distribution A. Approved for public release; distribution unlimited.
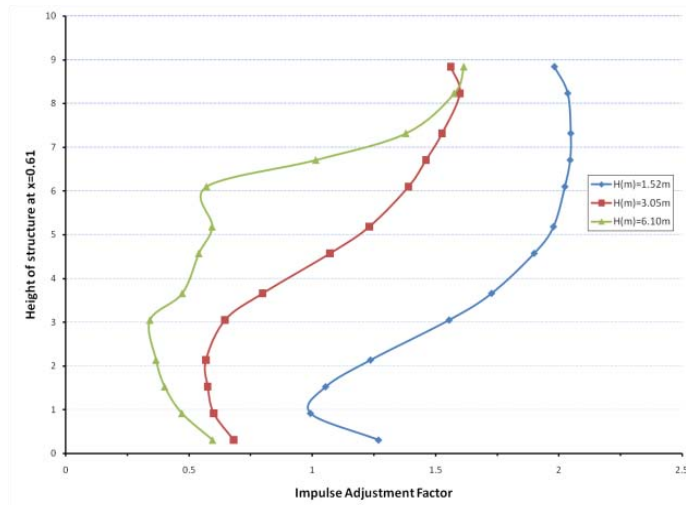
(a)
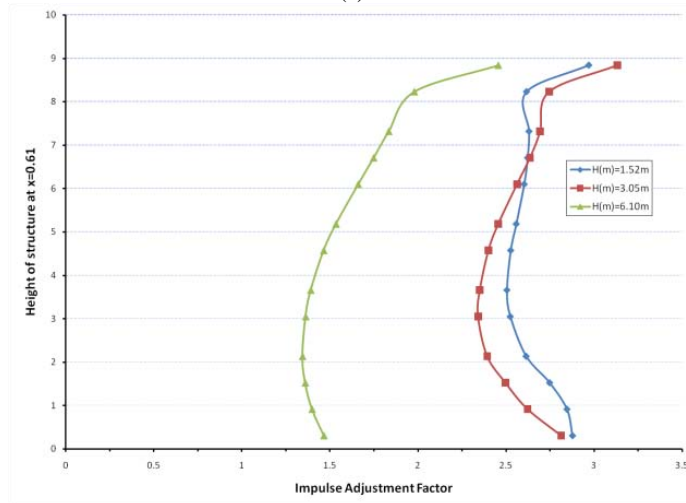
(b)
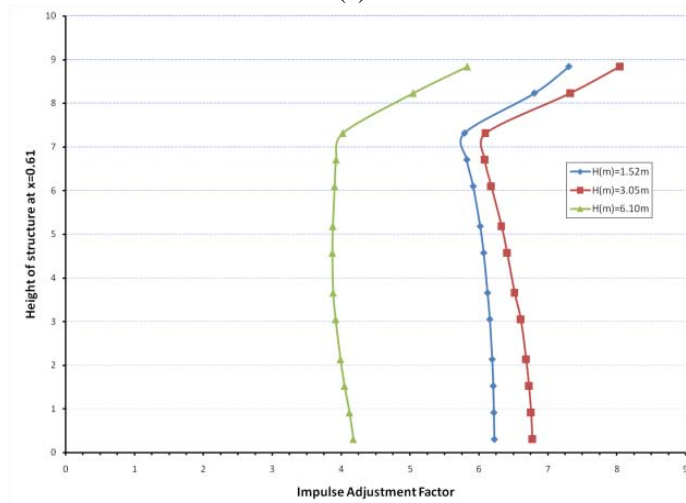
(c)

Figure B-33. Effect of Barrier Height on Impulse Factor, $W = 910.42$ kg-TNT, $d_1 = 7.62$ m, (a) $Z = 10.67$ m, (b) $Z = 18.26$ m, (c) $Z = 30.44$ m

B.5. Effect of Barrier-Structure Standoff to Pressure Adjustment Factors along Vertical Centerline of Structure
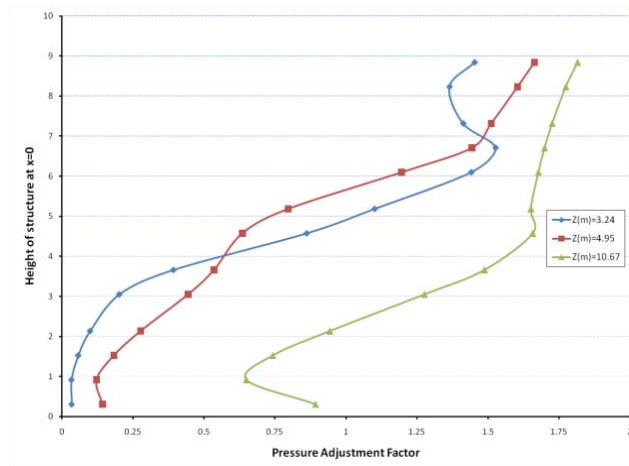

(a)
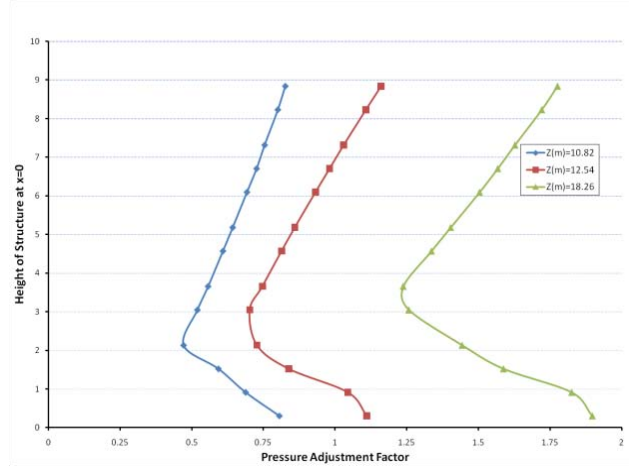
(b)
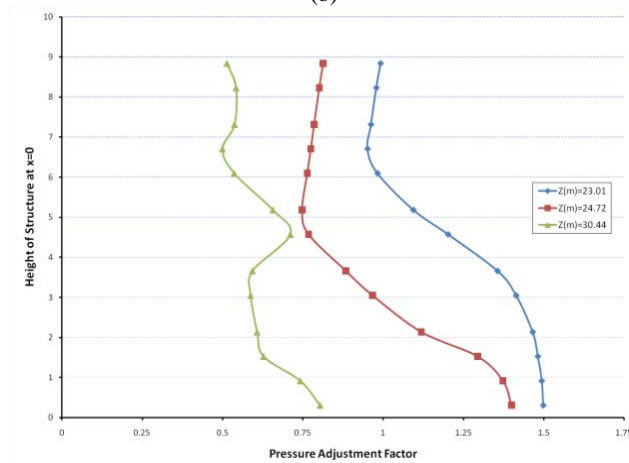
(c)

Figure B-34. Effect of Distance from Barrier to Structure, $W = 22.68$ kg-TNT, $H = 1.52$ m, (a) $d_2 = 3.05$ m, (b) $d_2 = 10.64$ m, (c) $d_2 = 22.82$ m
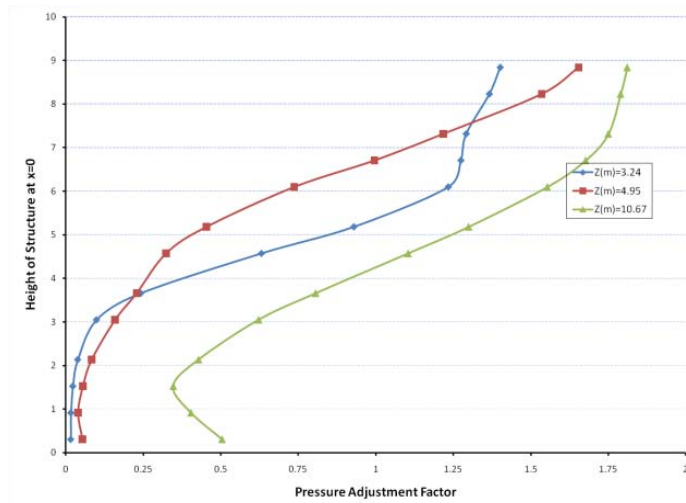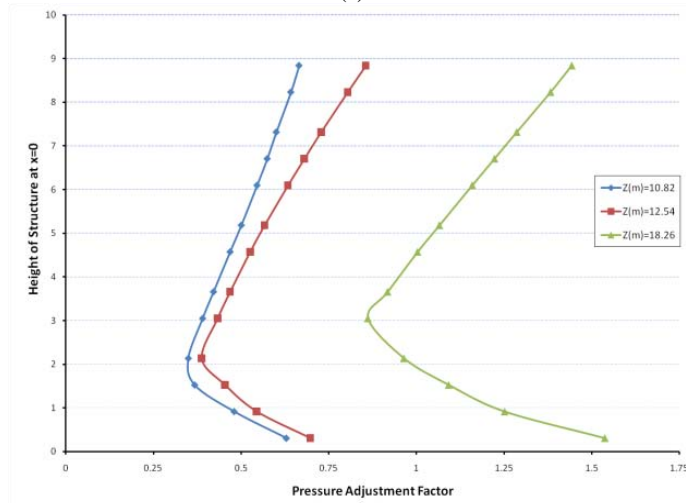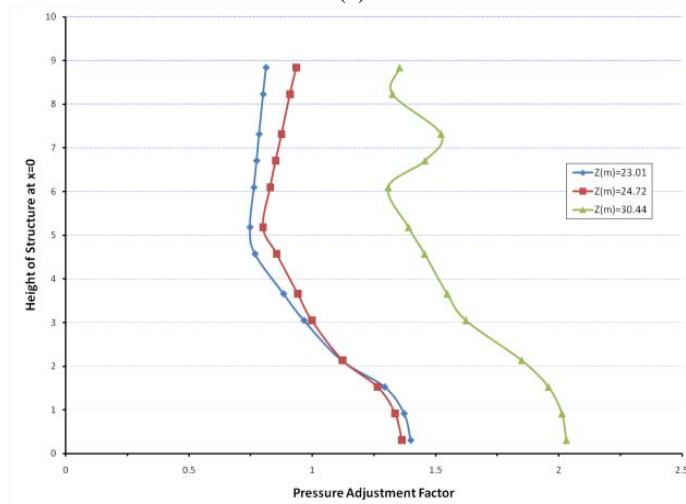
Figure B-35. Effect of Distance from Barrier to Structure, W = 22.68 kg-TNT, H = 3.05 m, (a) d_2 = 3.05 m, (b) d_2 = 10.64 m, (c) d_2 = 22.82 m
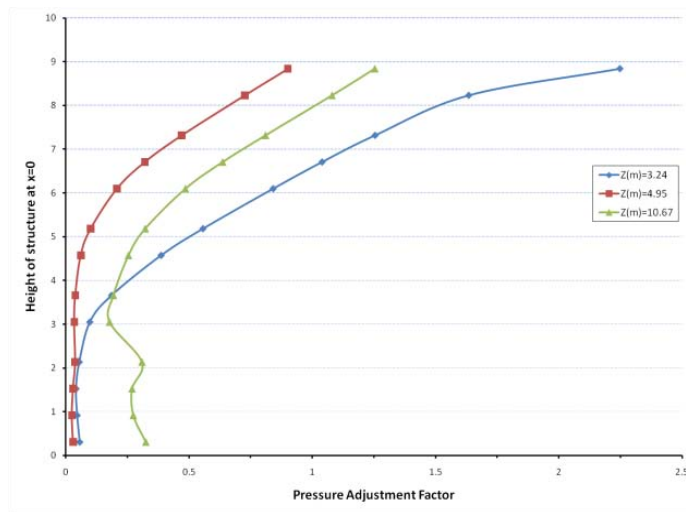
(a)
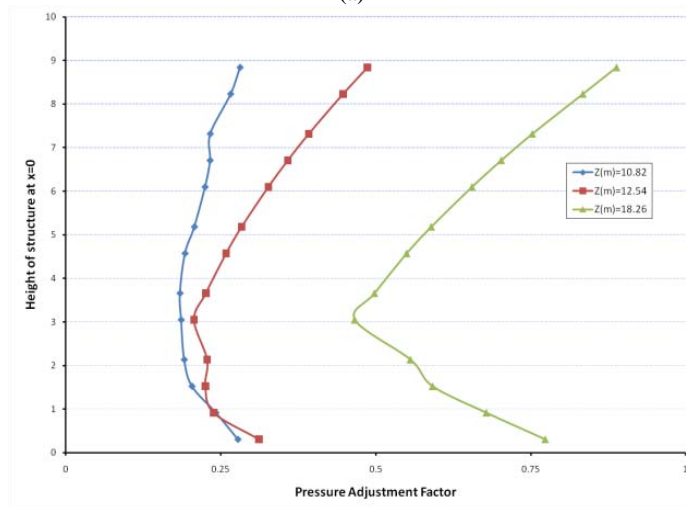
(b)
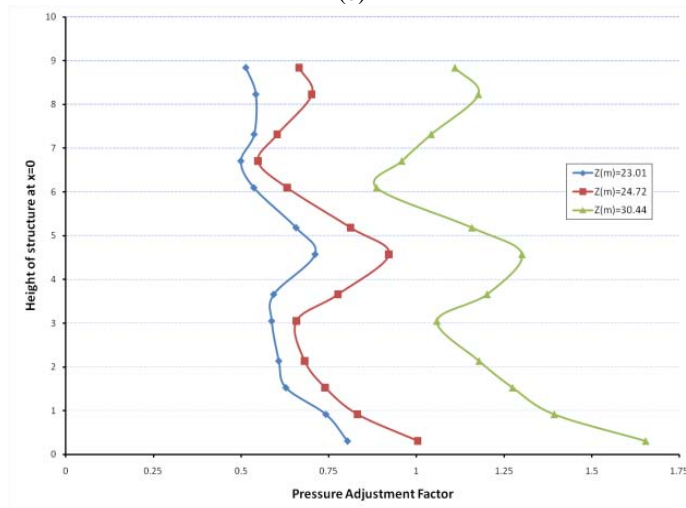
(c)

Figure B-36. Effect of Distance from Barrier to Structure, W = 22.68 kg-TNT, H = 6.10 m, (a) d_2 = 3.05 m, (b) d_2 = 10.64 m, (c) d_2 = 22.82 m
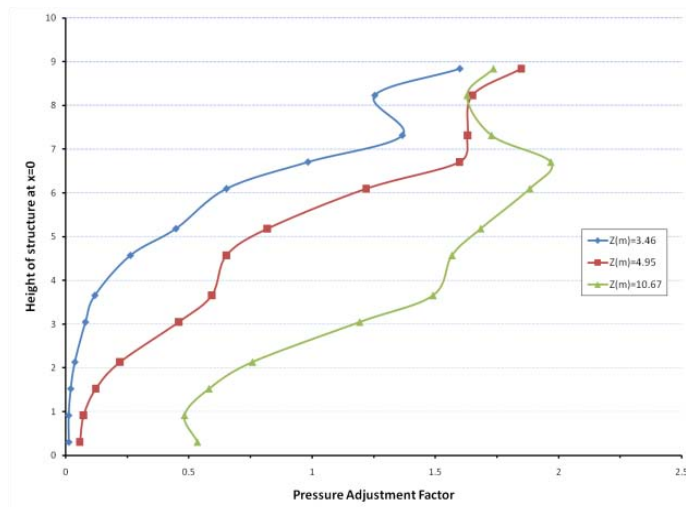
(a)
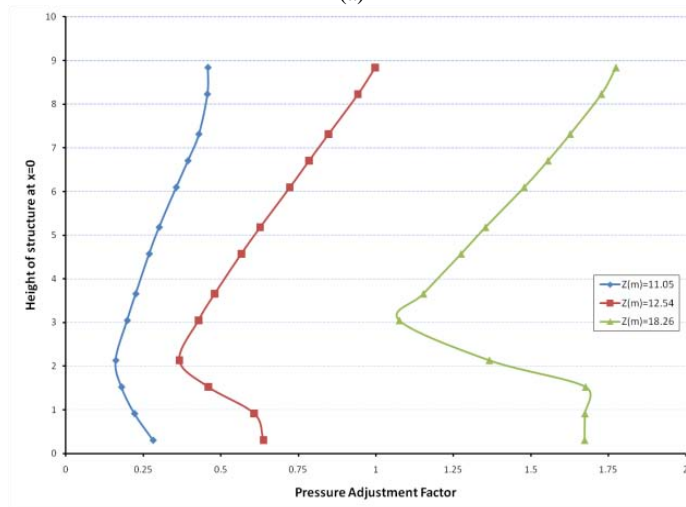
(b)
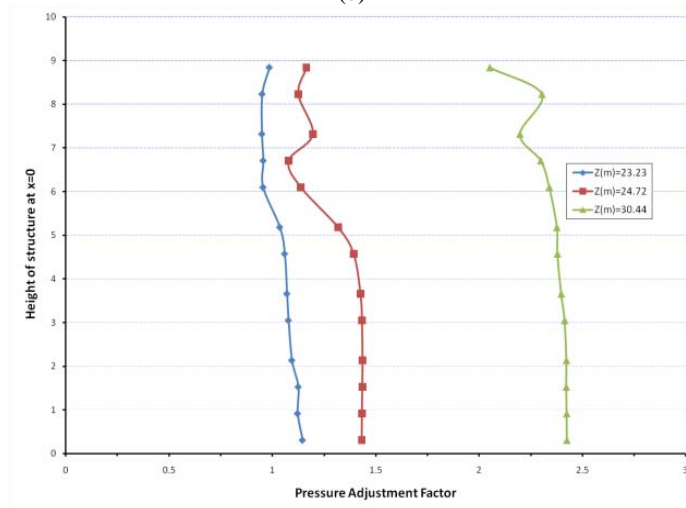
(c)

**Figure B-37. Effect of Distance from Barrier to Structure, W = 245.47 kg-TNT, H = 1.52 m, (a) d_2 = 3.05 m, (b) d_2 = 10.64 m, (c) d_2 = 22.82 m**
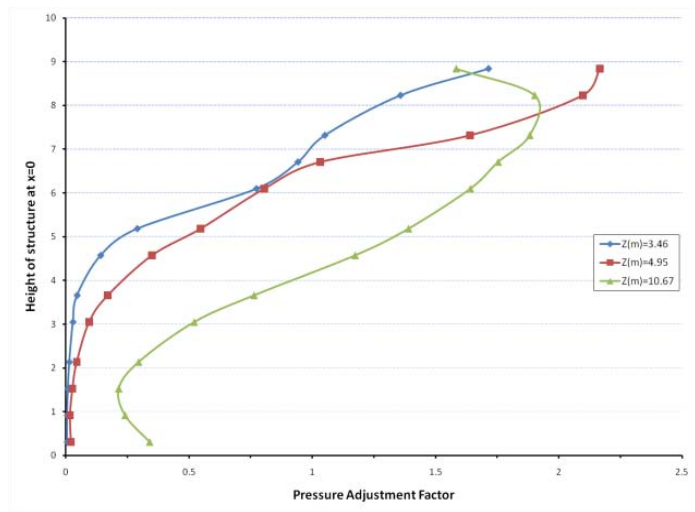
(a)
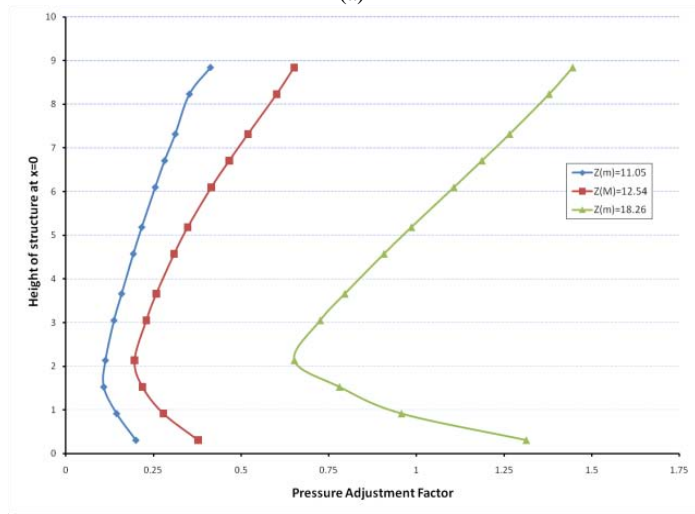
(b)
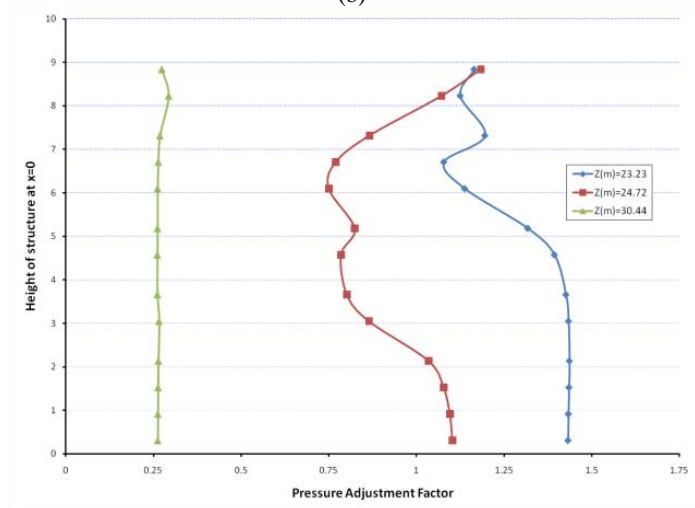
(c)

Figure B-38. Effect of Distance from Barrier to Structure, W = 245.47 kg-TNT, H = 3.05 m, (a) d_2 = 3.05 m, (b) d_2 = 10.64 m, (c) d_2 = 22.82 m

150
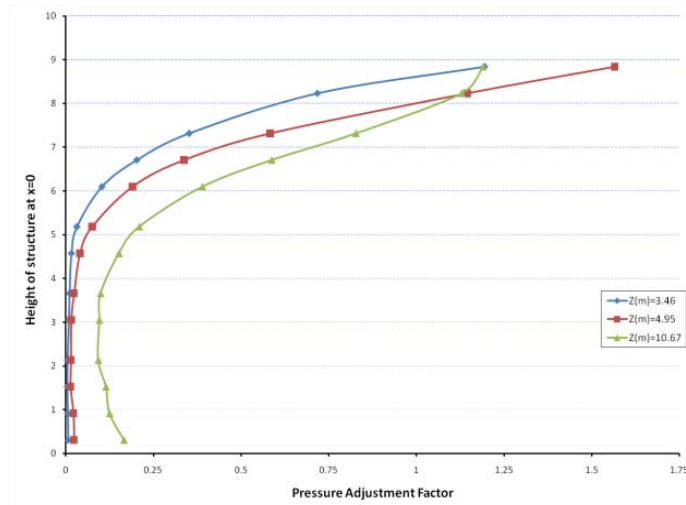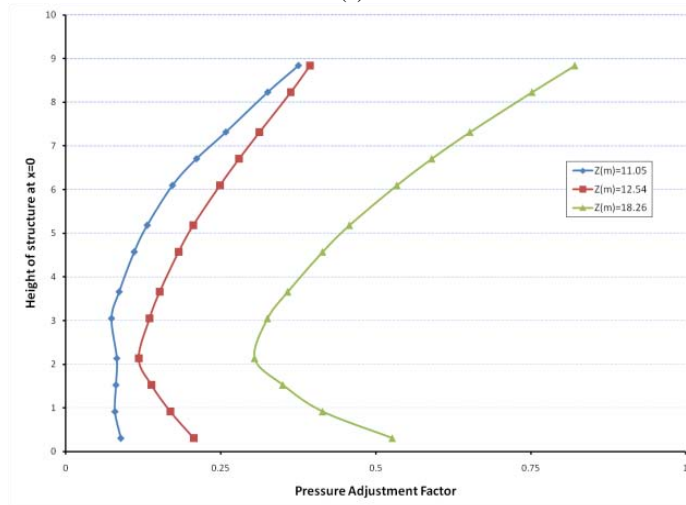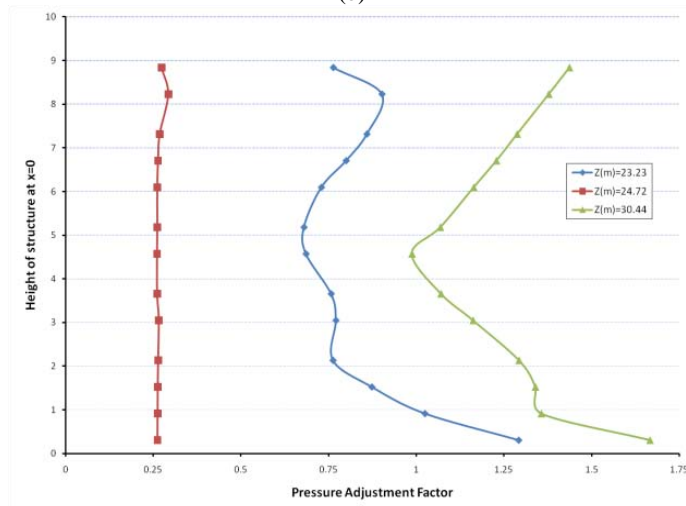
Figure B-39. Effect of Distance from Barrier to Structure, $W = 245.47$ kg-TNT, $H = 6.10$ m, (a) $d_2 = 3.05$ m, (b) $d_2 = 10.64$ m, (c) $d_2 = 22.82$ m

151
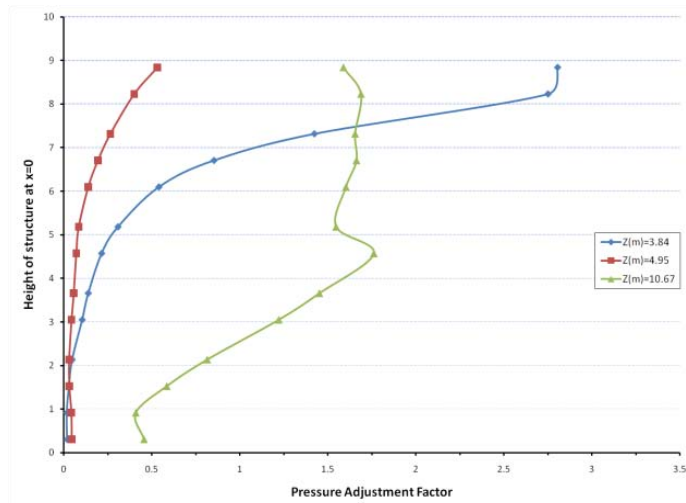
(a)
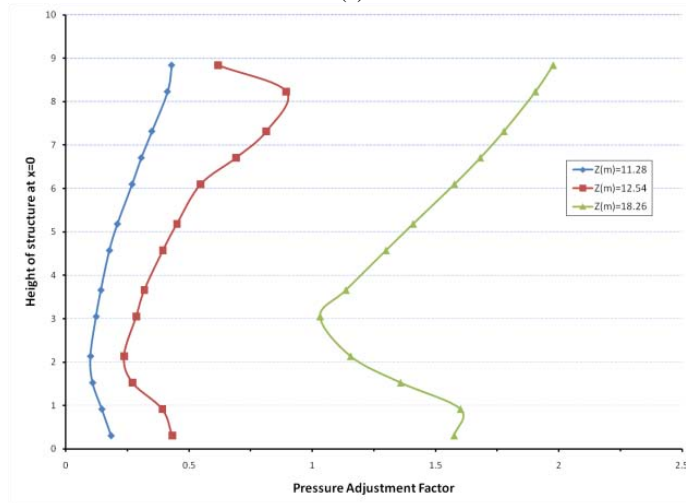
(b)
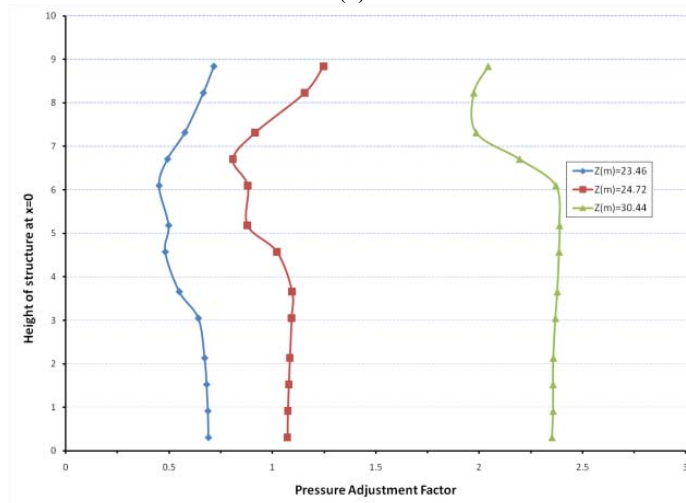
(c)

Figure B-40. Effect of Distance from Barrier to Structure, W = 910.42 kg-TNT, H = 1.52 m, (a) d_2 = 3.05 m, (b) d_2 = 10.64 m, (c) d_2 = 22.82 m

152
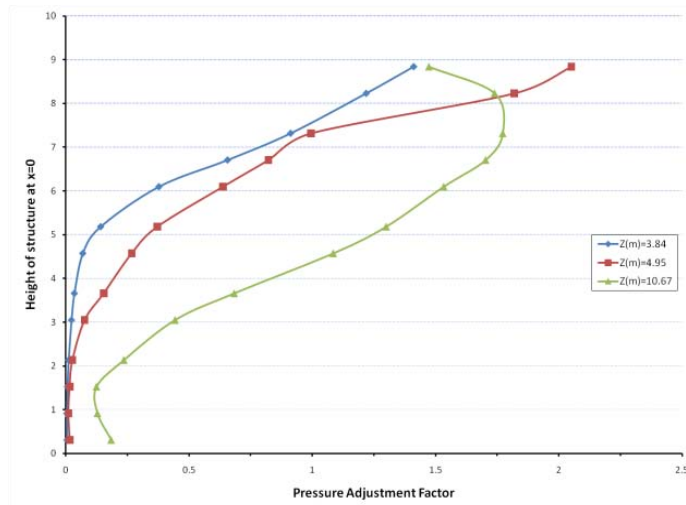
(a)
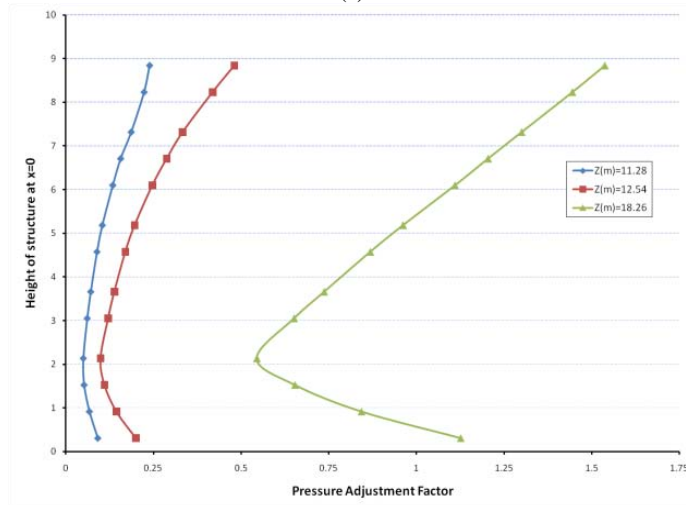
(b)
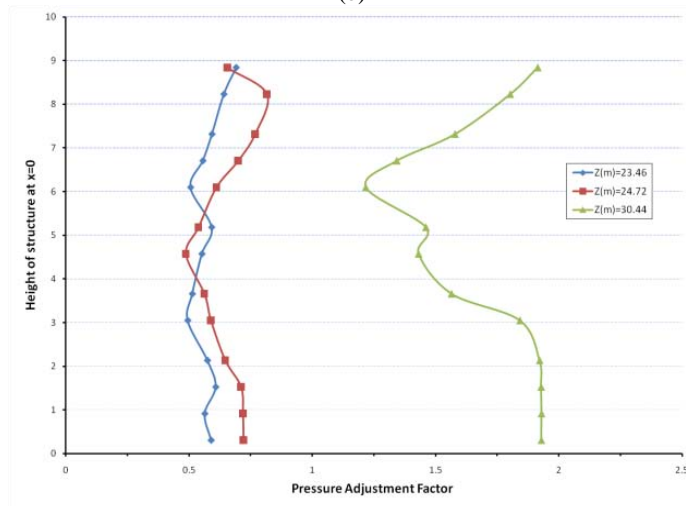
(c)

Figure B-41. Effect of Distance from Barrier to Structure, W = 910.42 kg-TNT, H = 3.05 m, (a) d_2 = 3.05 m, (b) d_2 = 10.64 m, (c) d_2 = 22.82 m

153
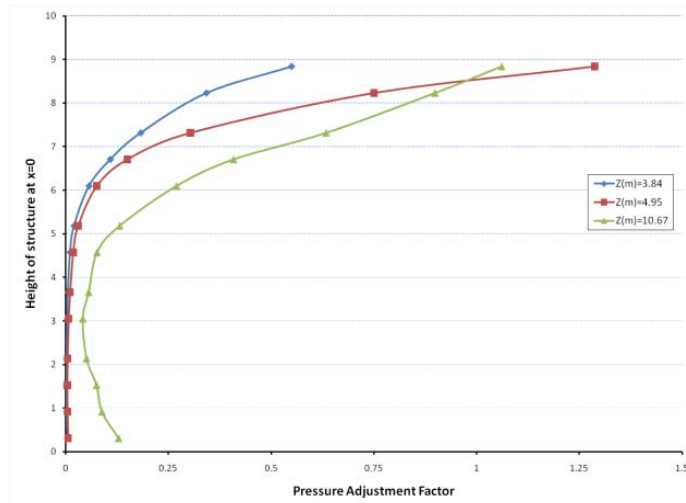
(a)
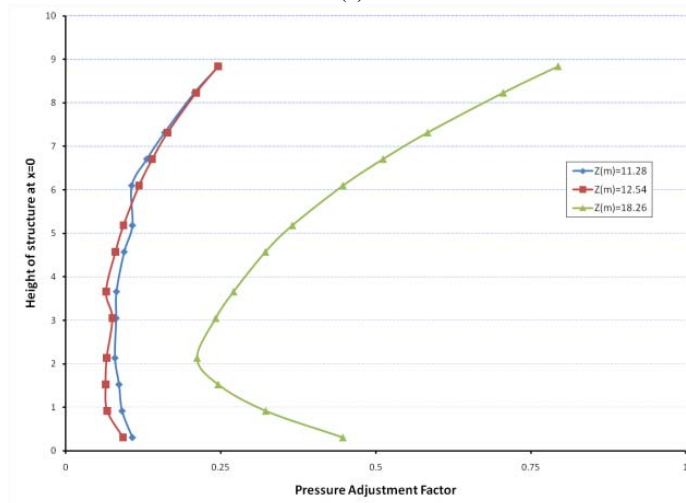
(b)
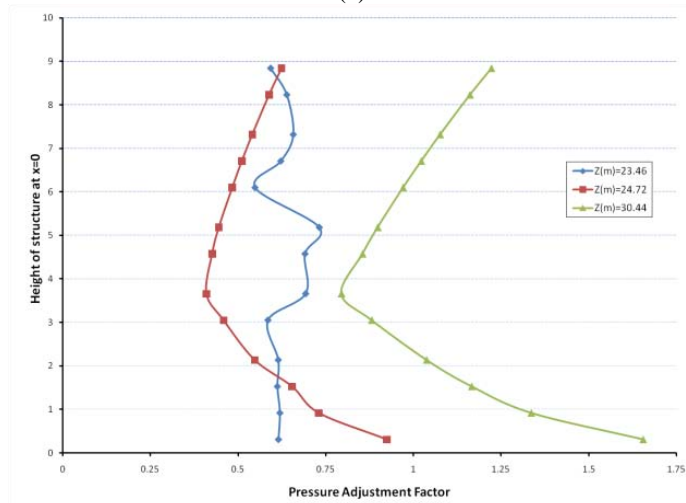
(c)

Figure B-42. Effect of Distance from Barrier to Structure, $W = 910.42$ kg-TNT, $H = 6.10$ m, (a) $d_2 = 3.05$ m, (b) $d_2 = 10.64$ m, (c) $d_2 = 22.82$ m

154

B.6. Effect of Barrier-Structure Standoff to Pressure Adjustment Factors along Vertical 0.61 m From Center of Structure
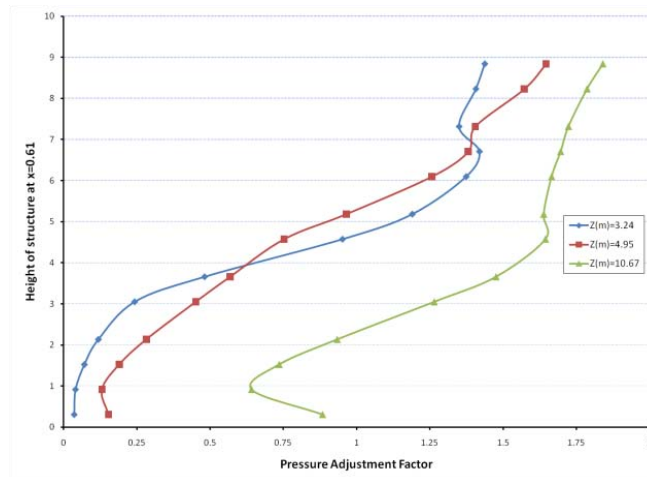
(a)
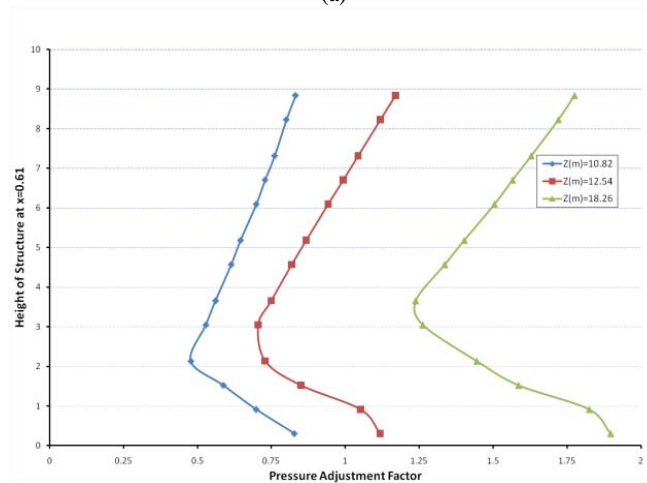
(b)
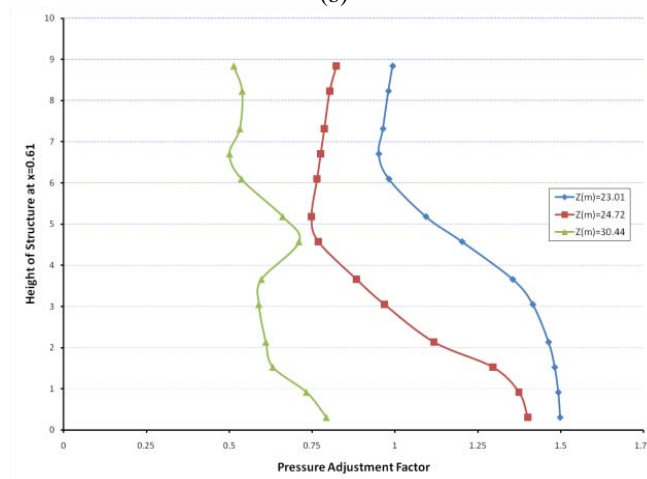
(c)

Figure B-43. Effect of Distance from Barrier to Structure, W = 22.68 kg-TNT, H = 1.52 m, (a) d_2 = 3.05 m, (b) d_2 = 10.64 m, (c) d_2 = 22.82 m

155
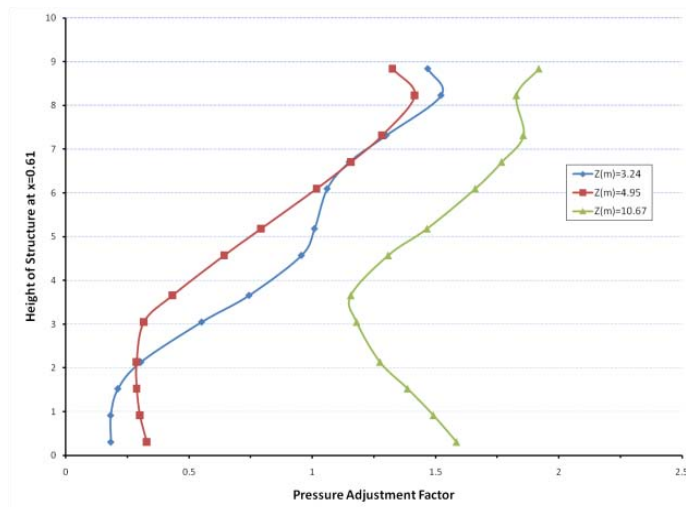
(a)
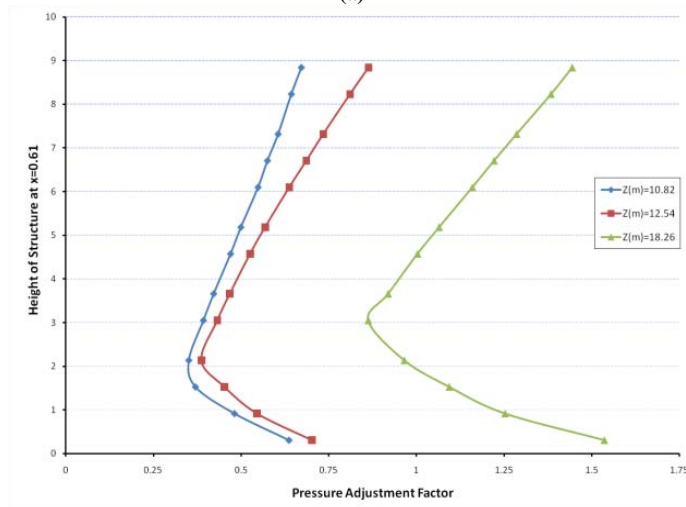
(b)
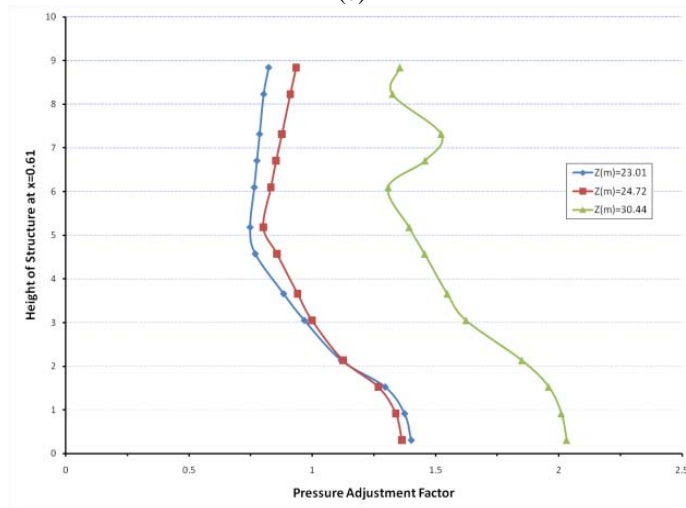
(c)

Figure B-44. Effect of Distance from Barrier to Structure, W = 22.68 kg-TNT, H = 3.05 m, (a) d_2 = 3.05 m, (b) d_2 = 10.64 m, (c) d_2 = 22.82 m
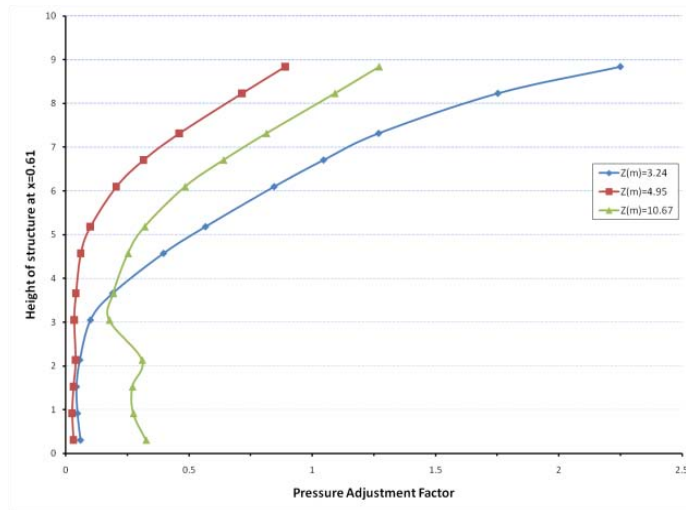
(a)
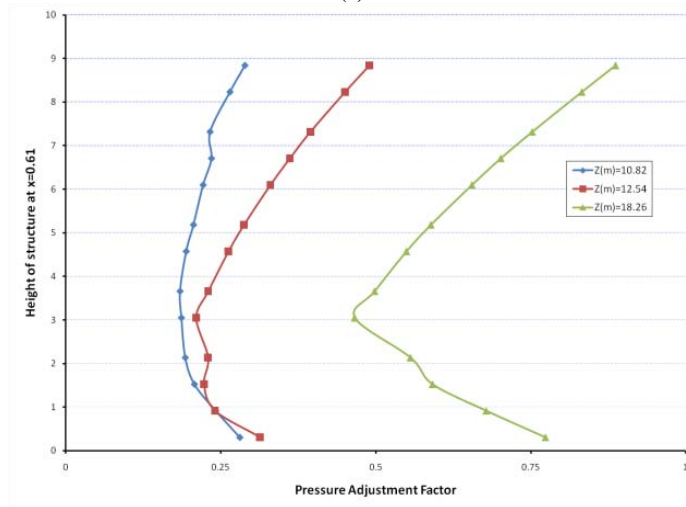
(b)
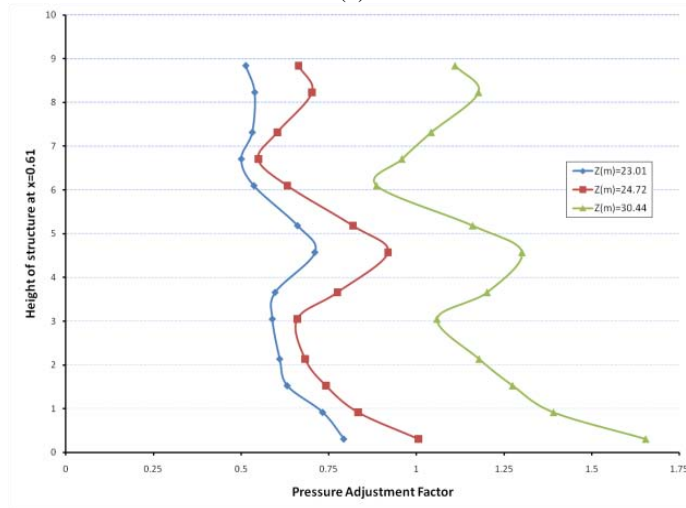
(c)

Figure B-45. Effect of Distance from Barrier to Structure, $W = 22.68$ kg-TNT, $H = 6.10$ m, (a) $d_2 = 3.05$ m, (b) $d_2 = 10.64$ m, (c) $d_2 = 22.82$ m
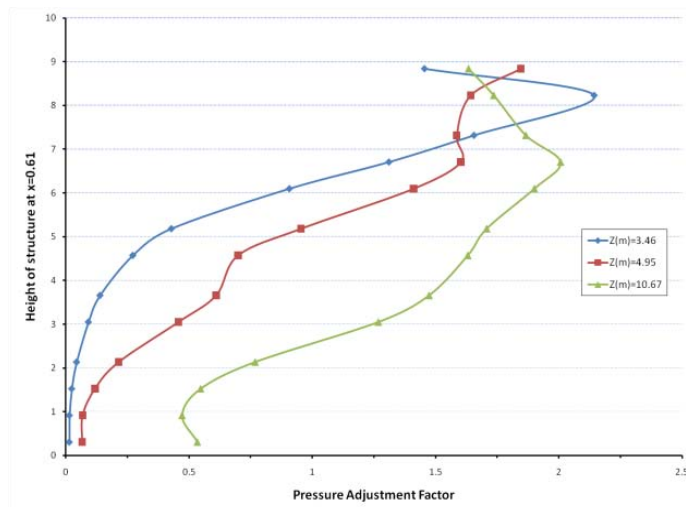
(a)
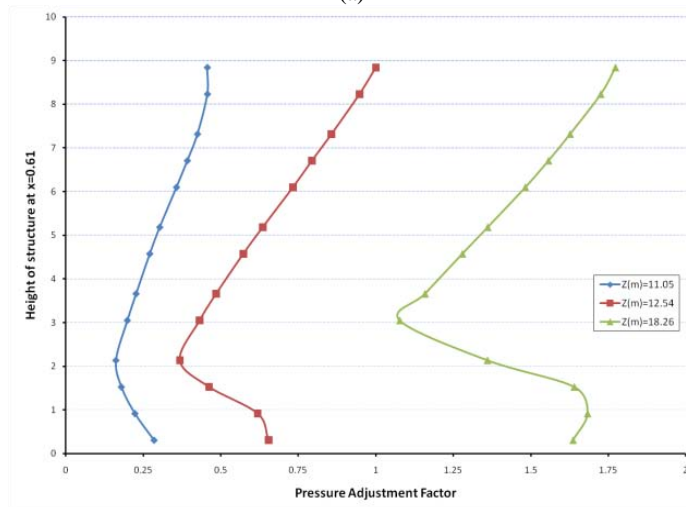
(b)
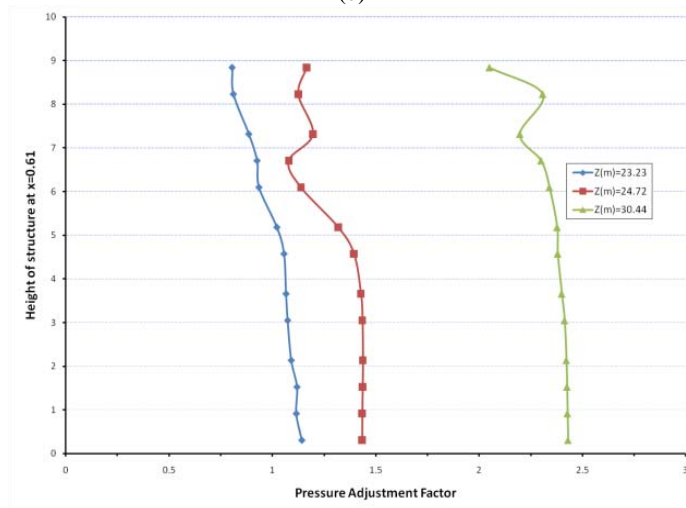
(c)

Figure B-46. Effect of Distance from Barrier to Structure, $W = 245.47$ kg-TNT, $H = 1.52$ m, (a) $d_2 = 3.05$ m, (b) $d_2 = 10.64$ m, (c) $d_2 = 22.82$ m
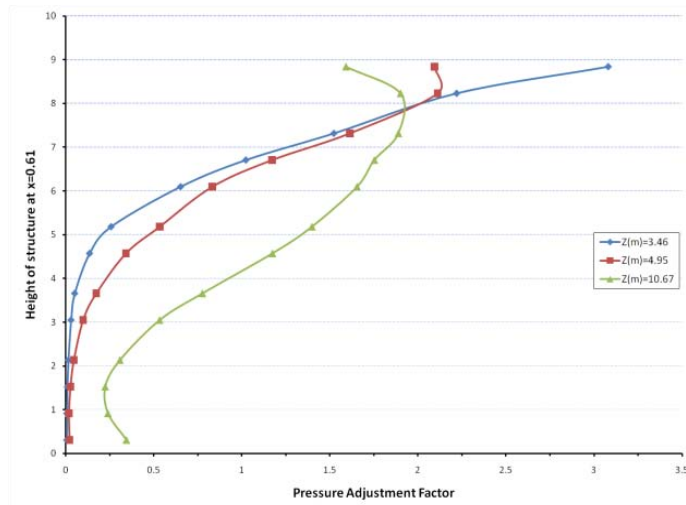
(a)
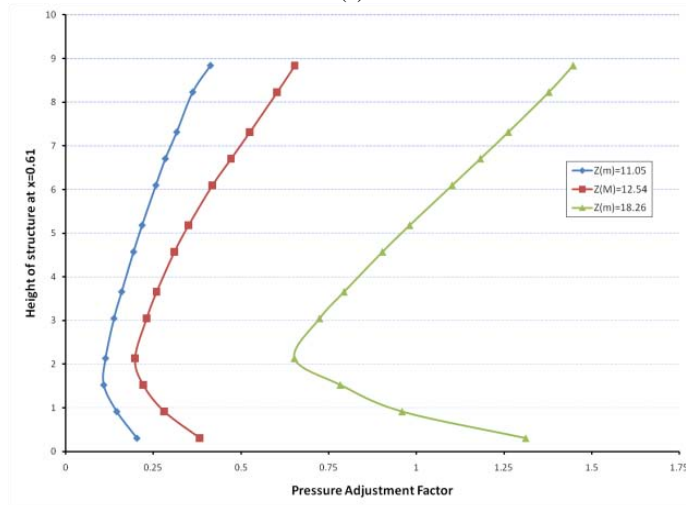
(b)
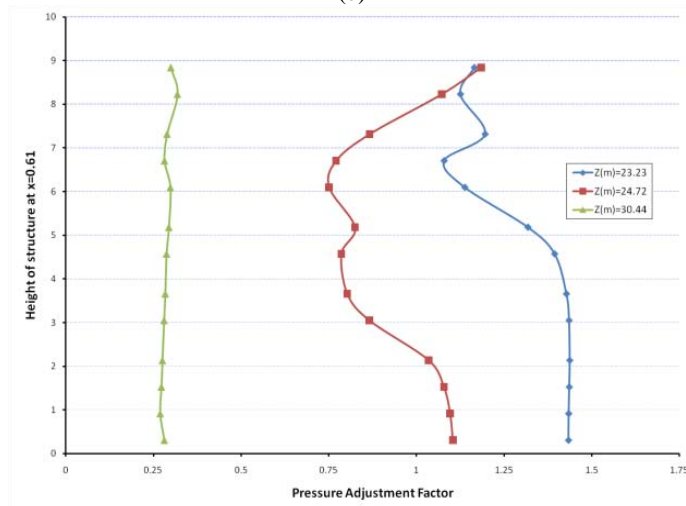
(c)

Figure B-47. Effect of Distance from Barrier to Structure, W = 245.47 kg-TNT, H = 3.05 m, (a) d_2 = 3.05 m, (b) d_2 = 10.64 m, (c) d_2 = 22.82 m
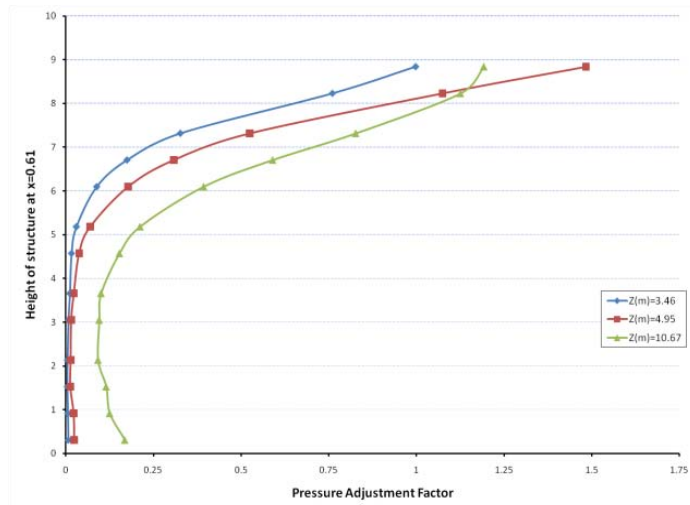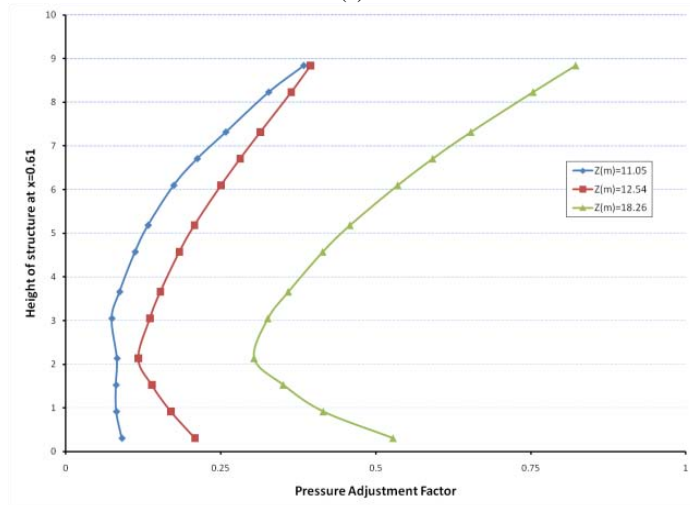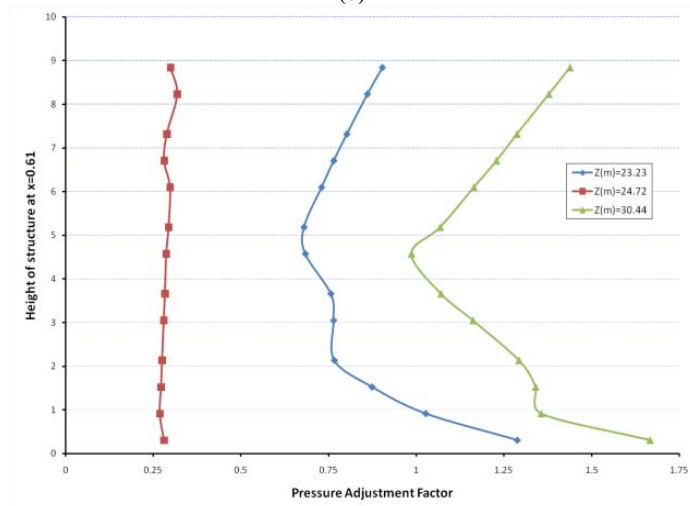
Figure B-48. Effect of Distance from Barrier to Structure, W = 245.47 kg-TNT, H = 6.10 m, (a) d_2 = 3.05 m, (b) d_2 = 10.64 m, (c) d_2 = 22.82 m
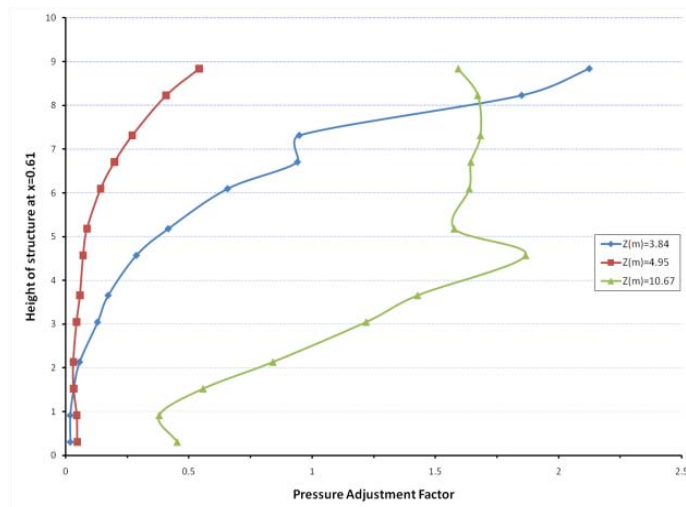
(a)
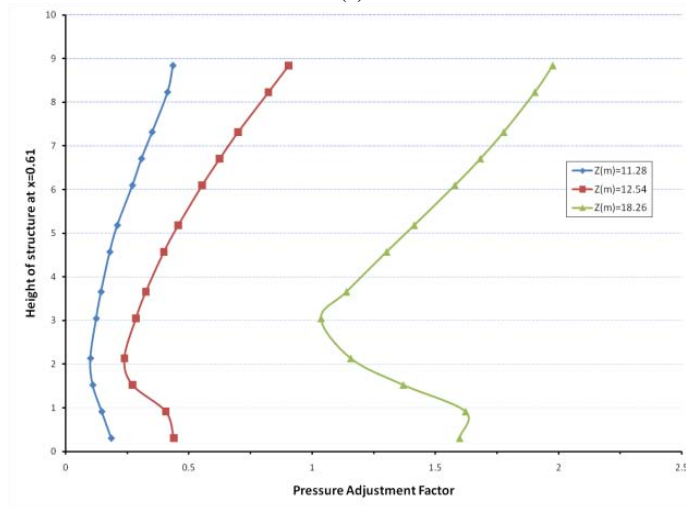
(b)
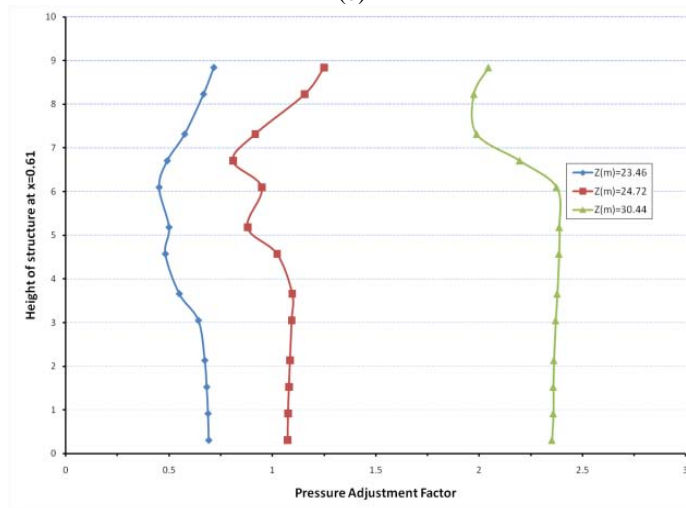
(c)

Figure B-49. Effect of Distance from Barrier to Structure, W = 910.42 kg-TNT, H = 1.52 m, (a) d_2 = 3.05 m, (b) d_2 = 10.64 m, (c) d_2 = 22.82 m

161
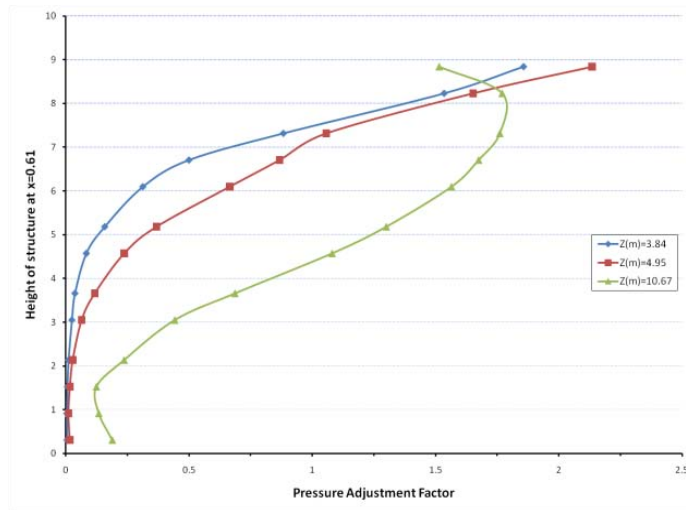
(a)
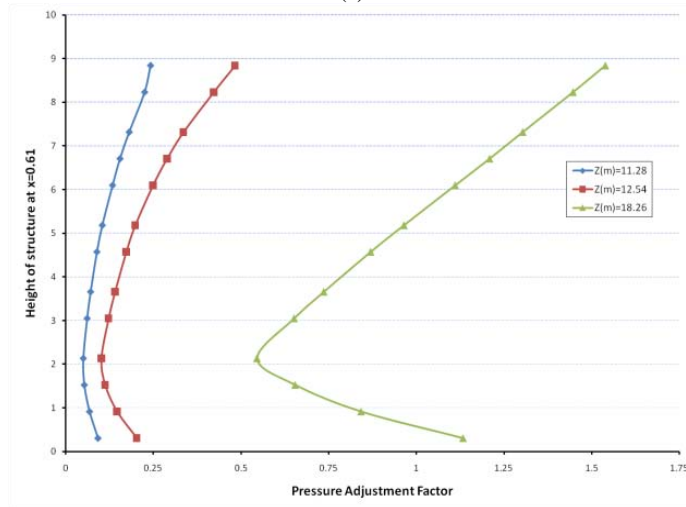
(b)
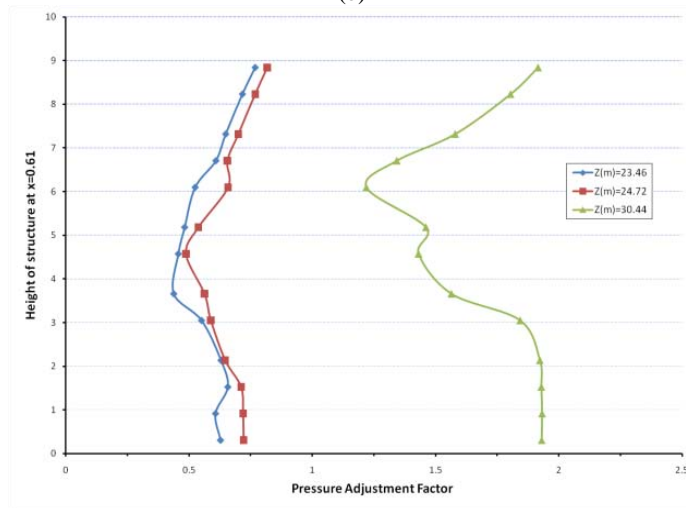
(c)

Figure B-50. Effect of Distance from Barrier to Structure, W = 910.42 kg-TNT, H = 3.0552 m, (a) d_2 = 3.05 m, (b) d_2 = 10.64 m, (c) d_2 = 22.82 m
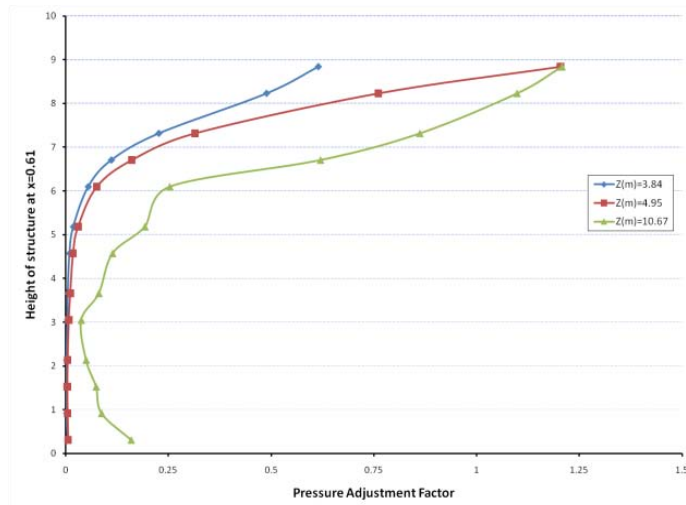
(a)
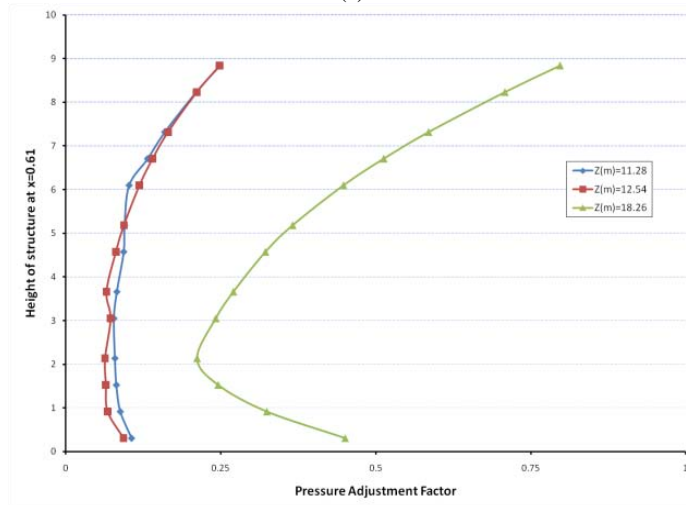
(b)
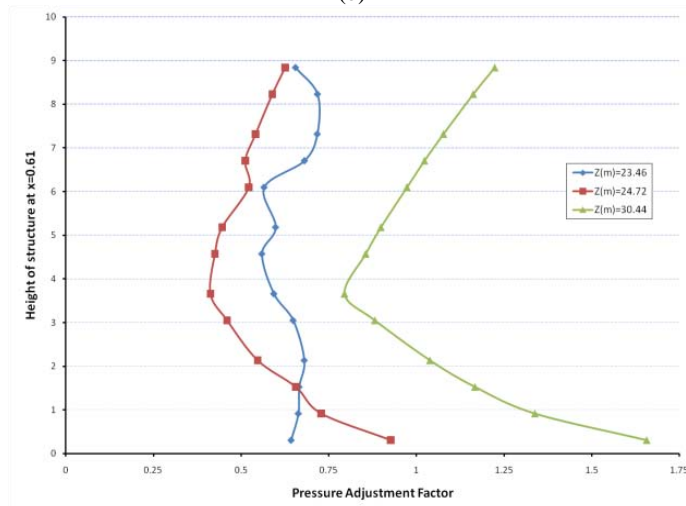
(c)

Figure B-51. Effect of Distance from Barrier to Structure, W = 910.42 kg-TNT, H = 6.10 m, (a) d_2 = 3.05 m, (b) d_2 = 10.64 m, (c) d_2 = 22.82 m

163

B.7. Effect of Barrier-to-Structure Standoff on Impulse Adjustment Factors along Vertical Centerline of Structure
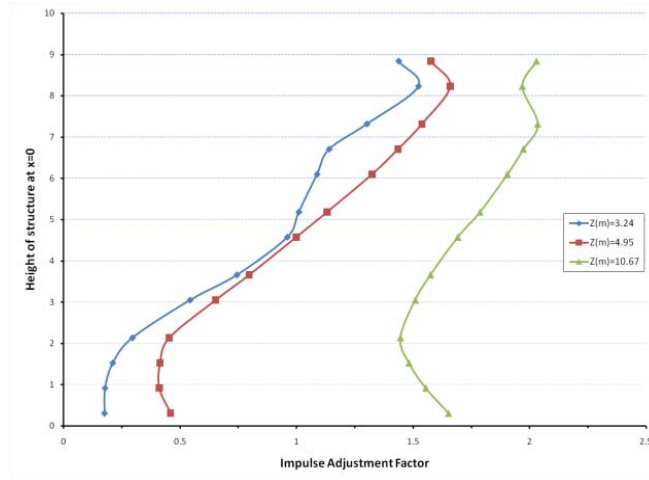

(a)
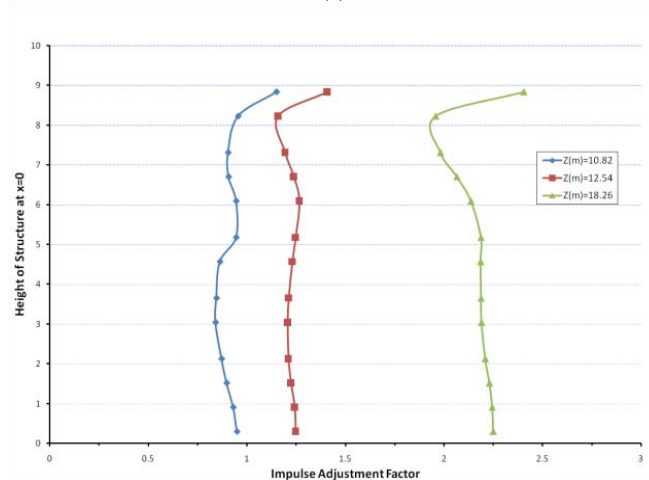
(b)
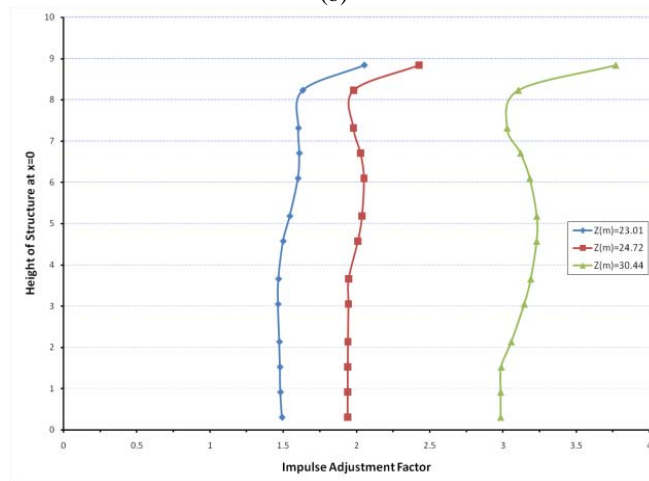
(c)

Figure B-52. Effect of Distance from Barrier to Structure, $W = 22.68$ kg-TNT, $H = 1.52$ m, (a) $d_2 = 3.05$ m, (b) $d_2 = 10.64$ m, (c) $d_2 = 22.82$ m
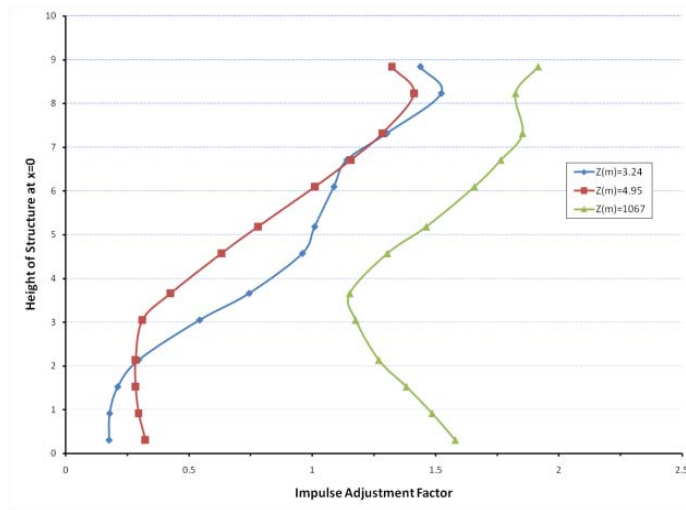
(a)
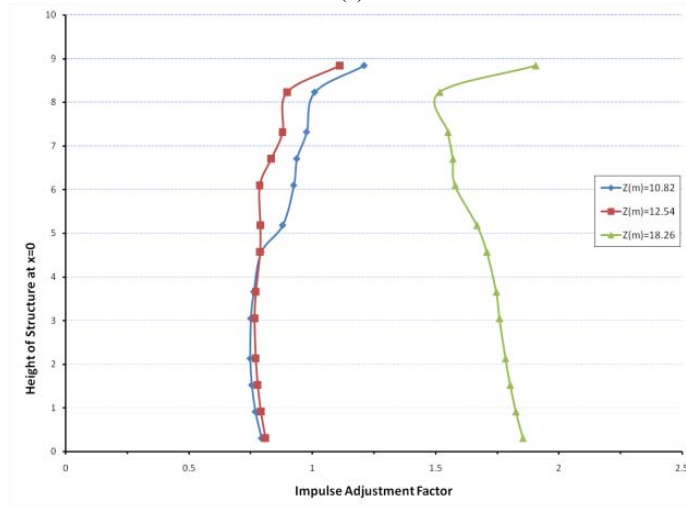
(b)
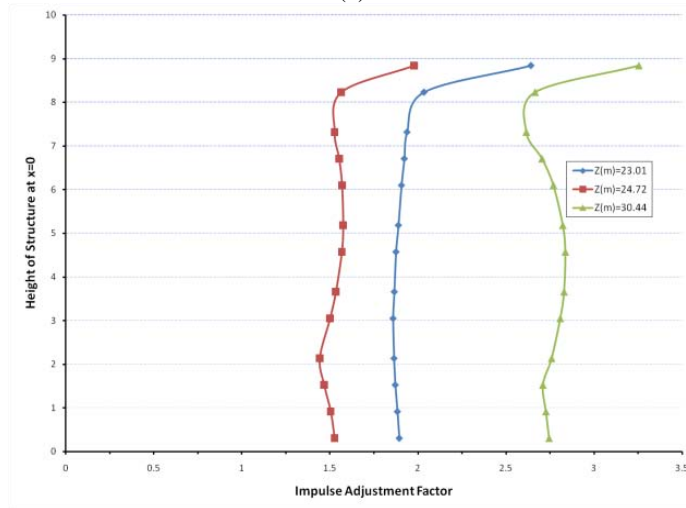
(c)

Figure B-53. Effect of Distance from Barrier to Structure, W = 22.68 kg-TNT, H = 3.05 m, (a) d_2 = 3.05 m, (b) d_2 = 10.64 m, (c) d_2 = 22.82 m

165
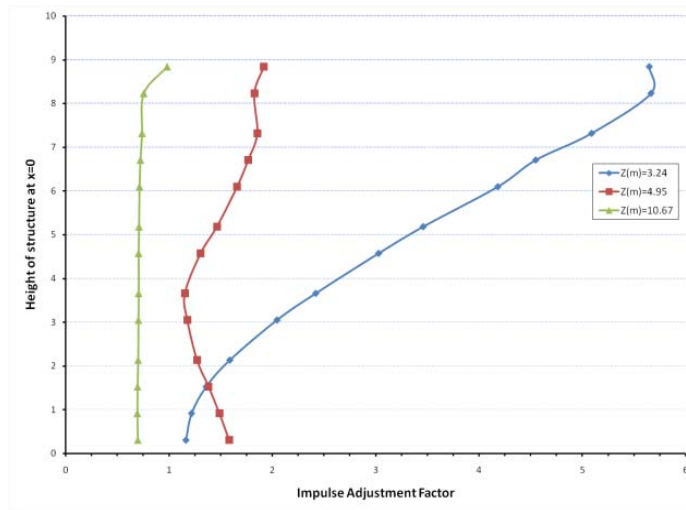
(a)
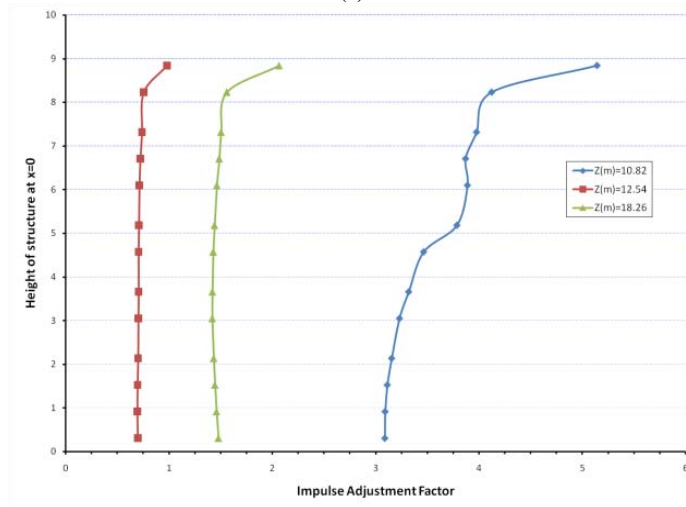
(b)
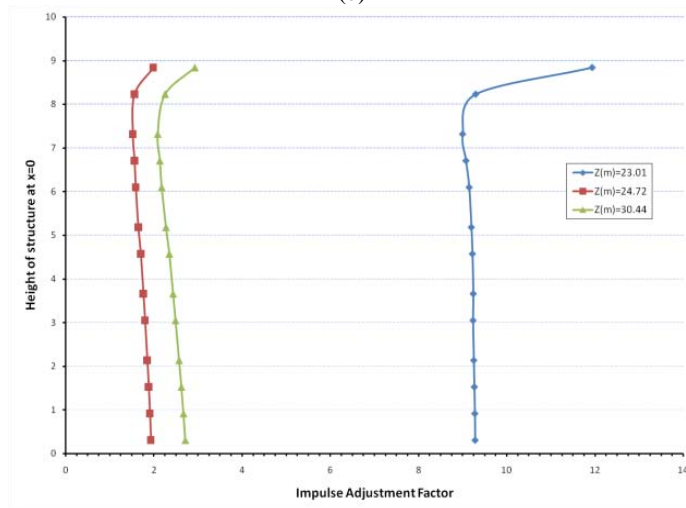
(c)

Figure B-54. Effect of Distance from Barrier to Structure, W = 22.68 kg-TNT, H = 6.10 m, (a) d_2 = 3.05 m, (b) d_2 = 10.64 m, (c) d_2 = 22.82 m

166
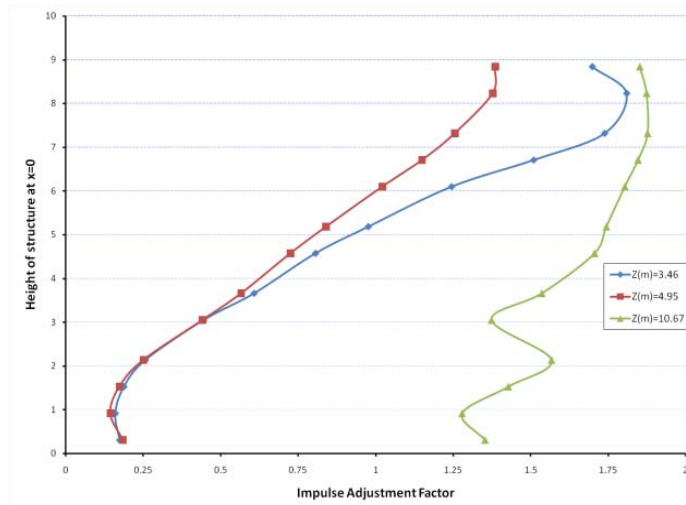
(a)
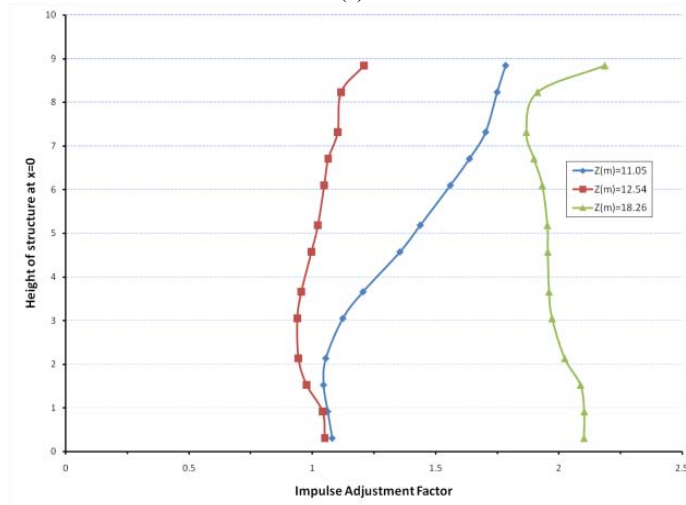
(b)
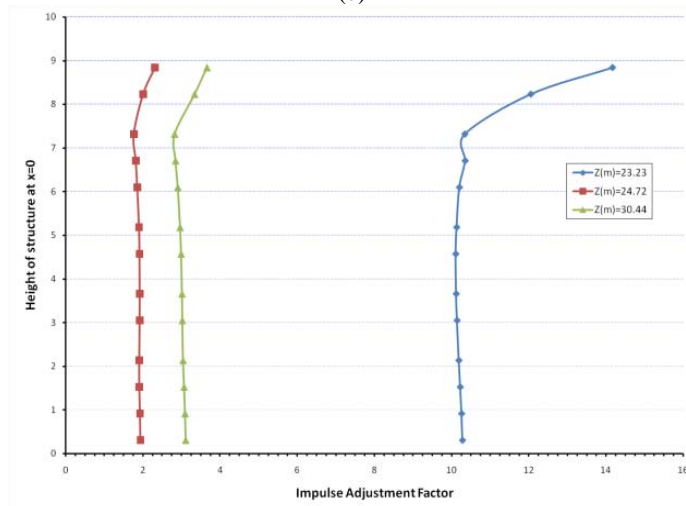
(c)

Figure B-55. Effect of Distance from Barrier to Structure, W = 245.47 kg-TNT, H = 1.52 m, (a) d_2 = 3.05 m, (b) d_2 = 10.64 m, (c) d_2 = 22.82 m

167
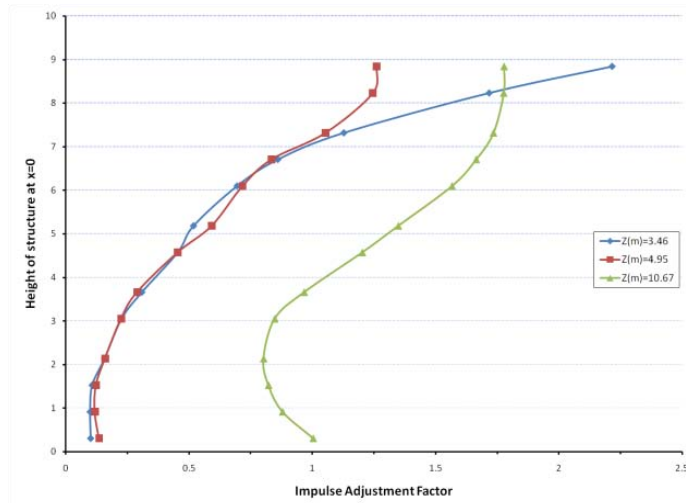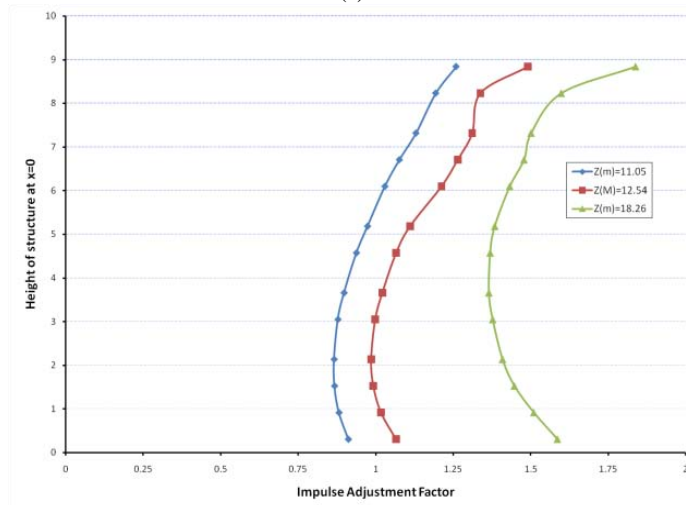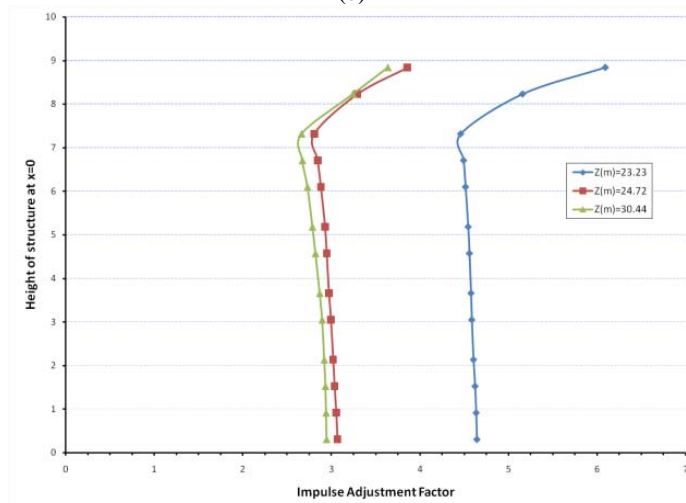
Figure B-56. Effect of Distance from Barrier to Structure, $W = 245.47$ kg-TNT, $H = 3.05$ m, (a) $d_2 = 3.05$ m, (b) $d_2 = 10.64$ m, (c) $d_2 = 22.82$ m
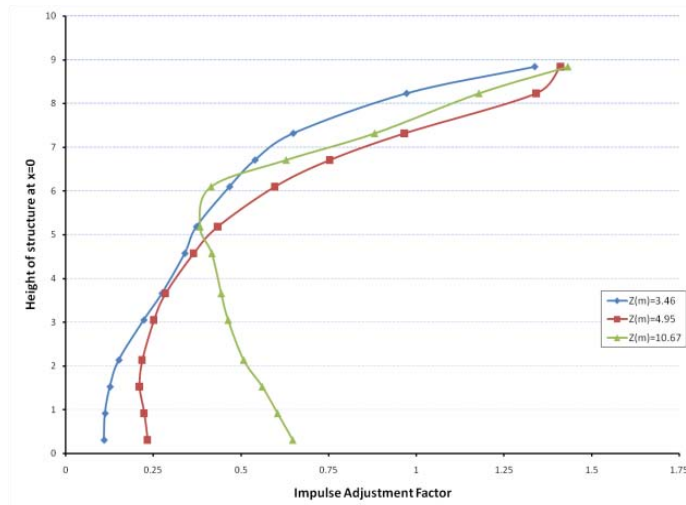
(a)
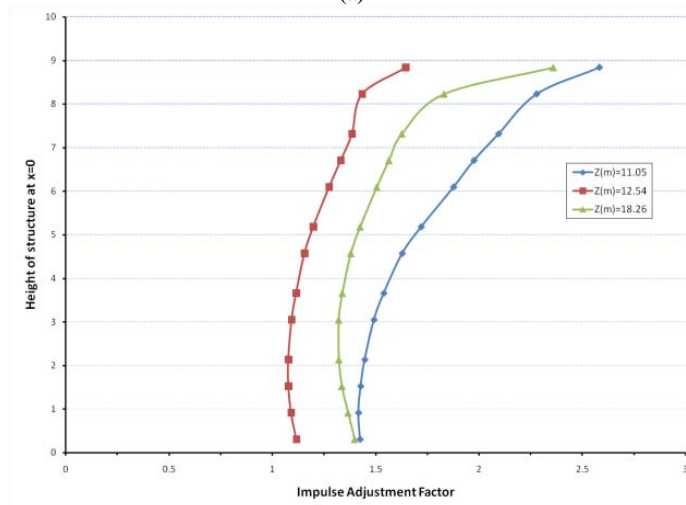
(b)
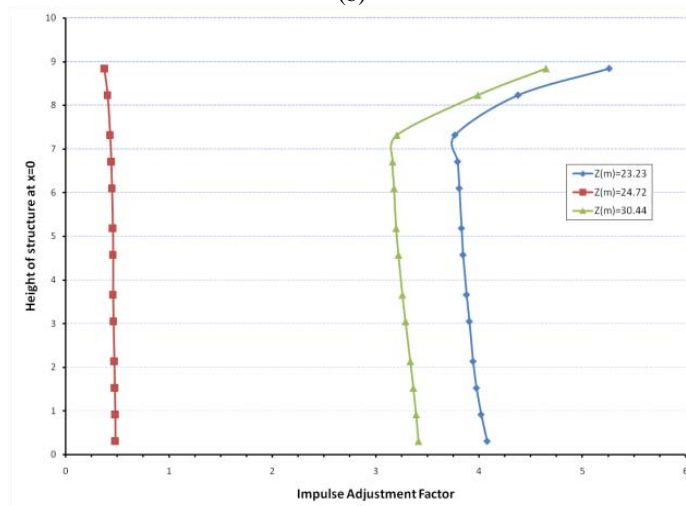
(c)

Figure B-57. Effect of Distance from Barrier to Structure, W = 245.47 kg-TNT, H = 6.10 m, (a) d_2 = 3.05 m, (b) d_2 = 10.64 m, (c) d_2 = 22.82 m
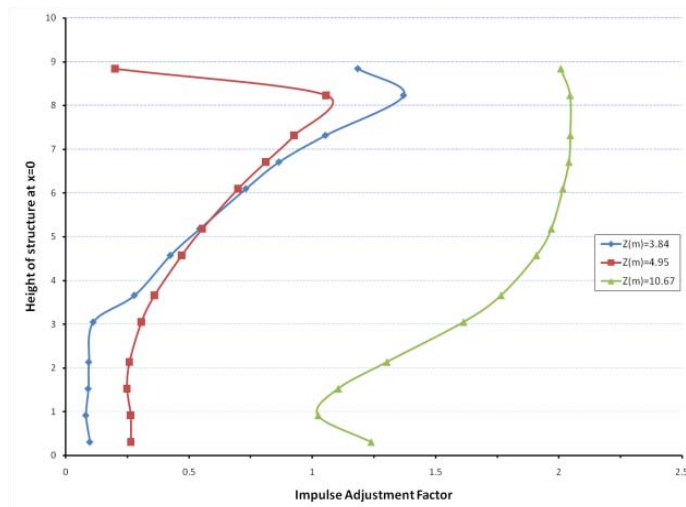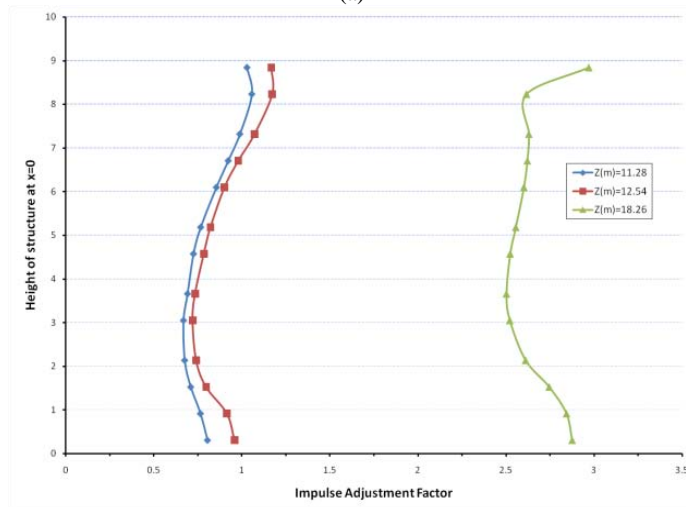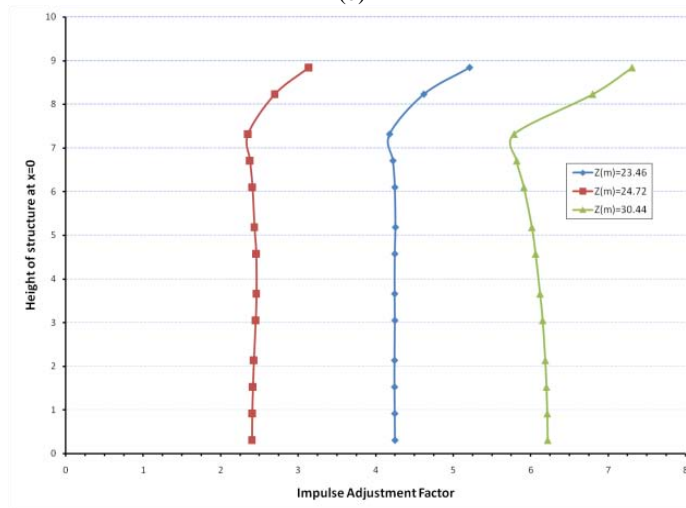
Figure B-58. Effect of Distance from Barrier to Structure, W = 910.42 kg-TNT, H = 1.52 m, (a) d_2 = 3.05 m, (b) d_2 = 10.64 m, (c) d_2 = 22.82 m

170
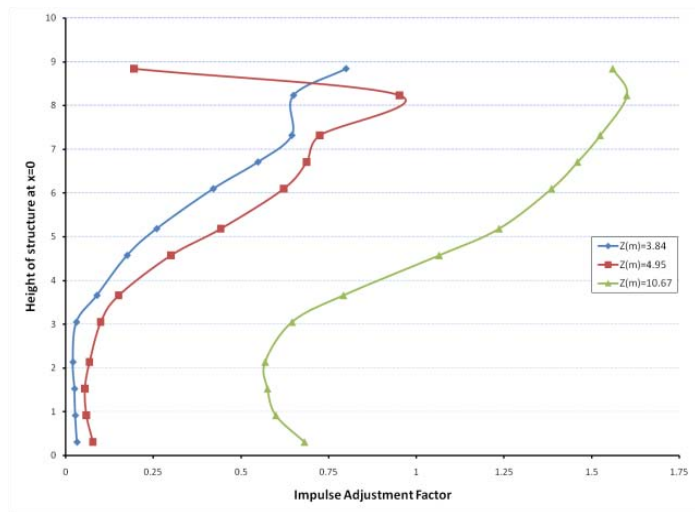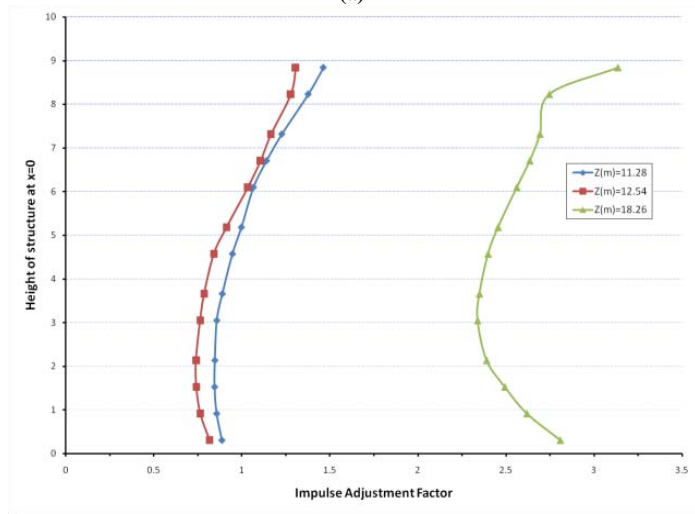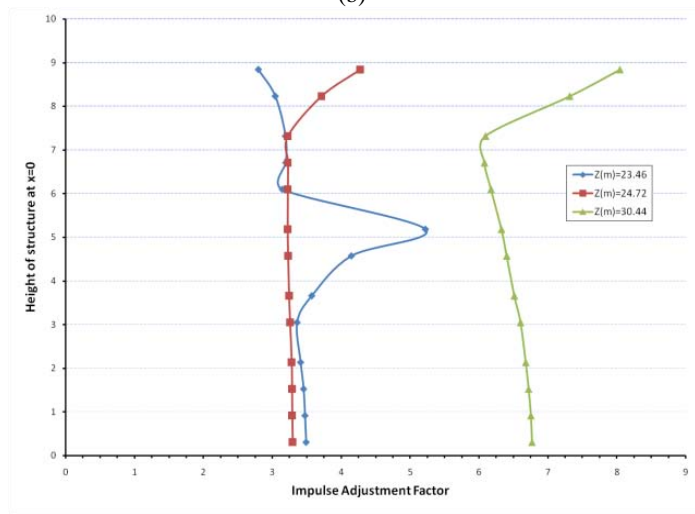
Figure B-59. Effect of Distance from Barrier to Structure, W = 910.42 kg-TNT, H = 3.05 m, (a) d_2 = 3.05 m, (b) d_2 = 10.64 m, (c) d_2 = 22.82 m

171
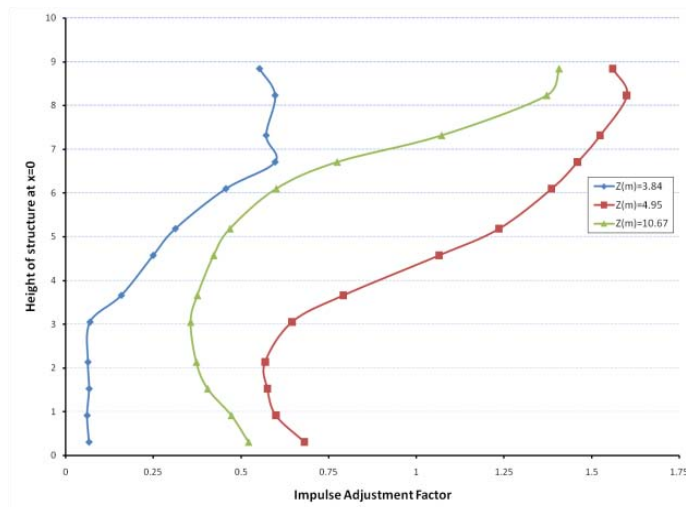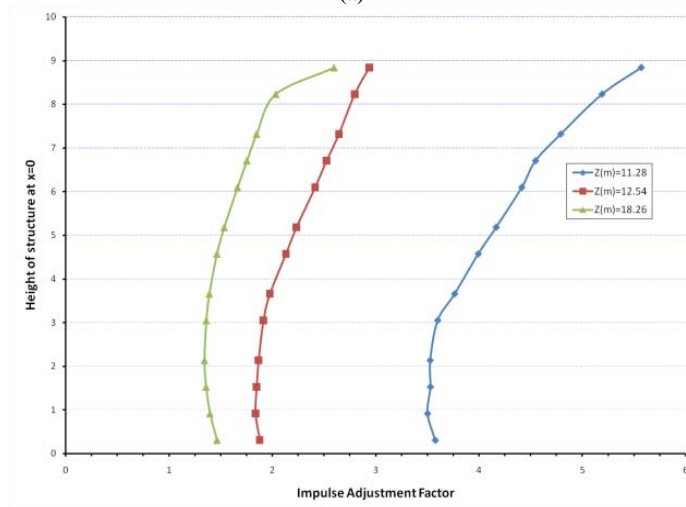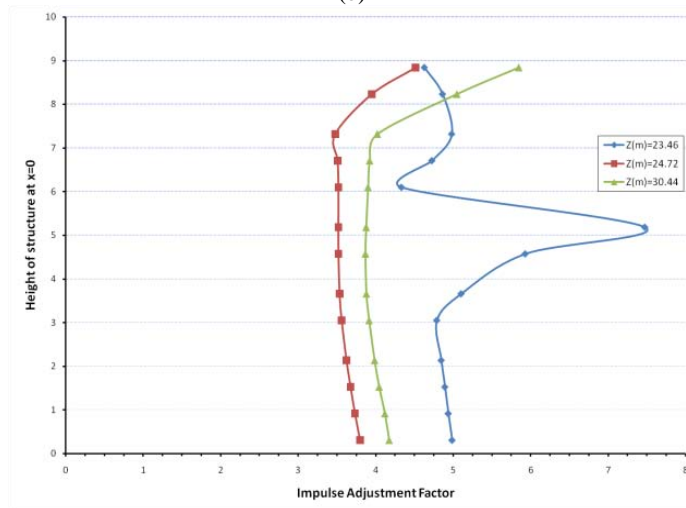
Figure B-60. Effect of Distance from Barrier to Structure, W = 910.42 kg-TNT, H = 6.10 m, (a) d_2 = 3.05 m, (b) d_2 = 10.64 m, (c) d_2 = 22.82 m

(a)

(b)

(c)

Figure B-61. Effect of Distance from Barrier to Structure, W = 22.68 kg-TNT, H = 1.52 m, (a) d_2 = 3.05 m, (b) d_2 = 10.64 m, (c) d_2 = 22.82 m

173
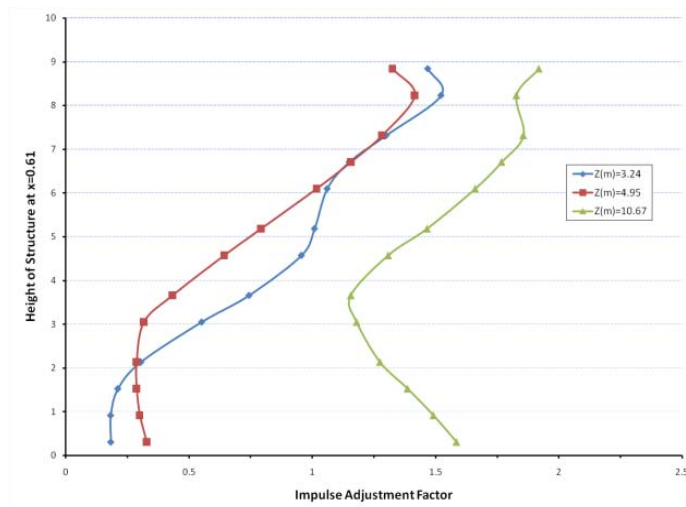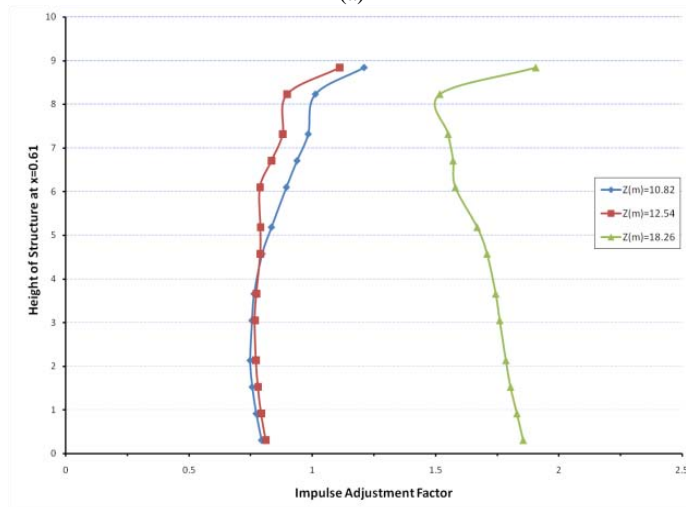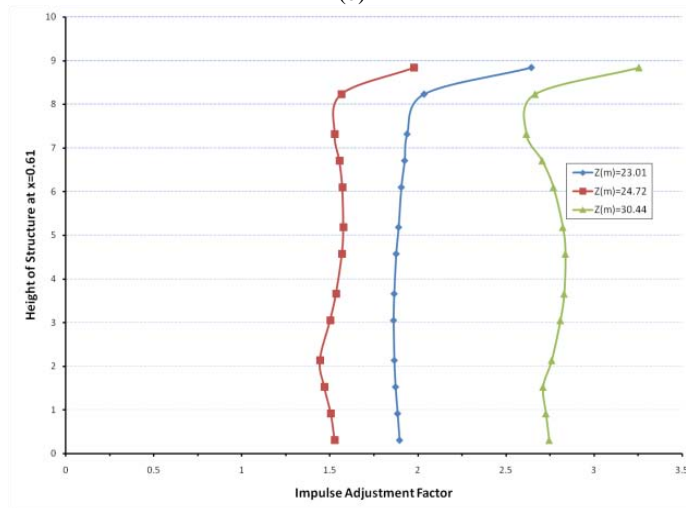
Figure B-62. Effect of Distance from Barrier to Structure, W = 22.68 kg-TNT, H = 3.05 m, (a) d_2 = 3.05 m, (b) d_2 = 10.64 m, (c) d_2 = 22.82 m

174
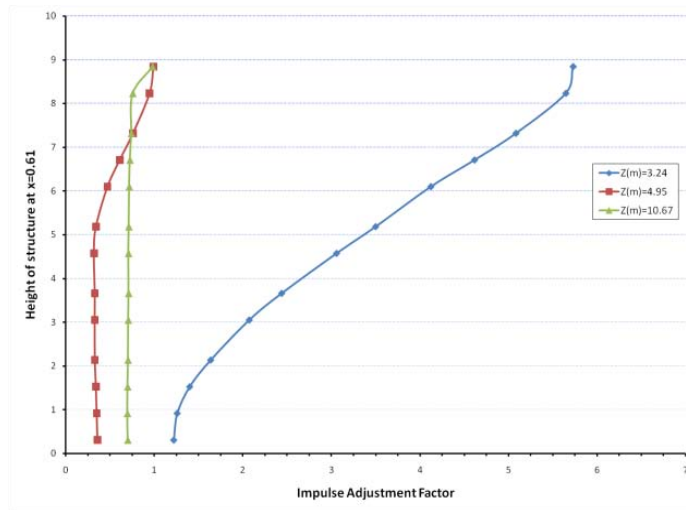
(a)
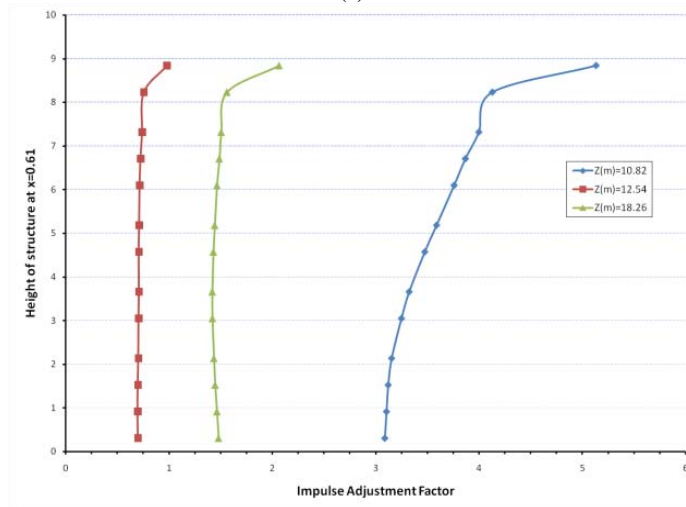
(b)
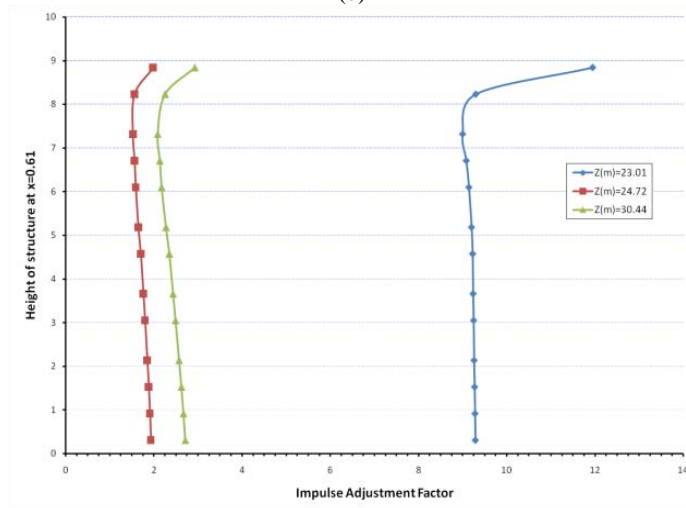
(c)

Figure B-63. Effect of Distance from Barrier to Structure, W = 22.68 kg-TNT, H = 6.10 m, (a) d_2 = 3.05 m, (b) d_2 = 10.64 m, (c) d_2 = 22.82 m
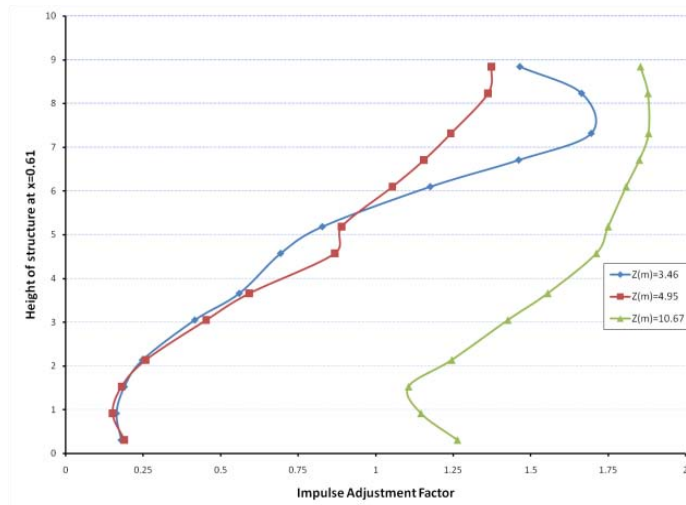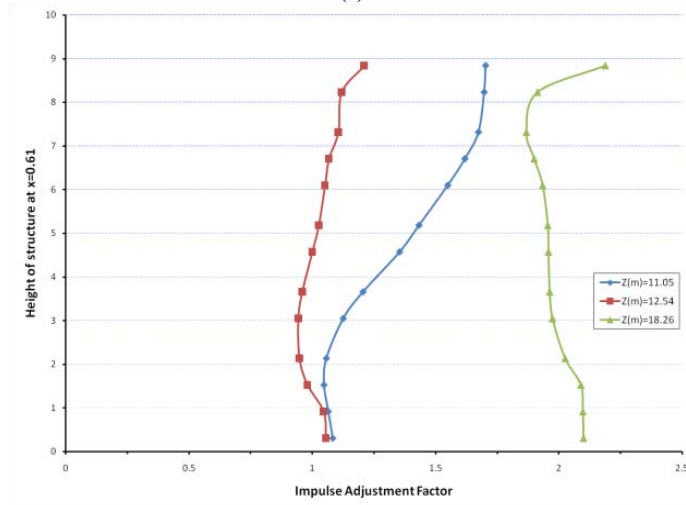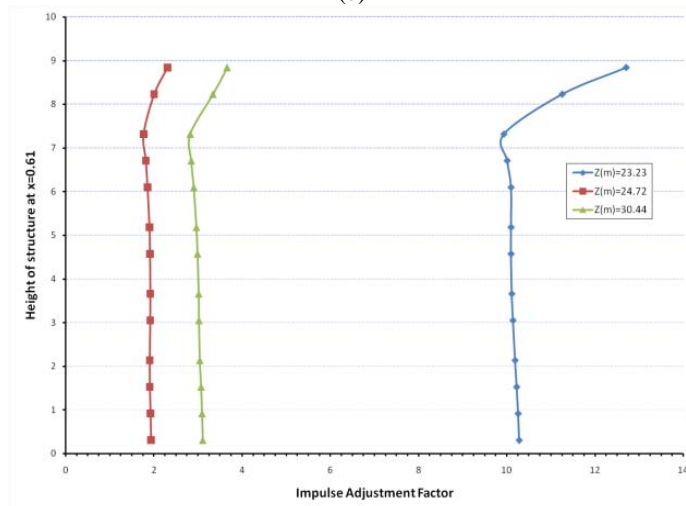
Figure B-64. Effect of Distance from Barrier to Structure, W = 245.47 kg-TNT, H = 1.52 m, (a) d_2 = 3.05 m, (b) d_2 = 10.64 m, (c) d_2 = 22.82 m
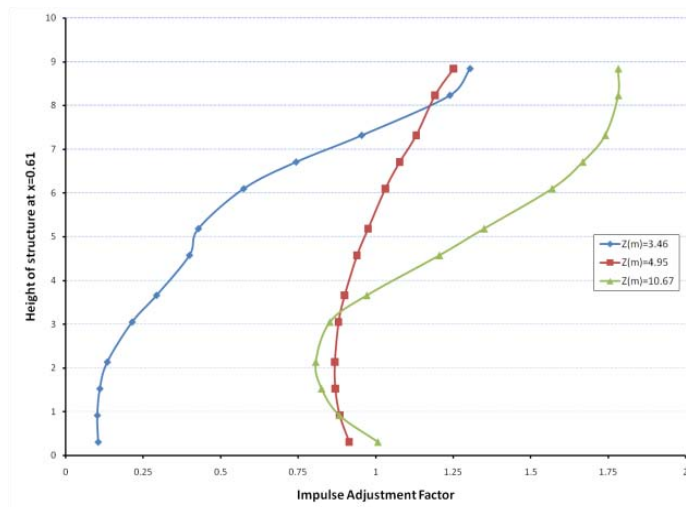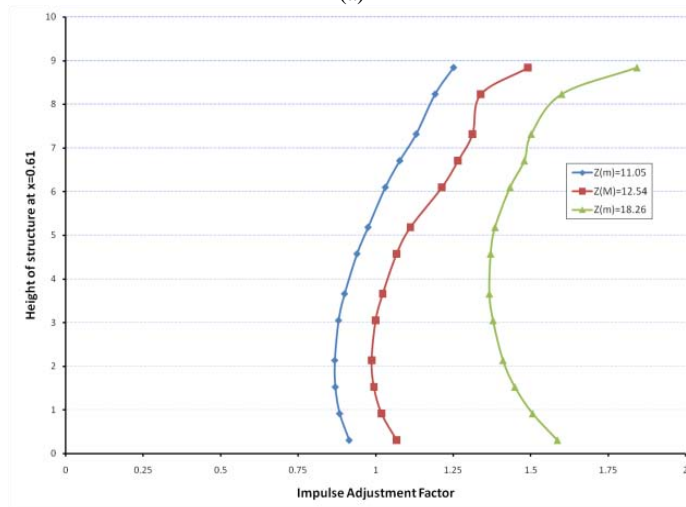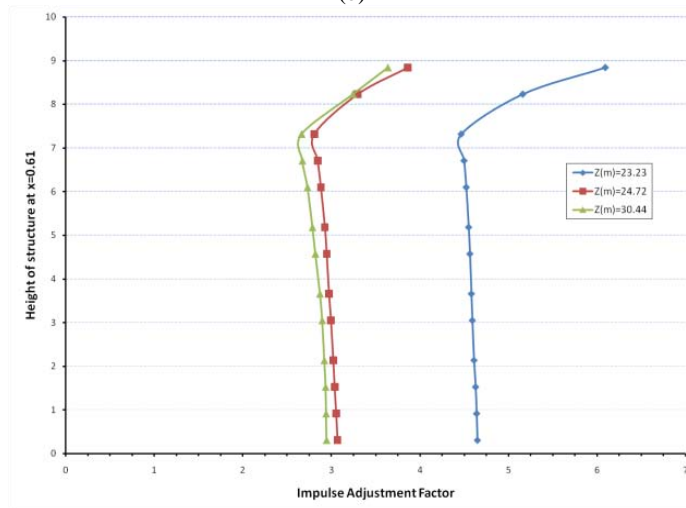
Figure B-65. Effect of Distance from Barrier to Structure, W = 245.47 kg-TNT, H = 3.05 m, (a) d_2 = 3.05 m, (b) d_2 = 10.64 m, (c) d_2 = 22.82 m
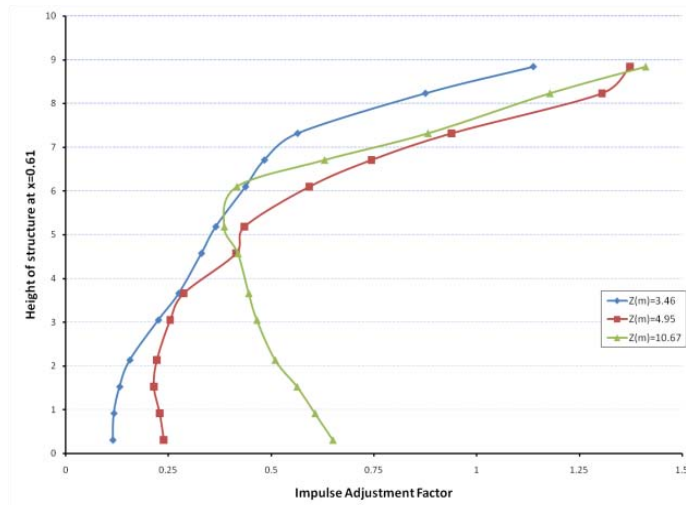
(a)
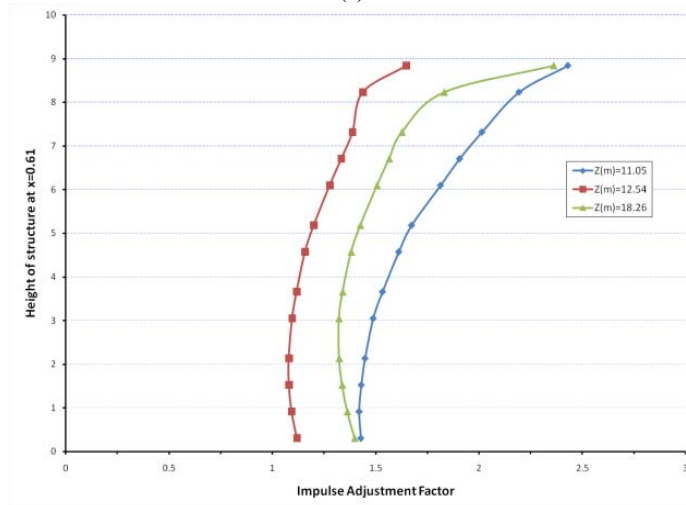
(b)
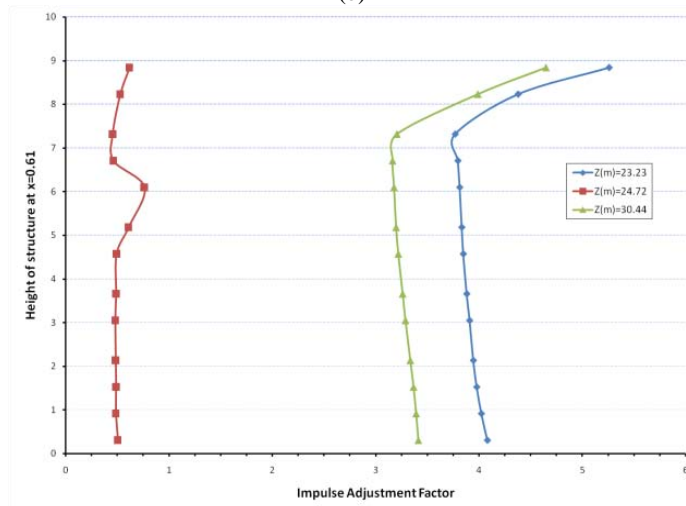
(c)

Figure B-66. Effect of Distance from Barrier to Structure, $W = 245.47$ kg-TNT, $H = 6.10$ m, (a) $d_2 = 3.05$ m, (b) $d_2 = 10.64$ m, (c) $d_2 = 22.82$ m
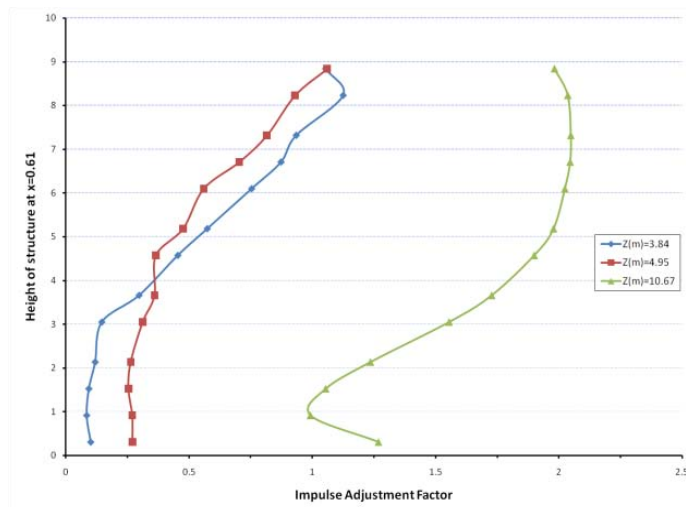
(a)
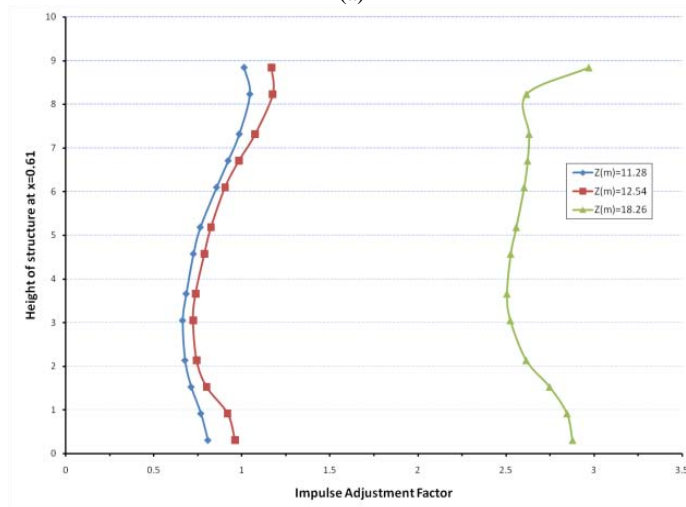
(b)
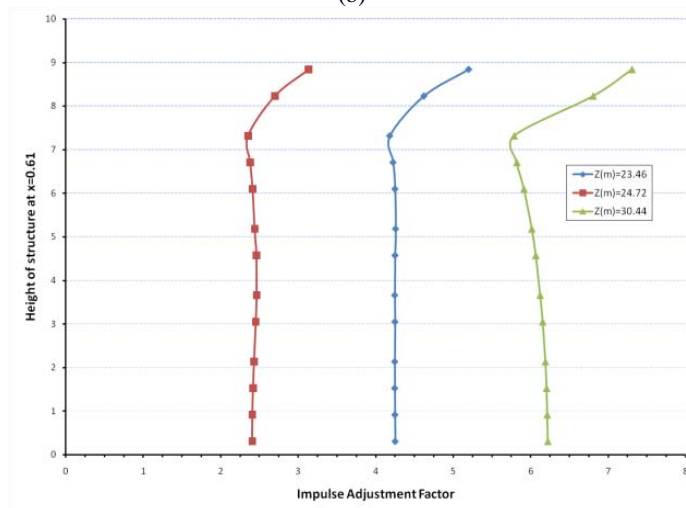
(c)

Figure B-67. Effect of Distance from Barrier to Structure, W = 910.42 kg-TNT, H = 1.52 m, (a) d_2 = 3.05 m, (b) d_2 = 10.64 m, (c) d_2 = 22.82 m
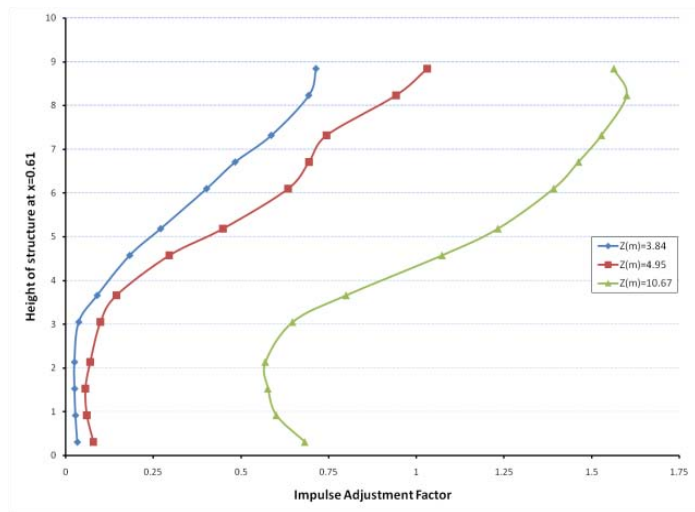
(a)
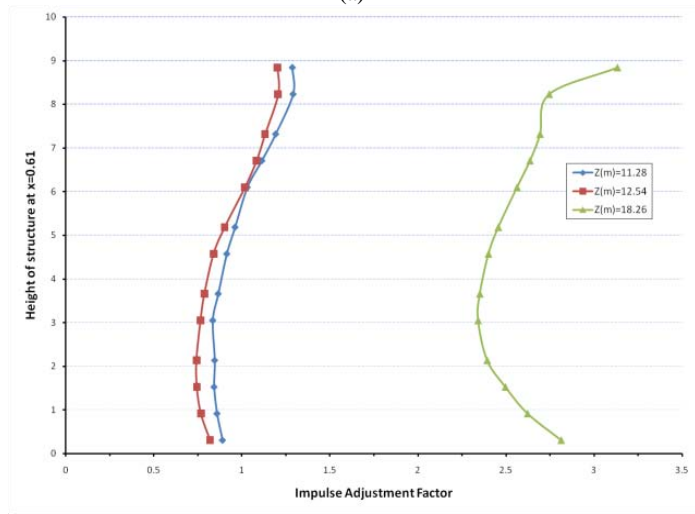
(b)
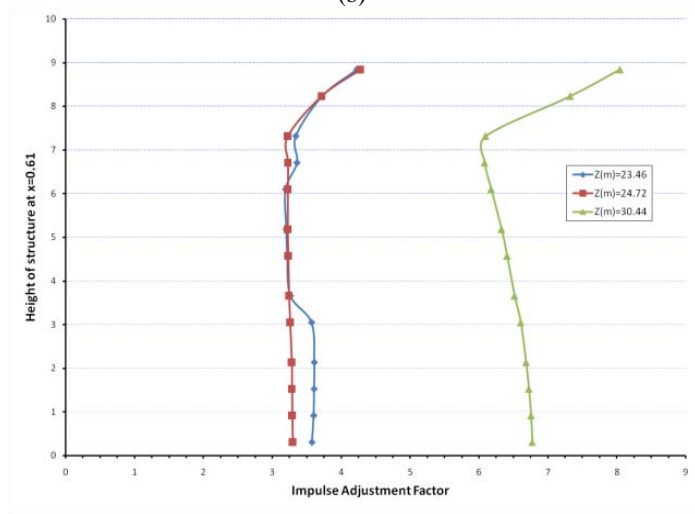
(c)

Figure B-68. Effect of Distance from Barrier to Structure, W = 910.42 kg-TNT, H = 3.05 m, (a) d_2 = 3.05 m, (b) d_2 = 10.64 m, (c) d_2 = 22.82 m

180
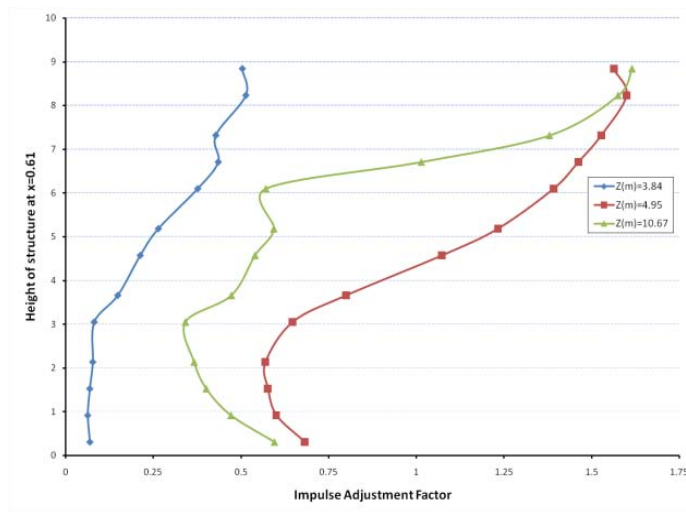
(a)
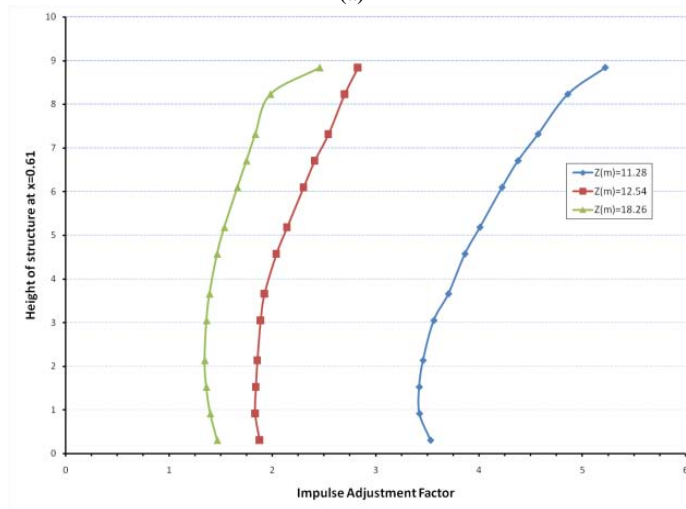
(b)
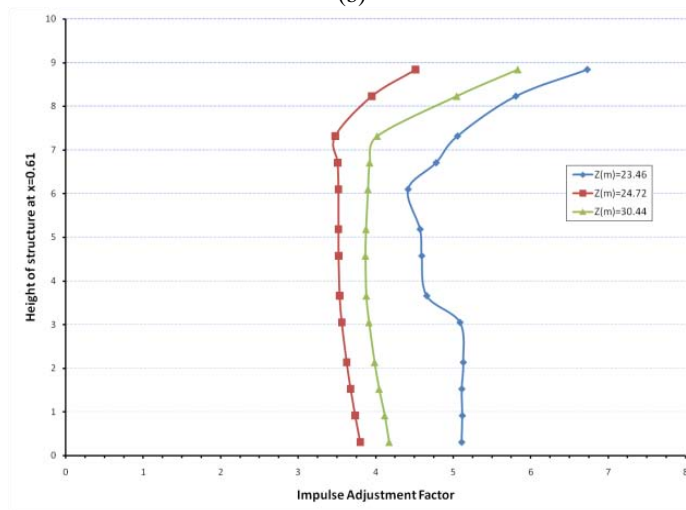
(c)

Figure B-69. Effect of Distance from Barrier to Structure, W = 910.42 kg-TNT, H = 6.10 m, (a) d_2 = 3.05 m, (b) d_2 = 10.64 m, (c) d_2 = 22.82 m

181

Appendix C: ANN SCATTER PLOTS

C.1. Evenly Spaced Grid Training Progression

C.1.1. Pressure ANN Progression – Evenly Spaced Grid
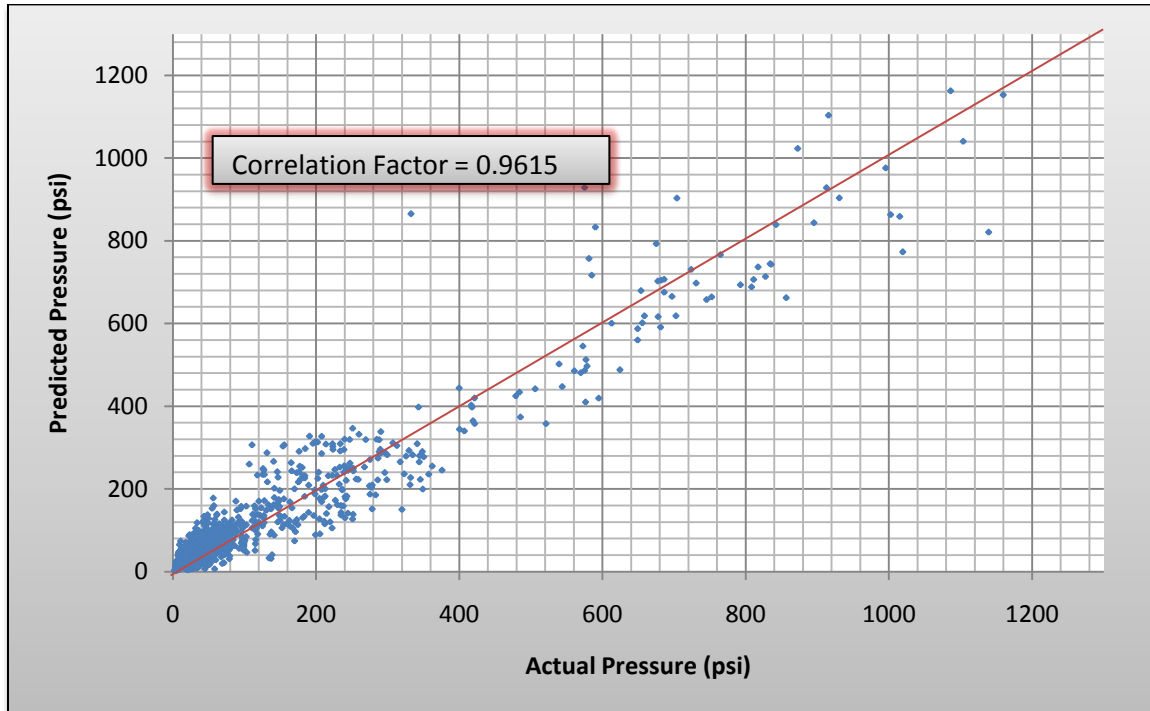
Figure C-1. Pressure ANN – 100 Neurons – Evenly Spaced Grid
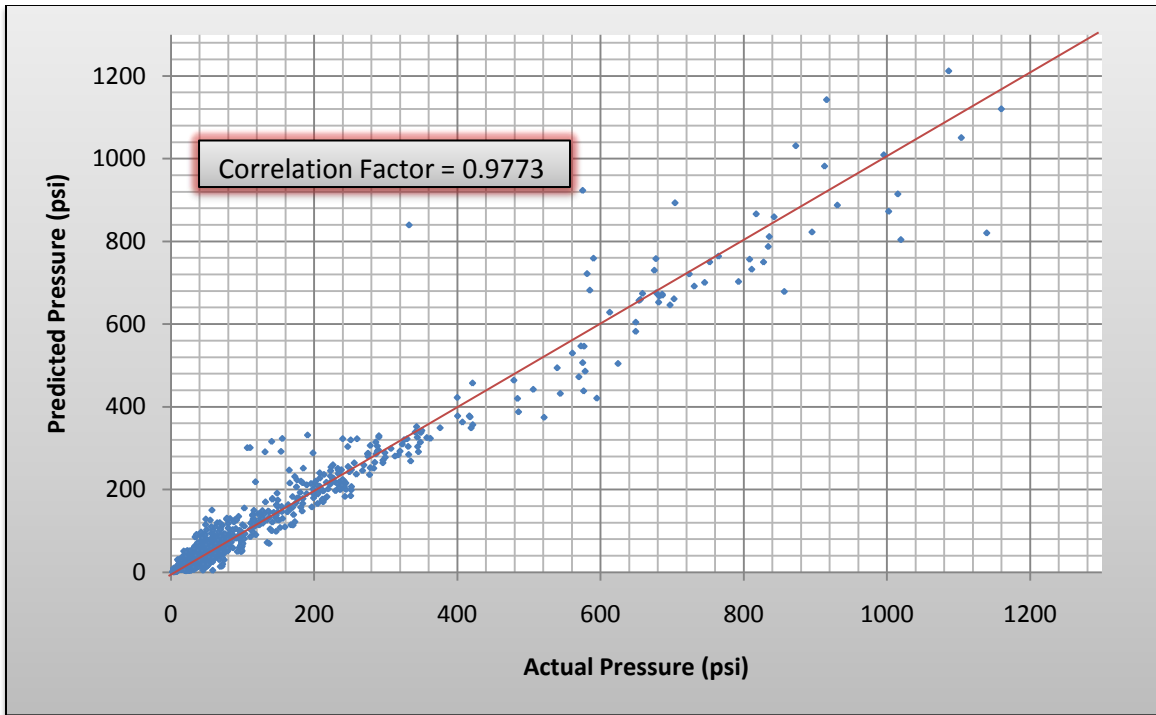
**Figure C-2. Pressure ANN – 200 Neurons – Evenly Spaced Grid**
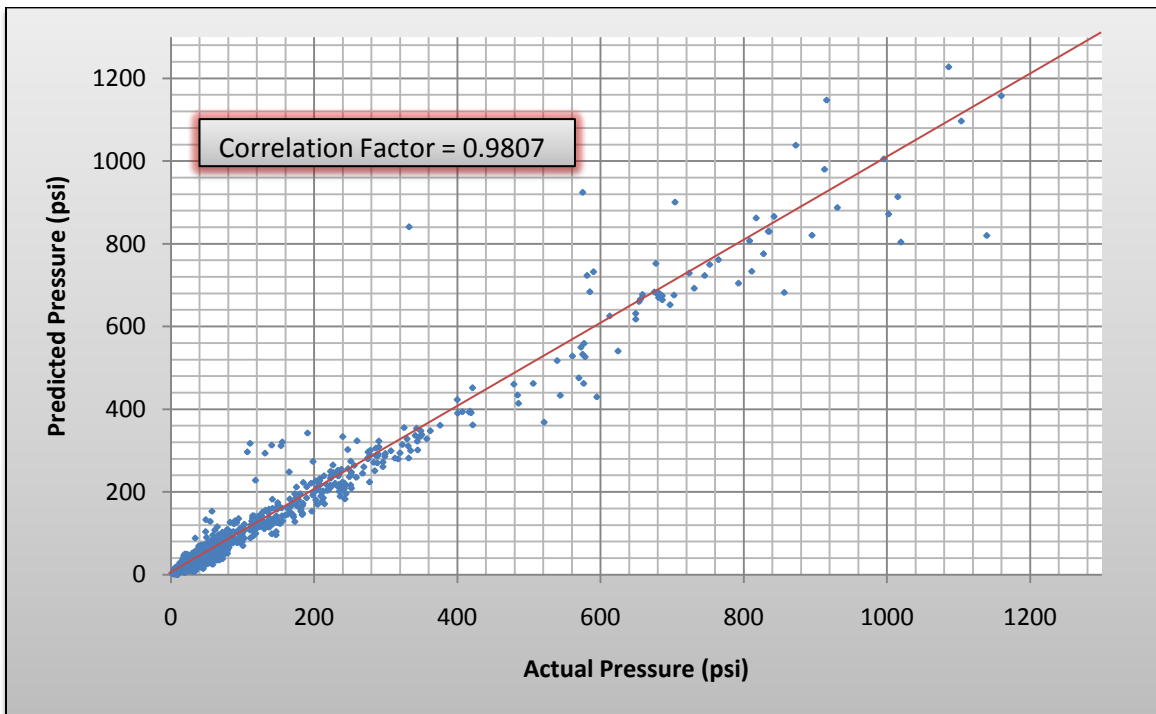
**Figure C-3. Pressure ANN – 300 Neurons – Evenly Spaced Grid**
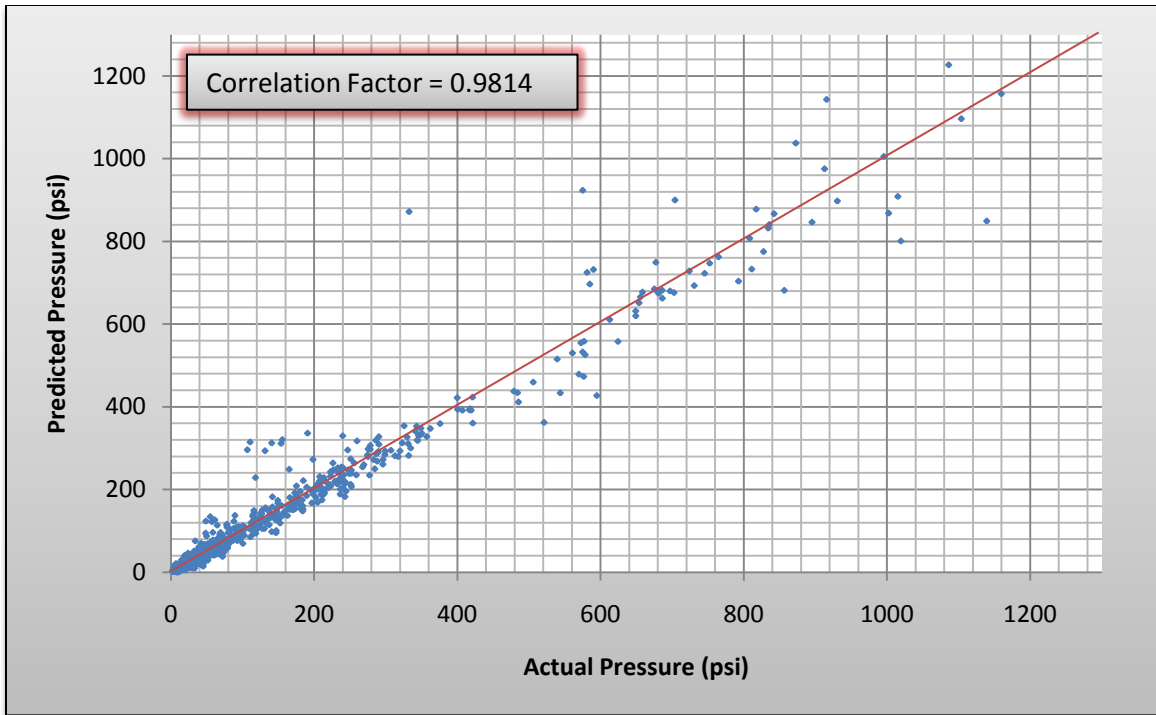
Figure C-4. Pressure ANN – 400 Neurons – Evenly Spaced Grid
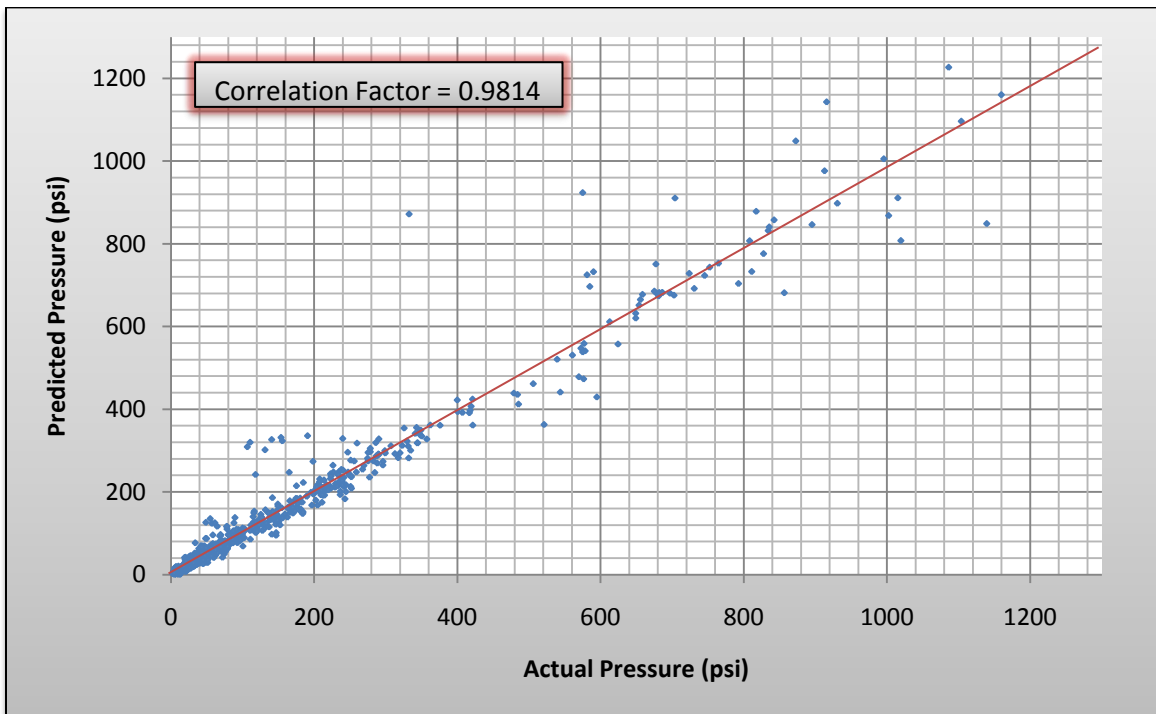
Figure C-5. Pressure ANN – 500 Neurons – Evenly Spaced Grid

184

C.1.2. Impulse ANN Progression – Evenly Spaced Grid
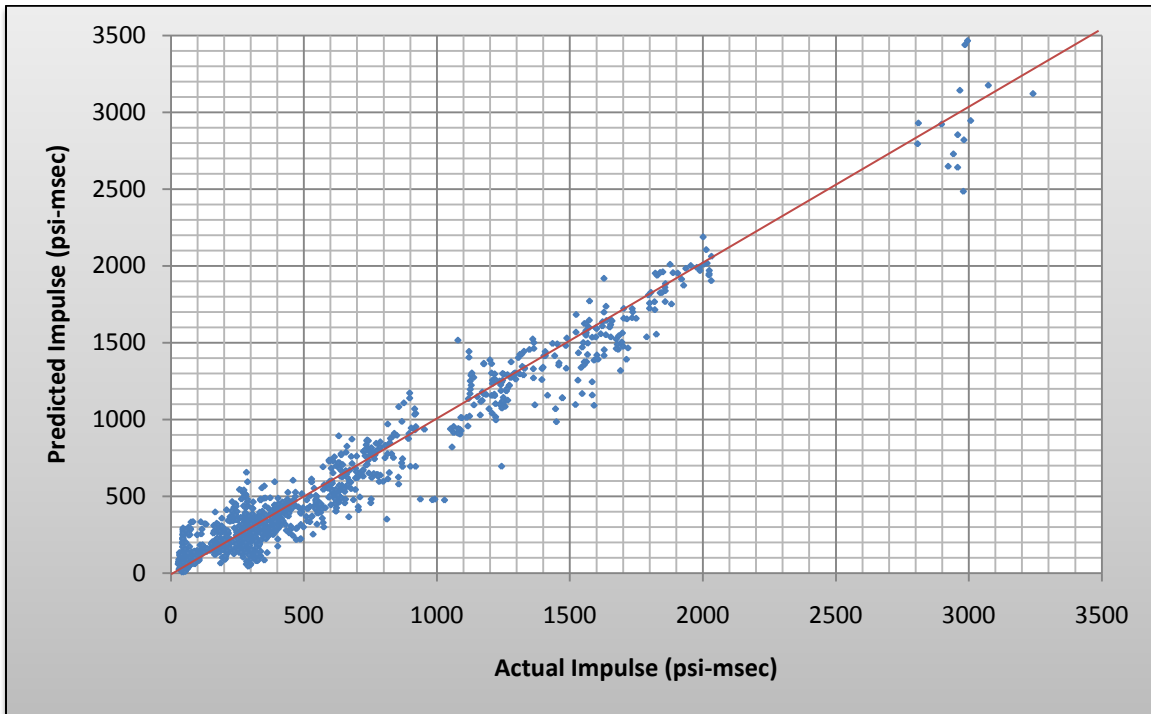
Figure C-6. Impulse ANN – 100 Neurons – Evenly Spaced Grid
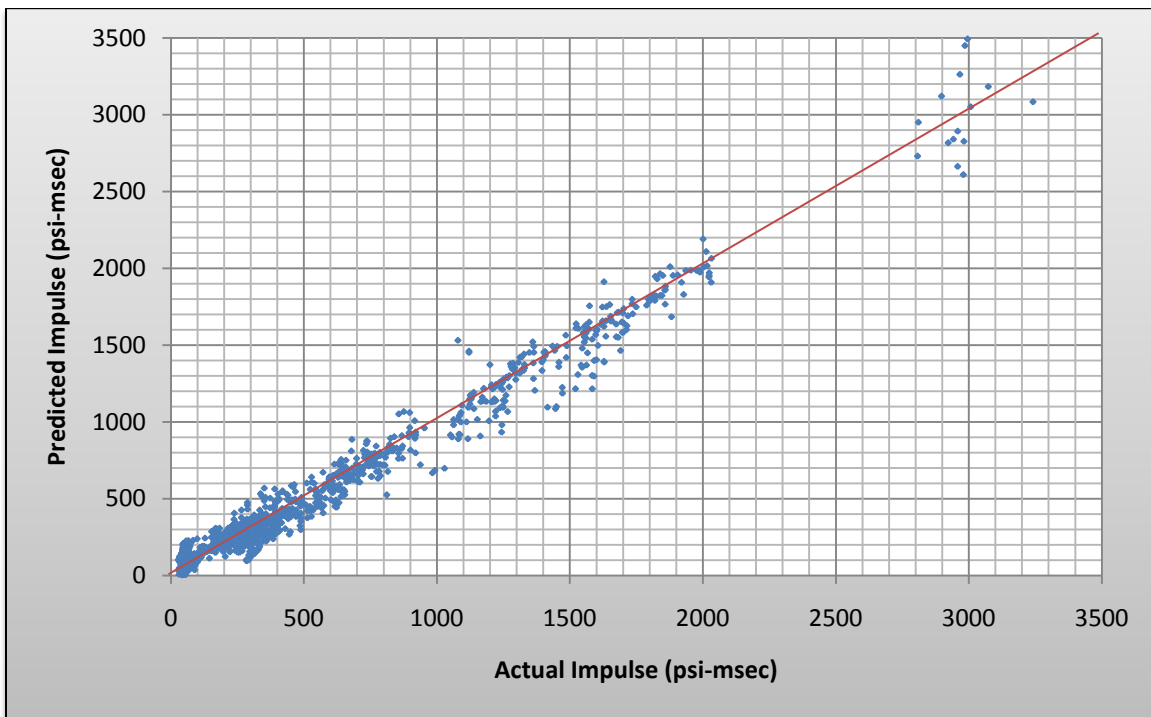
Figure C-7. Impulse ANN – 200 Neurons – Evenly Spaced Grid
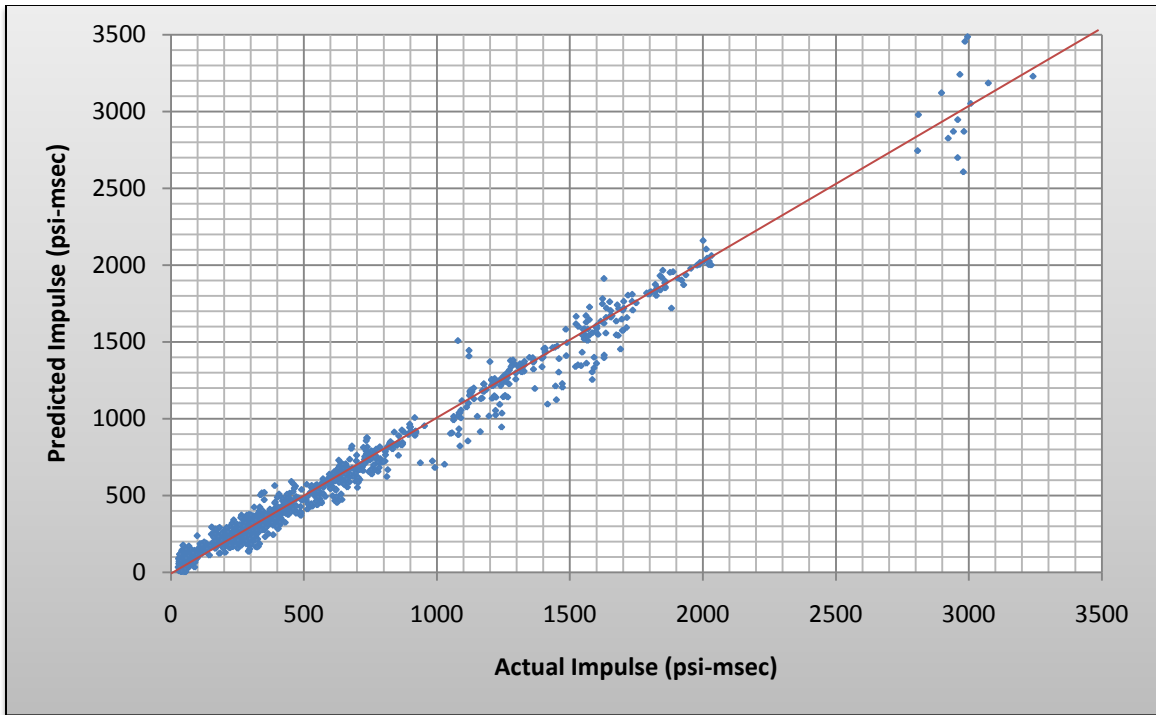
Figure C-8. Impulse ANN – 300 Neurons – Evenly Spaced Grid
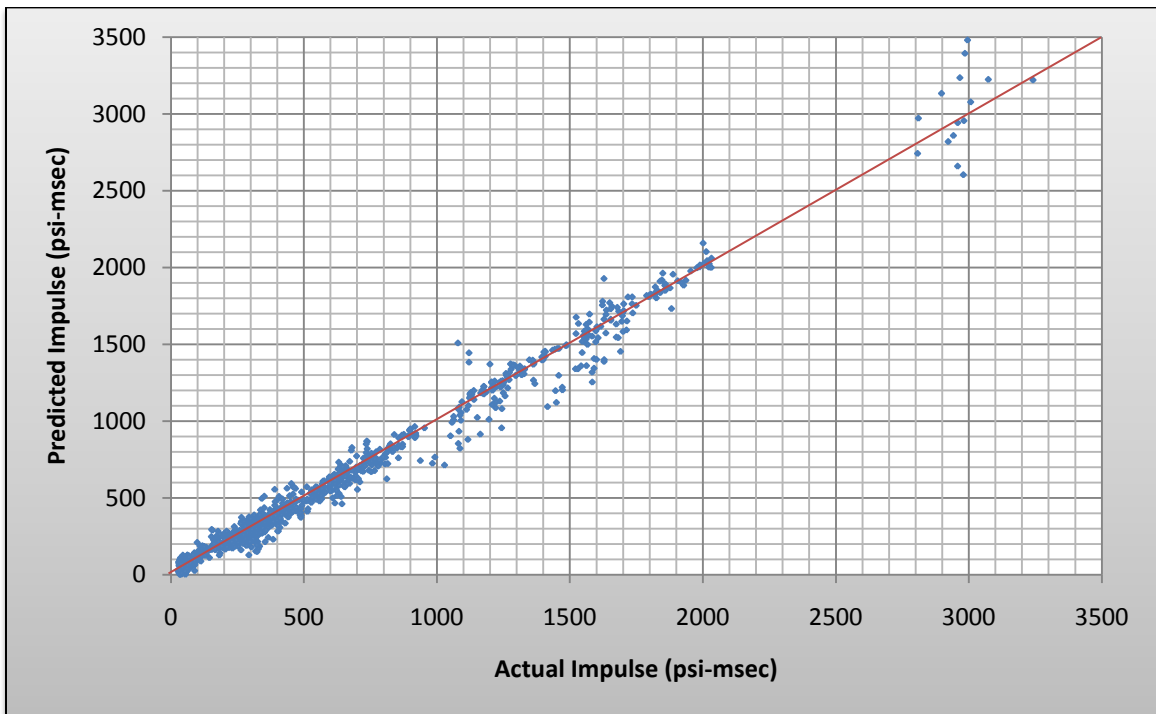
**Figure C-9. Impulse ANN – 400 Neurons – Evenly Spaced Grid**
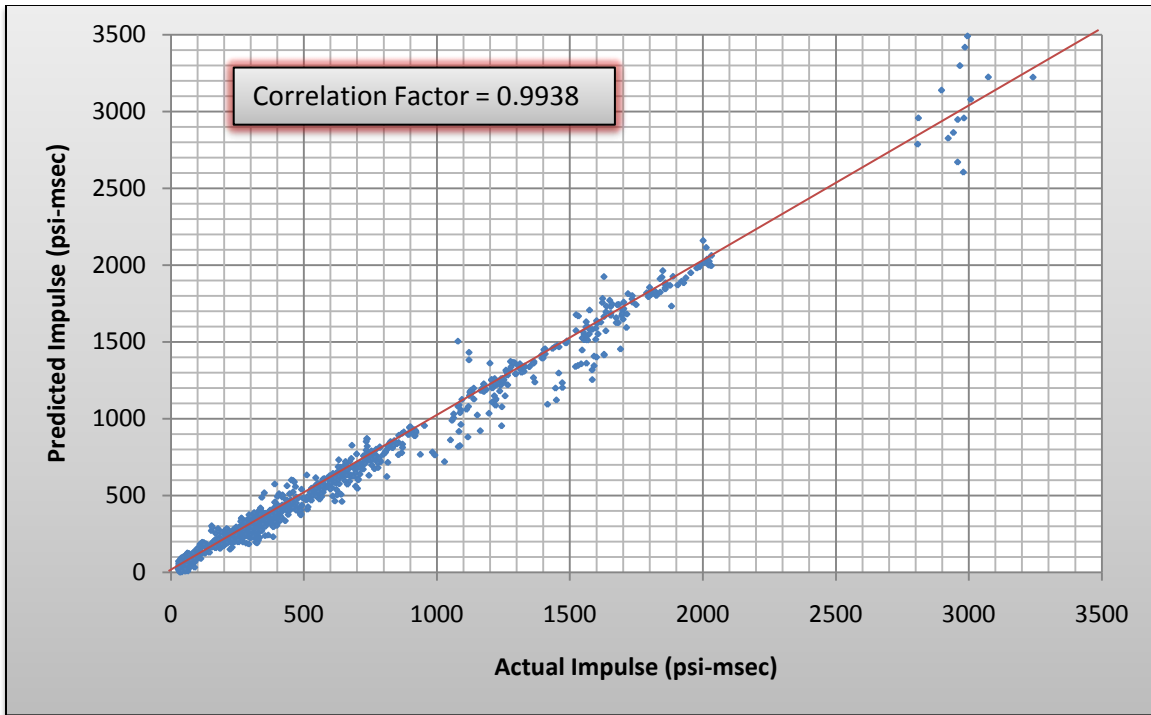
**Figure C-10. Impulse ANN – 500 Neurons – Evenly Spaced Grid**

## C.1.3. Time of Arrival (TOA) ANN Progression – Evenly Spaced Grid
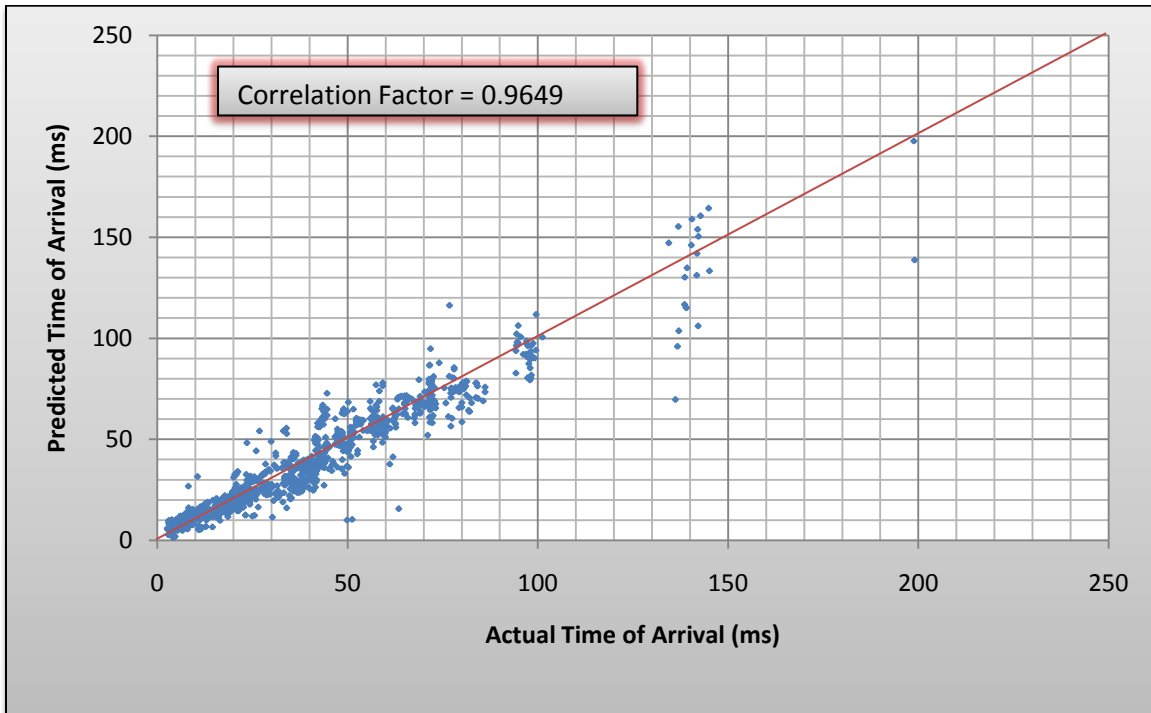
Figure C-11. TOA ANN – 100 Neurons – Evenly Spaced Grid
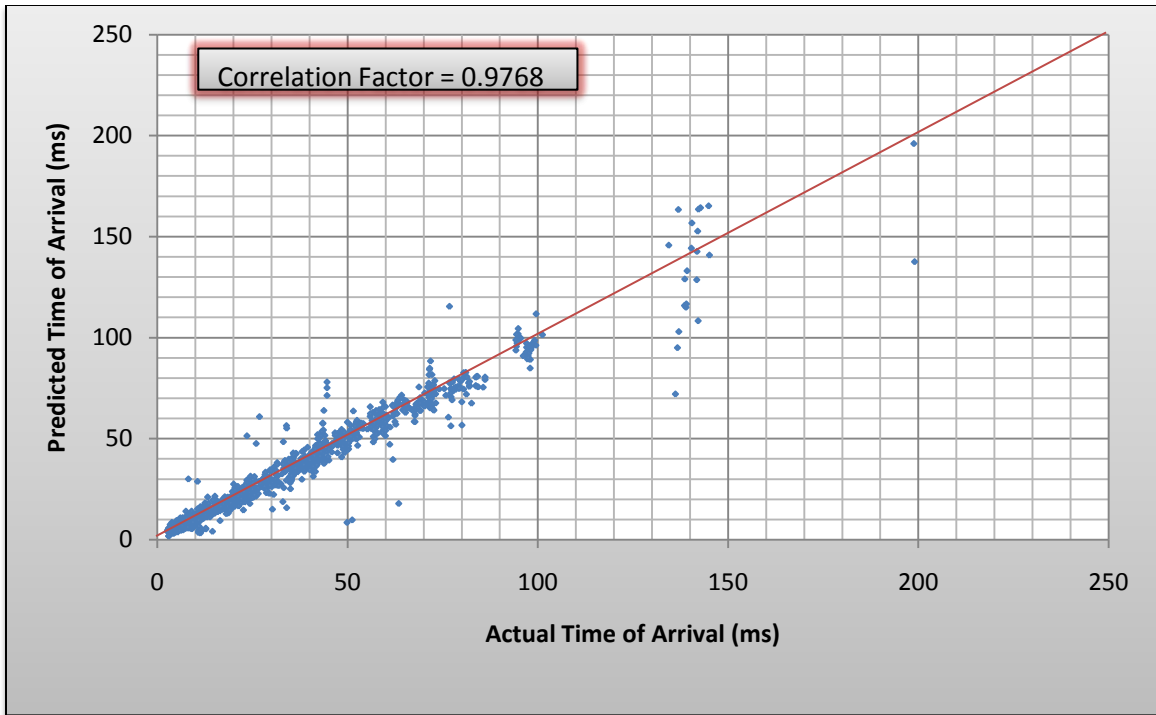
Figure C-12. TOA ANN – 200 Neurons – Evenly Spaced Grid
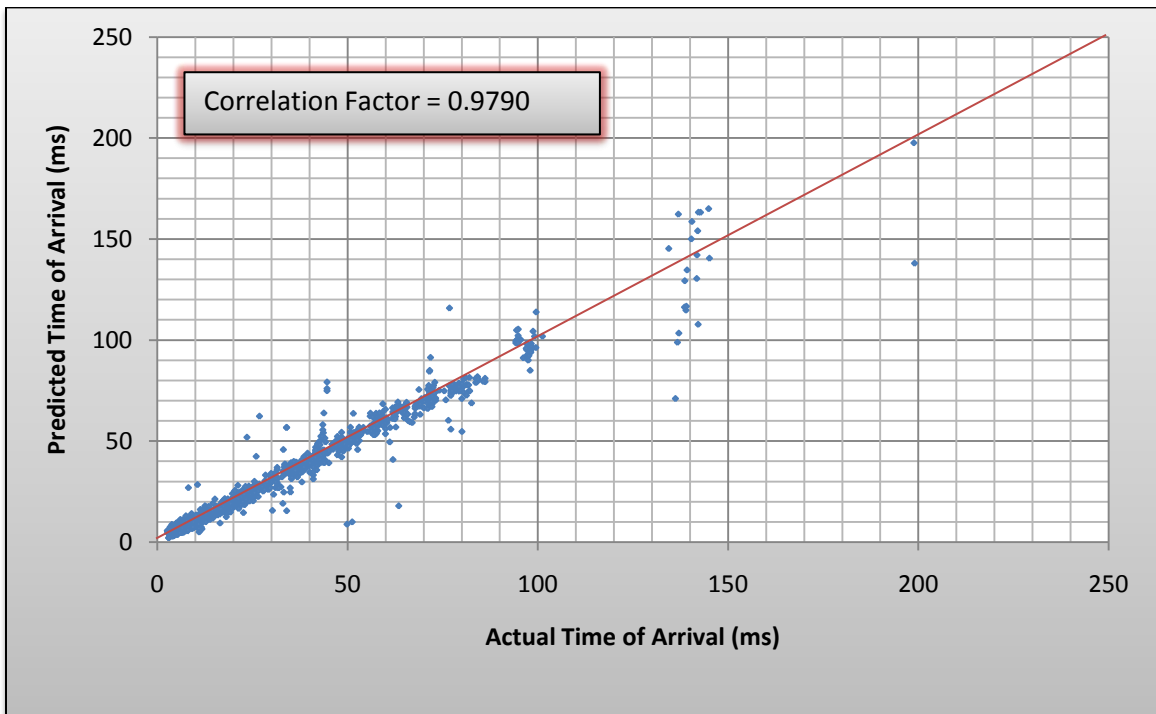
Figure C-13. TOA ANN – 300 Neurons – Evenly Spaced Grid
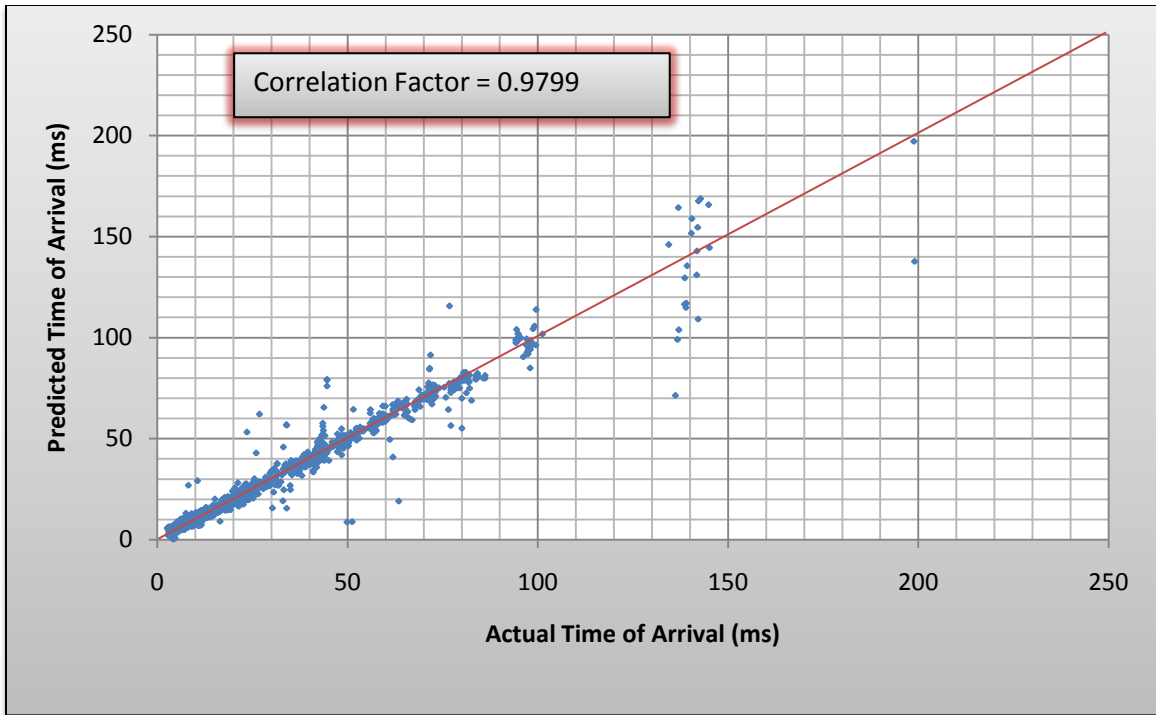
Figure C-14. TOA ANN – 400 Neurons – Evenly Spaced Grid
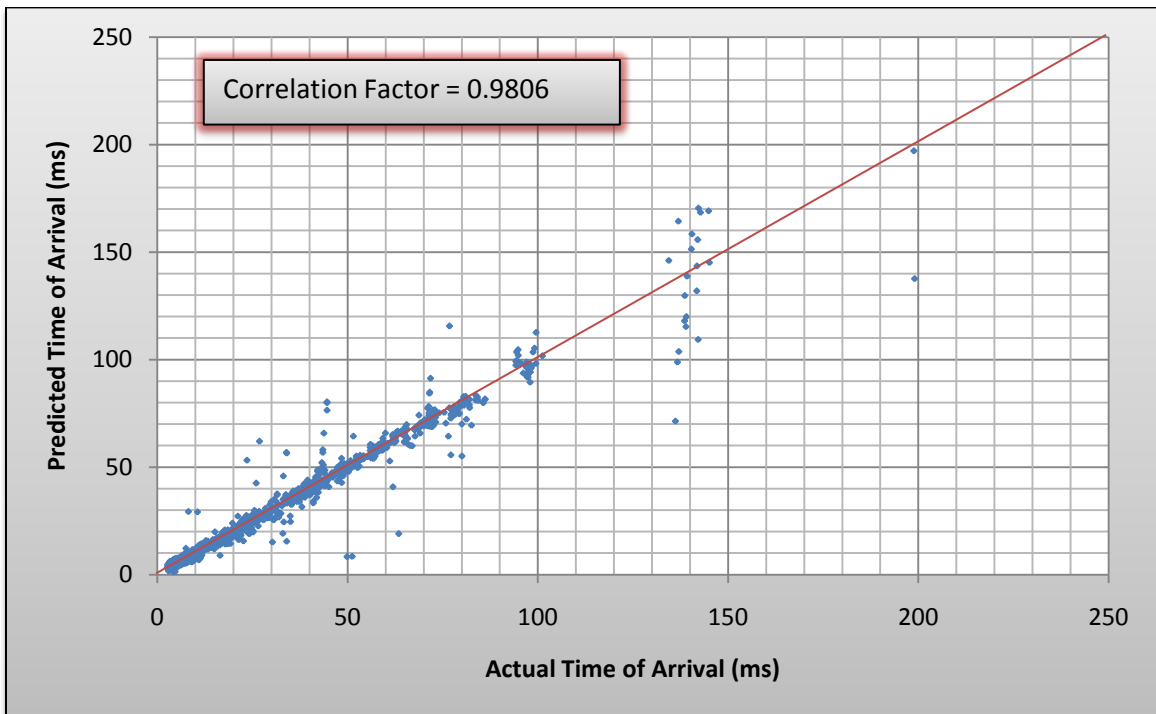
Figure C-15. TOA ANN – 500 Neurons – Evenly Spaced Grid

C.1.4. Positive Phase Duration ANN Progression – Evenly Spaced Grid
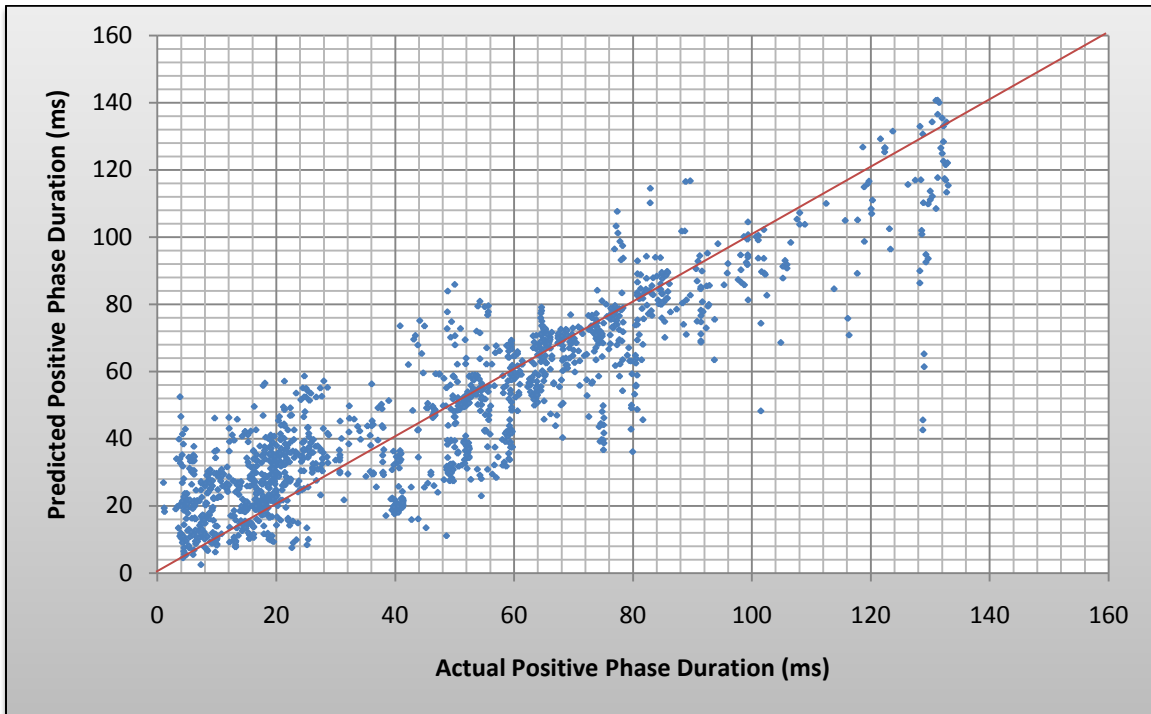
**Figure C-16. Duration ANN – 100 Neurons – Evenly Spaced Grid**
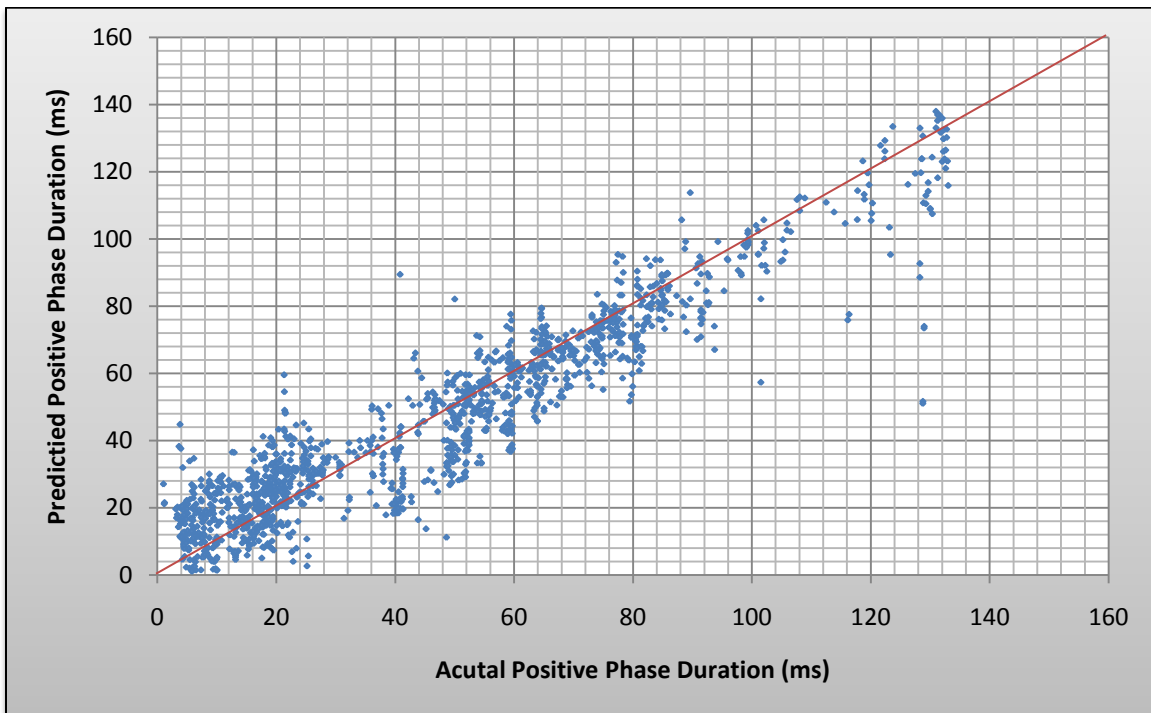
Figure C-17. Duration ANN – 200 Neurons – Evenly Spaced Grid
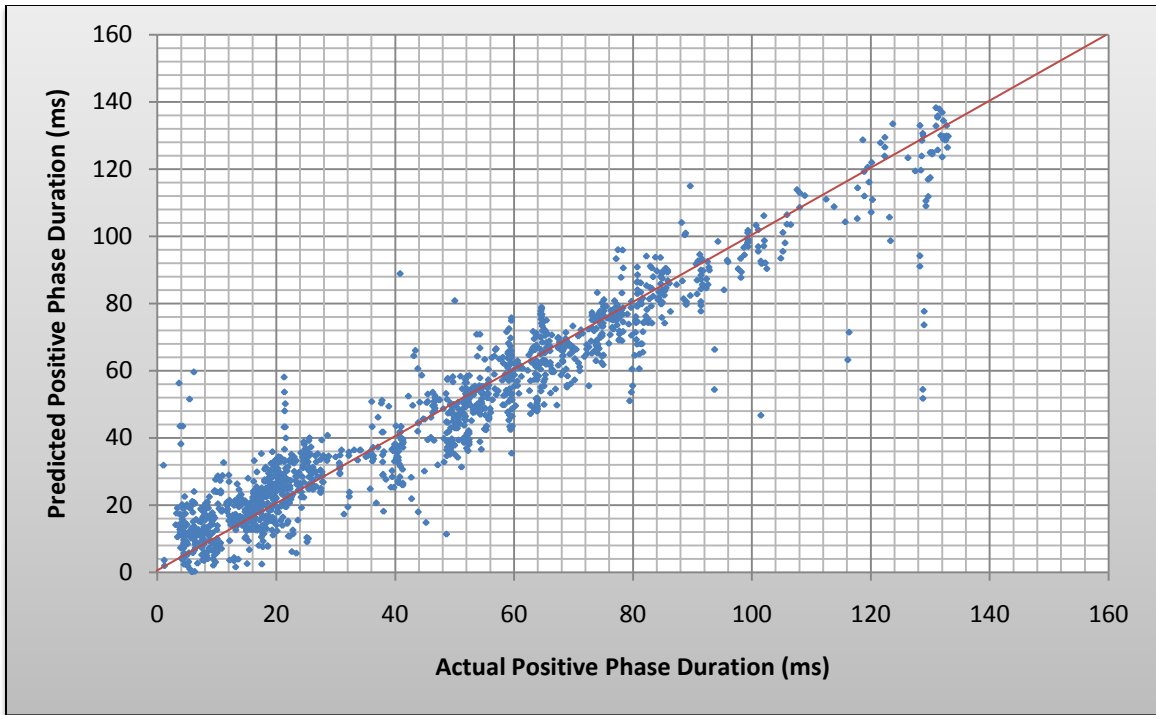
Figure C-18. Duration ANN – 300 Neurons – Evenly Spaced Grid
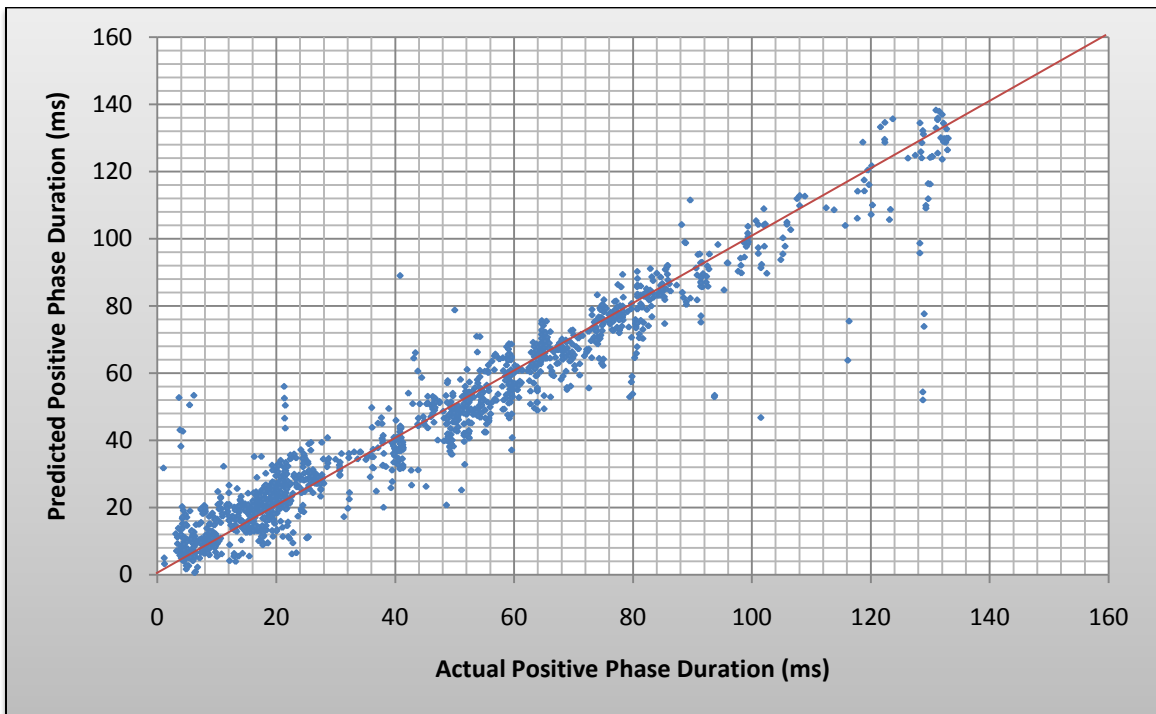
Figure C-19. Duration ANN – 400 Neurons – Evenly Spaced Grid

191
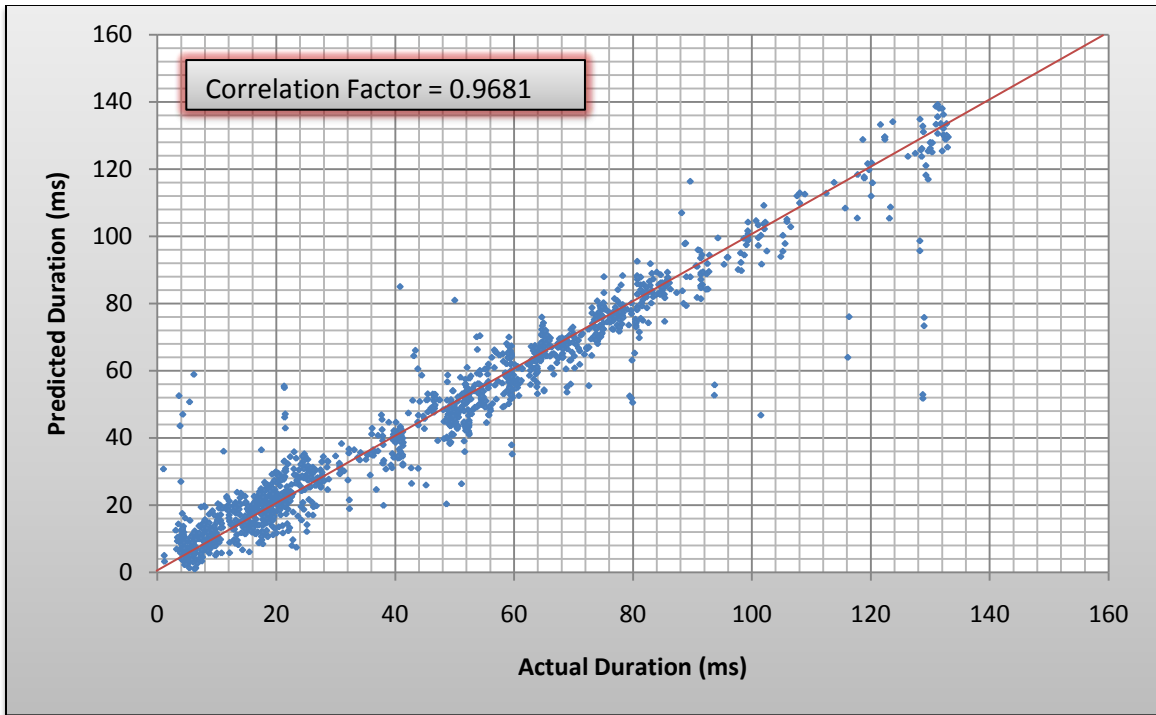
Figure C-20. Duration ANN – 500 Neurons – Evenly Spaced Grid

C.2. BIASED GRID TRAINING PROGRESSION

C.2.1. Pressure ANN Progression – Biased Grid
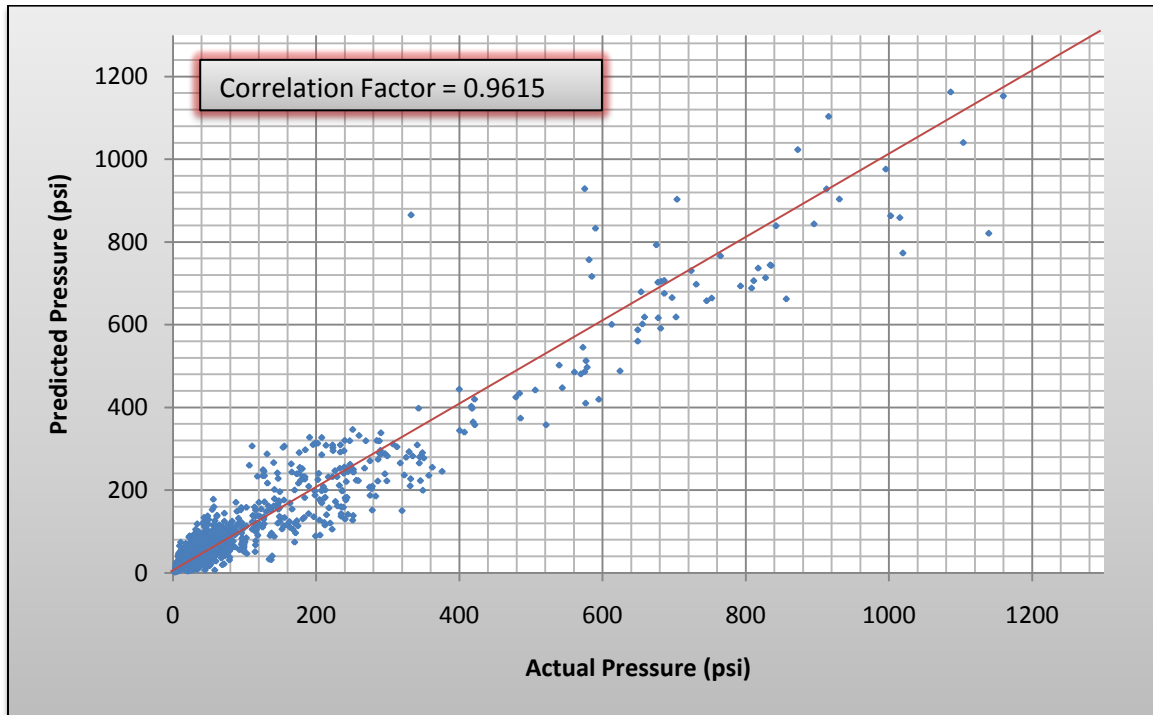
**Figure C-21. Pressure ANN – 100 Neurons – Biased Grid**
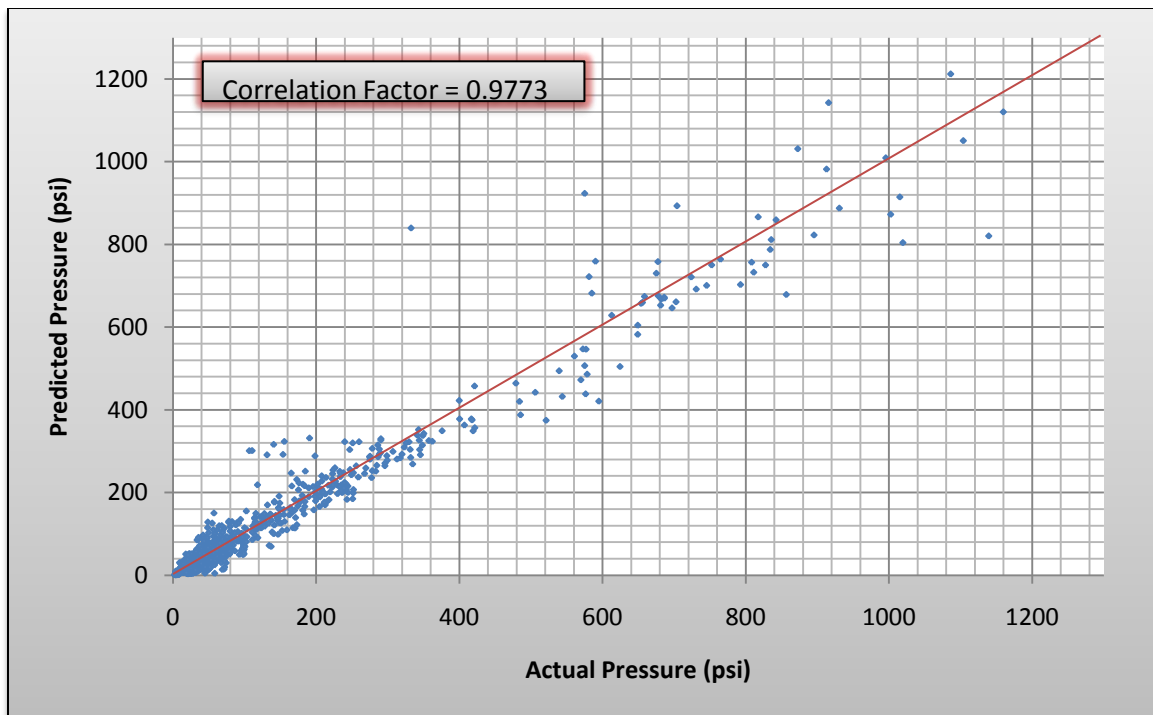
Figure C-22. Pressure ANN – 200 Neurons – Biased Grid
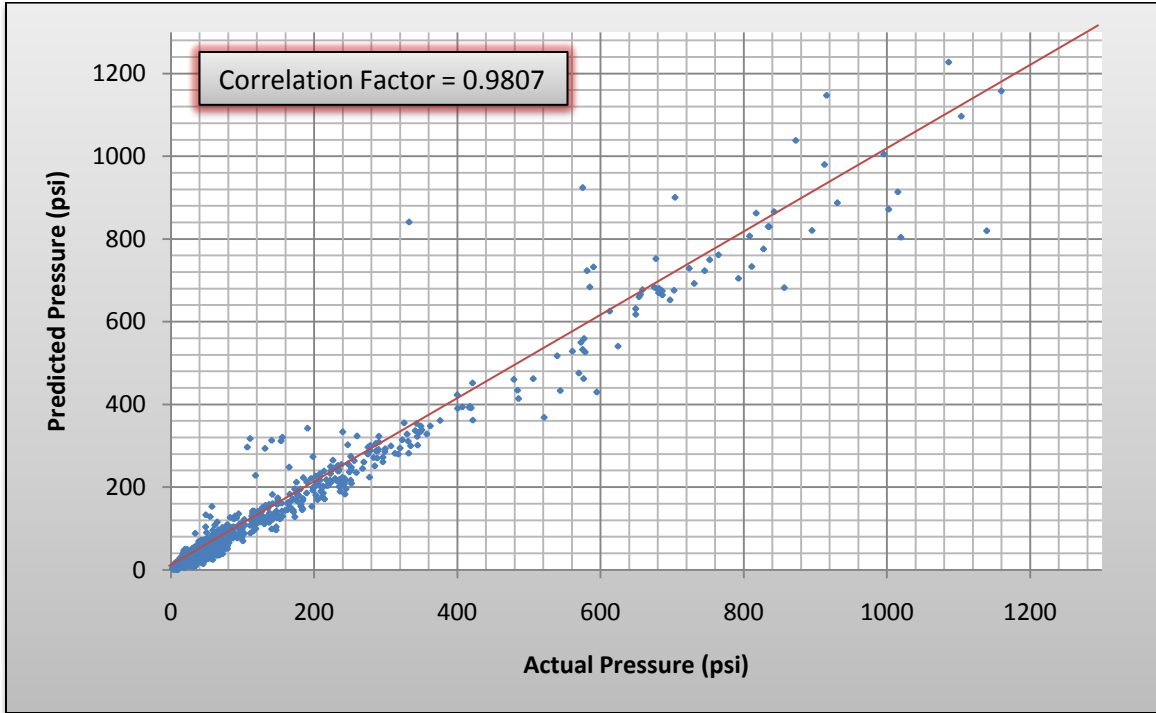
**Figure C-23. Pressure ANN – 300 Neurons – Biased Grid**
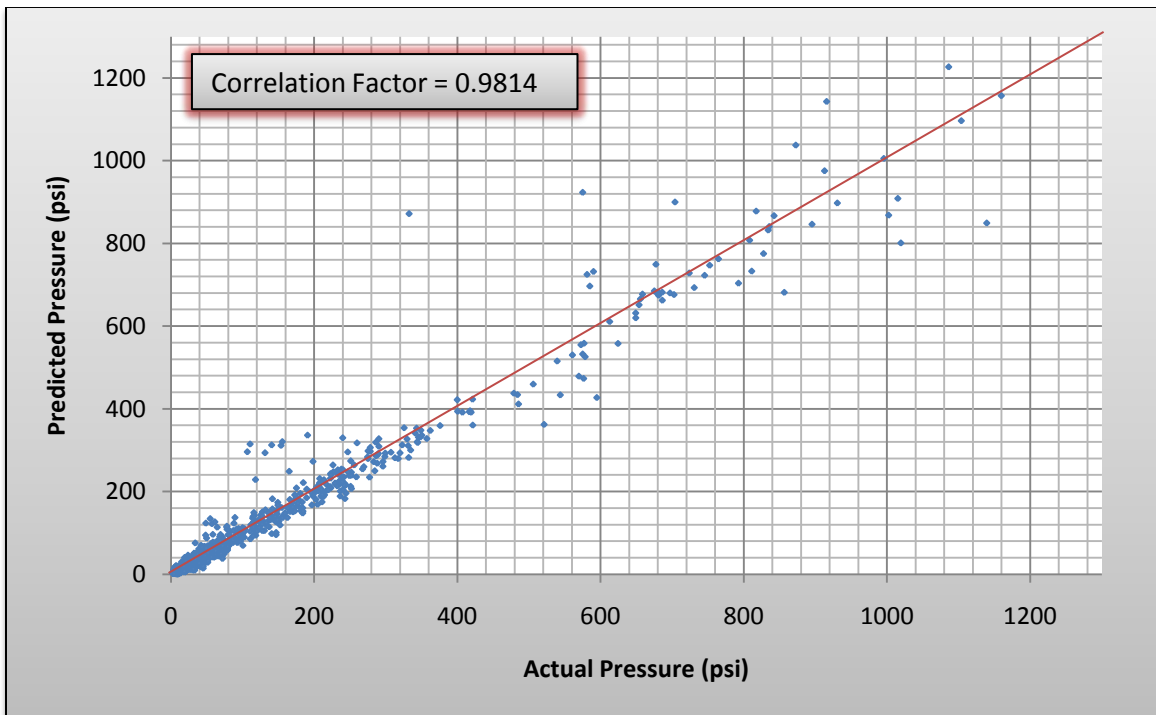
**Figure C-24. Pressure ANN – 400 Neurons – Biased Grid**
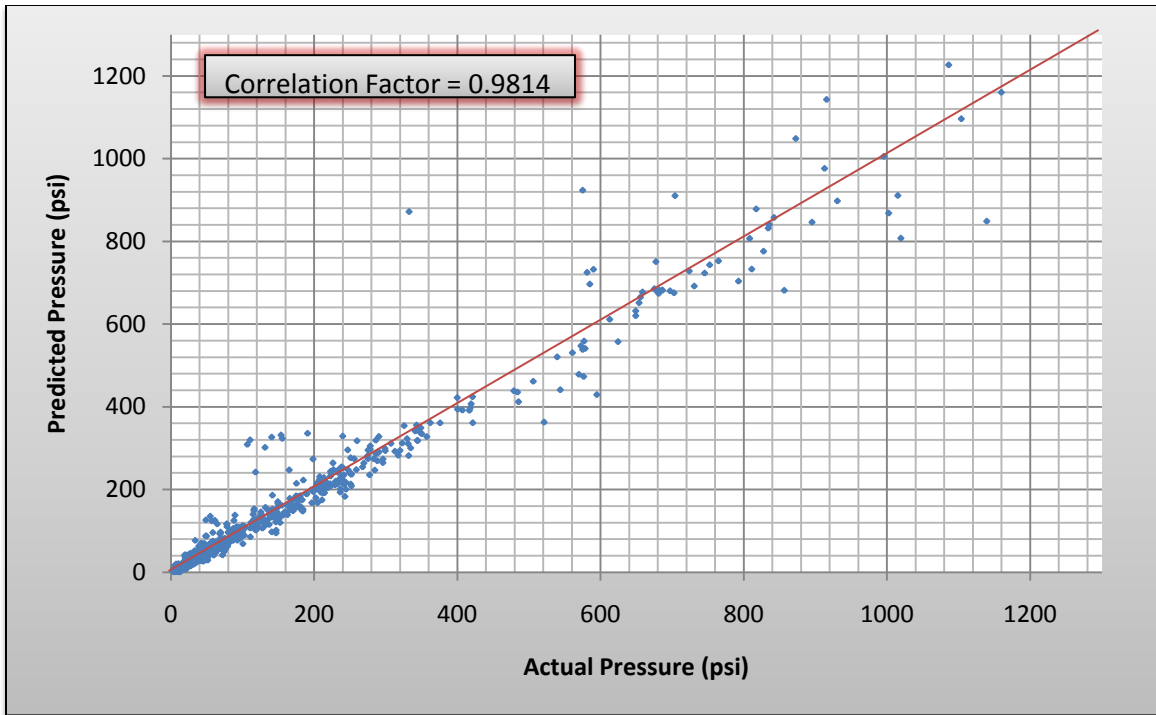
**Figure C-25. Pressure ANN – 500 Neurons – Biased Grid**

C.2.2. Impulse ANN Progression – Biased Grid
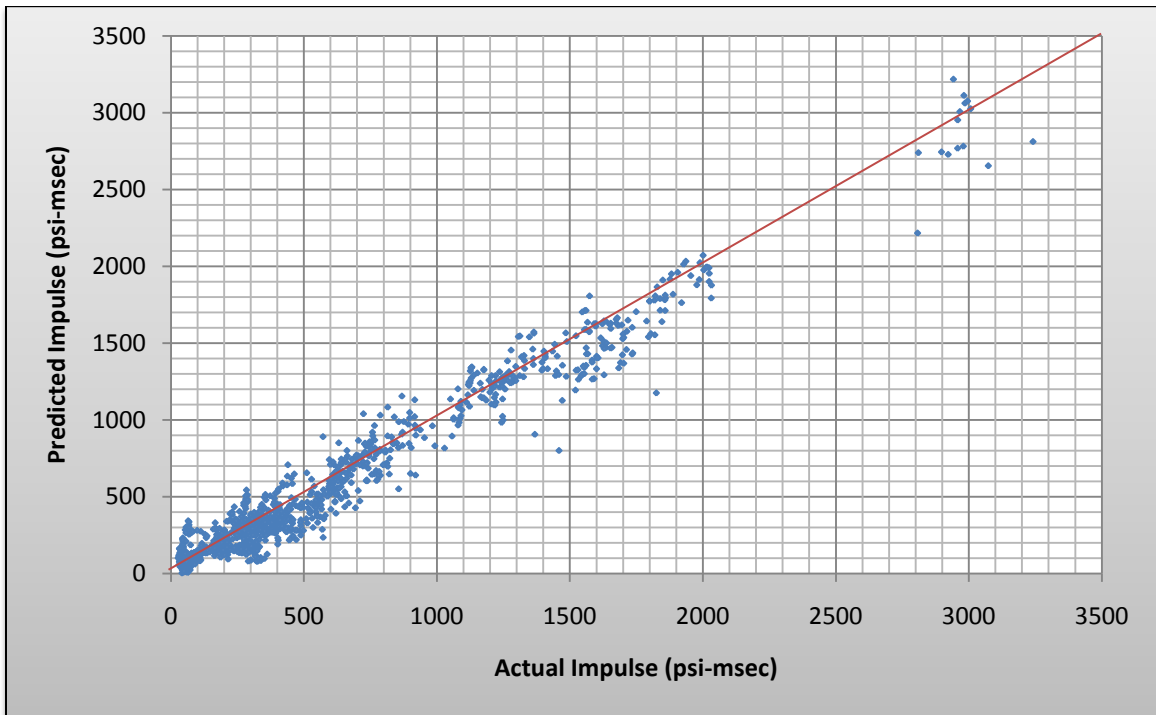
**Figure C-26. Impulse ANN – 100 Neurons – Biased Grid**
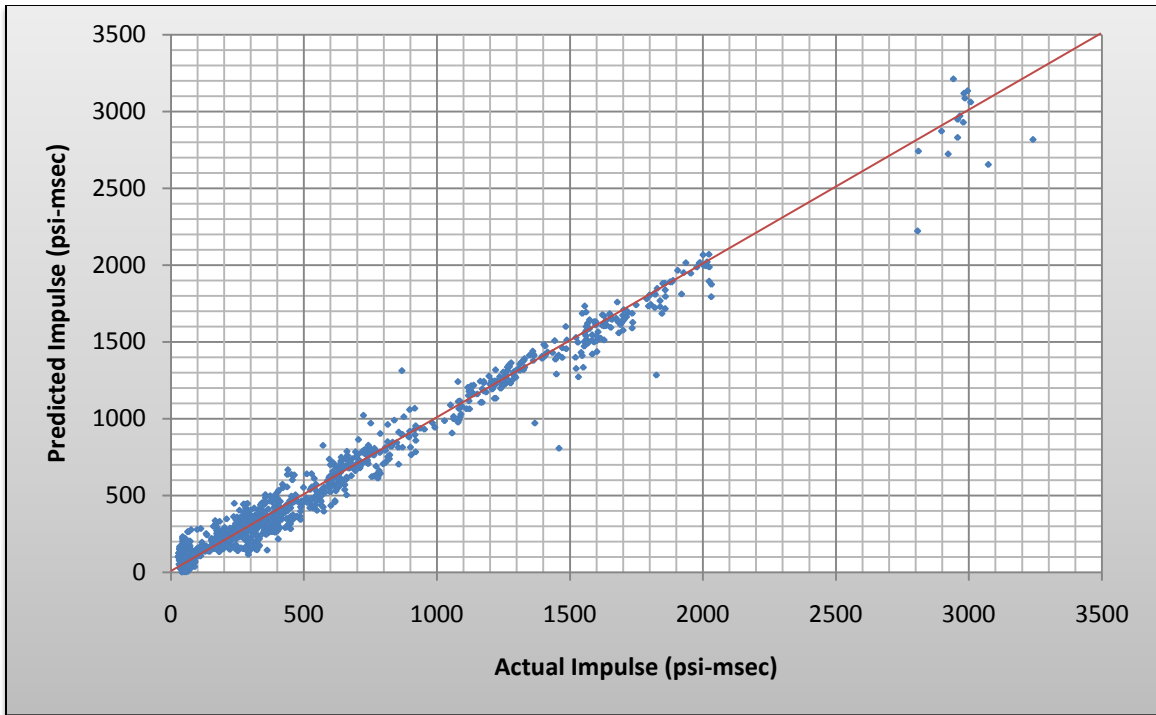
Figure C-27. Impulse ANN – 200 Neurons – Biased Grid
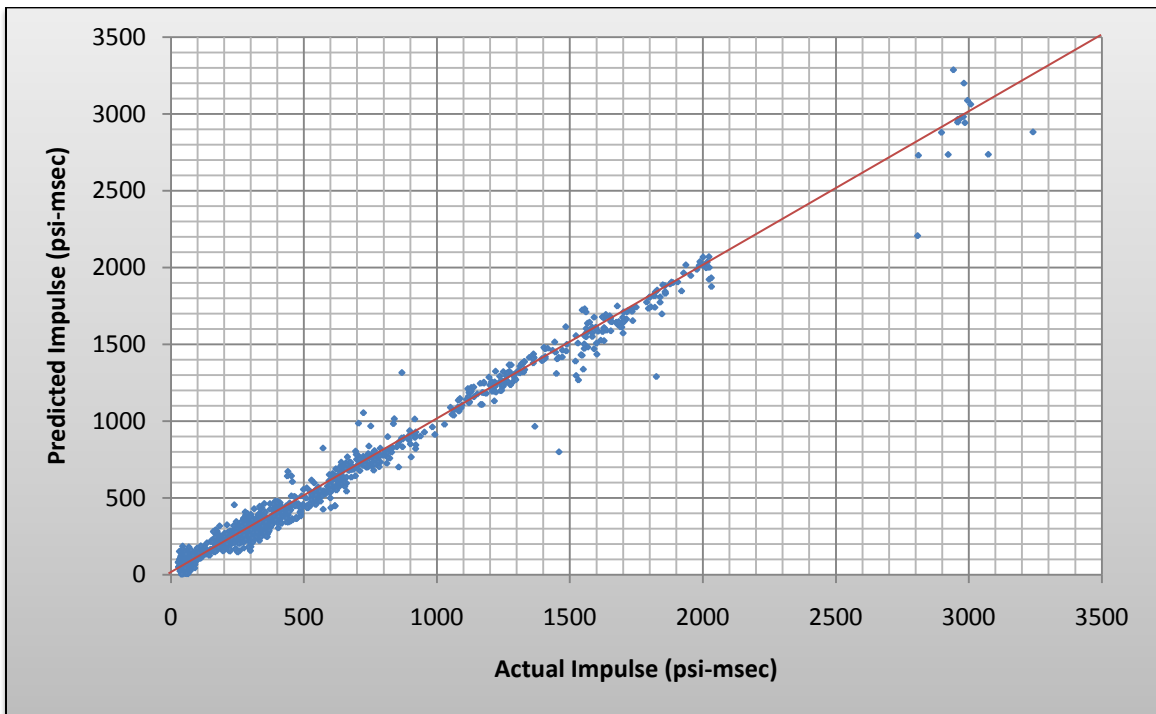
Figure C-28. Impulse ANN – 300 Neurons – Biased Grid
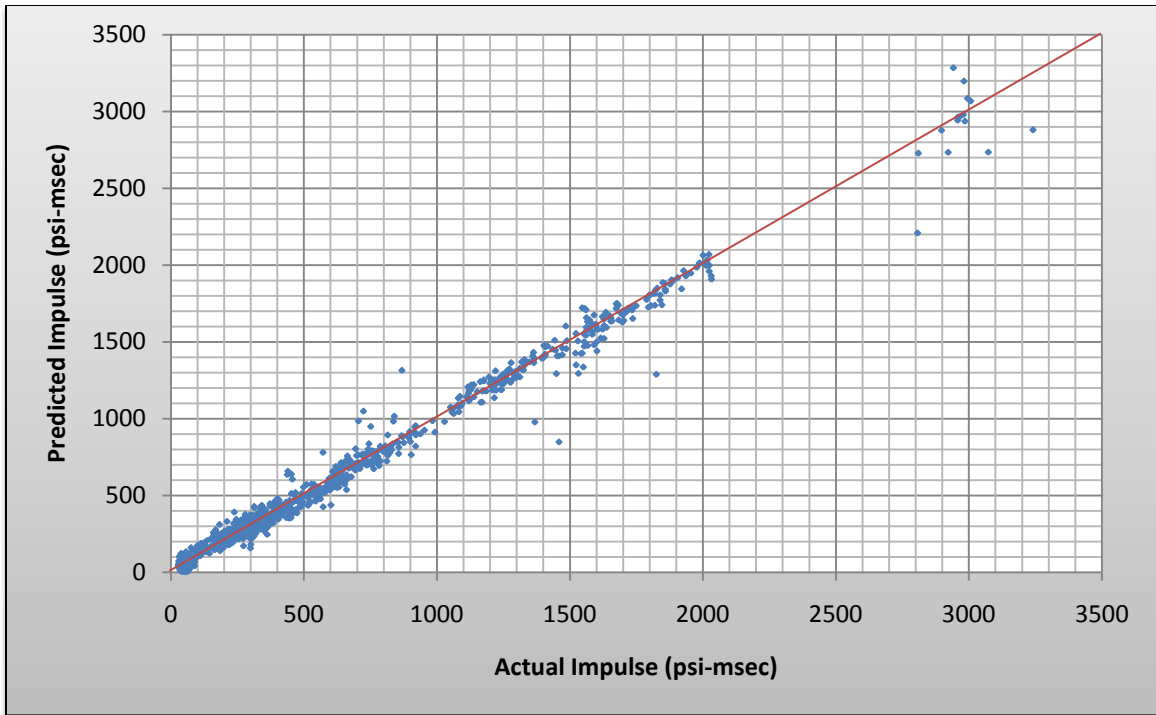
Figure C-29. Impulse ANN – 400 Neurons – Biased Grid

Correlation Factor = 0.9938
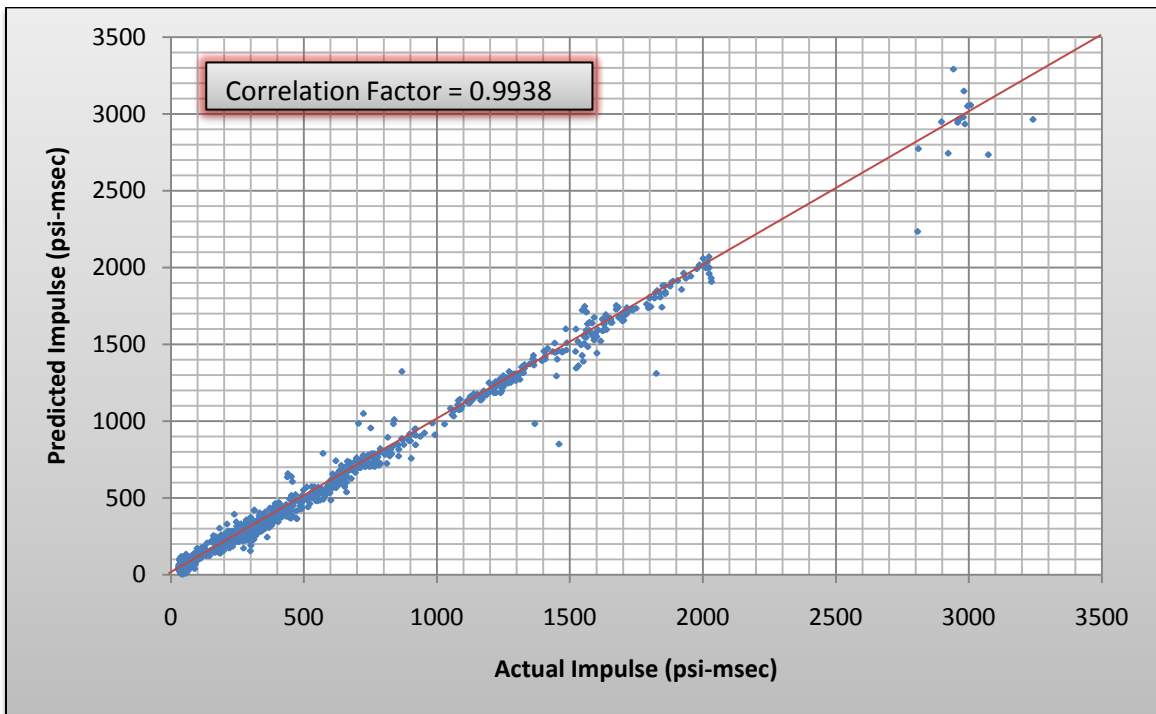
Figure C-30. Impulse ANN – 500 Neurons – Biased Grid

197

C.2.3. Time of Arrival (TOA)ANN Progression – Biased Grid
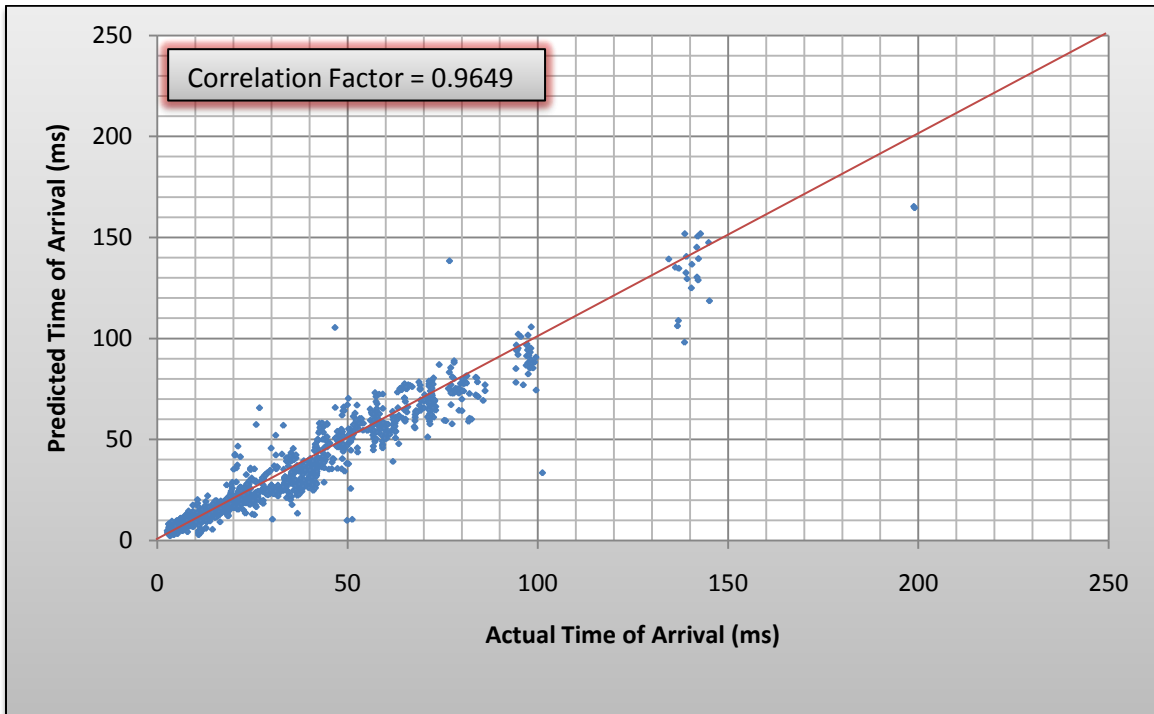
Figure C-31. TOA ANN – 100 Neurons – Biased Grid
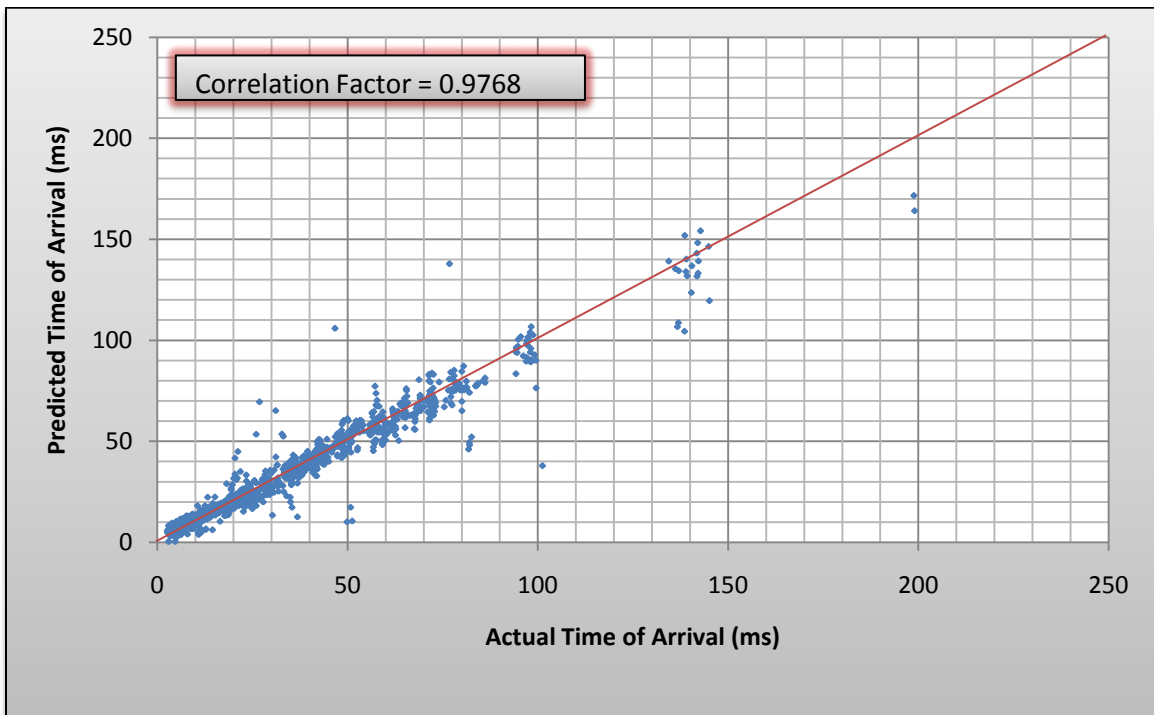
Figure C-32. TOA ANN – 200 Neurons – Biased Grid
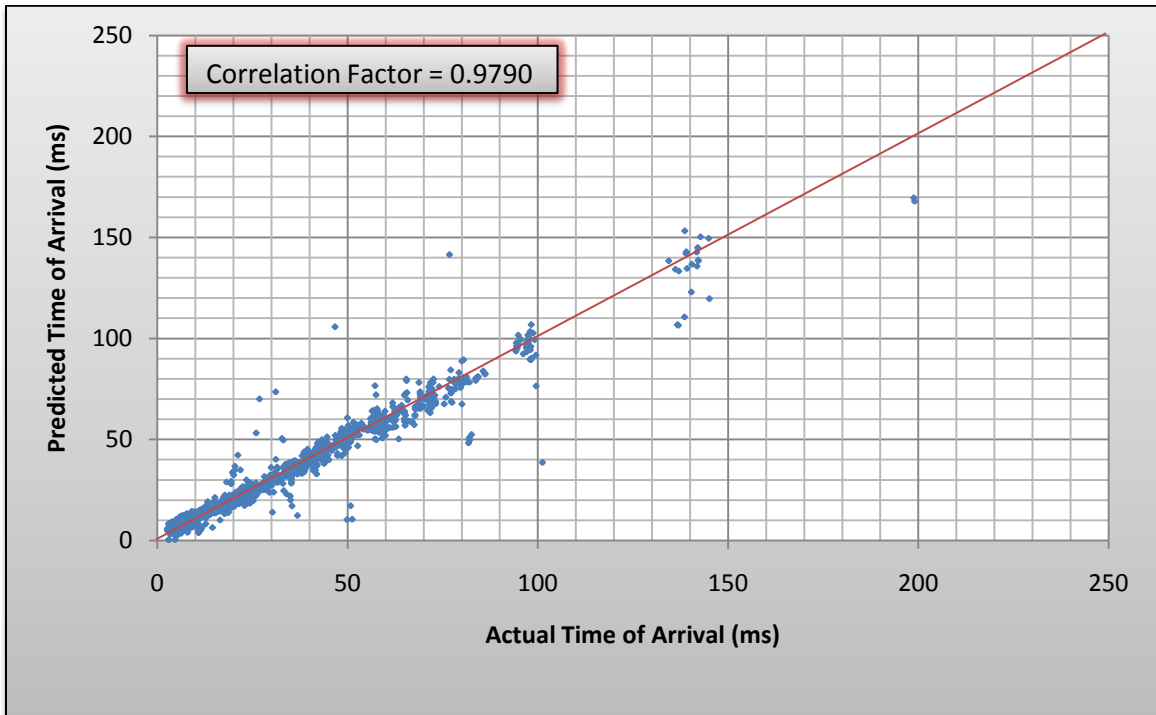
Figure C-33. TOA ANN – 300 Neurons – Biased Grid
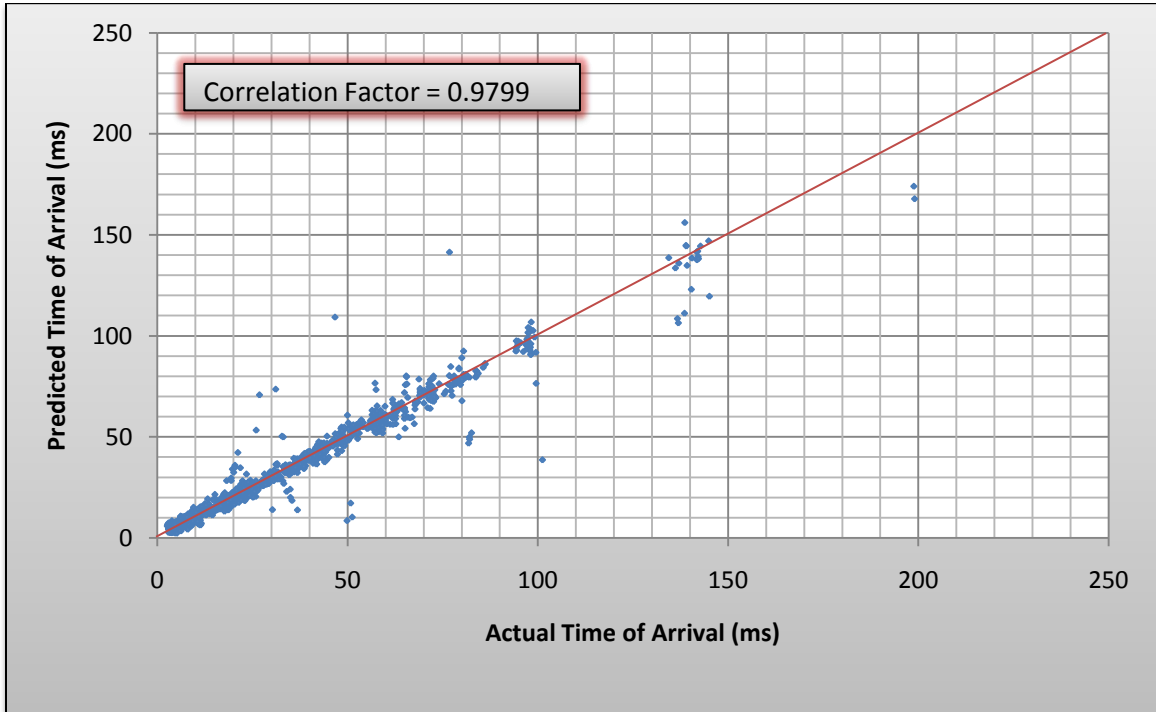
Figure C-34. TOA ANN – 400 Neurons – Biased Grid

199
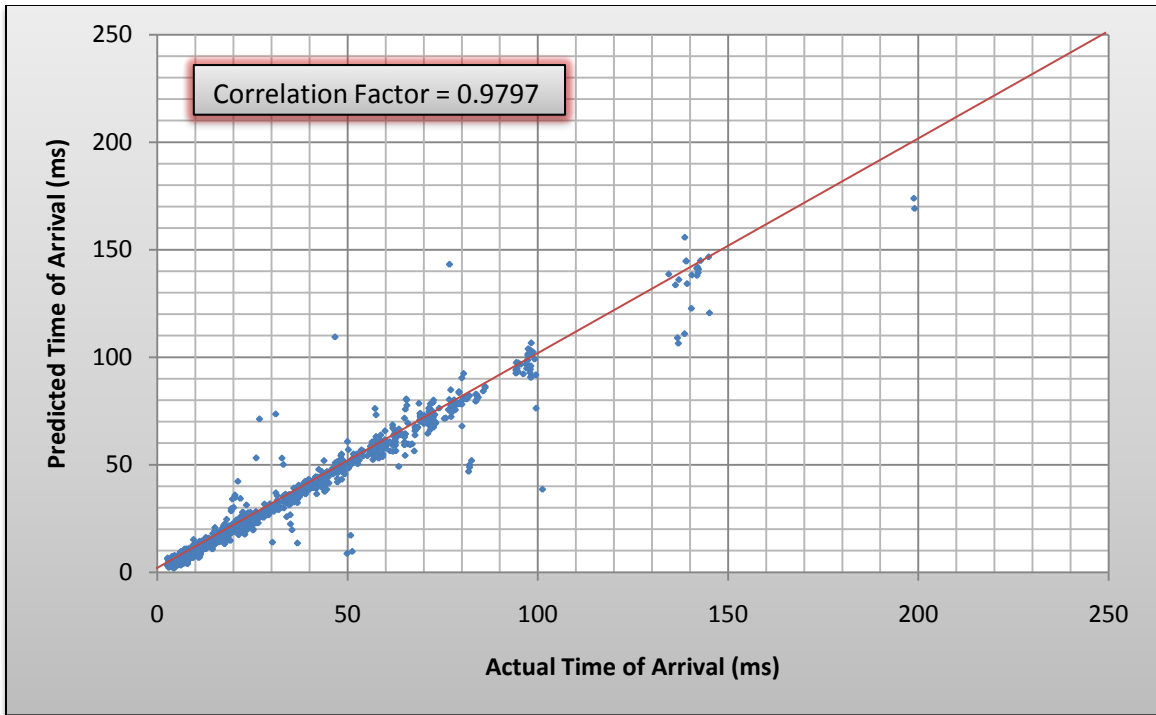
Figure C-35. TOA ANN – 500 Neurons – Biased Grid

C.2.4. Duration ANN Progression – Biased Grid
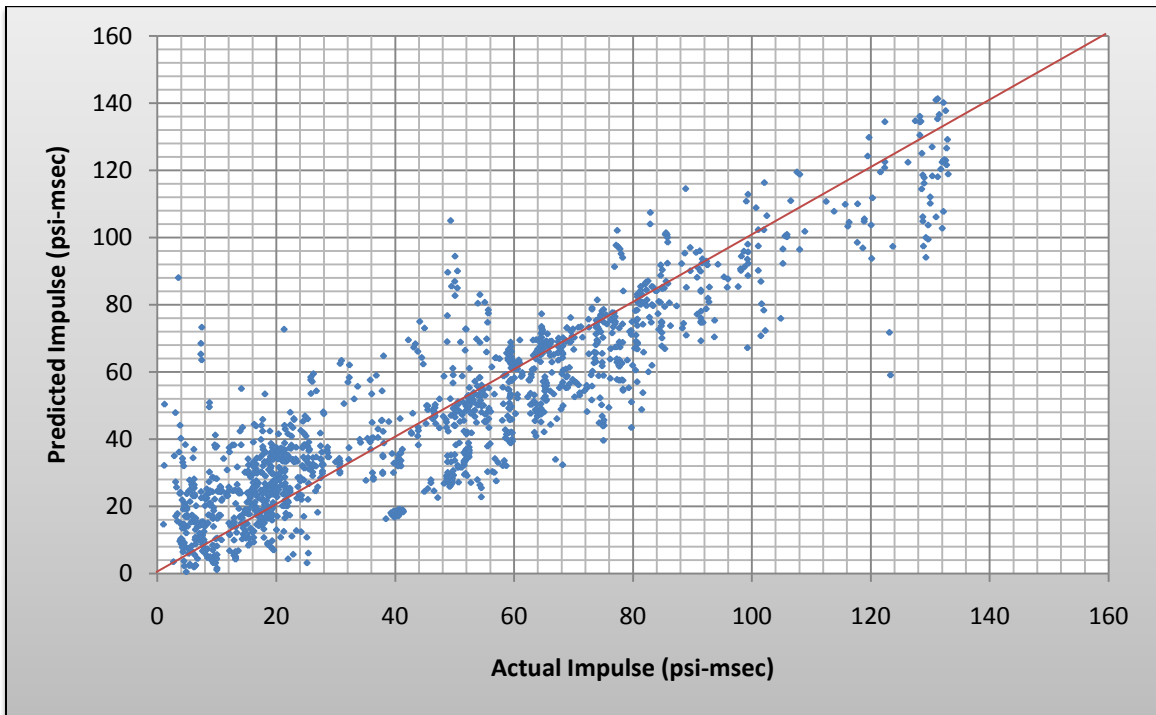
Figure C-36. Duration ANN – 100 Neurons – Biased Grid
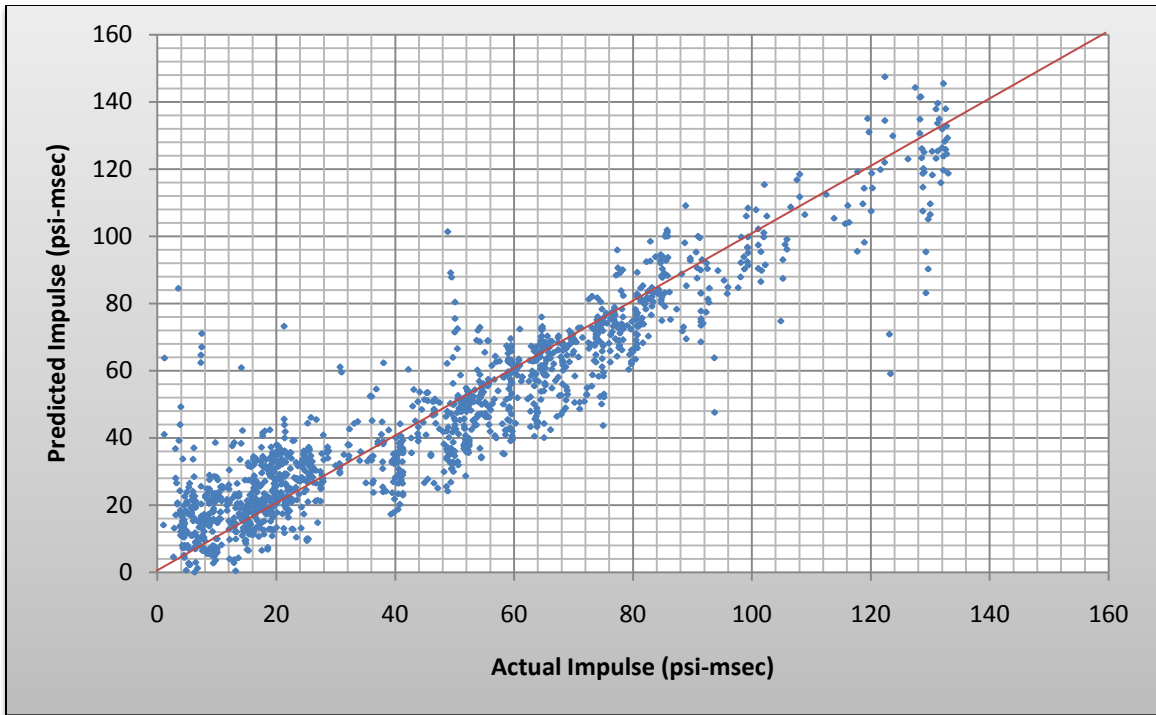
Figure C-37. Duration ANN – 200 Neurons – Biased Grid
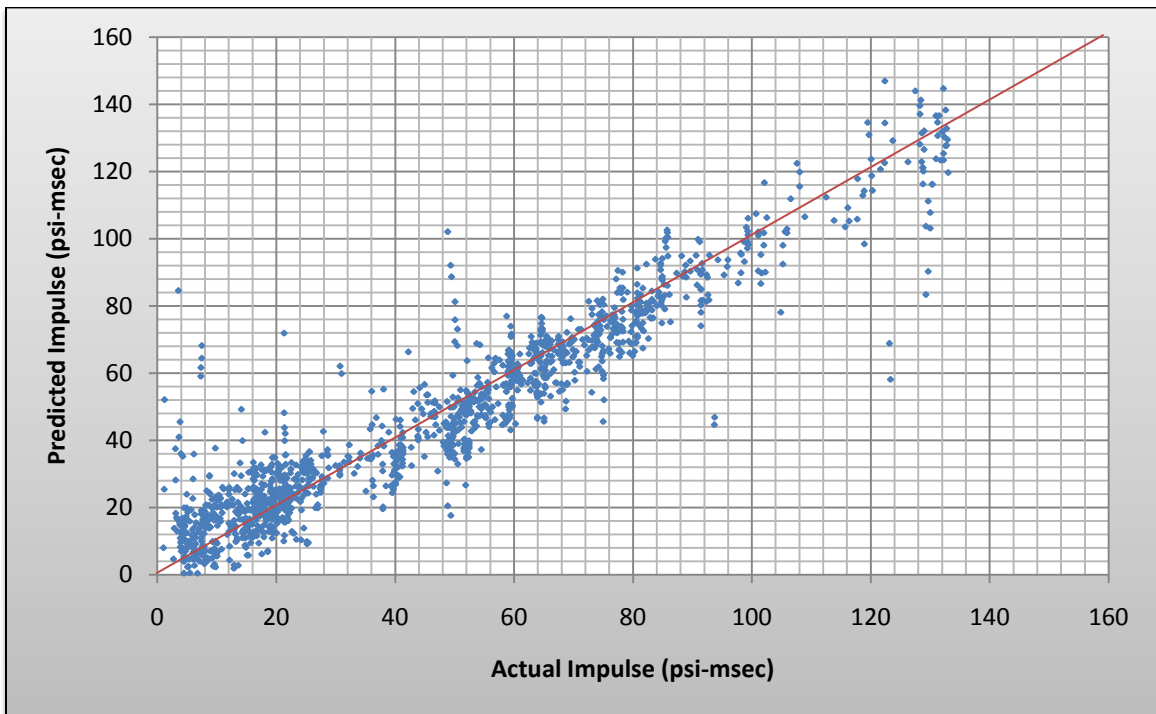
**Figure C-38. Duration ANN – 300 Neurons – Biased Grid**
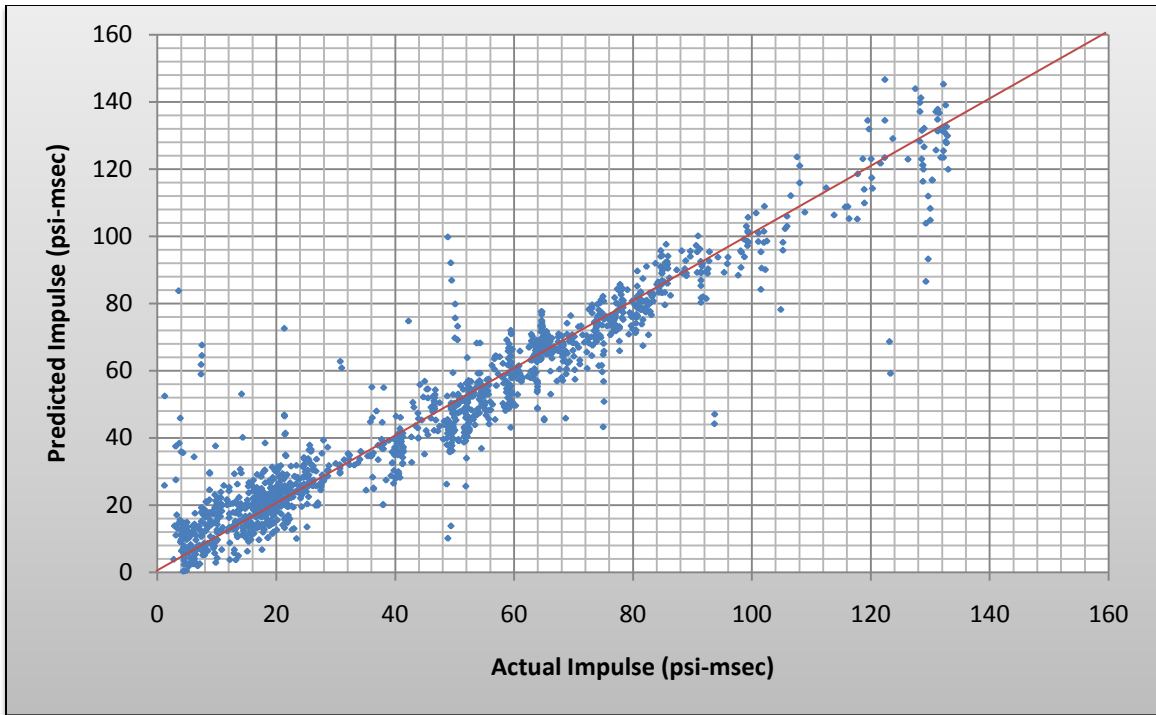
**Figure C-39. Duration ANN – 400 Neurons – Biased Grid**

Correlation Factor = 0.9681
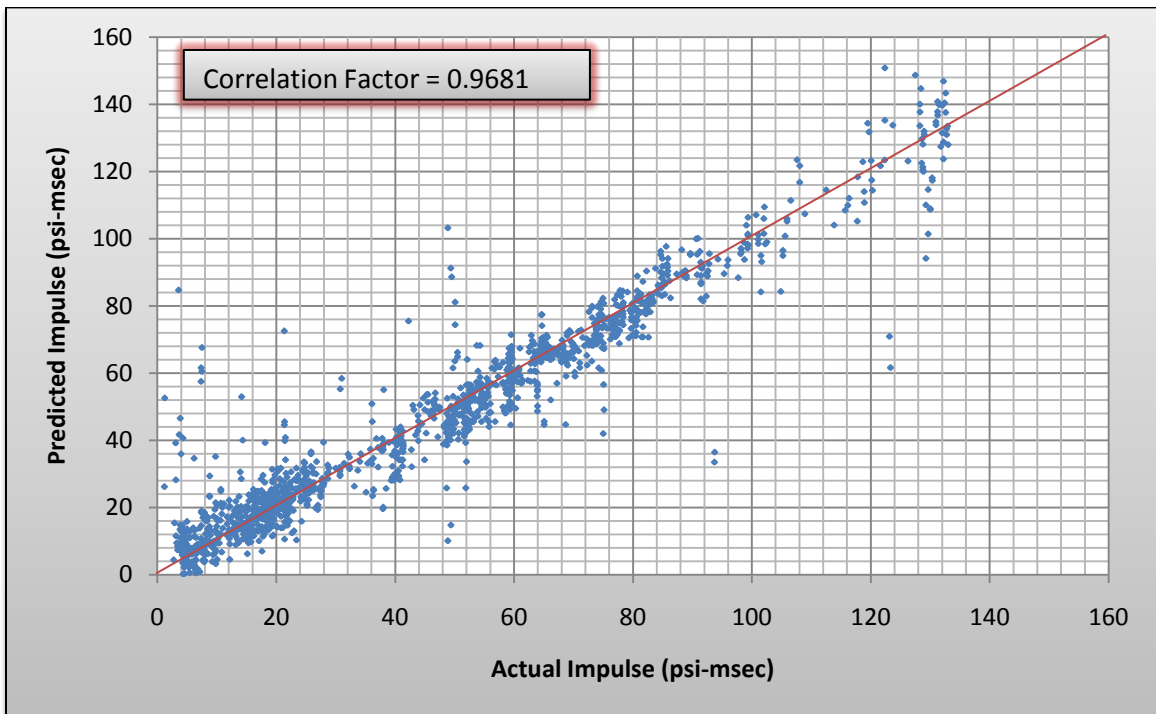
Figure C-40. Duration ANN – 500 Neurons – Biased Grid

LIST OF SYMBOLS, ABBREVIATIONS, AND ACRONYMS

2D	two-dimensional
3D	three-dimensional
A	Jones–Wilkins–Lee equation of state linear constant
ADINA	commercial modeling code
AF_I	adjustment factor for the impulse load
AF_p	adjustment factor for the pressure load
ALE	arbitrary Lagrangian–Eulerian
ANN	artificial neural network
AUTODYN	commercial blast modeling hydrocode
B	Jones–Wilkins–Lee equation of state linear constant
b	thickness of barrier wall
CFD	computational fluid dynamics
CMU	concrete masonry unit
CSD	computational solid dynamics
CTH	government owned shock physics modeling code
cm	centimeter
d_1	distance from the explosive to the barrier wall
d_2	distance from the barrier wall to the building surface
DYNA2D	government owned finite element modeling code
DYSMAS	government owned hydrocode
E_o	detonation energy per unit volume
EOS	equation of state
e	specific internal energy
e_a^{21}	relative solution difference between the finest grid and the next finest grid size
FEFLO	blast modeling code
FSI	fluid–structure interaction
f_1, f_2, f_3	computational result at the respective mesh refinement level
ft	feet
GCI	grid convergence index
GCI^{21}	between the finest grid solution, f_1, and the next-coarsest grid solution, f_2
g	gram
H	height of the barrier wall
h_S	height of the building
I_1, I_2, I_3	Impulse values from computational methods at the corresponding mesh refinement
i	impulse
JWL	Jones–Wilkins–Lee (equation of state)
kg	kilogram
kPa	kilopascal
lb	pound
LS-DYNA	commercial finite element modeling code
MAE	mean absolute error
MPa	megapascal
MPM	Material Point Method
m	meter

mm	millimeter
ms	millisecond
psi	pounds per square inch
p	rate of convergence
p_1, p_2, p_3	Impulse values from computational methods at the corresponding mesh refinement
R_1, R_2	Jones–Wilkins–Lee equation of state non-linear constants
R1, R2 …	gauge placements (illustrated in Figure 18)
RGIN	radial Gaussian
RMSE	root mean square error
r_{ji}	mesh refinement ratio
SHAMRC	blast modeling code
SPH	Smoothed Particle Hydrodynamic
T	temperature of explosive gas in Jones–Wilkins–Lee equation of state
TM5-1300	free-field blast model (*cf.* Figure 8)
TNT	2-,4-,6-trinitrotoluene
t_{dur}	duration of positive phase of impulse
t_{oa}, TOA	time of arrival of blast front
V	ratio of the volume of detonation products to the volume of undetonated high explosive
W	amount of TNT detonated in the model
w_S	width of the building in meters
y (unit)	height of explosive effect at the building's front face is specified length unit
Z	distance from the explosive to the building in meters
γ	ratio of specific heats
ρ	mass density
ω	Jones–Wilkins–Lee equation of state non-linear constant